

# **Results and Interpretation of Hydraulic and Tracer Testing in the Prow Pass Tuff at the C-Holes**

**Yucca Mountain Project Milestone SP32E7M4  
(BA..)**

Paul W. Reimus  
Andrew Adams  
Marc J. Haga  
Andrew Humphrey  
Timothy Callahan  
Ioana Anghel  
Dale Counce\*

With contributions from staff of the United States Geological Survey

Chemical Sciences and Technology Division  
Earth and Environmental Sciences Division  
Los Alamos National Laboratory

Property of CRWMS-M&O  
Technical Information Center  
1211 Town Center Drive  
Las Vegas, NV 89144  
(702) 295-3615

April 1999

## Contents

	<u>Page</u>
Executive Summary .....	iv
1.0 Introduction .....	1.1
2.0 Equipment and Instrumentation Used in Testing .....	2.1
3.0 Hydraulic Tests in Prow Pass Interval .....	3.1
4.0 Conservative Tracer Testing in the Prow Pass Tuff .....	4.1
5.0 Reactive Tracer Test in the Prow Pass Tuff .....	5.1
6.0 Batch Measurements of Lithium Sorption to C-Holes Tuffs .....	6.1
7.0 Dynamic Laboratory Transport Experiments .....	7.1
8.0 Diffusion Cell Experiments .....	8.1
9.0 Discussion of Differences in Conservative and Reactive Tracer Test Interpretations ..	9.1
10.0 Quality Assurance Status of Data and Interpretations .....	10.1
Appendix A: Hydraulic Tests in the Prow Pass Tuff, May to September 1998, Yucca Mountain, Nye County, Nevada .....	A.1
Appendix B: Tracer Tests in the Prow Pass Tuff, June to September 1998, Yucca Mountain, Nye County, Nevada .....	B.1
Appendix C: Reactive Tracer Testing in the Bullfrog Tuff .....	C.1
Appendix D: Description of Mathematical Models in Computer Codes RELAP and RETRAN .....	D.1

# **Results and Interpretation of Hydraulic and Tracer Testing in the Prow Pass Tuff at the C-Holes**

Paul W. Reimus

Andrew Adams

Marc J. Haga

Andrew Humphrey

Timothy Callahan

Ioana Anghel

Dale Counce

With contributions from staff of the United States Geological Survey

## **Executive Summary**

Predicting the future performance of a potential high-level nuclear waste repository at Yucca Mountain requires understanding saturated-zone groundwater flow and radionuclide transport processes. To test conceptual saturated zone flow and transport models at the field scale, Los Alamos National Laboratory (Los Alamos) and the United States Geological Survey (USGS) conducted a series of cross-hole hydraulic and tracer tests over a distances of ~30-80 meters (with a hydraulic observation well also located about 850 meters away) in fractured tuffs ranging from about 125 to 200 meters below the water table at the C-Holes (a cluster of 3 wells located about 1.5-km from the potential repository footprint).

The testing was conducted in the Prow Pass member of the Crater Flat Tuff in 3 overlapping phases from June 1998 through January 1999. The 3 phases were: (1) hydraulic testing (USGS lead), (2) conservative tracer testing (USGS lead), and (3) reactive tracer testing (Los Alamos lead). Hydraulic responses indicated a delayed water yield characteristic of a fissure-block aquifer. The Prow Pass Tuff was found to be hydraulically connected to the overlying Calico Hills formation but not to underlying units. Fracture hydraulic conductivities in the hydraulic test(s) were estimated to range from 0.8 to 1.0 m/d, and matrix hydraulic conductivities were estimated to range from 0.000003 to 0.0002 m/d. Fracture storativity was estimated to be 0.00004, and matrix storativity estimates ranged from 0.0003 to 0.0004. Overall storativity was estimated to be 0.0004.

Conservative tracer testing involved simultaneous injection of iodide ion (as sodium iodide) and 2,4,5-trifluorobenzoic acid (TFBA) into UE-25 c#3 while UE-25 c#2 was pumped at about 19.5 liters/min. 30% of the water produced from c#2 was recirculated into c#3 (located about 30 meters from c#2). The tracer responses yielded estimates of longitudinal dispersivity, flow porosity, and matrix diffusion parameters for use in performance assessment models.

Reactive tracer testing was conducted between c#3 and c#2 using the same test configuration and approximately the same flow rates as in the conservative tracer test. Tracers in the reactive tracer test included pentafluorobenzoic acid (PFBA), bromide ion, chloride ion, lithium ion, and three different polystyrene microspheres used as colloidal tracers. The tracer responses yielded estimates of longitudinal dispersivity, flow porosity, matrix diffusion parameters, sorption parameters for lithium, and colloid transport parameters as a function of colloid size and injection solution chemistry.

Both the conservative and reactive tracer tests were analyzed (independently by USGS and Los Alamos staff) using conceptual single- and dual-porosity model formulations. Flow porosity estimates from both tests were less than 0.01. Longitudinal dispersivity estimates ranged from 4.5 to 64 meters when wellbore mixing was assumed to be small, with differences attributable to different assumptions regarding the flow fields and tracer travel distances. Matrix diffusion parameters were reported in different ways for the two tests (reflecting the different models used). For conservative tracer testing, a clear determination of whether a single- or dual-porosity model best explained the tracer data could not be made. However, for reactive tracer testing, a dual-porosity conceptual model was clearly needed to explain the tracer responses. Estimates and uncertainty bounds for fracture apertures, fracture spacing, matrix porosity, and effective matrix diffusion coefficients (derived from the lumped parameters used to describe the diffusion processes) are discussed in the report. Deduced sorption parameters for lithium ion were greater than laboratory-derived sorption parameters, suggesting that the laboratory-derived parameters may be conservative when used in field-scale performance assessment calculations. Microsphere transport was highly attenuated relative to the solute tracers in the reactive tracer test, indicating significant filtration of these colloid tracers over the distance and time scales of the test.

This report also includes the results and interpretations of laboratory tests conducted to support and constrain the interpretations of the field tracer tests. Laboratory testing included batch lithium sorption experiments, dynamic transport experiments in crushed and fractured tuff columns, and diffusion cell experiments to measure solute matrix diffusion coefficients. Stand-alone reports by USGS authors on hydraulic and conservative tracer testing in the Prow Pass Tuff are also included as appendices. For completeness, the results and interpretation of a reactive tracer test conducted in the Bullfrog Tuff at the C-holes in 1996-1997 is included as an appendix.

## 1.0 Introduction

Yucca Mountain, Nevada, located about 145 km northwest of Las Vegas, is the site of a potential high-level nuclear waste repository. It currently is undergoing extensive characterization and assessment to determine its suitability for such a role. Current plans call for wastes emplaced within Yucca Mountain to be isolated from the accessible environment by a system of multiple barriers. These include "engineered barriers," consisting of components within the repository itself, and a two-part "geologic barrier," consisting of (1) the unsaturated tuff between the repository and the regional aquifer below, and (2) the saturated-zone aquifer system extending from directly below the repository to the down-gradient wells and springs that mark the final groundwater discharge zone. The characterization of groundwater flow and radionuclide transport processes within the saturated zone is the subject of this study.

To support this characterization process, a number of hydraulic and tracer tests have been conducted in the saturated zone at a three-well complex known as the C-holes complex (UE-25c#1, UE-25c#2, and UE-25c#3), which is located approximately 2 km southeast of the potential repository footprint. Fig. 1-1 shows the location and surface layout of the C-holes. The C-holes were drilled on a two-tiered drill pad in a channel of an ephemeral stream that cuts through Bow Ridge, a spur of Yucca Mountain. The lower tier of the pad, in which borehole UE-25 c#1 (c#1) was drilled, is at an altitude of about 1,130.5 m above sea level. The upper tier, in which boreholes UE-25 c#2 (c#2) and UE-25 c#3 (c#3) were drilled, is at an altitude of about 1,132.3 m. The C-holes are 30.4-76.6 m apart at the land surface (Fig. 1-1), but they deviate substantially at depth. An additional observation well for hydraulic responses, UE-25 ONC#1 (ONC#1), is located on the west side of Bow Ridge at an altitude of 1,162.8 m, 874.8 m northwest of c#2 and 851.3 m northwest of c#3.

The C-holes were completed to a depth of 914 m below land surface in easterly dipping Miocene tuffaceous rocks (Table 1-1), which have been offset by high-angle, northerly and northwesterly trending faults (Day and others, 1998). The tuffaceous rocks consist of nonwelded to densely welded ash-flow tuff with intervals of ash-fall tuff and volcaniclastic rocks. In the vicinity of the C-holes, the tuffaceous rocks are estimated to be 1,040 to 1,590 m thick. These tuffaceous rocks are pervaded by tectonic and cooling fractures that predominantly strike northward and dip westward at high angles (Geldon, 1996, pp. 7-10). The water table in the vicinity of the C-holes ranges from about 335 to 520 m below the land surface (O'Brien et al., 1995). In the C-holes, depths to water range from 400 to 402 m. Water in the tuffaceous rocks generally flows southeasterly beneath Yucca Mountain (Tucci and Burkhardt, 1995) and discharges as springs in the Amargosa Desert and Death Valley (D'Agnese et al., 1997). Regional flow patterns can be disrupted by faults acting as conduits or barriers to flow (Geldon et al., 1998). Several thousand meters of Paleozoic carbonate rocks underlie the tuffaceous rocks starting about 455 m below the bottom of the C-holes, or ~1370 m below land surface.

The Miocene tuffaceous rocks in the area of the C-hole complex comprise a single aquifer, in which the volume and direction of ground-water flow are controlled mainly by proximity to faults, fracture zones, and partings (Geldon et al., 1998). Flow within the Miocene tuffaceous rocks at the C-hole complex comes from discrete intervals with layered heterogeneity (Geldon, 1996, pp. 13-20). The composite transmissivity of Miocene tuffaceous rocks within 3 km of the C-holes decreases northwesterly from 2,600 to 700 m<sup>2</sup>/d and averages about 2,300 m<sup>2</sup>/d (Geldon et al., 1997). The storativity of these rocks ranges from 0.0005 to 0.003. In contrast to the tuffaceous rocks, Paleozoic carbonate rocks in the Yucca Mountain area have a

transmissivity between 4,800 and 10,800 m<sup>2</sup>/d and a storativity of 0.0005 (Leap and Belmonte, 1992).

Fig. 1-2 depicts the hydrogeology below the water table at the C-holes complex. Hydrogeologic interval boundaries are delimited by the location of transmissive intervals, which typically comprise a small part of the geologic units in which they occur and can overlap two geologic units. The geologic units below the water table at the C-holes are depicted in Fig. 1-3, along with fracture densities and estimated average matrix porosities in each unit. A consistent observation in all hydrogeologic units below the water table is that bulk permeabilities (determined from aquifer tests) exceed matrix permeabilities (determined from laboratory core measurements) by 2 to 6 orders of magnitude (Geldon, 1996, p. 70; Geldon, 1993, pp. 63-64). This high bulk-to-matrix permeability contrast indicates that field-scale features, such as faults and fracture zones, strongly influence flow in tuffaceous rocks. Flow logs in the C-holes indicate that most flow in the Miocene tuffaceous rocks is from discrete fracture zones and intervals with the largest matrix permeability.

Although flow in the Miocene tuffaceous rocks occurs predominantly in fractures, most of the water in these rocks is stored in the pores of the matrix. Matrix porosities in the C-holes range from about 0.10 to 0.35. Radionuclide and tracer transport in fractures, therefore, could be attenuated by diffusive mass transfer between the fractures and the rock matrix, a process known as matrix diffusion. Matrix diffusion in fractured systems has been discussed and modeled at length by Neretnieks (1980); Grisak and Pickens (1980); Tang et al. (1981); Maloszewski and Zuber (1983, 1985); and Moench, (1995). A system exhibiting fracture and matrix flow frequently is called a "dual-porosity, dual permeability" system. When the matrix permeability is small compared to the fracture permeability (e.g., smaller by a factor of 100 or more), the matrix permeability can be assumed negligible in transport calculations, and the system is then often referred to as simply a "dual-porosity" system. It has been suggested elsewhere that the saturated zone in the vicinity of Yucca Mountain should behave as a dual-porosity system (Robinson, 1994). This concept has important transport implications, particularly for sorbing radionuclides, because it suggests that solutes moving through fractures will have access to a very large surface area for sorption once they diffuse out of fractures and into adjacent matrix pores.

In 1996 and 1997, hydraulic and tracer tests were conducted in the lower part of the Bullfrog Tuff of the Crater Flat Group in the C-holes (the Lower Bullfrog hydrogeologic interval in Fig. 1-2). As reported Geldon et. al. (1997), the hydraulic tests confirmed that the Lower Bullfrog interval is a dual-permeability aquifer at the C-holes complex, with the matrix permeability being much smaller than the fracture permeability. The tracer tests in this interval, particularly the reactive tracer test (Reimus et al. 1998, Section 2.0), confirmed that a dual-porosity conceptual transport model was consistent with field-scale transport observations. These tests are not discussed further here (however, Appendix C is a chapter from Reimus et al. 1998 that presents the results and interpretation of reactive tracer tests in the Lower Bullfrog interval).

This report presents the results and interpretations of hydraulic and tracer tests conducted from June 1998 to January 1999 in the lower part of the Prow Pass Tuff of the Crater Flat Group in the C-holes (the Prow Pass hydrogeologic interval in Fig. 1-2). The locations of the packers used to isolate the test interval in each C-hole are shown in Figs. 1-2 and 1-3. Table 1-2 gives the locations of other downhole equipment and instrumentation installed in the C-holes and in ONC-1 for Prow Pass testing. Although the Prow Pass Tuff in the C-holes is 140 to 147 m thick

(Table 1-1), the Prow Pass interval in these boreholes is 59 to 74 m thick (Table 1-2), and zones with relatively large fracture or matrix permeability that transmit water within the Prow Pass interval of c#1, c#2, and c#3 have total thicknesses of 19 to 32 m (Fig. 1-2).

The Prow Pass testing was conducted in three phases (with overlap between each phase): (1) hydraulic testing, (2) conservative tracer testing, and (3) reactive tracer testing. The results and interpretation of these tests are presented in Sections 3.0, 4.0, and 5.0 of this report, respectively. Equipment and instrumentation common to all tests are described briefly in Section 2.0. Sections 6.0, 7.0, and 8.0 present the results of laboratory batch sorption tests, dynamic transport tests, and diffusion tests, respectively, conducted at Los Alamos National Laboratory to support the interpretation of the field tracer tests and to offer comparisons between laboratory and field data. These last three sections were taken largely from Reimus et al. (1998, Sections 3.0, 4.0, and 5.0), with minor modifications. Appendices A and B are reports on hydraulic and conservative tracer testing written for this document by USGS authors. Summaries of these reports are contained in Sections 3.0 and 4.0. Appendix C contains the results and interpretations of reactive tracer test that was conducted from 1996 to 1997 in the Lower Bullfrog interval by LANL (Reimus et al., 1998, Section 2.0). This appendix is included in this report because the final interpretations of that test never have been documented in a Yucca Mountain Site Characterization Project Level 3 milestone report. Appendix D contains a description of the mathematical models used to interpret the reactive tracer tests in the Prow Pass and Lower Bullfrog intervals (from Reimus et al., 1998, Appendix A).

## Section 1.0 References

- Geldon, A. L. 1993. *Preliminary Hydrogeologic Assessment of Boreholes UE-25 c#1, UE-25 c#2, and UE-25 c#3, Yucca Mountain, Nye County, Nevada, 1993.* USGS/WRI-92-4016. Denver, Colorado: U.S. Geological Survey, pp. 35-37, 63-64, 68-70. TIC Catalog # 210506. RIS Accession # MOL.19960808.0136.
- Geldon, A. L. 1996. *Results and Interpretation of Preliminary Aquifer Tests in Boreholes UE-25c#1, UE-25c#2, and UE-25c#3, Yucca Mountain, Nye County, Nevada.* Water-Resources Investigations Report 94-W-0412. Denver, Colorado: U.S. Geological Survey, pp. 7-10, 13-20, 70. TIC Catalog # 223656
- Geldon, A. L., Umari, A. M. A., Fahy, M. F., Earle, J. D., Gemmell, J. M., and Darnell, J., 1997, *Results of Hydraulic and Conservative Tracer Tests in Miocene Tuffaceous Rocks at the C-Hole Complex, 1995 to 1997, Yucca Mountain, Nye County, NV,* Yucca Mountain Site Characterization Project Milestone SP23PM3, U. S. Geological Survey, Denver, CO. MOL.19980122.0412.
- Geldon, A.L., Umari, A.M.A., Earle, J.D., Fahy, M.F., Gemmell, J.M., and Darnell, Jon. 1998. *Analysis of a multiple-well interference test in Miocene Tuffaceous rocks at the C-hole complex, May-June 1995, Yucca Mountain, Nevada:* U.S. Geological Survey Water-Resources Investigations Report 97-4166, 33 p. MOL.19980514.0524.

D'Agnese, F.A., Faunt, C.C., Turner, A.K., and Hill, M.C. 1997. *Hydrogeologic evaluation and numerical simulation of the Death Valley regional ground-water flow system, Nevada and California*: U.S. Geological Survey Water-Resources Investigations Report 96-4300, 124 p. TIC Catalog # 235008.

Grisak, G. E. and J. F. Pickens. 1980. "Solute Transport through Fractured Media, 1: The Effect of Matrix Diffusion." *Water Resour. Res.*, 16(4), 719-730. RIS Accession # NNA.19890315.0006.

Leap, D.I., and Belmonte, P.M. 1992. Influence of pore pressure on apparent dispersivity of a fissured dolomitic aquifer: Dublin, Ohio, *Ground Water*, V. 30, no. 1, p. 87-95. TIC Catalog # 239275.

Maloszewski, P., and A. Zuber. 1983. "Interpretation of Artificial and Environmental Tracers in Fissured Rocks with a Porous Matrix." In *Isotope Hydrology*, pp. 635-651. Vienna, Austria: International Atomic Energy Agency (IAEA). (Submitted to RIS for Accession # 5/21/99.)

Maloszewski, P., and A. Zuber. 1985. "On the Theory of Tracer Experiments in Fissured Rocks with a Porous Matrix." *J. Hydrology*, 79, 333-358. TIC Catalog # 222390.

Moench, A.F., 1995, Convergent radial dispersion in a double-porosity aquifer with fracture skin: Analytical solution and application to a field experiment in fractured chalk, *Water Resources Research*, V.31, No.8, p.1823-1835. TIC Catalog # 23312.

Neretnieks, I. 1980. "Diffusion in the Rock Matrix: An Important Factor in Radionuclide Migration?" *J. Geophys. Res.*, 85(B8), 4379-4397. (Submitted to RIS for Accession # 5/21/99.)

Nye County Nuclear Waste Repository Project Office, 1995, Borehole UE-25 ONC #1 and USW NRG-4 drilling and instrumentation report, Yucca Mountain, Nevada: Pahrump, Nev., Nye County Nuclear Waste Repository Program, various paging. RIS Accession # MOL.19960910.0231.

O'Brien G.M., Tucci, Patrick, and Burkhardt, D.J. 1995. *Water levels in the Yucca Mountain area, Nevada, 1992*: U.S. Geological Survey Open-File Report 94-311, 74 p. MOL.19951219.0019.

Reimus, P. W., Haga, M. J., Callahan, T. L., Anghel, I., Turin, H. J., Counce, D. 1998. *C-Holes Update Report: Reinterpretation of the Reactive Tracer Test in the Bullfrog Tuff and Results of Laboratory Testing*, Yucca Mountain Site Characterization Project Milestone Report SP32E2M4SZ, Los Alamos National Laboratory, Los Alamos, NM, Sections 2.0, 3.0, 4.0, 5.0, and Appendix A. (Submitted to RIS for Accession # 5/21/99.)

Robinson, B. A. 1994. "A Strategy for Validating a Conceptual Model for Radionuclide Migration in the Saturated Zone beneath Yucca Mountain." *Rad. Waste Mgmt. & Env. Restor.*, 19, 73-96. TIC Catalog # 222513.

Tang, D. H., E. O. Frind, and E.A. Sudicky. 1981. "Contaminant Transport in a Fractured Porous Media: Analytical Solution for a Single Fracture." *Water Resour. Res.*, 17(3), 555-564. TIC Catalog # 225368. RIS Accession # NNA.19900711.0084.

Tucci, Patrick, and Burkhardt, D.J. 1995. *Potentiometric-surface map, 1993, Yucca Mountain and vicinity, Nevada: U.S. Geological Survey Water-Resources Investigations Report 95-4149*, 15 p. TIC Catalog # 222866.

## Section 1.0 Tables

Table 1-1. Stratigraphy of Miocene tuffaceous rocks in the C-hole area (Geldon et al., 1998; Nye County Nuclear Waste Repository Project Office, 1995). (DTN GS970708312314.007 [for C-holes only]).

Geologic Unit	Depth below land surface, in meters			
	UE-25 ONC#1	UE-25 c#1	UE-25 c#2	UE-25 c#3
Timber Mountain Group				
Rainier Mesa Tuff	30-68	not present	not present	not present
Paintbrush Group				
Tiva Canyon Tuff	68-188	0-96	21-88	24-88
Topopah Spring Tuff	188-368	96-406	88-401	88-396
Calico Hills Formation	368-420	406-516	401-510	396-496
Crater Flat Group				
Prow Pass Tuff	420-469 <sup>+</sup>	516-656	510-652	496-644
Bullfrog Tuff	not reached	656-828	652-829	644-814
Tram Tuff	not reached	828-914 <sup>+</sup>	829-914 <sup>+</sup>	814-914 <sup>+</sup>

Table 1-2. Prow Pass Test Packer and Transducer Locations (c#2 and c#3 string settings Provided by the Nevada Test Site management and operations contractor; c#1 settings from Previous reports; ONC#1 settings from Nye County; depths in meters below land surface) (DTN GS970708312314.007 [c#1] and DTN GS990408312315.002 [c#2 and c#3]).

Feature	UE-25 c#1	UE-25 c#2	UE-25 c#3	UE-25 ONC#1
<b>Calico Hills</b>				
Top (bottom of casing in C-holes; bottom of packer 13 in ONC#1)	418	416	417	408
Transducer	None	486	472	450
Packer 1 in C-holes; packer 14 in ONC#1 (deflated in tests)	None	488-490	473-475	434-435
Bottom (top of packer 2 in C-holes; top of packer 15 in ONC#1)	547	531	540	450
<b>Prow Pass</b>				
Top (bottom of packer 2; bottom of packer 15 in ONC#1)	549	533	542	452
Upper transducer	552	587	592	458
Lower transducer	None	589	593	Not applicable
Bottom (top of packer 3 in C-holes; bottom of hole in ONC#1)	605	606	610	469
Guard packer (packer 3a)	None	612-614	616-618	Not applicable
<b>Upper Bullfrog</b>				
Top (bottom of packer 3 or 3a)	607	614	618	Not applicable
Transducer	610	616	620	Not applicable
Bottom (top of packer 4 in c#1; bottom of hole in others)	698	910	900	Not applicable
<b>Lower Bullfrog</b>				
Top (bottom of packer 4)	700	Not applicable	Not applicable	Not applicable
Transducer	703	Not applicable	Not applicable	Not applicable
Bottom (top of packer 5)	797	Not applicable	Not applicable	Not applicable

## Section 1.0 Figures

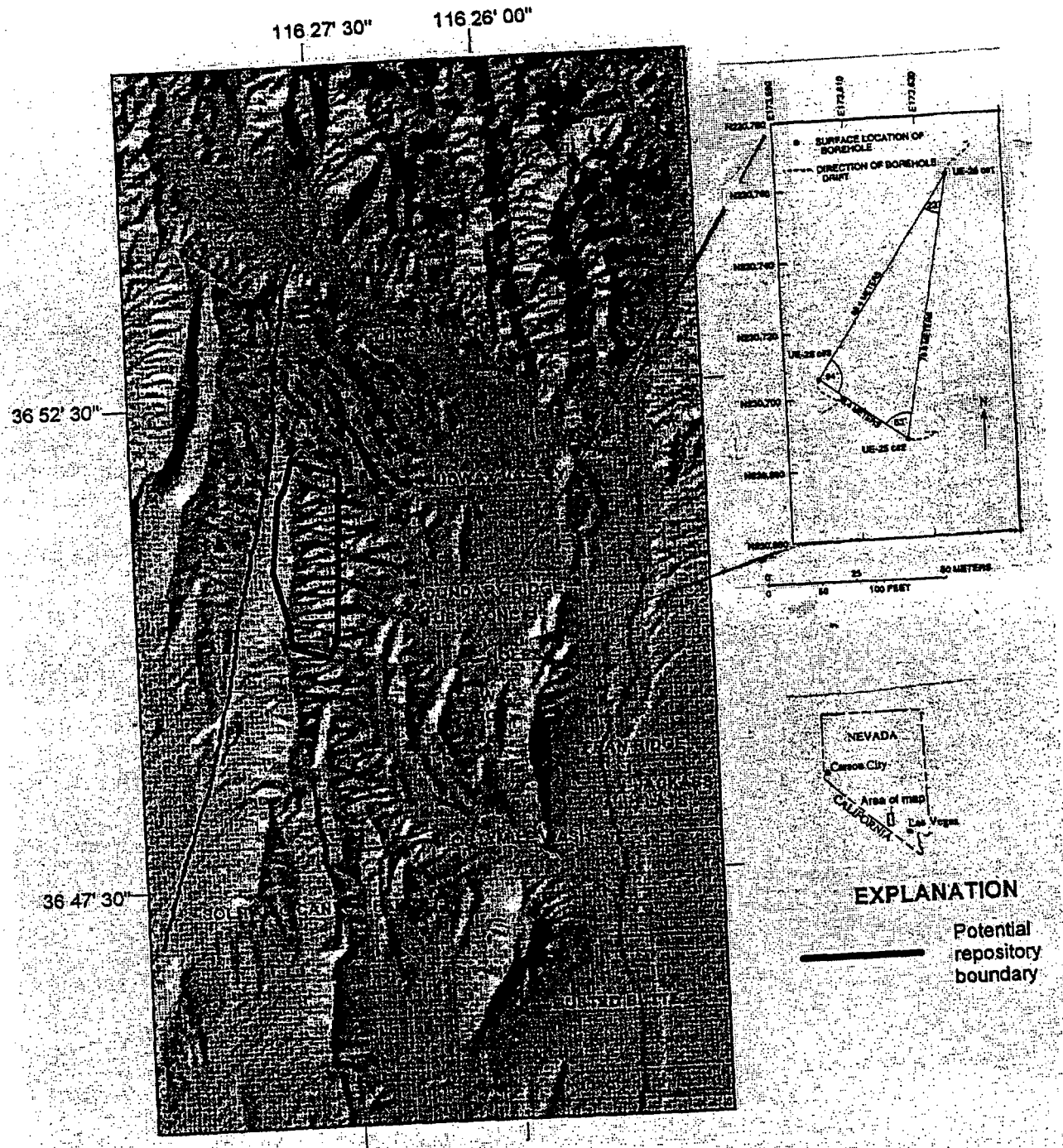


Figure 1-1. Location of the C-holes complex, boreholes UE-25c#1, UE-25c#2, and UE-25c#3 (C-holes map is referenced to Nevada State Zone 2 coordinates), and borehole UE-25 ONC#1.

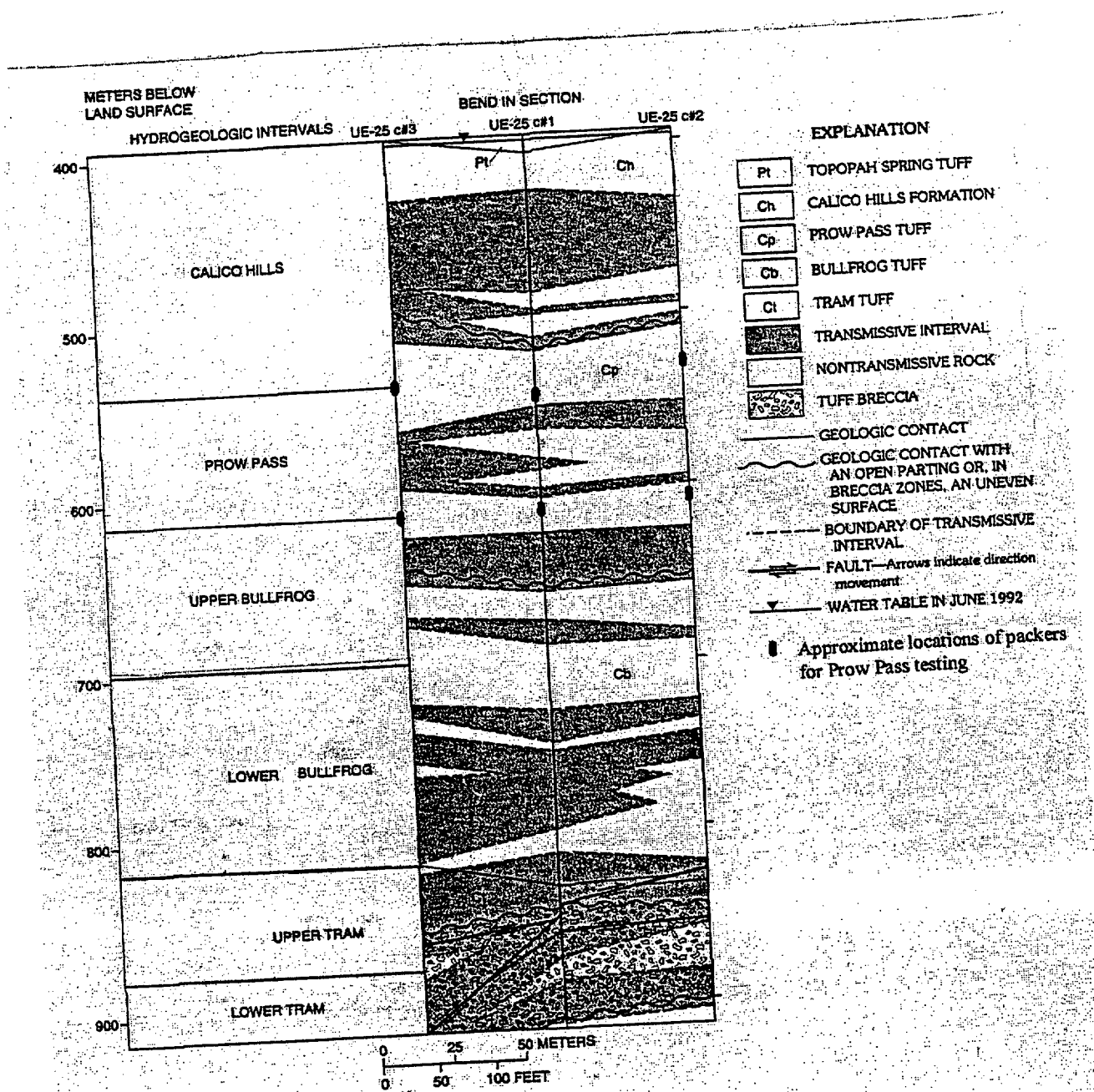
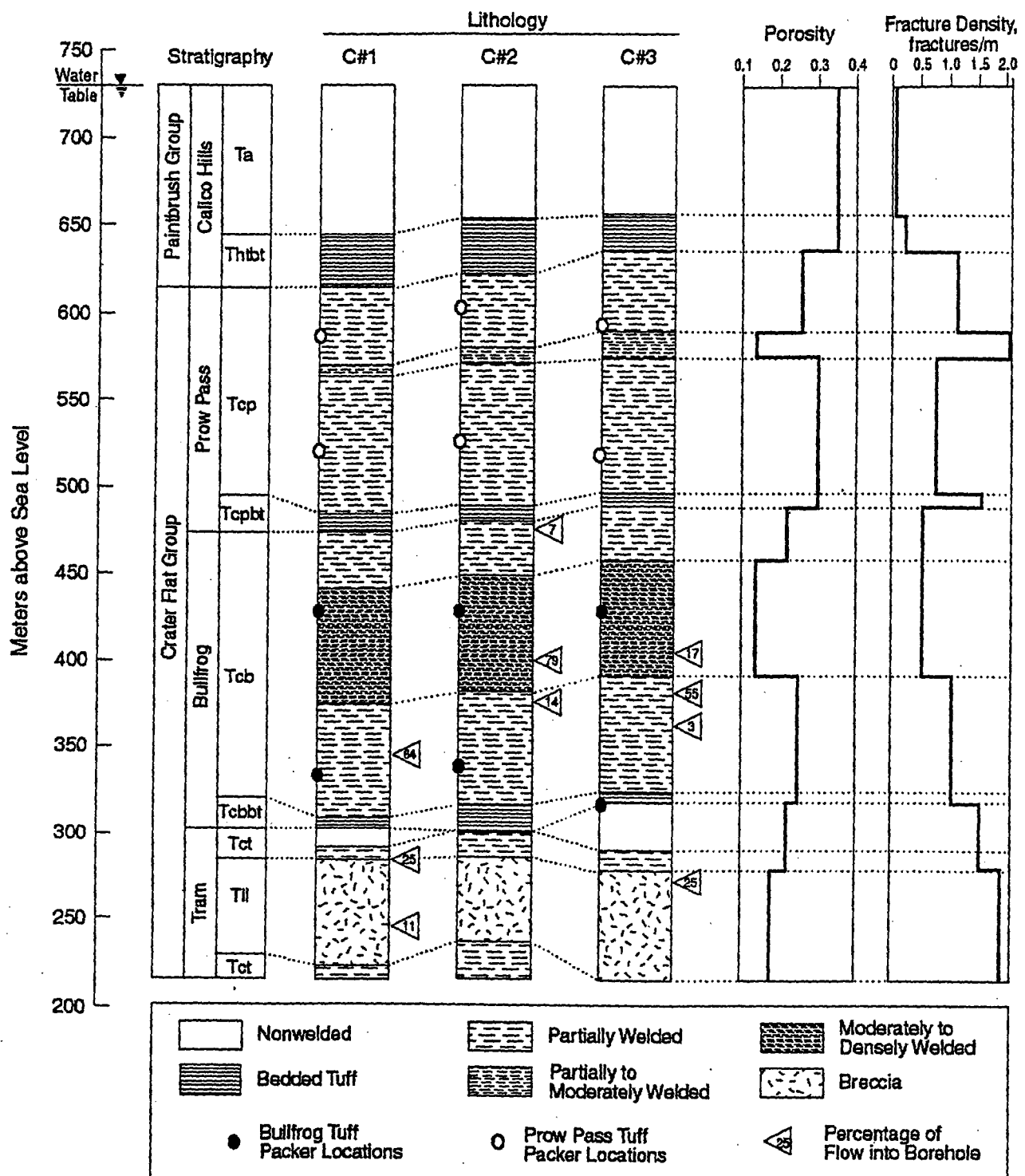


Figure 1-2. Hydrogeologic intervals in the C-holes





## **2.0 Equipment and Instrumentation Used in Testing**

Equipment and instrumentation used for hydraulic and tracer testing of the Prow Pass test interval at the C-holes is described briefly in the following sections. Monitoring equipment installed in ONC#1 is described by the Nye County Nuclear Waste Repository Project Office (1995).

### **2.1 Packers**

Dual-mandrel packers manufactured by TAM International, Inc., were installed in the C-holes at depths specified in Table 1-2. The packers are about 1.8 m long and have a diameter of about 22 cm when deflated. Suspended on 7.30-cm-diameter tubing, each packer contains twelve pass-through tubes to allow packer-inflation lines and electrical cable to be installed in the borehole. The packers were inflated individually by the injection of argon gas through 0.64-cm, stainless steel tubing. Inflation pressures, which were about 1,034 kPa above hydrostatic pressure at the depths at which packers were emplaced, ranged from about 2,758 to 5,861 kPa.

### **2.2 Pressure and Temperature Transducers**

Continuous records of pressure and temperature in packed-off intervals were obtained using absolute pressure transducers manufactured by Paroscientific, Inc. (Absolute pressure transducers record water pressure plus atmospheric pressure, whereas differential pressure transducers record only the water pressure). The transducers used in the C-holes were strapped onto the 7.30-cm-diameter tubing on which the packers were suspended. A well screen installed in the 7.30-cm-diameter tubing was opened to allow transducers to sense pressures in the Prow Pass (and to allow movement of water and tracers). The transducer signal was recorded at user-specified intervals by monitoring software installed on a personal computer (PC) in the office trailer at the C-hole complex.

### **2.3 Barometers**

A nonsubmersible, temperature-compensated pressure transducer manufactured by Paroscientific, Inc., was used as a barometer during the hydraulic tests discussed in this report. The barometer, which was emplaced in a temperature-controlled office trailer at the C-hole complex, operates in the same way as the transducers installed in the C-holes to record water pressure. The factory-calibrated accuracy of this barometer is  $\pm$  0.005 percent of its full operating range (103 kPa). The barometer was checked periodically against another barometer of the same type, which, also, was located in the office trailer.

### **2.4 Downhole Pumps**

Multi-stage Centrilift submersible pumps with a capacity of 0.3 to 1.3 L/s were emplaced in c#2 and c#3 in April 1998 for the Prow Pass hydraulic and tracer tests. The pumps, enclosed in protective shrouds, were installed into the tubing holding the packers

and transducers. The pump intake depth was 599.8 m in c#2 and 604.1 m in c#3. The pumps were powered by a 250 KW generator, and their frequencies were regulated by a variable-speed controller. Approximately 70% of the water pumped from c#2 was transported through a 15-cm-diameter pipeline to a leachfield in Fortymile Wash, about 8 km from the C-hole complex. The remaining 30% was recirculated into c#3 (see section 2.5).

## 2.5 Tracer Injection and Mixing Equipment

In c#2 and c#3, a 2.5-cm-diameter stainless steel flexible tube was lowered inside the 7.3-cm-diameter tubing to allow for injecting liquids from the surface into the test zone. The bottom of the 2.5-cm-diameter tube landed in a special fitting in 7.3-cm-diameter tubing. Water and tracer exited the 2.5-cm-diameter tubing through a pressure-sensitive "cracking" valve that was set to open at about 1,034 kPa above the pressure that the valve would sense if the tubing were filled with water all the way to the surface. This setting was intended to ensure that the tubing would remain full of water when injection or recirculation was not taking place. It also allowed for a more controlled injection or recirculation rate. The excess pressure required to open the cracking valve was supplied by a Moyno positive displacement pump on the surface.

A recirculation loop was set up in c#3 to pump the solution in the injection zone of c#3 to the surface through the annular space between the 7.3-cm-diameter tubing and the 2.5-cm-diameter tube, and then reinject it through the 2.5-cm-diameter tube. This process was intended to mix the tracer solution after injection. Mixing was attempted a few times during conservative tracer testing and once during reactive tracer testing, but it could not be sustained because the closed loop could not dissipate the heat generated by the pump motor, even with a refrigeration unit at the surface. Heat dissipation was necessary to keep the temperature in the test interval from rising to unacceptable levels.

During the tracer tests in which c#3 was used as the injection well, tracer-laden water from c#2 was reinjected into the Prow Pass test interval of c#3 through the 2.5-cm-diameter tube. The recirculated water passed through a plastic holding tank on its way from the pumped well to the injection well. The Moyno pump was used to inject tracers as described above.

A different tracer-injection system was used in c#1 than in c#3. In c#1, a rigid 4.2-cm-diameter tube was installed inside the 7.3-cm-diameter tubing, upon which the packers and transducers were suspended. A cracking valve installed at the bottom of the 4.2-cm-diameter tube allowed the tracer solution to flow into the Prow Pass interval when the pressure inside the injection tubing exceeded a specified amount.

## 2.6 Flowmeters

Vortex flowmeters were installed in c#2 and c#3 to record instantaneous and cumulative flow. Signal output from each flowmeter was converted from milliamperes to volts by wiring the flowmeter circuit to a temperature-compensated, 100-ohm resistor and using a multimeter to measure the voltage drop across the resistor. The flowmeter signal

was recorded at user-specified intervals by monitoring software installed on a personal computer (PC) in the office trailer at the C-hole complex. A regression equation developed on the basis of the flowmeter calibration was used by the software program to convert the voltage signal from the flowmeter to a pumping rate. Periodically, pumping rates recorded by the PC were checked against the cumulative volume recorded at the wellhead of c#2 or c#3 divided by the time elapsed in which the volume was pumped. Generally good agreement was maintained between recorded and computed pumping rates.

## **2.7 Data Acquisition and Instrument Control**

Data acquisition from, and control of, the transducers, barometer, flowmeter, and an automated water sampler used for hydraulic and tracer tests at the C-hole complex were accomplished with commercially available, graphic-language software called Labview (Johnson, 1995), which was installed on the PC in the office trailer. Labview is a Windows-based application that makes the PC monitor screen look and act like an instrument panel.

Two separate programs were written for data acquisition and instrument control. One program communicated with the transducers, barometer, and flowmeter; the other program communicated with the automated water sampler during tracer tests. The two programs ran simultaneously. Small utility programs (called "transfer programs") were written to transfer information back and forth between the two main programs in order to facilitate synchronization of the automated sampler operation with data acquisition from the transducers, barometer, and flowmeter.

The program communicating with the transducers, barometer, and flowmeter processed digital signals from these instruments through the serial-communications port of the PC and a digital multimeter. Equations written into the programs converted signal output into standard engineering units. This information was displayed on the PC monitor screen, written to a text file on the PC's hard drive, and backed up to a disk drive at user-specified intervals.

## **2.8 Automated Water Sampler**

A small volume of the water pumped out of c#2 was passed continuously through an automated sampler housed in a trailer near the borehole. This water was sampled for tracers at user-specified intervals programmed into the Labview data-acquisition and instrument-control software. The automated sampler was designed and built for tracer tests in the C-holes. Samples were obtained when the data-acquisition and instrument-control software opened a solenoid valve on a moving carriage assembly and filled 250-ml bottles placed in racks below the carriage assembly.

## **2.9 Onsite Analytical Equipment for Tracers**

Chemical analyses were conducted onsite during conservative tracer testing using high-pressure liquid chromatography. In this analytical procedure, a small aliquot of sampled water is injected into a fixed-volume loop in the high-pressure liquid chromatograph (HPLC). The injected water, together with a mobile-phase solvent is

forced by a ternary pump through a reverse-phase chromatographic column. This column retards the passage of constituents dissolved in the sample to different extents and results in characteristic "retention times" for different constituents. Outflow from the column moves through an ultraviolet (UV) detector. Attenuation of UV light passing through the detector is proportional to the concentration of tracers. If tracer is detected, a peak in a chromatogram drawn by an integrator interfaced to the detector will occur at a retention time anticipated from previously run standards. The integrator computes the area under the peak, which is converted to a concentration by prior calibration of standards. The Harry Reid Center, University of Nevada at Las Vegas, conducted all of the onsite analyses of conservative tracer testing samples for the USGS.

All tracers injected in the reactive tracer test were analyzed by Los Alamos National Laboratory. Samples were brought to Los Alamos for the analyses. Analytical methods are discussed in Section 5.2.

## Section 2.0 References

Johnson, G., 1995, Labview: graphical programming and application development: New York, N.Y., McGraw-Hill, 606 p. (Submitted to RIS for Accession # 5/21/99.)

Nye County Nuclear Waste Repository Project Office, 1995. Borehole UE-25 ONC #1 and USW NRG-4 drilling and instrumentation report, Yucca Mountain, Nevada: Pahrump, Nev., Nye County Nuclear Waste Repository Program, various paging. MOL.19960910.0231.

### **3.0 Hydraulic Tests in Prow Pass Interval**

Pumping in c#2 to create a forced hydraulic gradient for tracer tests in the Prow Pass interval at the C-hole complex began June 2, 1998 and continued uninterruptedly until September 22, 1998. The pump in c#2 shut off for 70 minutes on September 22 as one of two packers at the bottom of the Prow Pass interval (number 3) was being deflated. Injection of water into c#3 to expedite tracer transport began June 11 and continued without interruption until September 2. The injection pump was off briefly on September 2 and 3, while injection tubing was removed from c#3. Tracers were injected into c#3 on June 17 and into c#1 on July 31.

Responses of c#1, c#3, and ONC#1 to pumping June 2-11, in advance of the tracer tests, were analyzed as a constant-rate withdrawal test. After water injection into c#3 began on June 11, the superimposed effects of pumping water from c#2, injecting water into c#3, injecting tracers into c#3 and c#1, operating a mixing pump in c#3 intermittently, and mechanical problems that affected pumping and injection rates made it difficult to analyze data from the C-holes quantitatively. However, ONC#1 was far enough away from the pumping and injection wells that a water-level rise in ONC#1 resulting from injecting water into c#3 clearly could be separated from relatively minor drawdown in the well caused by pumping c#2. The water-level rise in ONC#1 from June 11 to September 1 was analyzed as a constant-rate injection test.

#### **3.1 Performance Tests**

Hydraulic and tracer tests in the Prow Pass interval were preceded by pump-performance, step-drawdown, and 1-day hydraulic tests conducted in c#2 and c#3 from April 21 to May 29, 1998. These tests were designed primarily to determine whether c#2 could be used as a pumping well for tracer tests and what the optimum pumping rate should be. These tests, also, were analyzed to determine values of hydraulic properties that would be expected from a longer hydraulic test that was planned to precede tracer tests in the Prow Pass. Fluctuations in water and atmospheric pressures between performance tests indicated barometric efficiency values (Table 3-1) for the C-holes and ONC#1 that were used to analyze hydraulic tests in the Prow Pass.

#### **3.2 Analytical Methods**

Although rock at the C-hole complex is fractured pervasively, hydrogeologic intervals respond to pumping as an equivalent porous medium (Geldon, 1996; Geldon et al., 1998). Therefore, solutions developed for porous media were used to analyze data from hydraulic tests in the Prow Pass interval. Most of the data were analyzed using the method of Streltsova-Adams (1978) for a fissure-block aquifer. The method of Cooper and Jacob (1946) for an infinite, homogeneous, isotropic, confined aquifer was used to analyze drawdown in observation wells as a function of distance from the pumping well. Analysis of data in this study was restricted to observation wells, because most water-level changes in pumping wells at the C-hole complex are too large and rapid to be explained solely by hydraulic properties of the pumped interval (Geldon, 1996).

#### **3.3 Constant-Rate Withdrawal Test**

A constant-rate withdrawal (CRW) test in the Prow Pass interval started June 2, 1998. The pumping well for this test was c#2, and the observation wells for the test were c#1, c#3, and ONC#1.

Prior to starting the test, the packer in c#2 between the Prow Pass and Calico Hills intervals was deflated, and the two intervals, together, were pumped for 37 minutes at a rate of 0.57 L/s to fill tubing in the pumping well to the level of the flowmeter. After pumping stopped, the packer in c#2 between the Prow Pass and Calico Hills intervals was reinflated. With slight residual effects from the pre-test pumping (which were removed to analyze the test), pumping for the CRW test in the Prow Pass began at 16:00:02. Discharge averaged 0.33 L/s between June 2 and 11, a period of 12,500 minutes. Pumping water into c#1 on June 5 to attempt a tracer test, injecting argon gas into c#1 on June 9 to blow sediment out of the tracer injection valve, and testing the downhole mixing pump in c#3 on June 10 briefly disturbed discharge from c#2 and pressures in c#1 and c#3. The CRW test was terminated on June 11, 1998 at 08:19 when operations began to start a tracer test between c#3 and c#2.

The pumping in c#2 caused 135 m of drawdown in the Prow Pass interval of c#2 three minutes after pumping started. However, the water level rebounded 22 m in the next 9 minutes. Subsequently, drawdown increased steadily but slowly and was about 128 m after 12,500 minutes of pumping. On the basis of an equation given by Lohman (1979) and values of transmissivity and storativity determined in this and previous tests, only 1.04 percent of this drawdown (1.34 m) is estimated to have resulted from stressing the aquifer.

The pumping in c#2 caused oscillatory drawdown in the Prow Pass interval of observation wells. After 12,500 minutes of pumping, this drawdown was 54 cm in c#3 (Fig. 3-1), 12 cm in c#1 (Fig. 3-2), and 0.9 cm in ONC#1. Plotted on log-log scales, drawdown in the Prow Pass interval of c#1 and c#3 indicated delayed yield that is characteristic of a fissure-block aquifer (Streltsova-Adams, 1978).

The pumping in c#2 indicated that the Calico Hills and Prow Pass intervals are connected by fractures beyond borehole walls, because the Calico Hills responded to pumping in the Prow Pass wherever it was monitored. During the CRW test, the water level in the Calico Hills was drawn down as much as 19 cm in c#2 and 12 cm in c#3. In contrast, no drawdown was observed below the Prow Pass in c#2 and c#3 and below the Upper Bullfrog in c#1 during this test. The Upper Bullfrog drawdown in c#1 was 55 cm. The general lack of a response to pumping below the Prow Pass probably indicates that the highly permeable Lower Bullfrog and Upper Tram intervals in the C-holes were isolated from the Prow Pass interval during the CRW test.

The response to pumping of the Calico Hills in the C-holes and the Upper Bullfrog in c#1 made it necessary to apportion flow among the responding intervals to determine hydraulic properties. Lacking a flow survey for the test conditions, interval flow was determined by solving analytical equations simultaneously for interval discharge and transmissivity. To make the number of equations equal to the number of unknowns, it was assumed that (1) transmissivity values for the Calico Hills and Prow Pass intervals in the C-holes are constant, (2) the transmissivity of the Calico Hills is  $5.6 \text{ m}^2/\text{d}$  (on the basis of previous hydraulic tests), and (3) flow laterally and vertically within the Calico Hills interval was the same in each of the C-holes during the test. These assumptions were based on analyses and interpretations of previous hydraulic tests, borehole flow surveys, borehole geophysical logs, and other information, that are discussed in reports by Geldon (1996) and Geldon and others (1997).

Calculations indicated that the Prow Pass interval contributed 94 percent of the total flow in c#2 and c#3 but only 24 percent of the flow in c#1. The substantially different flow from the Prow Pass in c#1 does not seem reasonable because lithologic changes that might account for variable flow do not occur in the Prow Pass interval at the C-hole complex. It is more likely that flow from the Calico Hills interval or the transmissivity of either or both the Prow Pass and Calico Hills intervals is not constant throughout the C-hole complex. Unquantifiable uncertainty results from failure to apportion flow satisfactorily.

Hydraulic properties of the Prow Pass interval determined from analyses of drawdown during the CRW test are summarized in Table 3-2. Hydraulic test results are discussed in more detail in Appendix A at the back of this report.

### 3.4 Constant-Rate Injection Test

From June 11 to September 1, 1998, a period of 118,159 minutes, 676,973 L of water were pumped into c#3 to conduct tracer tests. The injection rate ranged from 0.032 to 0.16 L/s before tracers were injected into c#3 on June 17, but it subsequently was stabilized by periodic valve adjustments. From June 11 to September 1, the injection rate averaged 0.095 L/s.

As water was being injected into c#3 from June 11 to September 1, 2,311,290 L of water were withdrawn from c#2 at an average rate of 0.33 L/s. Injecting water into c#3 caused the discharge from c#2 to oscillate wildly within a range of 0.05 L/s. The discharge from c#2 ranged from 0.30 to 0.35 L/s after water injection into c#3 started. Lowering the frequency of the pump in c#2 and increasing backpressure on it between August 3 and 31 decreased the discharge from c#2 to a range of 0.28-0.33 L/s after August 31.

Water levels in the Prow Pass interval of c#2 oscillated as much as 10 m between readings due to injection of water into c#3. Although the water injection into c#3 caused drawdown in the Prow Pass interval of c#2 to decrease from 128 to 115 m in the first 11 days after it began, pumping in c#2 eventually predominated over the superimposed effects of the water injection. From June 22 to September 1, the range in c#2 drawdown increased from 115-125 m to 130-143 m (Fig. 3-3).

Drawdown in the Prow Pass interval of c#3 decreased from +0.58 m to a range typically between -25 and -30 m between June 11 to September 1 (the period of continuous injection of water into c#3) (Fig. 3-4). This pronounced water-level rise was affected slightly by periodically adjusting the injection rate. Drawdown fluctuated markedly from +87 to -32 m while tracers were injected into c#3 on June 17 and 18.

Drawdown in the Prow Pass interval of c#1 was disturbed significantly by tracer-test operations in c#3 and c#1 from June 11 to September 1. Injection of water into c#3 decreased drawdown in c#1 from 13 to 2.8 cm between June 11 and July 27, but drawdown subsequently increased and ranged from 4.0 to 7.9 cm by September 1 (Fig. 3-5). Injection of tracers into c#3 on June 17 increased drawdown from 8.9 cm to as much as 13 cm, whereas tracer injection in c#1 on July 31 decreased drawdown from +5.9 to -174 cm and then increased it to +10 cm. Removal of injection tubing from c#1 on June 26 to replace a cracking valve increased drawdown from 10 to 217 cm and then decreased it to -16 cm. Reinstallation of the tubing on July 13 increased drawdown from 5.5 to 10 cm and then decreased it to -1,150 cm.

Drawdown in ONC#1 decreased irregularly from +1.1 to -2.3 cm between June 11 and September 1 (Fig. 3-6). Sharply increased drawdown about 9,000 minutes after injection of water into c#3 began may be related to tracer injection into c#3 on June 17, although the timing of this spike does not correlate precisely with the timing of tracer injection in c#3.

Water-level rises in the C-holes from June 11 to September 1, 1998 were very irregular and were too disturbed by tracer-test operations to be analyzed quantitatively. However, the water-level rise in ONC#1 during this period (with superimposed drawdown from pumping c#2 removed) could be matched to the type curves of Streltsova-Adams (1978) for a fissure-block aquifer. As discussed in more detail in Appendix A, this analysis indicated transmissivity of 30 m<sup>2</sup>/d, fracture hydraulic conductivity of 2 m/d, insignificant matrix hydraulic conductivity, and storativity of 0.002 (90 percent of which is in the matrix). The Prow Pass in ONC#1 and the C-

holes have equally low permeability, but storativity is an order of magnitude larger between ONC#1 and the C-holes than at the C-hole complex.

### Section 3.0 References

- Cooper, H.H., Jr., and Jacob, C.E., 1946, A generalized graphical method for evaluating formation constants and summarizing well-field history: *American Geophysical Union Transactions*, v. 27, no. 4, p. 526-534. TIC Catalog # 225279.
- Geldon, A.L., 1996, Results and interpretation of preliminary aquifer tests in boreholes UE-25c #1, UE-25c #2, and UE-25c #3, Yucca Mountain, Nye County, Nevada: *U.S. Geological Survey Water-Resources Investigations Report 94-4177*, 119 p. TIC Catalog # 223656.
- Geldon, A.L., Umari, A.M.A., Fahy, M.F., Earle, J.D., Gemmell, J.M., and Darnell, Jon, 1997, Results of hydraulic and conservative tracer tests in Miocene tuffaceous rocks at the C-hole complex, 1995 to 1997, Yucca Mountain, Nye County, Nevada: *U.S. Geological Survey Milestone Report SP23PM3* (to U.S. Department of Energy), various paging. MOL.19980122.0412.
- Geldon, A.L., Umari, A.M.A., Earle, J.D., Fahy, M.F., Gemmell, J.M., and Darnell, Jon, 1998, Analysis of a multiple-well interference test in Miocene Tuffaceous rocks at the C-hole complex, May-June 1995, Yucca Mountain, Nevada: *U.S. Geological Survey Water-Resources Investigations Report 97-4166*, 33 p. MOL.19980514.0524.
- Lohman, S. W. 1979. Groundwater hydraulics. *U.S. Geological Survey Professional Paper 708*, 70 p. TIC Catalog # 237291.
- Streltsova-Adams, T.D., 1978, Well testing in heterogeneous aquifer formations, in Chow, V.T., ed., *Advances in hydroscience*, New York, N.Y., Academic Press, v. 11, p. 357-423. (Submitted to RIS for Accession # 5/21/99.)

## Section 3.0 Tables

Table 3-1. Barometric efficiency in the C-holes and UE-25 ONC#1 (no DTN assigned).

Interval	UE-25 C#1	UE-25 C#2	UE-25 C#3	UE-25 ONC#1
Calico Hills	Not applicable	0.93	0.94	Not applicable
Prow Pass	0.96	.93	1.0	0.99
Upper Bullfrog	.99	.93	$\leq 1.0$	Not applicable
Lower Bullfrog	.97	Not applicable	Not applicable	Not applicable

Table 3-2. Hydraulic properties of the Prow Pass interval in the C-holes (no DTN assigned).

Borehole	UE-25 c#1	UE-25 c#3
Test dates	June 2-11, 1998	June 2-11, 1998
Period of record (min)	12,500	12,500
Analyzed data	Drawdown	Drawdown
Transmissivity ( $m^2/d$ )	30	30
Hydraulic conductivity, fractures ( $m/d$ )	1	0.8
Hydraulic conductivity, matrix ( $m/d$ )	0.000003	0.0002
Hydraulic conductivity ( $m/d$ )	No Data	No Data
Storativity, fractures	0.00004	0.00004
Storativity, matrix	0.0003	0.0004
Storativity	0.0004	0.0004

## Section 3.0 Figures

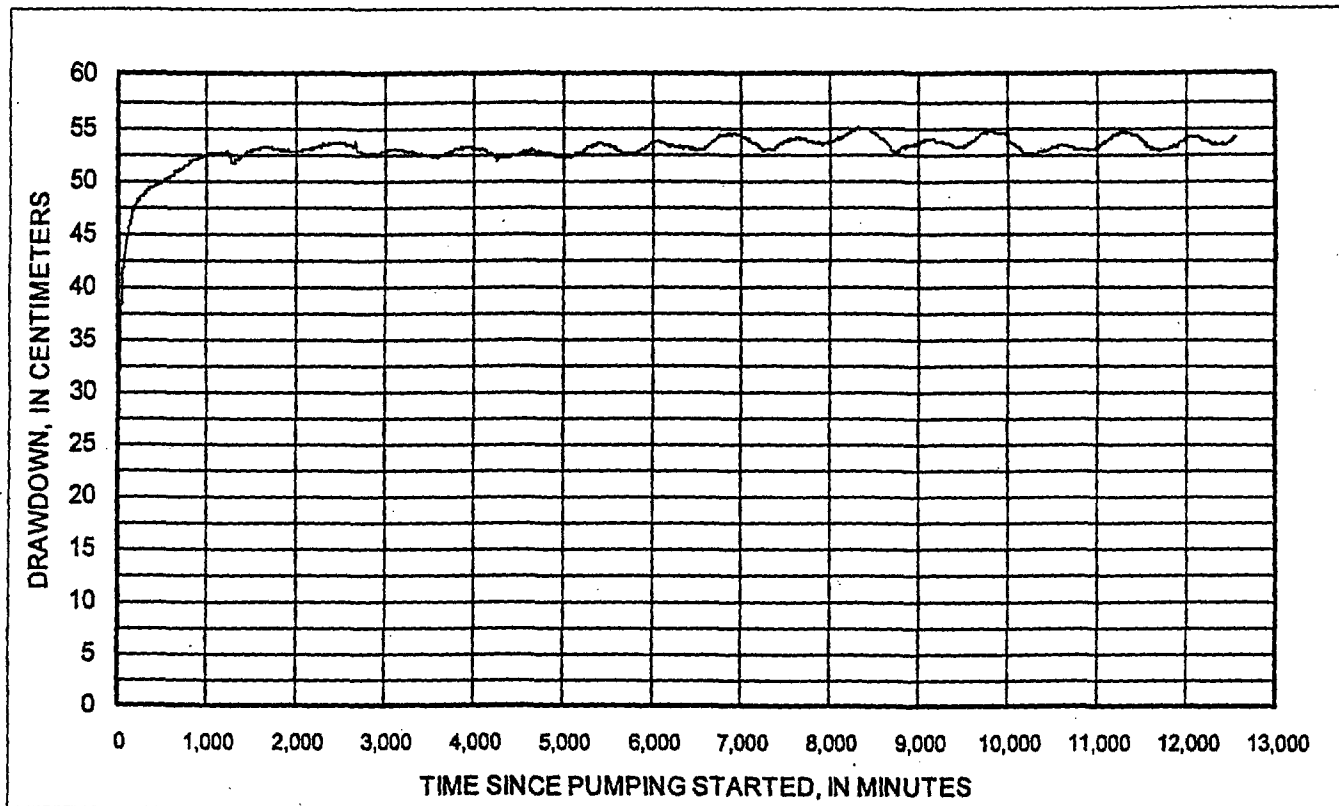


Figure 3-1. UE-25 c#3 Prow Pass drawdown, June 2-11, 1998 (DTN GS990408312315.002).

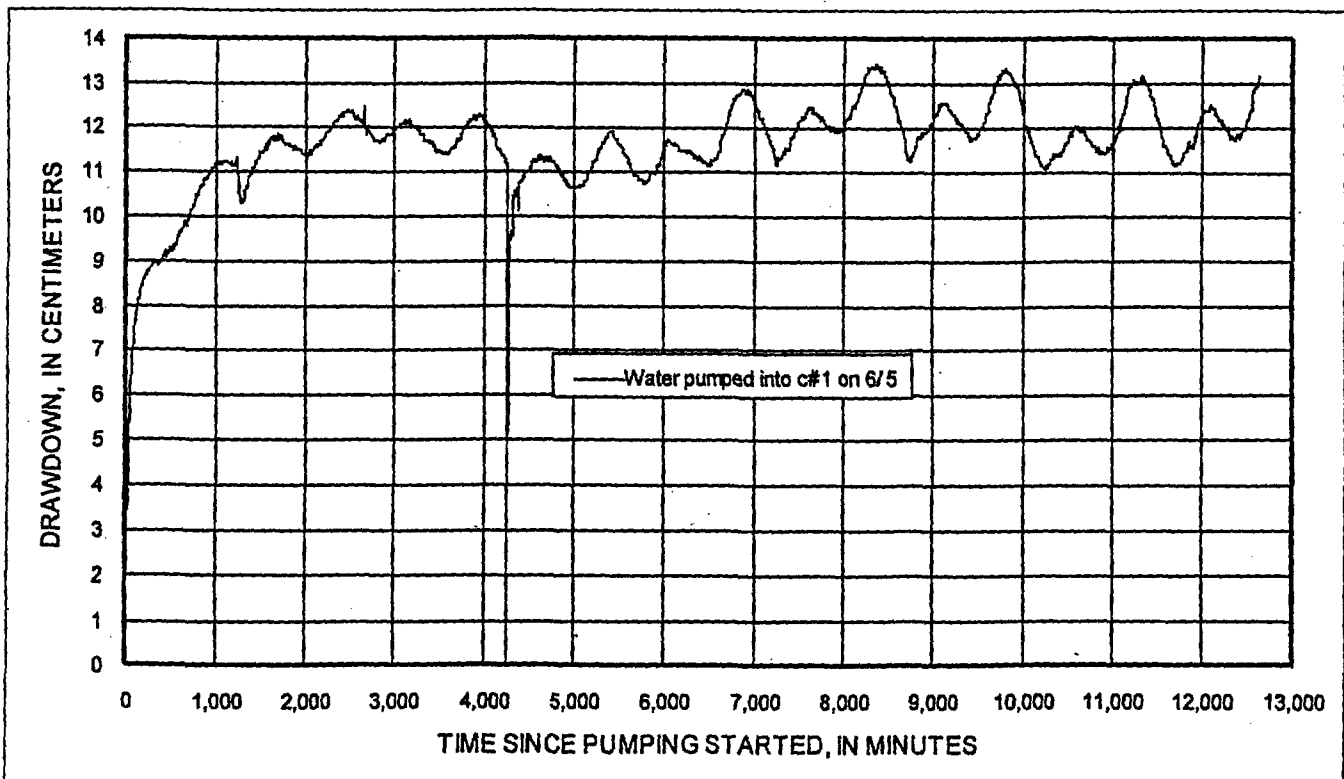


Figure 3-2. UE-25 c#1 Prow Pass drawdown, June 2-11, 1998 (DTN GS990408312315.002).

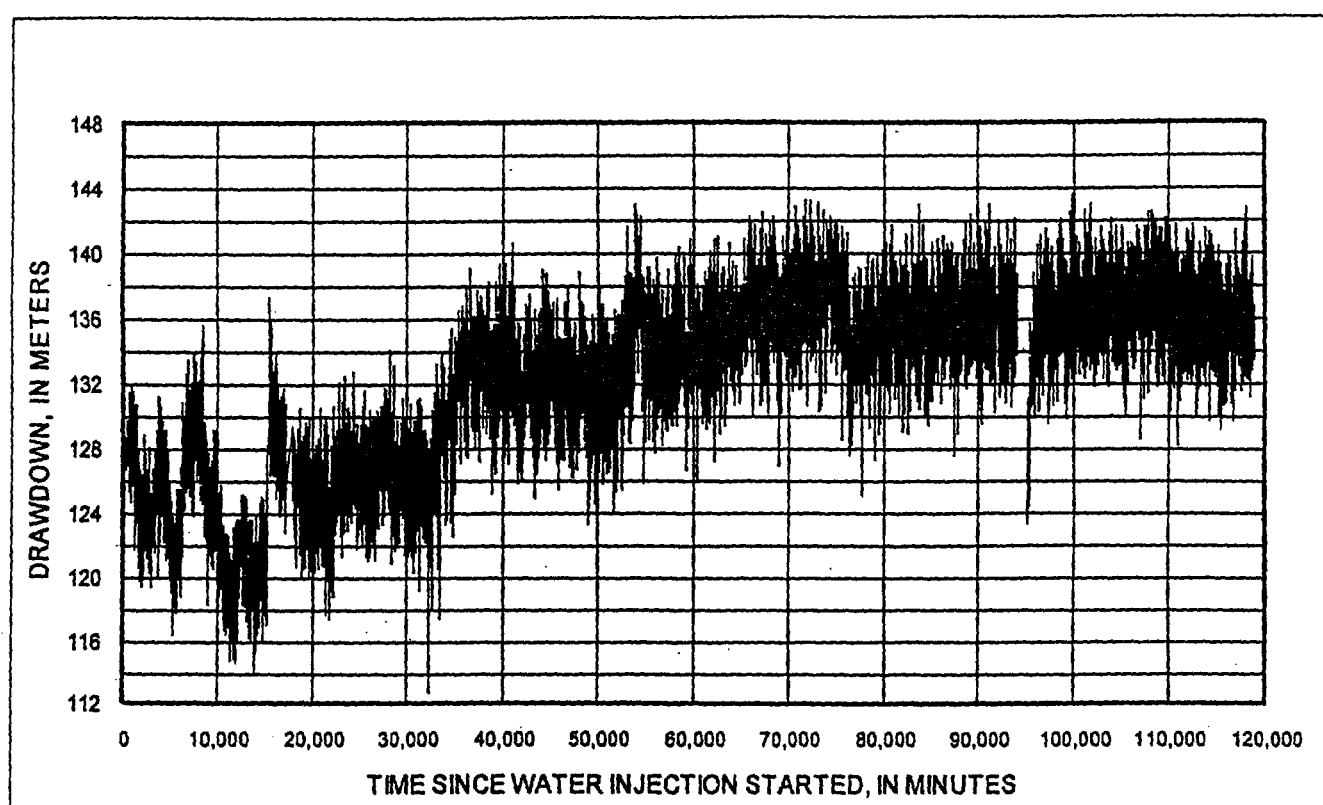


Figure 3-3. UE-25 c#2 Prow Pass drawdown, June 11 to September 1, 1998 (DTN GS990408312315.002).

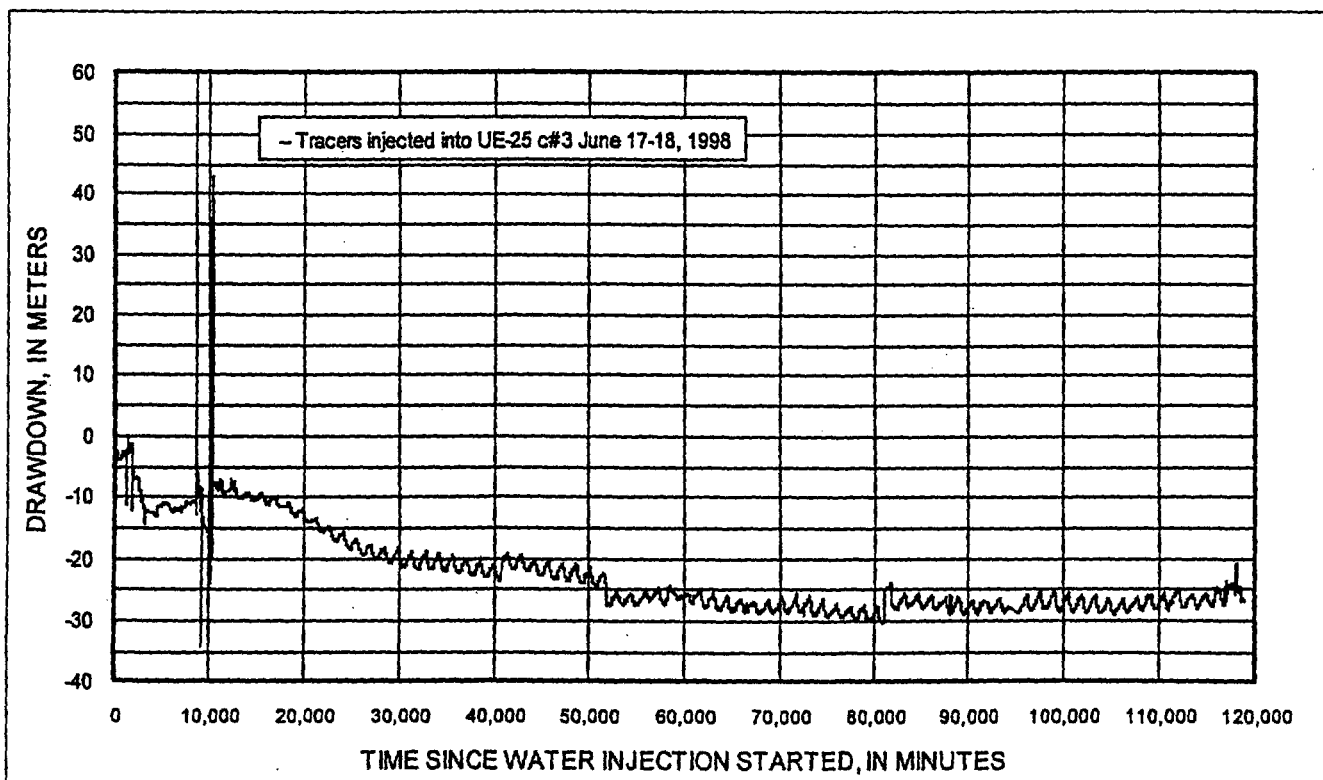


Figure 3-4. UE-25 c#3 Prow Pass drawdown, June 11 to September 1, 1998 (DTN GS990408312315.002).

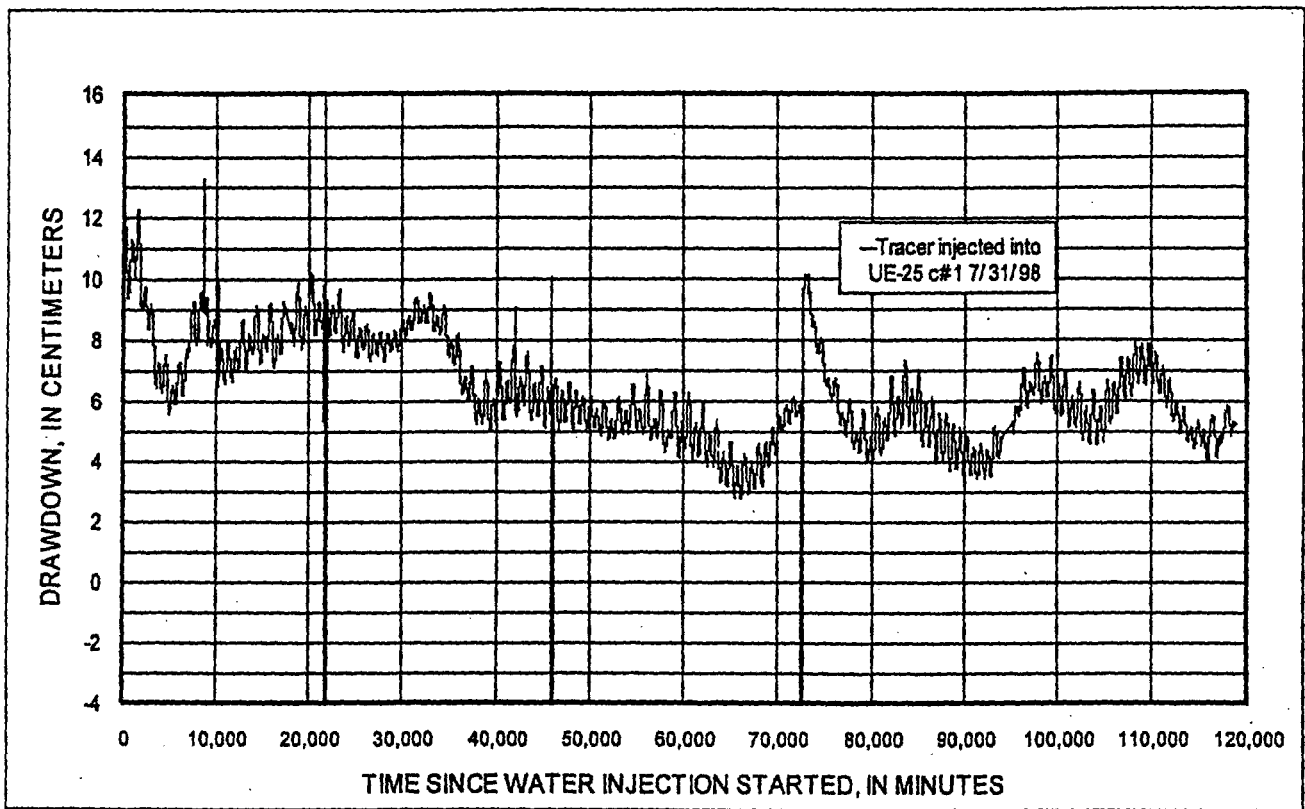


Figure 3-5. UE-25 c#1 Prow Pass drawdown, June 11 to September 1, 1998 (DTN GS990408312315.002).

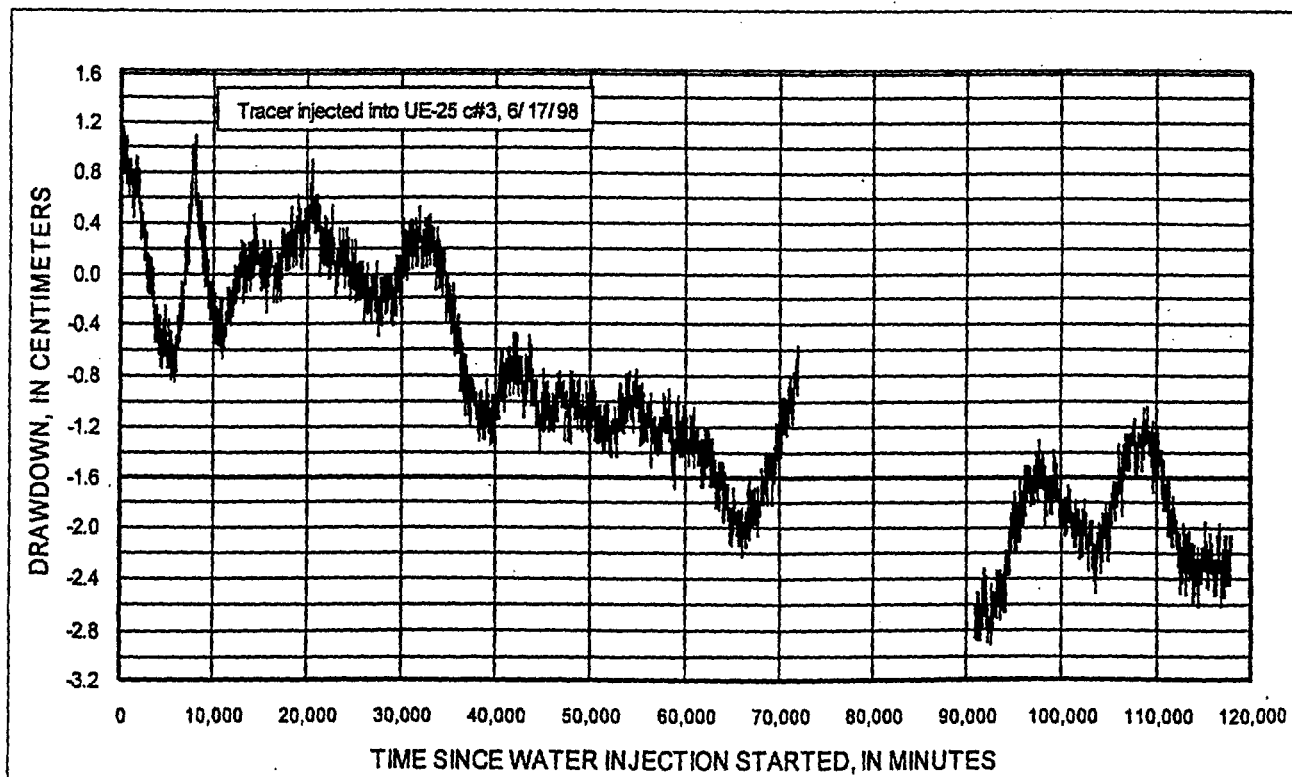


Figure 3-6. UE-25 ONC#1 Prow Pass drawdown, June 11 to September 1, 1998 (DTN GS990408312315.002)

#### 4.0 Conservative Tracer Testing in the Prow Pass Tuff

On June 17, 1998, a partial-recirculation conservative tracer test was initiated from UE-25c#3 to UE-25c#2 by injecting approximately 14.83 kilograms of 2,4,5 trifluorobenzoic acid (TFBA) and 12.26 kilograms of iodide (in the form of sodium iodide) into UE-25c#3 while UE-25 c#2 was pumped at the rate of approximately 0.33 liters per second (l/s). The concentration of 2,4,5 TFBA was 14,239 ppm in the injected slug and that of iodide 14,307 ppm. Out of the 0.33 l/s pumped from UE-25c#2, 0.095 l/s were continuously reinjected into the Prow Pass interval of UE-25c#3. Approximately forty hours after the injection, breakthrough of the tracers occurred in water pumped out of UE-25 c#2. The peak for the 2,4,5 TFBA breakthrough curve, with a concentration of approximately 3.8 ppm ( $C_{max}$  for 2,4,5 TFBA), occurred 6.74 days after tracer injection, and the peak for iodide, with a concentration of approximately 2.6 ppm ( $C_{max}$  for iodide), at 7 days (Fig. 4-1). On September 4, 79 days after tracer injection, the concentration of 2,4,5 TFBA had decreased to approximately 0.52 ppm, and that of iodide to approximately 0.357 ppm. The remainder of this section presents interpretations of the data obtained between June 17 and September 1, 1998.

The iodide and 2,4,5 TFBA breakthrough curves were analyzed using the single- and dual-porosity analytical solutions of the advection-dispersion equation, commonly used to describe the flow of solutes in ground water, as given in Moench (1989, 1995, and 1996). The curves were first analyzed assuming Moench's single-porosity solution. In this case, the aquifer is considered to be an equivalent porous medium made up of a network of fractures, some of them continuous, and some discontinuous with connecting segments of matrix (Fahy, 1997). The porosity of this network of fractures and connecting segments of matrix, through which flow of solutes occurs, is referred to herein as "flow porosity," Fahy (1997).

For the single-porosity solution, two different flow regimes were considered, purely-convergent and partially-recirculating. Although the actual flow regime established for the test was partially recirculating, a purely-convergent flow regime was considered because its analysis was simpler and provided a stepping stone to the analysis of the more complex, partially-recirculating flow regime.

The single-porosity, purely-convergent solution is obtained directly from the Moench (1995) solution to the advection-dispersion equation. This solution, the output of which is in the form of a breakthrough curve (values of concentration versus time) at the pumped well, requires the following input parameters: pumping rate; aquifer thickness; distance between, and radii of, injection and withdrawal wells; and mixing lengths in the injection and withdrawal wells. In all solutions presented in this section, the following values were used: pumping rate of 3.3 l/s (represents the average rate for the test), aquifer thickness of 61 m (represents the average thickness of the Prow Pass interval between UE-25 c#2 and UE-25 c#3), distance between injection and pumping wells of 29 m (represents the calculated average distance, within the Prow Pass interval, between boreholes UE-25 c#2 and UE-25 c#3), radii of injection and pumping wells of 13.97 cm (nominal value: caliper log shows variations, larger and smaller than 13.97 cm), and borehole mixing length of 30.5 m (assumed: discussed below). Three additional input parameters, the mass and concentration of tracer slug injected, and the duration of slug injection are optional. Because all breakthrough curves were normalized to their own maximum concentrations, the need for specifying the mass and concentration of the injected tracer slug was

obviated. The duration of slug injection also was not needed because instantaneous slug injection—rather than the finite-duration slug injection—was assumed in the purely-convergent solution presented. The medium parameters required are the flow porosity, the longitudinal dispersivity, and the retardation coefficient of the tracer specific to the medium. The flow porosity and longitudinal dispersivity are different for each of the solutions presented. The retardation coefficient used for all solutions was 1.0 indicating that iodide and 2,4,5 trifluorobenzoic acid are considered conservative with respect to the Prow Pass tuff.

The single-porosity, purely-convergent solution to the advection-dispersion equation, obtained directly from Moench (1995) for fitted values of 0.07% and 1.45 m corresponding to the flow porosity and longitudinal dispersivity, respectively, is presented in fig. 4-2, along with the iodide and 2,4,5 TFBA breakthrough curves. All breakthrough curves, such as the ones in fig. 4-2, were normalized by dividing the measured concentrations by their own maximum concentration,  $C_{\max}$ , rather than by the concentration of the injected mass slug,  $C_0$ . (A discussion on the different representation of the effects of matrix diffusion using the two methods of normalization is presented later in this section when dual-porosity solutions are described.) Longitudinal dispersivity is a measure of the porous medium's ability to disperse a solute along streamlines. Transverse dispersivity, which represents the medium's ability to disperse a solute in a direction perpendicular to streamlines, is not obtainable from this analysis method and flow geometry. The above longitudinal dispersivity of 1.45 m and the 29 m flow length correspond to a Peclet number of 20, where the Peclet number is a dimensionless parameter formed in Moench (1995) by dividing the distance between injection and pumping wells by the longitudinal dispersivity.

The fitted values of longitudinal dispersivity and flow porosity may be sensitive to the mixing lengths assumed for the injection and pumped wells. The mixing lengths represent those lengths within the boreholes through which the tracer enters or exits the aquifer. The 30.5 m mixing length assumed for all solutions in this section is based on the thickness of the transmissive interval within the packed-off Prow Pass tuff (the transmissive interval within the Prow Pass hydrogeologic interval in UE-25 c#3 is shown in fig. 5, p. 9 of Geldon and others, 1998, to be approximately 33.8 m.) That is, the 30.5 m mixing length is consistent with the hydrogeology of the Prow Pass interval.

However, uncertainty accompanies any estimate of the transmissive interval within a borehole. The residence time of the tracer slug within the borehole is directly proportional to the mixing length. To evaluate the effect of the mixing length on the fitted longitudinal dispersivity and flow porosity, the 30.5 m mixing length used for all solutions in this section is considered to be one end member of a range, and the effect of another end member, that of 0.3 m mixing length, on the results of the single-porosity purely-convergent solution, is investigated. In addition to introducing uncertainty as to the length of the transmissive interval, an assumed mixing length of 0.3 m decreases the residence time of the tracer slug in the injection borehole which would simulate the effect of borehole flushing due to partial recirculation. Data collected during the tracer injection indicate that the borehole was flushed in 8.5 hours (the concentration in the injected interval was measured in the field and found to rise from below detection limit to 2,721 ppm and then back to below detection limit in 8.5 hours. The concentration in the injection interval was measured as 29 ppm, 2721 ppm, 1552 ppm, 557 ppm, and 323 ppm at 5.5 hours; 6.5 hours; 7 hours, 35 minutes; 8 hours, 10 minutes; and 8.5 hours, respectively, after

injection.) Because the single-porosity purely-convergent solution is being discussed here, only the borehole-flushing effect of partial recirculation is relevant, which is the same as the effect of a chase fluid in a purely-convergent test. When the mixing length is reduced to 0.3 m and only the rising limb of the actual breakthrough curve (BTC) is matched to the theoretical breakthrough curve (BTC) from Moench (1995) (assuming minimal diffusion during the rising limb), a longitudinal dispersivity value of 4.27 m and a flow porosity value of 0.0016 are obtained as fitting parameters. So, by changing the mixing length from 30.5 m to 0.3 m, a 2- order-of-magnitude change, in both injection and pumping wells to capture uncertainty in transmissive interval length in the two wells and represent flushing the injection well, the estimates of longitudinal dispersivity and flow porosity change from 1.45 m and 0.0007 in the case of 30.5 m mixing length to 4.3 m and 0.0016 in the case of 0.3 m mixing length. This is a 3-fold change in the estimate of longitudinal dispersivity and a 2-fold change in the estimate of flow porosity, both less than an order-of-magnitude change. The estimated parameters, therefore, are not very sensitive to the mixing length.

The above porosity value of 0.07% is in the range of 0.001% to 1% cited in the literature to represent fracture porosity (see, for example, Freeze and Cherry, 1979, p. 408). This implies that the flow network for this test is composed predominately of fractures.

When the purely-convergent flow field of fig. 4-2 is replaced by a partially-recirculating flow field, the resulting solution to the advection-dispersion equation changes from the curve labeled "Moench solution" in fig. 4-2 to the curve labeled "Modified Moench solution" shown in fig. 4-3. The difference between the two solutions reflects the difference in flow field representation, and in the fitted values of longitudinal dispersivity and flow porosity used (or implied) for each solution. Two elements of partial-recirculation are represented in this solution. First, the flow field is different from that of purely-convergent flow. Rather than straight converging rays into the pumped well, the partially-recirculating flow field streamlines that are within the capture zone of the pumped well emanate from the injection well and curve towards the pumped well (fig. 4-4a). The streamlines shown in fig. 4-4a are lines of equal stream function values, where the stream function of the partial recirculation field is calculated as the sum of the stream functions of a 0.33 l/s sink and a 0.095 l/s source, 29 m apart. The volume of rock between pairs of these curved streamlines constitute distinct pathways for the solute (tracer) to take from the injection to the pumped well. Three such inter-streamline pathways (fig. 4-4a) are assumed for the partial-recirculation analysis in this section. The Moench (1995) single-porosity, purely-convergent solution is viewed as the solution of the advection-dispersion equation along a single straight pathway, that represented by the rock between the pair of bounding streamlines from the injection to the pumped well (fig. 4-4b). This solution, for a particular longitudinal dispersivity value and an initial value of flow porosity, is then applied to each of the above three distinct pathways with a proper delay factor to account for the differences in lengths, or swept volumes, of these pathways relative to the straight purely-convergent pathway from injection to pumped well. The significance of using the designation "initial value" for the flow porosity used for the three pathways will be explained later in this section.

The above three solutions from Moench (1995), for a particular longitudinal dispersivity value and an initial value of flow porosity, and with appropriate delay factors, assuming an instantaneous-slug-injection, are then superimposed to obtain what is considered to be the system's unit response function. The summed curve represents what is seen at the pumped well

in response to an instantaneous input function at the injection well in a partial-recirculation flow field.

The second element of partial recirculation is that the reinjected water contains a concentration of the tracer, and so the tracer is continuously reintroduced into the aquifer. In order to represent this, it was assumed that the concentration of reinjected tracer as a function of time, the injection concentration curve, was the same as the breakthrough curve of the tracer at the pumped well, but lagged by a certain duration, due to travel through surface plumbing. This lag represents the length of time it would take the tracer to be recirculated from the discharge/sampling point of the pumped well at the surface to the downhole point in the injection well where it enters the aquifer. For the calculations presented here, it was assumed that this lag duration is approximately 1 hour. The injection concentration curve was padded at the beginning by 2 hours of very high concentrations representing the "top hat" finite-duration slug injection that preceded the concentrations resulting from the recirculated tracer.

The injection concentration curve is then convolved (Levenspiel, 1972) with the unit response function to produce the calculated partial-recirculation breakthrough curve at the pumped well. The parameter fitting process performed here involves the visual comparison of actual and calculated partial-recirculation curves for a set of input parameters (longitudinal dispersivity, initial flow porosity, and the three inter-streamline pathway delay factors) and the trial-and-error selection of the set of parameters that minimizes the difference between these two curves.

Employing the parameter fitting process above, a longitudinal dispersivity of 0.27 m and an initial flow porosity of 0.00045, which result in the calculated partial-recirculation breakthrough curve presented in fig. 4-3, were selected as "optimal" for the single-porosity, partial-recirculation, case. The delay factors for the three inter-streamline pathways, inherent in the calculation of the breakthrough curve of fig. 4-3, were initially assumed to be 1.83 days for the first pathway, 3.5 days for the second, and 7.5 days for the third. (Each delay factor is calculated by multiplying the volume of the corresponding inter-streamline pathway by the initial flow porosity of 0.00045, and then dividing the result by the flow rate that is carried by the inter-streamline pathway, which is equal to the difference in the stream function values of the bounding streamlines.) However, use of these delay factors produced a calculated breakthrough curve that did not fit the actual breakthrough curve very well. The fit was substantially improved by changing the delay factors to 2.01 days, 2.99 days, and 3.11 days, which resulted in the calculated breakthrough curve of fig. 4-3. Because these three delay factors are not the ones indicated by the volumes of rock calculated for the three inter-streamline pathways, they are interpreted to represent the uncertainty in either the initial, single, flow porosity value or in the assumed streamline pattern and resulting rock volumes. In the first approach, the volumes of rock calculated for the three inter-streamline pathways is considered correct, in which case the deviation of optimal delay factors from those calculated with the single initial porosity value is interpreted to imply that the three pathways in fact have varying flow porosities (hence the "initial porosity" designation.) Given the rock volumes for the three pathways, the optimal delay factors of 2.01 days, 2.99 days, and 3.11 days represent flow porosities of 0.0005, 0.0004, and 0.0002 for the three pathways. This reflects uncertainty in the assumption of a homogeneous medium with one flow porosity value. In the second approach, the initial flow porosity is considered correct and the deviation of the optimal delay factors from those calculated with the rock volumes of fig. 4-4a is interpreted to reflect the uncertainty in the calculated pathway rock

volumes. But because the rock volumes were calculated assuming the streamline pattern of a homogeneous medium, this in turn represents uncertainty in the underlying homogeneity assumption—the same conclusion as the one reached from the first approach. The above modified delay factors were used in all partial-recirculation solutions in this section.

The results shown in figs. 4-2 and 4-3 indicate that if the breakthrough curves of 2,4,5 TFBA and iodide are analyzed as if they result from a purely-convergent flow field, ignoring that the real flow field is partially recirculating, some error in the derived parameters occurs. A longitudinal dispersivity of 1.45 m is obtained when purely-convergent conditions are assumed, 5 times the 0.27 m obtained when the partial- recirculation flow field is recognized. The flow porosity of 0.0007 obtained for purely-convergent conditions is 56% higher than the initial flow porosity of 0.00045 obtained for partial-recirculation.

Note that although the purely-convergent solution in fig. 4-2 matches the data on the rising limb better than the partial-recirculation solution in fig. 4-3, the latter matches the data on the falling limb better, especially in the tail of the breakthrough curve. The solution in fig. 4-3 attempts to capture all the elements of partial recirculation, whereas the solution in fig. 4-2 doesn't. The fact that the partial-recirculation solution in fig. 4-3 doesn't match the data any better than it does indicates that, although it attempts to incorporate all elements of partial recirculation, it does not capture everything that in fact takes place in the field. For example, one element that has not been incorporated into the partial recirculation solution in fig. 4-3 is the effect on the flow field of the natural gradient. Incorporating the natural gradient would alter the streamline pattern of fig. 4-4a to some extent and lead to different inter streamline pathway volumes and resulting delay factors. Also, representation of the effects of partial recirculation can be improved by using more than three inter-streamline pathways. In the dual-porosity case, the medium is assumed to be comprised of flow and storage components. Advection and hydrodynamic dispersion, as represented by the advection/dispersion equation, occur in the "flow" component. Matrix diffusion is represented as a source/sink term in the advection/ dispersion equation and occurs in the storage component. The flow component is conceptualized as a flow network of 1) continuous fractures and 2) discontinuous fractures with interconnecting segments of matrix. The porosity of the flow component of the medium is referred to as the "flow porosity" in this section (same as for the single-porosity case.) The storage component is assumed to consist of dead-end fractures and the part of the matrix not contributing to the flow network. The porosity of the storage component of the medium is referred to as the "storage porosity" in this section.) The flow network is represented by a longitudinal dispersivity and a flow porosity, and the storage component by a storage porosity and a dimensionless matrix diffusion coefficient.

The calculated dual-porosity solution is predicated upon the single-porosity, partial- recirculation solution presented earlier, i.e. a longitudinal dispersivity of 0.27 m and an initial flow porosity of 0.00045. The same process of superimposing three purely-convergent solutions with delay factors—representing either the flow porosities, or the uncertainty in the streamline pattern and resulting rock volumes, of the three inter-streamline pathways—to obtain the medium's unit response function, followed by the latter's convolution with the delayed input concentration curve, is employed. However, the starting purely-convergent solution used is the dual-porosity—rather than the single-porosity—Moench (1995) solution, and it requires, in addition to the input parameters presented earlier for the single-porosity solution, the medium's

storage porosity and dimensionless matrix diffusion coefficient (the latter defined below). Two calculated breakthrough curves obtained this way, for a storage porosity of 0.001 and two dimensionless matrix diffusion coefficients (gamma), namely 0.0001 and 0.001, are presented in fig. 4-5, along with the actual breakthrough curves of 2,4,5 TFBA and iodide.

The free-water molecular diffusion coefficients of 2,4,5 TFBA and iodide are  $8.0 \times 10^{-6}$  cm<sup>2</sup>/sec and  $18.0 \times 10^{-6}$  cm<sup>2</sup>/sec, respectively (Bowman, 1984; Skagius and Neretnieks, 1986). When a solution is placed in a porous medium and it diffuses into the matrix, the extent of matrix diffusion is represented by the dimensionless matrix diffusion parameter, gamma, defined in table 1, p. 1826, of Moench (1995). This parameter represents the extent of matrix diffusion, i.e. the matrix diffusion flux and resulting effect on the breakthrough curve. For a specific distance between injection and pumping wells, test interval thickness, and assumed representative matrix block dimension, the dimensionless diffusion coefficient is directly proportional to the product of the porosity of the matrix (the storage porosity) and the free-water diffusion coefficient of the solute, and inversely proportional to the flow rate. This implies that, for a certain flow rate, the larger the storage porosity, the greater the effect on matrix diffusion resulting from a specific change in the free-water diffusion coefficient of a tracer. The above relationships will be evident from the effects of changing the storage porosity and free-water diffusion coefficient on the calculated breakthrough curves, as shown below.

Fig. 4-5 shows the effects on matrix diffusion—as represented by two calculated breakthrough curves—of changing the free-water diffusion coefficient by a factor of 10, for fixed storage porosity, 0.001, and fixed flow rate. (A gamma change of 0.001 to 0.0001 implies a change in the free-water diffusion coefficient by a ratio of 10 to 1, because the storage porosity and flow rate are held constant.) Fig. 4-6, shows that when the storage porosity is increased from 0.001 to 0.01, the effect on matrix diffusion of the same change in the free-water diffusion coefficient as that in fig. 4-5 is markedly larger. The calculated breakthrough curve with the higher free-water diffusion coefficient (corresponding to a gamma of 0.001) is more retarded, relative to that with the lower coefficient, in fig. 4-6 than it is in fig. 4-5. It should be noted here that the effects of matrix diffusion on a breakthrough curve (BTC) are seen as a reduction in peak if the BTC is normalized by the mass injected, and a delay if it is normalized by its maximum concentration. Figs. 4-5 and 4-6 use the latter method. The 10 to 1 ratio of the free-water diffusion coefficient used for the two calculated BTCs shown in figs. 4-5 and 4-6 is larger than the ratio of 18 to 8 (i.e. 2.25 to 1) of the free-water diffusion coefficient of iodide relative to that of 2,4,5 TFBA.

When the ratio in free-water diffusion coefficients of the two calculated BTCs is fixed at that of iodide and 2,4,5 TFBA, i.e. 2.25 to 1 (gamma ratio of 0.001 to 0.000444), the results shown in figs. 4-7 and 4-8 are obtained. Fig. 4-7 shows the two calculated BTCs, with gamma values of 0.001 and 0.000444 for a storage porosity of 0.001, and fig. 4-8 shows the two BTCs with the same gamma values for a storage porosity of 0.01. As in figs. 4-5 and 4-6, the effects of matrix diffusion increase with increasing storage porosity for the same change in the water-diffusion coefficient, or in gamma. In contrast to figs. 4-5 and 4-6, the calculated BTCs in figs. 4-7 and 4-8 show less effects of matrix diffusion for a particular storage porosity, because of the smaller ratio in the free-water diffusion coefficient, or in gamma, used for the two curves. The separation between calculated BTCs in fig. 4-8 is similar to that between the actual 2,4,5 TFBA and iodide curves, which would suggest a storage porosity value of approximately 0.01. This result is combined with earlier ones to indicate a dual-porosity medium with an initial

flow porosity of 0.00045 (which may represent three inter-streamline pathways of flow porosities ranging from 0.0002 to 0.0005), a storage porosity of 0.01, and a longitudinal dispersivity of 0.27 m. The flow porosity and longitudinal dispersivity characterize a flow network within this medium comprised of 1) continuous fractures and 2) discontinuous fractures with interconnecting segments of matrix. The storage porosity characterizes a storage component of the conceptualized dual-porosity medium consisting of dead-end fractures and the part of the matrix not contributing to the flow network.

## Section 4.0 References

- Bowman, R.S., 1984, Evaluation of some new tracers for soil water studies, *Journal of the Soil Science Society of America*, v. 48, p. 987-993. (Submitted to RIS for Accession # 5/21/99.)
- Day, W.C., Dickerson, R.P., Potter, C.J., Sweetkind, D.S., San Juan, C.A., Drake, R.M., II, and Fridrich, C.J., 1998, Bedrock geologic map of the Yucca Mountain area, Nye County, Nevada: *U.S. Geological Survey Geologic Investigations Map I-2627*, scale 1:24,000. TIC Catalog # 238732.
- Fahy, M.F., 1997, Dual-porosity analysis of conservative tracer testing in saturated volcanic rocks at Yucca Mountain in Nye County, Nevada: *International Journal of rock mechanics and mining science*, v.34, No.3/4, Paper 074. TIC Catalog # 237601.
- Freeze, R.A., and Cherry, J.A., 1979, *Groundwater*: Englewood Cliffs, N.J., Prentice-Hall, 604 p. TIC #217571.
- Geldon, A.L., Umari, A.M.A., Earle, J.D., Fahy, M.F., Gemmell, J.M., and Darnell, Jon, 1998, Analysis of a multiple-well interference test in Miocene Tuffaceous rocks at the C-hole complex, May-June 1995, Yucca Mountain, Nevada: *U.S. Geological Survey Water-Resources Investigations Report 97-4166*, 33 p. MOL.19980514.0524.
- Levenspiel, O., 1972, *Chemical reaction engineering*, second edition, New York, John Wiley and Sons. RIS Accession # NNA.19910207.0015.
- Moench, A.F., 1989, Convergent radial dispersion: a Laplace transform solution for aquifer tracer testing: *Water Resources Research*, v.25, no.3, p. 439-447. TIC Catalog # 238281.
- Moench, A.F., 1995, Convergent radial dispersion in a double-porosity aquifer with fracture skin: Analytical solution and application to a field experiment in fractured chalk: *Water Resources Research*, v.31, no.8, p.1823-1835. TIC #233132.
- Moench, A.F., 1996, Correction to "Convergent radial dispersion: a Laplace transform solution for aquifer tracer testing": *Water Resources Research*, v.32, no.5, p. 1475. (Submitted to RIS for Accession # 5/21/99.)

Skagius, K., and Neretnieks, I., 1986, Porosities and diffusivities of some nonsorbing species in crystalline rocks: *Water Resources Research*, v. 22, no. 3, p. 389-398. TIC Catalog # 225291.

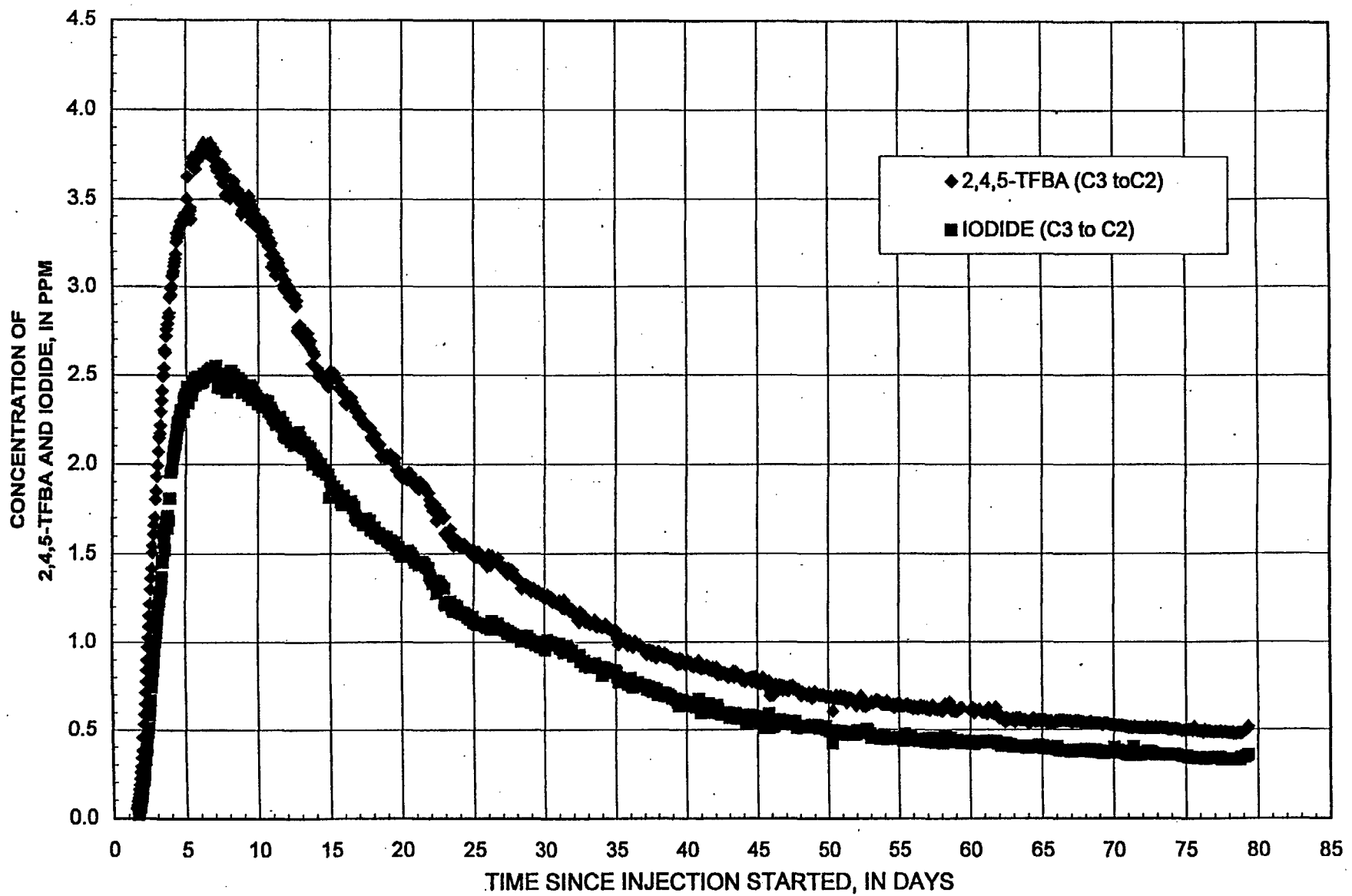


Figure 4-1. BREAKTHROUGH CURVES FOR 2,4,5 TFBA  
AND IODIDE TRACER TEST (DTN GS9908312315.001)

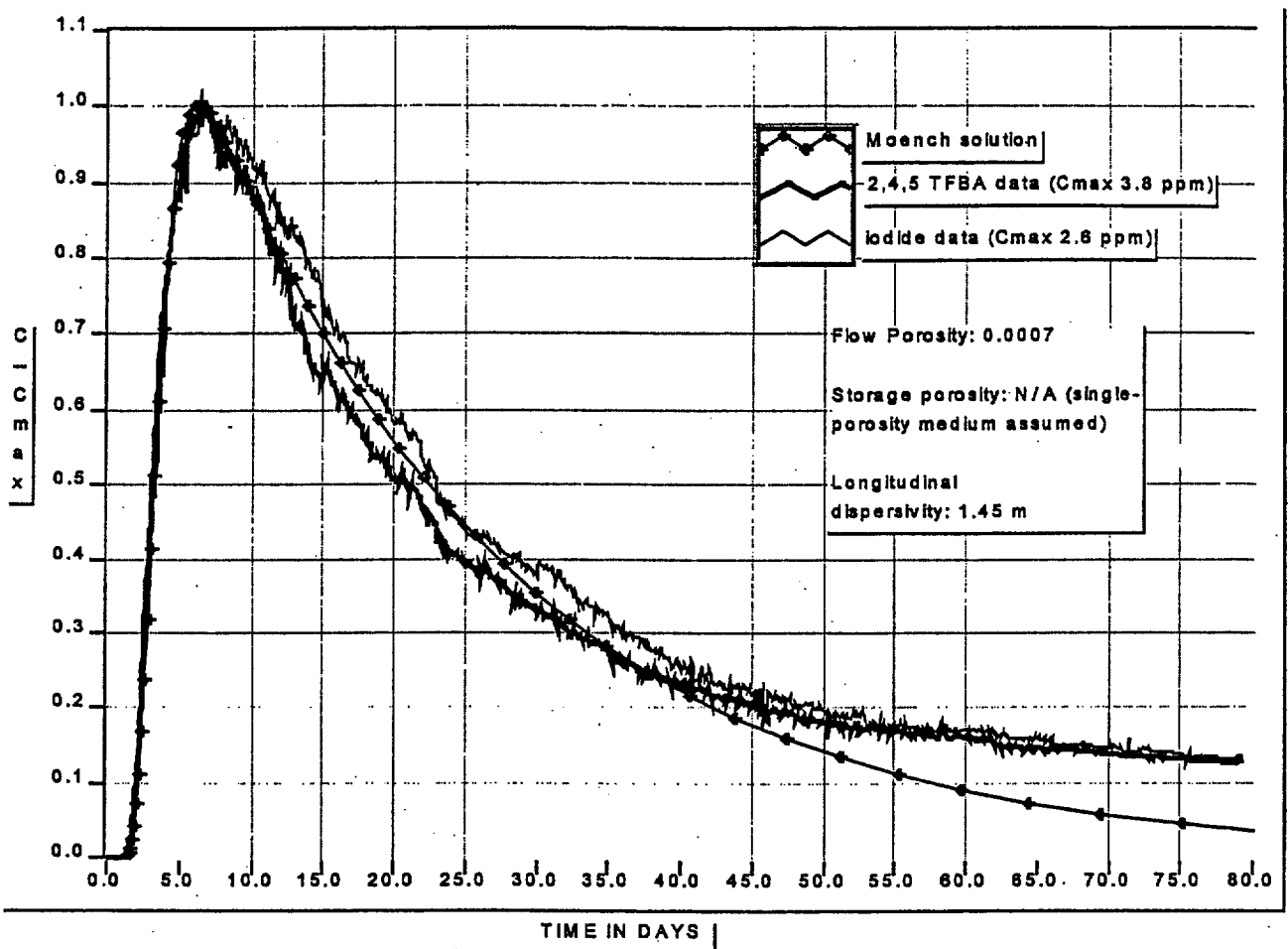
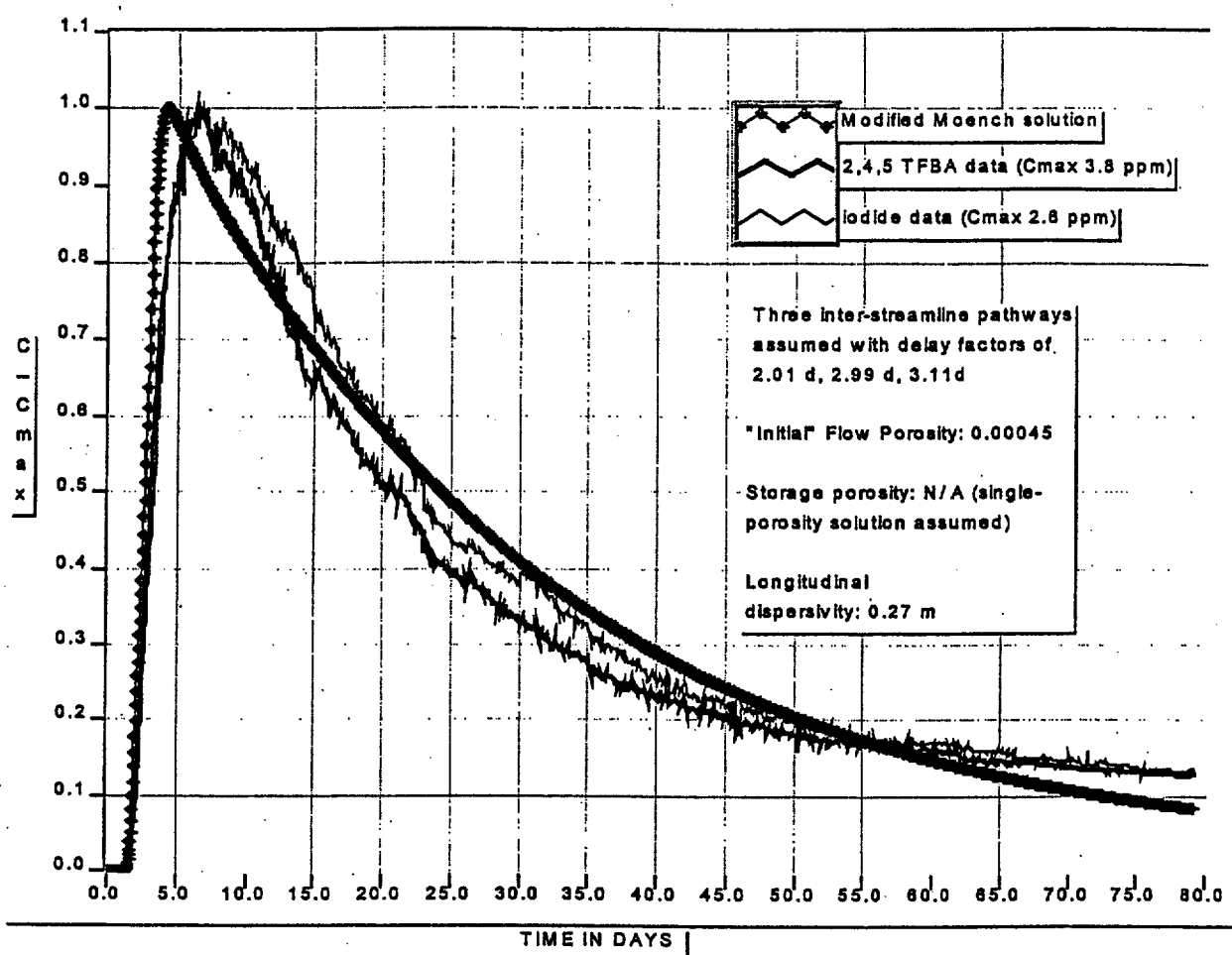


FIGURE 3 . BREAKTHROUGH CURVE FOR 6/17/98 2,4,5 TFBA AND IODIDE TRACER TEST,  
MATCHED BY SINGLE-POROSITY, PURELY CONVERGENT MOENCH (1995) SOLUTION

Figure 4-2. Breakthrough curves for 6/17/98 2,4,5 TFBA and iodide tracer test, matched by single-porosity, purely-convergent Moench (1995) solution. (Data - DTN GS9908312315.001; Model Results - No DTN assigned).



**FIGURE 4 . BREAKTHROUGH CURVE FOR 6/17/98 2,4,5 TFBA AND IODIDE TRACER TEST, MATCHED BY SINGLE-POROSITY, PARTIAL-RECIRCULATION SOLUTION DERIVED FROM MOENCH (1995)**

Figure 4-3. Breakthrough curves for 6/17/98 2,4,5 TFBA and iodide tracer test, matched by single-porosity, partial-recirculation solution derived from Moench (1995). (Data - DTN GS9908312315.001; Model Results - No DTN assigned).

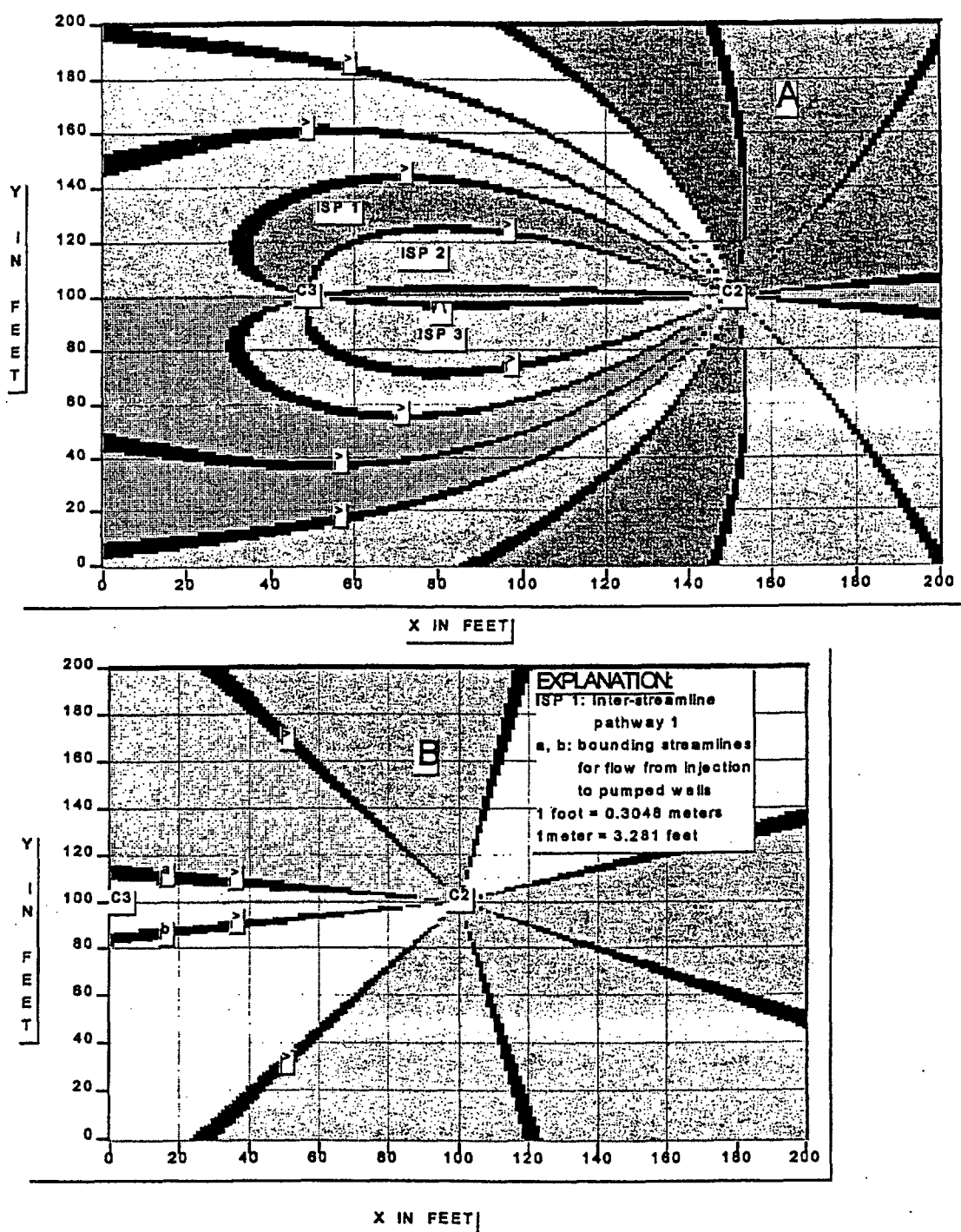
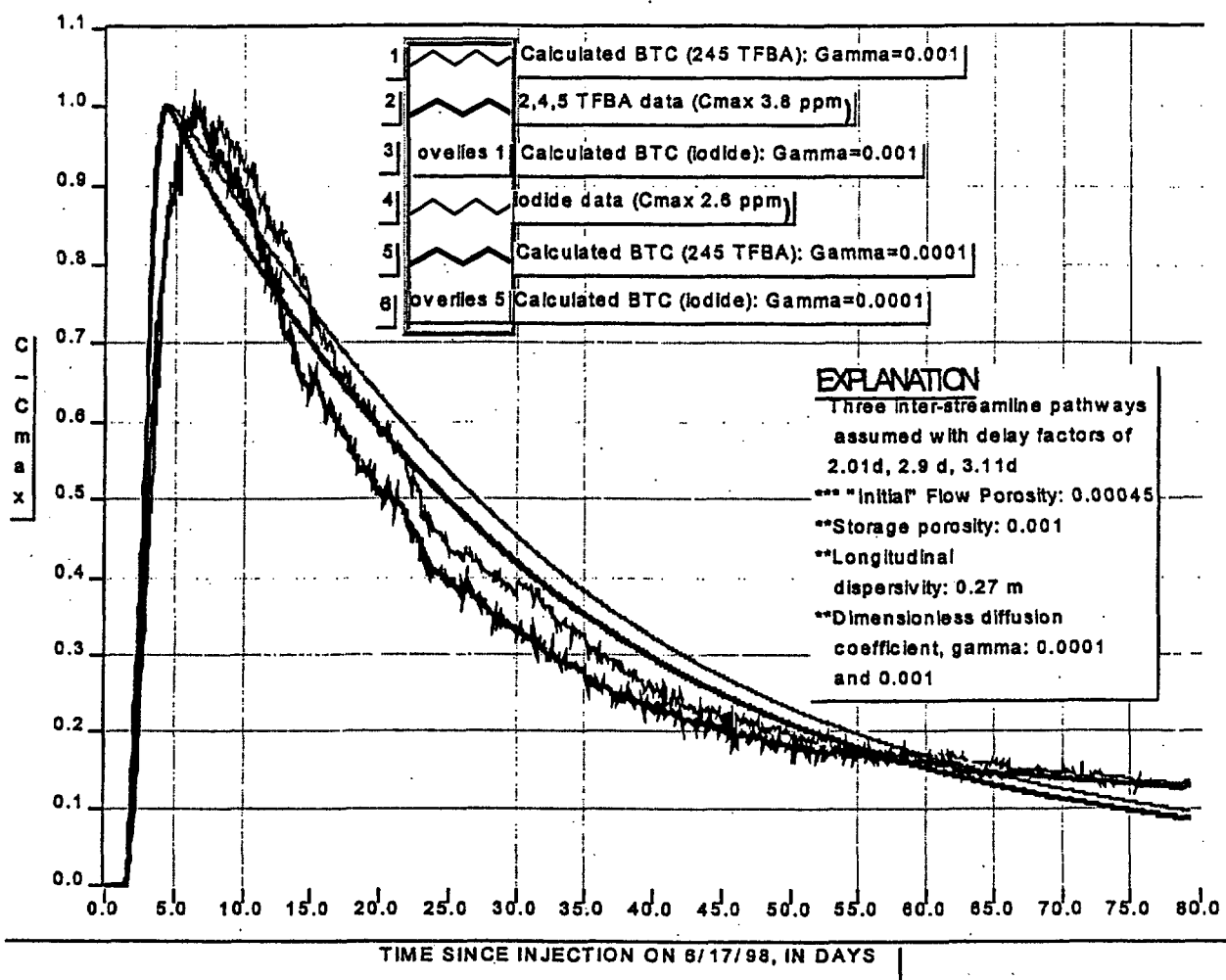


FIGURE 5. STREAMLINES: A) FOR PARTIAL-RECIRCULATION FLOW FIELD; B) FOR PURELY-CONVERGENT FLOW FIELD

Figure 4-4. Streamlines (A) for partial-recirculation flow field and (B) for purely-convergent flow field. These figures were generated by a non-Q software package.



**FIGURE 6 . BREAKTHROUGH CURVE FOR 6/17/98 2,4,5 TFBA AND IODIDE TRACER TEST, MATCHED BY DUAL-POROSITY, PARTIAL-RECIRCULATION SOLUTION DERIVED FROM MOENCH (1995), WITH STORAGE POROSITY OF 0.001 AND DIMENSIONLESS DIFFUSION COEFFICIENTS, GAMMA, OF 0.0001 AND 0.001**

Figure 4-5. Breakthrough curves for 6/17/98 2,4,5 TFBA and iodide tracer test, matched by dual-porosity, partial-recirculation solution derived from Moench (1995), with storage porosity of 0.001 and dimensionless diffusion coefficients, gamma, of 0.0001 and 0.001. (Data - DTN GS9908312315.001; Model Results - No DTN assigned).

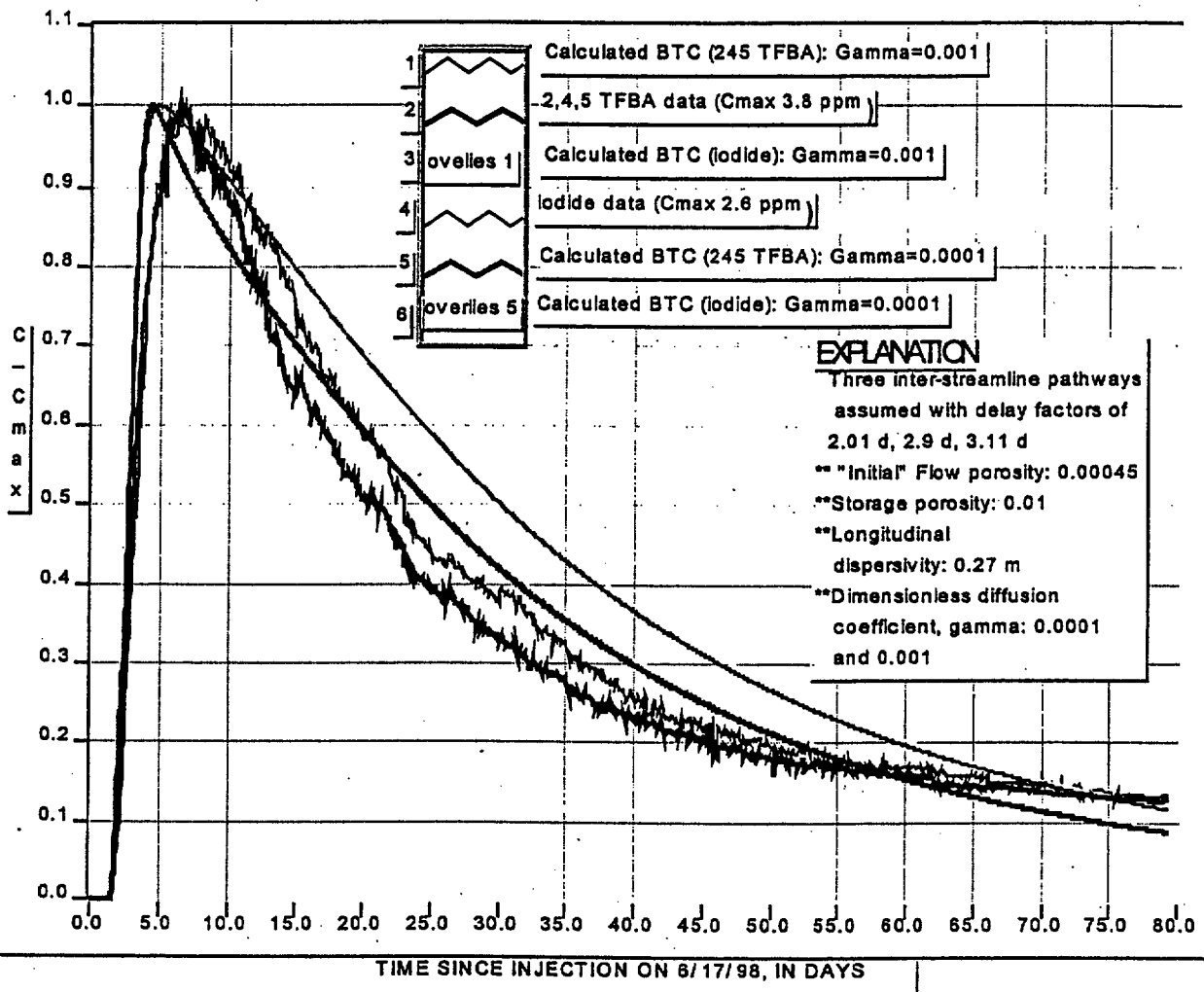


FIGURE 7. BREAKTHROUGH CURVE FOR 8/17/98 2,4,5 TFBA AND IODIDE TRACER TEST, MATCHED BY DUAL-POROSITY, PARTIAL-RECIRCULATION SOLUTION DERIVED FROM MOENCH (1995), WITH STORAGE POROSITY OF 0.01 AND DIMENSIONLESS DIFFUSION COEFFICIENTS, GAMMA, OF 0.0001 AND 0.001

Figure 4-6. Breakthrough curves for 6/17/98 2,4,5 TFBA and iodide tracer test, matched by dual-porosity, partial-recirculation solution derived from Moench (1995), with storage porosity of 0.01 and dimensionless diffusion coefficients, gamma, of 0.0001 and 0.001. (Data - DTN GS9908312315.001; Model Results - No DTN assigned).

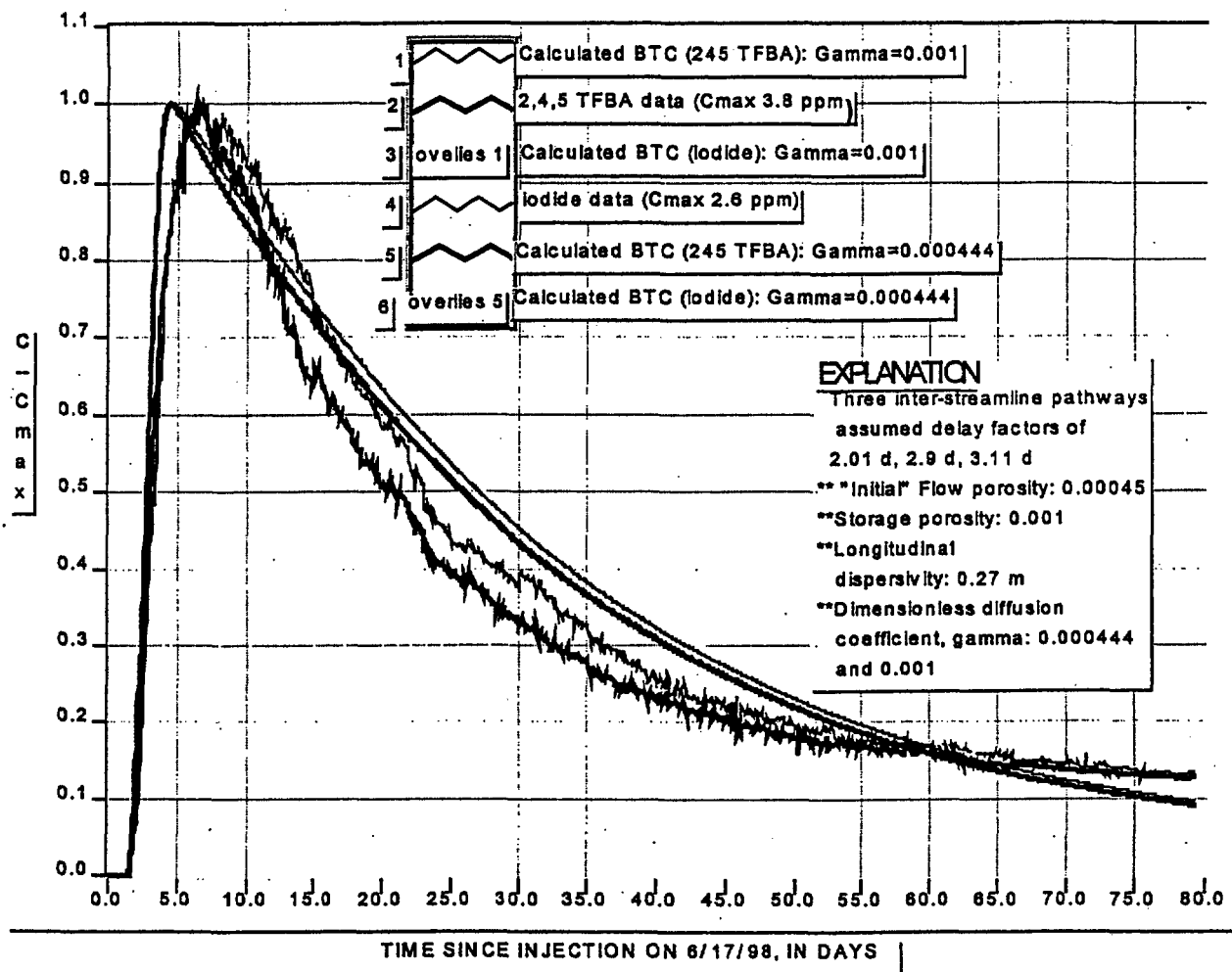


FIGURE 8 . BREAKTHROUGH CURVE FOR 6/17/98 2,4,5 TFBA AND IODIDE TRACER TEST, MATCHED BY DUAL-POROSITY, PARTIAL-RECIRCULATION SOLUTION DERIVED FROM MOENCH (1995), WITH STORAGE POROSITY OF 0.001 AND DIMENSIONLESS DIFFUSION COEFFICIENTS, GAMMA, OF 0.000444 AND 0.001

Figure 4-7. Breakthrough curves for 6/17/98 2,4,5 TFBA and iodide tracer test, matched by dual-porosity, partial-recirculation solution derived from Moench (1995), with storage porosity of 0.001 and dimensionless diffusion coefficients, gamma, of 0.000444 and 0.001. (Data - DTN GS9908312315.001; Model Results - No DTN assigned).

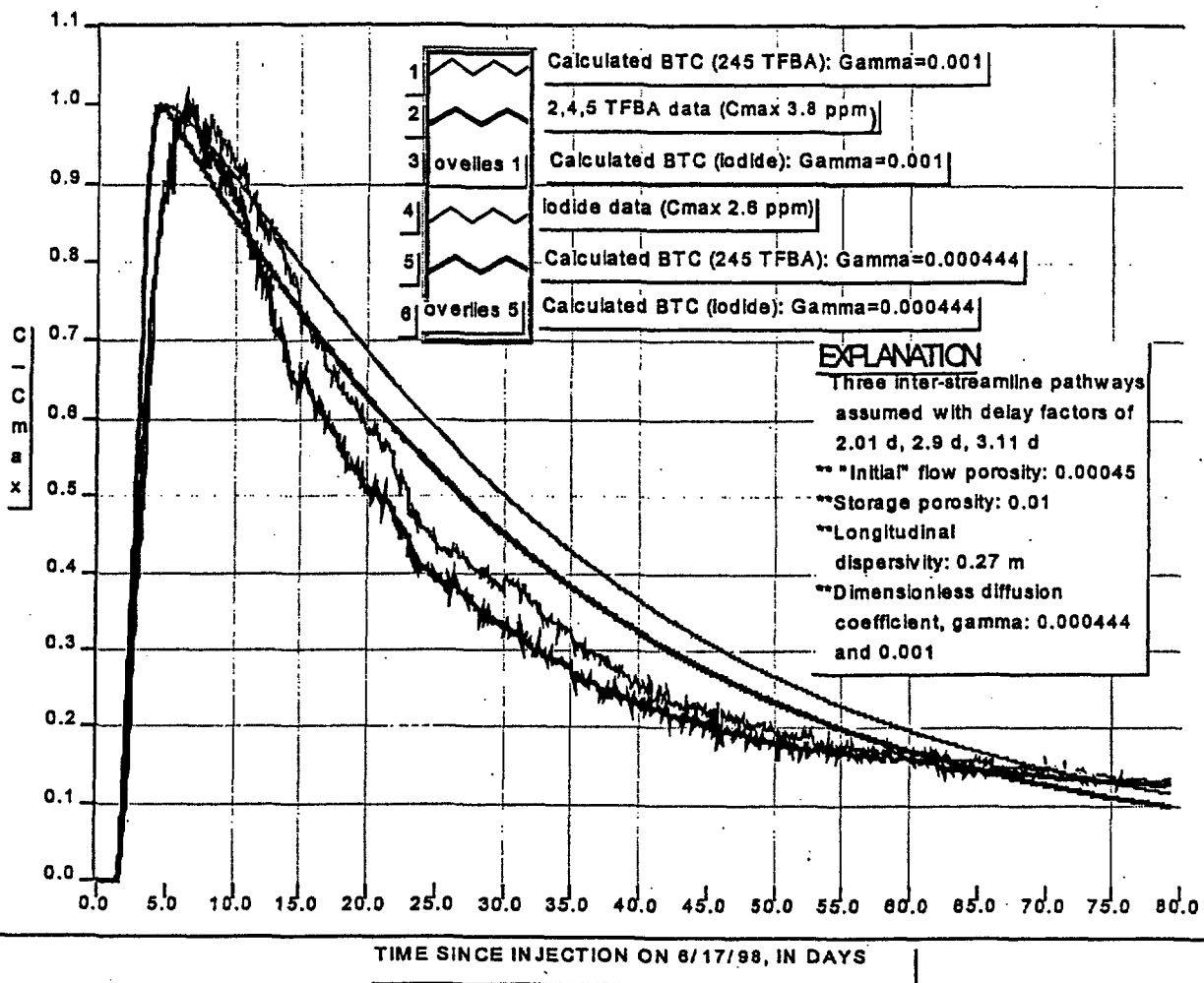


FIGURE 9. BREAKTHROUGH CURVE FOR 6/17/98 2,4,5 TFBA AND IODIDE TRACER TEST, MATCHED BY DUAL-POROSITY, PARTIAL-RECIRCULATION SOLUTION DERIVED FROM MOENCH (1995), WITH STORAGE POROSITY OF 0.01 AND DIMENSIONLESS DIFFUSION COEFFICIENTS, GAMMA, OF 0.000444 AND 0.001

Figure 4-8. Breakthrough curves for 6/17/98 2,4,5 TFBA and iodide tracer test, matched by dual-porosity, partial-recirculation solution derived from Moench (1995), with storage porosity of 0.01 and dimensionless diffusion coefficients, gamma, of 0.000444 and 0.001. (Data - DTN GS9908312315.001; Model Results - No DTN assigned).

## 5.0 Reactive Tracer Test in the Prow Pass Tuff

### 5.1 Test Objectives and Strategy

The reactive tracer test in the Prow Pass Tuff at the C-holes was conducted with the objectives of

- (1) testing/validating conceptual models of radionuclide transport through the saturated zone near Yucca Mountain (test both single- and dual-porosity models for solute transport, and a first-order filtration/resuspension rate model for colloid transport),
- (2) obtaining estimates of key saturated zone solute and colloid transport parameters in the Prow Pass Tuff, and
- (3) assessing the applicability of laboratory-derived sorption parameters to field-scale transport predictions for a monovalent cation ( $\text{Li}^+$ ).

To accomplish the test objectives, a forced-gradient, cross-hole tracer test was conducted that involved the injection of the following tracers:

- pentafluorobenzoate (PFBA),
- bromide ion,
- chloride ion,
- lithium ion,
- ~640-nm diameter carboxylate-modified-latex (CML) polystyrene microspheres dyed fluorescent blue,
- ~280-nm diameter CML microspheres dyed fluorescent orange, and
- ~280-nm diameter CML microspheres dyed fluorescent yellow.

The latter two microspheres were identical (from the same original batch) except that they were tagged with different dyes. All of the microspheres were obtained from Interfacial Dynamics, Inc., Portland, OR.

PFBA, bromide, and chloride are all nonsorbing monovalent anions. PFBA and bromide were used previously in the reactive tracer test in the Bullfrog Tuff at the C-holes. Laboratory testing has shown that these two tracers have diffusion coefficients that differ by about a factor of 3, with bromide having the larger coefficient because of its smaller ionic size (Section 8.0). Laboratory tests have also confirmed that these two tracers do not sorb to tuffs from the C-holes. Although laboratory testing has not been conducted to verify chloride behavior, chloride is chemically very similar to bromide, and it should have about the same diffusion coefficient as bromide (Newman 1973, pp. 229-230). Chloride was introduced to the tracer test primarily because lithium chloride is much cheaper and has twice as much lithium per unit mass as lithium bromide, allowing more lithium to be introduced into the system for less cost. However, chloride was less desirable than bromide as a tracer because of the relatively high chloride background concentration in the C-holes groundwater (~6 mg/L). Comparison of the nonsorbing solute tracers was expected to yield important information on matrix diffusion and dispersion in the flow system. In a dual-porosity system, a high-diffusivity tracer is expected to have a normalized breakthrough curve with a lower, slightly delayed peak and a longer tail relative to a low-diffusivity tracer (Robinson, 1994). However, in a single-porosity system (i.e., a classic porous medium) two such tracers should behave identically. Thus, if bromide and chloride appeared attenuated relative to PFBA, a dual-porosity system conceptualization would be suggested for solute transport in the Prow Pass Tuff.

Lithium is a cation that sorbs weakly to the C-holes tuffs by ion exchange. It was used previously in the Bullfrog Tuff reactive tracer test. Lithium sorption isotherms to several different tuff lithologies found below the water table at the C-holes have been determined in laboratory sorption tests under both static (batch) and dynamic (flowing) conditions. These tests have included all the major lithologies in the Prow Pass tracer test interval. The diffusion coefficient of lithium is expected to be intermediate between that of PFBA and bromide (about two-thirds of the bromide diffusion coefficient) (Newman, 1973, pp. 229-230), so in the absence of sorption, the lithium response in a tracer test in a dual-porosity system would be expected to fall between that of PFBA and bromide. Therefore, any attenuation of lithium relative to bromide, manifested either as a lower peak, a delayed peak, or both, could be attributed to sorption. A quantitative interpretation of the lithium response relative to that of bromide and PFBA could then yield estimates of sorption parameters that allow comparisons with laboratory-derived sorption parameters.

Fig. 5-1 shows generic responses of nonsorbing and sorbing solute tracers in both dual-porosity and single-porosity systems. Note that the difference in the responses of the nonsorbing solutes with different diffusion coefficients in a dual-porosity system is the result of matrix diffusion, as discussed above. This difference is not seen in a single-porosity system where there is very little or no stagnant water available for tracer storage. Fig. 5-1 also shows that sorbing solutes in a single-porosity system always have delayed arrival times relative to nonsorbing solutes, but in a dual-porosity system it is possible for them to have a similar arrival time with only a decrease in peak concentration relative to nonsorbing solutes. The latter response, in particular, would further support the concept of matrix diffusion (as opposed to diffusion only into stagnant free water in the system). In contrast to true matrix diffusion, diffusion into stagnant free water would be accompanied by very little sorption (because of lack of sorbing surfaces), resulting in a sorbing tracer response very similar to nonsorbing tracer responses. Qualitative comparisons of Fig. 5-1 and the tracer responses in the Prow Pass reactive tracer test were expected to provide the first indications of either single- or dual-porosity transport behavior in the Prow Pass flow system.

The CML microspheres were used in the Prow Pass reactive tracer test to study the potential for colloid transport and to obtain estimates of colloid filtration/resuspension coefficients in the Prow Pass Tuff. The blue (640-nm) and orange (280-nm) spheres were injected simultaneously two days before the solutes to study the size dependence of colloid transport and filtration under background groundwater chemistry conditions. The yellow (280-nm) spheres were injected simultaneously with the solute tracers to study the influence of the relatively high ionic strength of the injection solution ( $\sim 0.4 \text{ M}$ ) on the transport behavior of the spheres relative to identical spheres (the orange ones) injected two days earlier at the background ionic strength of  $\sim 0.003 \text{ M}$ . The spheres also potentially provide information on transport through fractures in the absence of matrix diffusion, as they have diffusion coefficients 3-4 orders of magnitude lower than the solutes, and they should therefore not very readily diffuse out of the fractures and into the matrix. The advantages and reasons for selecting the fluorescent-dyed microspheres as colloid tracers are discussed in Appendix C.

## 5.2 Test Procedure

The reactive tracer test procedure closely followed the procedure for conservative tracer testing between wells C#3 and C#2 in the Prow Pass Tuff, with the primary difference being that

the volumes of tracer solution injected were somewhat larger in the reactive tracer test. The packer locations were the same as in the conservative tracer test except that the second packer from the bottom of the string in C#2 was deflated prior to the test so that the production zone extended to the lowest packer in the hole (about 20 ft lower than in the conservative tracer test). The reactive tracer test was conducted under partially-recirculating flow conditions with C#2 pumped at ~19 L/min (~5 gpm) while approximately 30% of the produced water (5.7 L/min or 1.5 gpm) was recirculated into C#3. The recirculation was initiated and went essentially uninterrupted for over 3 months prior to the start of the reactive tracer test. All tracers were injected into C#3 without any interruption or change in system flow rates.

Two separate tracer injections were conducted for the reactive tracer test. Table 5-1 summarizes the times, tracer masses, and tracer concentrations associated with each injection. The first injection involved only two different sizes of microspheres and was conducted to study the influence of microsphere size on transport under minimally-perturbed groundwater chemistry conditions. The second injection included all of the solutes and the remaining microsphere. The rationale for these tracer injections was discussed in Section 5.1. Both injections involved dissolving or dispersing the tracers in water trucked in from well J-13, which is very similar in composition to that of C-holes water. However, whereas J-13 and C-holes water have a background ionic strength of ~0.003 M, the solute injection solution (second injection) had an ionic strength of ~0.4 M.

The reactive tracer test featured a ~10-hr mixing/sampling event of the injection interval in C#3 on Nov. 2, 1998. The mixing/sampling was accomplished by turning on a downhole pump in C#3 to bring water to the surface and then returning this water back to the zone in a closed loop along with the recirculated water from C#2. The pump drew water from near the bottom of the packed-off zone, while the injection port was located near the top of the zone. The flow rate of the mixing pump was ~30 L/min (~8 gpm), so the injection rate into the zone during mixing was ~36 L/min (~9.5 gpm) to maintain a net injection rate of ~5.7 L/min (~1.5 gpm). The startup of the downhole pump was complicated by the fact that the pipe carrying water to the surface was initially empty, and the injection zone was not capable of a net production rate of even 20 L/min. Thus, the pump had to be turned on and off in stages until the pipe to the surface was full of water and water began returning to the zone. This procedure resulted in several large pressure drawdowns of the injection zone before mixing was established. The mixing duration was limited to 10 hrs because the downhole pump added heat to the system, resulting in a steady temperature increase that would have eventually caused temperatures to exceed the upper calibration limit of the pressure transducers in the zone and possibly threaten other system components. A refrigerated chilling unit was plumbed into the mixing loop at the surface to extract heat from the loop and allow for greater mixing times. A total of 63 samples were collected from the mixing loop during the 10 hrs of mixing, starting at 5-min intervals and ending at 20-min intervals. These samples were analyzed for all tracers to determine (1) the fraction of each tracer remaining in the injection zone at the time of mixing and (2) how well the tracers were distributed in the zone prior to mixing.

The production and injection flows were interrupted 3 times during the latter portion of the tracer test. The times and durations of these interruptions are summarized in Table 5-2. The first interruption was unplanned and occurred as a result of a diesel generator failure. The latter two interruptions were intentional and coincided with the Thanksgiving and Christmas-New Year's holiday breaks, respectively. In addition to the practical consideration of avoiding staffing the remote field site over the holidays when few people are in the area, these flow

interruptions offered the opportunity to obtain independent measurements of matrix diffusion in the flow system. If a flow interruption is introduced during the tailing portion of a tracer test in a dual-porosity medium when tracers are diffusing back out of the matrix and into fractures, then a flow interruption will result in an increase in tracer concentrations when flow is resumed. The amount of this increase can be used to obtain estimates of matrix diffusion parameters in the system.

On Jan. 4, 1999, flow was resumed after the Christmas-New Year's shutdown without any recirculation into C#3. The progressing-cavity pump used for recirculation was damaged by a freeze-up over the shutdown, so the pump had to be sent off for repairs. The pump was reintroduced into the system on Jan. 13, 1999, so the test went for almost 10 days with no recirculation into C#3. After Jan. 13, the test was allowed to continue until Jan. 29, 1999, at which time the recirculation into C#3 was stopped and samples were no longer analyzed.

The water produced from C#2 was sampled at regular intervals throughout the test. Many of these samples were analyzed for the injected tracers as well as for other cations present in the groundwater (sodium, calcium, potassium, and magnesium). The other cations were of interest because when lithium sorbs to rock surfaces by ion exchange, some other cation must be released in order to maintain charge balance in solution. Sodium, calcium, and potassium are the most abundant cations in the natural groundwater, so it was expected that they would be the most likely to exchange for lithium.

All cations, including lithium, were analyzed by inductively-coupled plasma atomic emission spectrometry (ICP-AES). The anionic tracers were analyzed by liquid chromatography. The microspheres were analyzed qualitatively in the field by filtering groundwater samples and then viewing the filters with an epifluorescent microscope. Quantitative analysis of the microspheres was accomplished using flow cytometry in Los Alamos.

### 5.3 Test Results

The normalized concentration responses of all tracers at C#2 are shown in Figs. 5-2 and 5-3, with the latter figure showing the concentrations on a logarithmic scale so that the microsphere responses can be seen more clearly. The normalized concentrations were calculated by dividing the observed concentrations (with background concentrations subtracted) by the injection masses, and then multiplying the result by  $10^9$ . This normalization to injection mass allows an unbiased comparison of the tracer responses. The data are plotted as time since injection, so the blue and orange microsphere curves are "corrected" for the fact that these spheres were injected two days earlier than the other tracers. There is no curve shown for the yellow spheres because these spheres never arrived in quantifiable concentrations, although a very small number of them appeared on the microscope filters and in the flow cytometer analyses. The estimated recoveries of all tracers are listed in Table 5-3.

Fig. 5-2 indicates that the solute responses are consistent with dual-porosity transport behavior in the system (see Fig. 5-1 also). The bromide and chloride responses are both attenuated relative to the PFBA, and the lithium is significantly attenuated relative to all of the conservative tracers, with the attenuation seen as a lower peak concentration rather than a time delay. Qualitatively, these observations are all consistent with dual-porosity behavior illustrated in Fig. 5-1. The microspheres are extremely attenuated relative to the solute tracers, with the attenuation being much greater than in the previous Bullfrog Tuff reactive tracer test. The larger

blue spheres were less attenuated than the smaller orange ones injected at the same time. We offer no explanation for this behavior at the present time. The very low microsphere recoveries compared to the Bullfrog Tuff test are tentatively attributed to the "tighter" fracture system in the Prow Pass Tuff (as evidenced by the much lower hydraulic conductivity of the Prow Pass test interval). This tighter system would be expected to have smaller average fracture apertures and hence more opportunities for microspheres to collide with and attach to fracture surfaces. However, we cannot rule out the possibility that the microspheres used in the Prow Pass test had a stronger affinity for rock surfaces than those used in the Bullfrog test due to subtle surface chemistry and/or surface hydrophobicity differences. In fact, the filtration coefficients deduced from the Prow Pass and Bullfrog tracer tests are not all that different (suggesting similar rates of attachment) despite the much different sphere recoveries in the two tests (see Tables 5-7 and C-10). The difference in recoveries is tentatively attributed to greater sphere detachment/resuspension rates in the Bullfrog test; this was the assumed mechanism that accounted for nearly all of the Bullfrog sphere recovery.

One inconsistency in the tracer responses is the striking difference between the chloride and bromide breakthrough curves. As mentioned in Section 5.1, these anions were expected to behave very similarly, but bromide is clearly attenuated with respect to chloride. The J-13 water used for the tracer injections was slightly elevated in chloride concentration relative to the C-holes water (~7 mg/L instead of ~6 mg/L), but this was not enough to account for the observed difference. One possible explanation for the chloride behavior is that there may be a higher chloride concentration initially in the matrix than in the background groundwater (which was presumably produced from fractures). In this case, chloride diffusion into the matrix would be suppressed by a reduction in the concentration gradients that drive diffusion. Another possible explanation is that the background chloride concentration drifted upward during the test due to the arrival of water from another aquifer with a different water chemistry. Other explanations, such as subtle chemical or electrochemical interactions with other tracers or with the rocks (for instance, exchange of bromide for chloride in the rocks), could also be responsible for the observed behavior. Because of the much greater laboratory experimental database existing for bromide on this project and the fact that chloride background concentrations were quite high, more reliance was placed on the bromide data than the chloride data.

Fig. 5-2 also shows that there was a "rebound" in tracer concentrations after each of the flow interruptions during the latter portion of the test. Fig. 5-4 shows the rebounds after the second and third flow interruptions more clearly by plotting only the first 16 hrs of data after pumping resumed. The initially low concentrations measured in samples collected immediately after the resumption of pumping are attributed to purging of the production wellbore. The responses are qualitatively consistent with matrix diffusion behavior, although, as discussed in Section 5.4, the magnitude of the responses is difficult to attribute entirely to matrix diffusion.

Fig. 5-5 shows the responses of all tracers in C#3 during the mixing of the injection zone that was conducted on Nov. 2, 1998. It is apparent that all the tracers circulated around the mixing loop several times in a slug that gradually dispersed with time. The mean residence time in the loop was calculated to be a little over 3 hrs (obtained by dividing the volume of the packed-off interval and piping by the mixing flow rate). By comparison, the tracer transit times through the mixing loop (times from peak to peak) averaged about 2.5 hrs. This discrepancy between calculated and observed residence times suggests that the more dense tracer solution may have "sank" after injection into the packed-off interval, resulting in earlier arrival times at the pump intake at the bottom of the zone than simple volumetric flow rates would suggest.

However, it is also possible that the cooled water returning to the injection zone sank simply because of temperature-induced density differences between the resident water and the injected water. It is very interesting that there appeared to be some separation of the microsphere and solute tracers in the mixing loop after the first slug, with the microspheres leading the solutes by nearly one hour and appearing to be more dispersed than the solutes. This behavior is unexplained at the present time, but it argues against solute-induced density differences causing the shorter-than-calculated mixing loop residence times because if that were the case, the more dense solute slug would be expected to lead the microsphere slug (which should be less dense because the spheres have a specific gravity of 1.05 and they occupy a negligible volume fraction).

The fact that first arrival of tracers in the C#3 mixing loop was quite soon after the initiation of mixing and also that the first slug was of relatively short duration suggests that the tracers were initially stratified near the pump intake at the bottom of the injection zone. However, the maximum concentrations measured in the first slug were only about 1/9<sup>th</sup> of the calculated injection concentrations. The calculated amount of each tracer remaining in C#3 ranged from ~0.35 to ~0.6% of the injection mass (see Table 5-3), indicating that most of the tracer mass exited the injection borehole during the first ~5 weeks of the test. These recoveries were calculated by integrating the areas under the individual peaks in Fig. 5-5.

Fig. 5-6 shows the overall charge balance (above background) in the water produced from C#2 during the tracer test. As must be the case to maintain solution charge balance, the positive and negative charges are in very good agreement. Fig. 5-7 shows that the positive charges lost as a result of lithium sorption in the system are made up for primarily by sodium and calcium ions. These results clearly point to lithium exchange with sodium and calcium in the Prow Pass flow system. Sodium and calcium were injected only at negligible background concentrations in the test, so the "responses" of these ions must be attributed to exchange of lithium with calcium and sodium in the rocks.

#### 5.4 Test Interpretation

##### Summary of Models

The solute tracer responses were interpreted by simultaneously fitting the breakthrough curves prior to the first flow interruption using a semi-analytical, dual-porosity transport model, RELAP, which is described in detail in Appendix D and briefly summarized here (see also, Reimus and Dash, 1998, all pages). The physical, conceptual, and mathematical models assumed for the field transport system are depicted in Fig. 5-8. The equations shown at the bottom of Fig. 5-8 are Laplace-domain "transfer functions" that describe tracer residence time distributions within each of the system "components." The most important of these is the transfer function for the groundwater system, which is taken from Tang. et. al. (1981). This transfer function assumes 1-dimensional advective-dispersive transport in parallel-plate fractures with 1-dimensional diffusion (perpendicular to fracture flow) into a homogeneous, infinite matrix. It also assumes linear, equilibrium, reversible sorption of a reactive species and a constant flow velocity in the fractures. The time-domain expressions for fracture and matrix transport corresponding to this Laplace-domain expression are:

Fracture:

$$R_f \frac{\partial C_f}{\partial t} + v_f \frac{\partial C_f}{\partial x} - D_f \frac{\partial^2 C_f}{\partial x^2} - \frac{\phi D_m}{b\eta} \frac{\partial C_m}{\partial y} \Big|_{y=b} = 0 \quad (5.1)$$

Matrix:

$$R_m \frac{\partial C_m}{\partial t} - D_m \frac{\partial^2 C_m}{\partial y^2} = 0 \quad (5.2)$$

subject to the following initial and boundary conditions

$$C_f(x, 0) = 0 \quad (5.1a)$$

$$C_f(0, t) = \delta(t) \quad (5.1b)$$

$$C_f(\infty, t) = 0 \quad (5.1c)$$

$$C_m(y, x, 0) = 0 \quad (5.2a)$$

$$C_m(b, x, t) = C_f(x, t) \quad (5.2b)$$

$$C_m(\infty, x, t) = 0 \quad (5.2c)$$

where,  $C_f$  = tracer concentration in solution in fractures,  $M/L^3$

$C_m$  = tracer concentration in solution in matrix,  $M/L^3$

$v_f$  = fluid velocity in fractures,  $L/T$

$D_f$  = dispersion coefficient in fractures,  $L^2/T$

$D_m$  = molecular diffusion coefficient in matrix,  $L^2/T$

$\eta$  = porosity within fractures,

$\phi$  = matrix porosity, and

$b$  = fracture half aperture,  $L$ .

Laplace-domain model formulations assuming a finite matrix (Maloszewski and Zuber, 1983, 1985), radial flow (Moench, 1995; Becker, 1996, pp. 110-105 and 119-131) and rate-limited sorption (Maloszewski and Zuber, 1991) are also embodied in RELAP. These can be used to evaluate the sensitivity of the derived transport parameters to radial vs. linear flow, infinite vs. finite matrix, and equilibrium vs. rate-limited sorption. A detailed description of the mathematical development of the models embodied in RELAP is provided in Appendix D.

The transfer functions shown in Fig. 5-8 were multiplied together to describe transport throughout the system; a multiplication in the Laplace domain is equivalent to a convolution integral in the time domain (Jenson and Jeffreys, 1977, pp. 169-170). Although not shown explicitly in Fig. 5-8, recirculation of the production water from well c#2 into c#3 was also accounted for (see Appendix D). Unlike the Bullfrog Tuff reactive tracer test in which recirculation was insignificant (~3.3%), the 30% recirculation in the Prow Pass test was expected to have a significant effect on the interpretation of the test. Wellbore storage was accounted for by assuming that the boreholes were well-mixed, with the tracers experiencing an exponential-decay residence time distribution with a time constant equal to the volume of the interval divided by the volumetric flow rate into (injection well) or out of (production well) the interval. Note that an equation for wellbore mixing in the production well is not shown in Fig. 5-8 even though mixing was accounted for in the RELAP simulations. The Laplace domain solutions were then

inverted to the time domain using a Fourier-transform inversion technique (Appendix D). Because the Fourier-transform technique is very efficient (and stable), it could be performed thousands of times per minute on a computer workstation, making it practical to estimate model parameters by systematic, brute-force adjustments of their values to achieve a least-squares fit to the data. The only drawback to using RELAP to fit/simulate the tracer responses was that the Laplace transform approach is only capable of simulating steady-state flow conditions, so it was not possible to use RELAP to fit the data after the first flow interruption.

### Solutes (Before Flow Interruptions)

The fitting procedure involved first simultaneously fitting the PFBA and bromide data sets up to the first flow interruption assuming that both tracers were nonsorbing and that the bromide diffusion coefficient was a factor of 3 larger than that of PFBA. The PFBA and chloride data sets were also simultaneously fit assuming a factor of 3 difference between the diffusion coefficients of Cl and PFBA. The bromide and chloride data sets were not fit simultaneously because these tracers should have had nearly identical diffusion coefficients, resulting in very little predicted difference in their breakthrough curves, which is in contrast to the observed responses (see Section 5.3). The parameters that were adjusted to obtain the fits were (1) the mean residence time, (2) the Peclet number (inversely proportional to dispersivity), (3) the fraction of injected mass participating in the test, and (4) the matrix diffusion mass transfer parameter (with the proper ratios of tracer diffusion coefficients preserved). In each case, only a single set of pathways (i.e., a single set of fitted parameters) was used to fit the tracer responses up to the first flow interruption. (It was necessary to assume multiple "pathways" to explain the double-peaked responses in the Bullfrog Tuff reactive tracer test.) After obtaining the best-fitting model parameters for the PFBA-Br and PFBA-Cl data sets, the lithium response was fitted using the same parameters that offered the best fit to the nonsorbing tracers, but the fracture and matrix retardation coefficients were allowed to vary to achieve a fit. These simulations provided estimates of fracture and matrix retardation factors for lithium up to the first flow interruption. The lithium diffusion coefficient in all cases was assumed to be two-thirds that of bromide.

Figs. 5-9 and 5-10 show the results of fitting the PFBA-Br-Li and the PFBA-Cl-Li data sets, respectively, up to the first flow interruption. The corresponding best-fitting parameters associated with these fits are given in Tables 5-4 and 5-5, respectively. Table 5-4 also includes the parameters deduced from fitting the PFBA, bromide, and lithium responses in the previous Bullfrog Tuff reactive tracer test. Note that the best-fitting matrix diffusion mass transfer coefficient ( $\frac{\phi}{b} \sqrt{D_m}$ ) in the Prow Pass test is smaller in the case of the PFBA-Cl-Li fit (Table 5-5) than the PFBA-Br-Li fit (Table 5-4). This result is due to the smaller difference between the observed PFBA and Cl data sets than the PFBA and Br data sets; a smaller mass transfer coefficient is required to simultaneously fit the PFBA-Cl data if the ratio of Cl-to-PFBA and Br-to-PFBA diffusion coefficients is assumed to be the same (as they were). Note that the PFBA-Br-Li fit (Fig. 5-9) is better than the PFBA-Cl-Li fit (Fig. 5-10), which helps justify placing more confidence in the Br data than the Cl data when determining matrix diffusion parameters by comparison with the PFBA data.

All fits shown in Figs. 5-9 and 5-10 assumed an infinite fracture spacing (infinite matrix blocks). This does not imply a truly infinite matrix; it simply implies that the tracers did not

diffuse far enough into the matrix over the time scales of the test to begin encountering tracers from adjacent fractures. Several RELAP simulations with successively smaller finite fracture spacings were conducted to determine at what spacing the fits would begin to deviate from the infinite-matrix predictions. The spacing at which this occurred was 2.8 cm (i.e., a rough measure of the matrix diffusion distance for bromide), which was taken to be the lower bound for fracture spacing determined from the test. The 2.8 cm-fracture-spacing simulation offered a slightly improved fit to the bromide data (by raising the tail) while not significantly affecting the PFBA fit. The fact that bromide was beginning to fill up the matrix in this simulation resulted in a slowing of bromide matrix diffusion relative to PFBA during the latter portion of the test. The lithium breakthrough curves were not affected at all by the 2.8-cm fracture spacing (i.e., simulation results were identical to infinite-spacing case).

The best fits to the lithium data were achieved assuming no sorption at all in the fractures, and the data were also adequately fitted assuming linear, equilibrium sorption in the matrix. Kinetic (rate-limited) fits of the lithium data were not attempted because of the very good fit assuming equilibrium sorption and also because laboratory experiments have indicated that sorption kinetics are very fast relative to the time scales of the field responses. Nonlinear sorption simulations using RETRAN (see below) also were not attempted because of the adequacy of the linear fits and the fact that laboratory-derived lithium sorption isotherms to Prow Pass Tuffs were nearly linear.

The linear  $K_D$  sorption parameter deduced from the lithium fits assuming transport in either the central Prow Pass Tuff lithology or the lower Prow Pass Tuff lithology (the two predominant lithologies in the test interval) are listed in Table 5-6. These  $K_D$ s were calculated assuming matrix bulk densities and porosities that were measured in laboratory experiments using the following equation:

$$R = 1 + \frac{\rho_B}{\phi} K_D \quad (5.3)$$

where  $\rho_B$  = bulk density, g/cm<sup>3</sup>,

$\phi$  = porosity,

$K_D$  = linear distribution coefficient, cm<sup>3</sup>/g.

Lithium matrix  $K_D$ s derived from the Bullfrog Tuff reactive tracer test are also listed in Table 5-6. Four different values are given in this case because there were two separately-analyzed "pathways" in the test and two major lithologies in the test interval. The last column in Table 5-6 lists laboratory-measured  $K_D$ s for the various tuff lithologies that were considered likely to be involved in the field tests.

It is apparent that the field-derived  $K_D$ s obtained for both possible tuff lithologies in the Prow Pass Tuff greatly exceed laboratory-derived values. The same holds true for the second "pathway" in the Bullfrog Tuff. In the case of the first "pathway" in the Bullfrog Tuff, the field and laboratory values are in closer agreement, with the field values being greater than the laboratory values obtained over the entire range of concentrations in the sorption experiments but less than the laboratory values calculated at infinite dilution (using the asymptotic slope of the Langmuir isotherm).

## Microspheres

The microsphere responses were fitted assuming the same hydrologic parameters that offered the best simultaneous fit to the PFBA-Br data sets (the PFBA-Cl parameters were not used for the spheres). In this case, the matrix diffusion coefficients were set to zero (because the spheres have very small diffusion coefficients), and rate-limited fracture sorption parameters were adjusted to achieve a best fit to the data. Under these assumptions the governing equations used to fit the data were:

$$\frac{\partial C}{\partial t} + V \frac{\partial C}{\partial x} - D \frac{\partial^2 C}{\partial x^2} + k_{\text{filt}} C - k_{\text{res}} S = 0 \quad (5.5)$$

$$\frac{1}{b} \frac{\partial S}{\partial t} - k_{\text{filt}} C + k_{\text{res}} S = 0 \quad (5.6)$$

where,  $C$  = colloid concentration in solution, number/L

$S$  = colloid concentration on surfaces, number/L<sup>2</sup>

$V$  = flow velocity in fractures, L/T

$D$  = dispersion coefficient, L<sup>2</sup>/T

$k_{\text{filt}}$  = filtration rate constant (1/T) =  $\lambda V$ , where  $\lambda$  = filtration coefficient (1/L)

$k_{\text{res}}$  = resuspension rate constant, 1/L-T

$x, t$  = independent variables for distance and time, respectively.

Only the early microsphere responses were fitted because the later time responses (after 300 hrs) were consistently very near detection limits. The resulting fits to the early data are shown in Fig. 5-11, with corresponding best-fitting parameters listed in Table 5-7. The fits shown in Fig. 5-11 assumed no detachment or resuspension of the microspheres (i.e.,  $k_{\text{res}} = 0$ ). That is, the early responses were adequately fitted assuming irreversible filtration or attachment of spheres in the system. This result is in contrast to fits of the microsphere response in the Bullfrog Tuff reactive tracer test, where it was necessary to assume some detachment of the spheres to explain the late-time response (in fact, detachment accounted for all of the Bullfrog sphere response after about the first 100 hrs). However, detachment is also very likely responsible for the detectable, but barely quantifiable, responses of blue and orange microspheres throughout the Prow Pass test. The microsphere "pulse" at about 1000 hrs into the test (see Fig. 5-3) actually corresponded to a few days after mixing C#3, which suggests that the pressure and flow transients caused by the mixing may have mobilized/detached some microspheres. The timing of this response was consistent with the arrival time of the spheres after injection into C#3 on 9/23/98. A second large pulse in sphere concentrations occurred the day after the unplanned flow interruption on 11/14/98 (again, see Fig. 5-3), which further supports the hypothesis that flow and pressure transients may have resulted in microsphere detachment.

Because the late-time sphere responses were sporadic (possibly caused by the unsteady flow conditions) and very near quantifiable limits, no attempt was made to quantitatively model them. The fact that the late-time response did not follow any definitive trend that could be predicted or simulated using the simple assumptions embodied in equations (5.5) and (5.6) suggests that the model represented by these equations is inadequate to model colloid transport over long time scales under the conditions of the test. We speculate that models incorporating

stochastic detachment or detachment that is sensitive to flow transients (or possibly even water chemistry changes due to the decay of the solute tracer pulse) could offer improvements to better describe the late-time microsphere response. It is interesting that the peak concentrations of blue and orange microspheres occurred at about the same time that solutes began arriving at C#2 (note that the spheres were injected ~48 hrs before the solutes), and then the spheres rapidly decreased in concentration as the solute concentrations increased. This behavior may be purely coincidental, or it may hint that the increased ionic strength associated with the solutes caused the remaining spheres to attach more readily to rock surfaces. It is also interesting that there was a pressure increase of ~35 psi in C#3 starting about a day after the injection of the solutes began (or about six hrs after the injection pulse was over). This pressure increase persisted and gradually increased by another ~10 psi until C#3 was mixed on 11/2/98, at which time the pressure dropped back to about what it had been before the solute injection and remained at approximately that level (see Fig. 5-14, discussed below, for a graphical representation of the C#3 pressure history). This unexplained behavior suggests that the flow pathways out of C#3 may have become partially "clogged" shortly after solute injection, and that the pathways may have been "unclogged" by the pumping associated with the mixing of C#3. It is not known if this phenomenon was really "clogging" or if it had any influence on the microsphere responses.

The filtration coefficient listed in Table 5-7 for the yellow microspheres was not obtained from fitting, but rather it was the smallest filtration coefficient that resulted in a peak concentration of spheres that was at or below detection limits. This number can be considered a lower bound estimate of the yellow sphere filtration coefficient because any larger value will result in more filtration and an even lower recovery. The lack of recovery of yellow microspheres is tentatively attributed to the much higher ionic strength of the solution these spheres were injected in relative to the ionic strength associated with the injection of the other microspheres. It is well known that colloids are less stable at higher ionic strengths due to the collapse of electrostatic double-layers that provide stability against aggregation or attachment to solid surfaces. However, there were very few aggregates of any of the microspheres (including the yellow ones) observed in the samples obtained from the C#3 mixing loop.

### Solutes After Flow Interruptions

Modeling of the tracer responses after the flow interruptions was conducted according to the following procedure. The RELAP solute tracer fits were repeated assuming no dead time/volume in the injection and production intervals and no recirculation but with the same matrix diffusion mass transfer parameters that provided the best fits in the simulations discussed above. Although this procedure was not strictly valid from the standpoint of ignoring wellbore mixing and recirculation, it was considered acceptable from the standpoint of qualitatively predicting tracer responses after the flow interruptions in a dual-porosity system with appropriate matrix diffusion parameters and offering comparisons between the predicted and actual data. The simulations were conducted to obtain reasonable fits to the solute data under assumptions that were consistent with the capabilities of RETRAN, a numerical sister code to RELAP (see Appendix D for a detailed description). RETRAN does not simulate wellbore mixing or recirculation, but, unlike RELAP, it is capable of simulating flow interruptions. The fitted parameters from RELAP (prior to the first flow interruption) were used as inputs to RETRAN to simulate the entire reactive tracer test, including all of the flow interruptions. The fitted parameters from RELAP that were used in the RETRAN simulations are listed in Table 5-8.

Fig. 5-12 shows the actual and RETRAN-simulated solute responses over the entire tracer test (chloride not shown). RETRAN does not reproduce the RELAP simulations very well during the early portion of the test (the RELAP fits were much better), presumably because of the very large dispersion coefficient (small Peclet number) obtained in the RELAP fits and used in RETRAN. Differences between simulated RELAP and RETRAN tracer responses are generally smaller when lower amounts of dispersion are assumed. However, because the matrix diffusion parameters used in the RELAP and RETRAN simulations were identical, the RETRAN simulations should have provided good qualitative predictions of tracer responses after the flow interruptions.

Fig. 5-12 shows that the magnitude of the "rebounds" in normalized tracer concentrations after the flow interruptions are generally underpredicted by RETRAN, especially after the first flow interruption. If these "rebounds" are truly due to matrix diffusion, then there must be much more diffusion occurring during the shut-in periods than is deduced based on the tracer responses prior to the flow interruptions. The very sharp increases in tracer concentrations after the first flow interruption, which was only ~14 hrs, are especially suggestive of a large amount of matrix diffusion or some other phenomenon occurring over a very short time period.

Insights into why the responses are underpredicted by RETRAN are obtained by examining the results of RELAP simulations that assume the same parameters as in Table 5-8, but with no matrix diffusion. The simulated response in this case is compared to the actual PFBA and bromide responses in Fig. 5-13. The fact that the simulated response is higher than the actual responses at the time of the flow interruptions suggests that there is predicted to be net diffusion into the matrix rather than out of the matrix at the time of the interruptions. This is true despite the small amount of diffusion initially out of the matrix and into fractures during periods of no flow. A large rebound in tracer concentrations would be predicted only if there were a significant amount of net diffusion out of the matrix at the time of the flow interruptions (i.e., if the predicted response without matrix diffusion was significantly lower than the actual response). Attempts to obtain better agreement between the simulated and observed responses by reducing the assumed fracture spacing in the system (i.e., smaller matrix blocks) while maintaining the same diffusion rates improved the agreement slightly, but not significantly. Decreasing the fracture spacing decreases the time it takes for diffusion to transition from being net into the matrix to net out of the matrix.

Two possible explanations are offered for the higher-than-predicted tracer responses after the flow interruptions. The first explanation is that there is actually some flow into and out of the matrix when the downhole production pump in C#2 is turned off and on, respectively. Such flow may be possible because of the large pressure transients that occurred whenever the pump was turned on or off. The pressure in C#2 typically decreased by over 200 psi (~500 ft of drawdown) when the pump was first turned on and then gradually stabilized at a somewhat smaller drawdown. Conversely, the pressure increased dramatically when the pump was shut down. Pressure records in C#2 and C#3 during the reactive tracer test are shown in Fig. 5-14. The pressure transients were most pronounced near the borehole and damped out at increasing distances from the well, as indicated by the response in C#3 (and also the responses in C#1 shown in Fig. 3-5). The relatively short duration of the observed concentration spikes supports this concept of a near-borehole phenomenon. Tracer concentration spikes resulting from this mechanism cannot be predicted by RETRAN because RETRAN assumes no flow into or out of the matrix. The lithium responses are especially supportive of the matrix flow hypothesis, as the

combination of matrix diffusion and matrix sorption leads to predictions of essentially no change at all in concentrations after the flow interruptions, which is in contrast to the data.

The second possible explanation is that there are multiple rates of matrix diffusion in the system as a result of flow through multiple flow pathways that have different bulk matrix diffusion characteristics. Multiple-rate diffusion models have been used by others to explain tracer responses in field tests (Meigs et al. 1998). Although we did not have a multiple-rate diffusion model to exercise, it was possible to use RETRAN to qualitatively demonstrate the benefits of including at least one pathway with a large matrix diffusion mass transfer coefficient. Fig. 5-15 shows a simulated bromide response assuming a matrix diffusion mass transfer

coefficient,  $\frac{\phi}{b} \sqrt{D_m}$ , about 2.5 times larger than that deduced from the RELAP fits and with hydrologic parameters modified to produce a curve similar in shape to the actual tracer breakthrough curves. It should be noted that the Peclet number in this simulation had to be increased significantly (to 20; i.e., less dispersion) to allow matrix diffusion to account for most of the tail of the predicted breakthrough curve. In this case, with the exception of the response after the first flow interruption, the magnitude of the tracer responses after all interruptions are in reasonably good qualitative agreement with the observed responses. However, the fact that the responses after the first flow interruption are underpredicted still suggests that a component of flow may be at least partially responsible for the observed behavior. Also, the predicted breakthrough curve shown in Fig. 5-15 would have to be balanced by other flow pathways with much smaller matrix diffusion mass transfer coefficients than those deduced from the RELAP fits in order to obtain composite responses that match the tracer data.

#### Analysis of Dispersion Under Linear, Radial, and Recirculating Flow Conditions

Different mean residence times ( $\tau$ ) and Peclet numbers ( $Pe$ ) are reported in Tables 5-4 and 5-5 depending on whether linear or radial flow was assumed in RELAP. In a heterogeneous, confined aquifer, the flow velocity to a single production well with no recirculation into an injection well is expected to vary between linear and radial (National Research Council, 1996, pp. 252-259). Thus, if we assume that the Prow Pass test interval is reasonably confined, as suggested by the absence of any pressure responses above and below the packed-off zone, presenting the two sets of residence times and Peclet numbers in Tables 5-4 and 5-5 is a way of bounding these parameter estimates as a result of flow field uncertainty. The radial mean residence time is always less than the linear residence time, and the radial Peclet number is always greater than the linear Peclet number. This somewhat confusing result can be qualitatively explained by recognizing that the models implicitly assume that the dispersion coefficient is the product of the dispersivity ( $\alpha$ ) and the fluid velocity. Under this assumption, for a given dispersivity, a solute will tend to experience more dispersion in radial flow than in linear flow because any time the solute disperses ahead of the mean position, it will be subjected to a greater flow rate, and any time it disperses behind the mean position, it will be subjected to a slower flow rate. Thus, leading solute particles will tend to be swept further ahead and lagging solute particles will tend to lag further behind in radial flow than they would be in linear flow. In effect, the radial flow field has an additive effect to the dispersion that would be experienced in a linear flow field. Any breakthrough curve can always be fitted equally well assuming either type of flow field; only the values of the parameters will differ.

Of course, the flow field under conditions of 30% recirculation is technically neither linear or radial. Transport rates away from the injection well will initially be high and will decrease as tracers move away from the well, but rates will increase again as tracers move closer to the production well. Also, a certain amount of dispersion will be caused by the recirculating flow field due to streamlines of different lengths and different residence times. Fig. 5-16 shows a depiction of streamlines in a 30% recirculation flow field in a perfectly homogeneous, isotropic confined aquifer (i.e., a 2-dimensional flow system). This flow field was simulated using an unqualified software package known as 2WELLS\_2D, which can generate flow streamlines as well as tracer breakthrough curves in cross-hole tracer tests in homogeneous, isotropic systems under recirculating conditions (Reimus 1995, pp. 12-29). To obtain an estimate of the dispersion resulting from the flow field of Fig. 5-16, a breakthrough curve was simulated using the particle-tracking features of 2WELLS\_2D. In the simulation, it was assumed that there was no longitudinal or transverse dispersion of the particles within streamlines. The resulting dimensionless breakthrough curve is shown Fig. 5-17. Because the particles were not allowed to disperse within or across streamlines, this curve reflects the apparent dispersion that occurs as a result of the 30% recirculation flow field. Note that this is a "once-through" breakthrough curve that does not take into account the recirculation of particles through the system. To obtain an estimate of the actual non-flow-field-induced dispersion in the Prow Pass reactive tracer test, the dispersion deduced from the RELAP simulations was corrected for the apparent dispersion caused by the flow field using the following method:

- (1) The mean and variance of the breakthrough curve in Fig. 5-17 was calculated by standard statistical methods.
- (2) The variance of the best-fitting RELAP-simulated responses was calculated using the following equation (see Section 5.App for derivation):

$$\sigma^2 = 2 \frac{\tau^2}{Pe} \quad (5.4)$$

where  $\tau$  and  $Pe$  are the best-fitting parameters from the RELAP simulations.

- (3) It was assumed that the variance from step (2) was the sum of the variance due to the flow field and the variance due to true dispersion in the system. It was also assumed that these two processes are independent (uncorrelated). The variance of a process that is the sum of two independent processes is equal to the sum of the variances of the independent processes. Thus, the variance due to true dispersion in the system was taken to be the variance from step (2) minus the variance from step (1).
- (4) A Peclet number that represents true dispersion in the system was calculated from the variance resulting from step (3) by inserting the variance into equation (5.4) and rearranging to solve for  $Pe$ .

A once-through breakthrough curve was used for step (1) because the Peclet number from the RELAP simulations was calculated after deconvoluting the effects of recirculation (and wellbore mixing). The resulting Peclet numbers and dispersivities obtained for true dispersion in the system (after removing the dispersion due to recirculation) are given in Table 5-9. Section 5.App provides more details on the development and assumptions of this method.

## 5.5 Discussion of Uncertainties

There are several sources of uncertainty associated with the Prow Pass reactive tracer test interpretation. First, there are data uncertainties, which are related to the accuracy and precision of the tracer chemical analyses, including both random and systematic errors. Random errors were probably small because the breakthrough curve data are not widely scattered and show well-defined trends. The most significant sources of systematic errors would have been day-to-day differences in analytical instrument operation and in analytical standard preparation. However, repeat measurements on separate days indicate that these errors were also minimal.

Uncertainties in the model parameter estimates are related to uncertainties in the data, discussed above, and uncertainties in the uniqueness of the curve fits. Parameter uncertainty due to data scatter can generally be quantified by statistical measures such as "95% confidence intervals" (Draper and Smith, 1981, pp. 93-96 and pp. 472-473). For a given set of modeling assumptions, we expect this uncertainty to be relatively small given the smoothness of the breakthrough curve data, but we have left its quantification for future work. Uniqueness-of-fit uncertainties are lower when several tracer responses are analyzed simultaneously than when only a single response is analyzed because more constraints are placed on the interpretation. However, the inconsistency between the Br and Cl data, despite the fact that these tracers should behave nearly identically, is troublesome. The range of parameter values in Tables 5-4 and 5-5 can be considered to be a qualitative measure of the uncertainty associated with this inconsistency. As stated in Section 5.4, the bromide data were considered to be more reliable than the chloride data because of the high background chloride concentration in the groundwater. An additional interpretive uncertainty is associated with the fact that it is not possible to determine individual parameters with any degree of certainty when they are "lumped" with other uncertain model parameters. For instance, the single fitted lumped parameter,  $\frac{\phi}{b} \sqrt{D_m}$ , contains three uncertain parameters that cannot be measured independently in a field test.

Other uncertainties in the test interpretation include (1) assuming either radial or linear flow when the actual nature of the flow field is unknown, (2) the influence of the 30% recirculation on the apparent dispersion in the system, and (3) the possibility that the wellbore residence time functions could have been significantly different than an exponential decay with a time constant approximately equal to the borehole volume divided by the injection flow rate. The uncertainty associated with assuming either radial or linear flow (the two extremes in a confined aquifer) is reflected in the values of the mean residence times and Peclet numbers associated with these two assumptions in Tables 5-4 and 5-5. Matrix diffusion and sorption parameters are not affected by these flow field assumptions. The uncertainty associated with the 30% recirculation is addressed in Section 5.4, where it was shown that the recirculating flow field could have caused a significant amount of the observed dispersion. However, it should be noted that the method of accounting for flow field dispersion assumed a homogeneous, isotropic aquifer, which is very unlikely in fractured rock. Nevertheless, the approach allows a reasonable estimate of the true dispersion in the system with the effects of recirculation removed (see also Section 5.App). The wellbore residence time uncertainty was investigated by determining the sensitivity of the fitted parameters to assumed values of wellbore decay constants, ranging from  $0.11 \text{ hr}^{-1}$  (which assumes a ~9-hr mean residence time in the injection wellbore) to  $60 \text{ hr}^{-1}$  (which assumes a mean residence time of only one minute). Because of the long times until tracer

arrivals (~40 hr) and tracer peaks (~250 hr), the fits were essentially insensitive to the wellbore decay constants.

## 5.6 Ranges of Parameter Estimates for Performance Assessment

Table 5-10 provides ranges of physical parameter values derived from the field test interpretations. These ranges are intended to provide performance assessment modelers with lower and upper bounds for use in large-scale, abstracted transport models. Ranges of parameter values deduced from the reactive tracer test in the Bullfrog Tuff at the C-wells are also listed in Table 5-10. Lithium sorption parameters are not included in Table 5-10 because they are not directly relevant to any radionuclides of importance to performance assessment. However, both reactive tracer tests did establish that lithium sorption in the field was as strong or stronger than would have been predicted based on laboratory measurements, which suggests that predictions of sorbing radionuclide transport in the field based on laboratory sorption measurements should tend to be conservative.

The longitudinal dispersivity values in Table 5-10, were calculated using  $\alpha = L/Pe$ , where the travel distance, L, was assumed to take on minimum and maximum values of 30 and 80 m for the Prow Pass test, corresponding to the interborehole distance and the approximate distance between the bottom of one borehole and the top of the other (the maximum possible linear transport distance), respectively. To put the dispersivities in perspective, Fig. 5-18 shows boxes encompassing the range of calculated C-holes dispersivities superimposed on a plot of dispersivity vs. scale taken from Neuman (1990). It is apparent that longitudinal dispersivities at the C-holes are reasonably consistent with other data sets and with existing theories on the scale dependence of dispersion. It should be noted that the range of dispersivities in the Prow Pass test in Fig. 5-18 is almost completely encompassed by the range in the Bullfrog test (hence the nearly identical appearance of this figure and Figure 2-13 in Appendix C).

The values in Table 5-10 for fracture apertures and effective flow porosity are very uncertain and should be used with caution. Fracture aperture values were calculated from the best-fitting lumped matrix diffusion parameters,  $\frac{\phi}{b} \sqrt{D_m}$ , assuming that the matrix diffusion coefficients and matrix porosities measured in diffusion cell experiments (see Section 8.0) applied in the field. For the Prow Pass tracer test, the lower bound was calculated using the lumped matrix diffusion parameter obtained from simultaneously fitting the PFBA and Br data and assuming the matrix porosity and diffusion coefficients measured in the central Prow Pass Tuff. The upper bound was calculated using the lumped parameter from simultaneously fitting the PFBA and Cl data and assuming the matrix porosity and diffusion coefficients measured in the lower Prow Pass Tuff. The range of values is quite large primarily because of the uncertainty associated with which stratigraphic member, the central or lower Prow Pass Tuff (or both), transport pathways were located in. The upper Prow Pass Tuff was not considered because it was only a very small portion of the test interval. The assumptions and caveats associated with the Bullfrog Tuff values in Table 5-10 are discussed in Section C.7 of Appendix C).

Flow porosities were calculated using the following equation, which assumes homogeneous, isotropic, radial convergent flow of the entire production flow rate over the entire thickness of a confined test interval.

$$\eta = \frac{Q \tau}{\pi R^2 L} \quad (5.7)$$

where,  $\eta$  = flow porosity

$Q$  = production rate ( $\sim 1.14 \text{ m}^3/\text{hr}$ )

$\tau$  = mean residence time, hr

$R$  = distance between wells ( $\sim 30 \text{ m}$ )

$L$  = formation thickness ( $\sim 80 \text{ m}$ ).

Assuming radial convergent flow in a homogeneous, isotropic medium frequently results in high estimates of flow porosity if the medium is quite heterogeneous and contains a small number of fast-flowing channels because there is a relatively high probability that the injection well will not be located near the flow channels (unpublished results). However, the 30% recirculation should have helped offset this tendency for high porosity estimates because it would tend to "push" tracer mass away from the injection well and into faster flowing channels more rapidly, resulting in lower, more representative flow porosity estimates using equation (5.7). The assumption of a confined aquifer can also result in high flow porosity estimates if the aquifer is actually leaky as suggested by the analyses of the hydraulic responses (see Section 3.0). No attempt was made to correct mean residence times for the effects of recirculation because, theoretically, in a homogeneous isotropic medium, recirculation should not affect the mean residence time (although it can result in a very long-tailed breakthrough curves where a small amount of tracer mass has very long residence times, which can affect estimates of the mean). The upper and lower bounds on flow porosity in the Prow Pass tracer test are relatively narrow, reflecting the good agreement between the values obtained from the PFBA-Br data sets and the PFBA-Cl data sets.

A qualitative lower bound estimate of the fracture spacing was obtained by adjusting the spacing in RELAP until the bromide simulations began to deviate somewhat from the fits obtained assuming an infinite matrix, indicating that a significant amount of tracer mass was reaching the midway point between fractures. As noted in Section 5.4, this result was obtained assuming a fracture spacing of 2.8 cm. There was no attempt made to estimate an upper bound fracture spacing from the Prow Pass tracer data because the data were adequately fitted assuming an infinite matrix, which implies very large fracture spacings and very low fracture porosities. However, in reality, the fracture spacing must be finite; the model fits are simply indicating that the spacing was greater than the characteristic diffusion distance of the tracers into the matrix over the time of the tracer responses.

## 5.7 Conclusions

The tracer responses and the corresponding RELAP/RETRAN simulations lead to the following conclusions from the reactive tracer test in the Prow Pass Tuff:

- The relative responses of the PFBA, chloride, and bromide suggest that matrix diffusion occurred in the flow system between wells C#2 and C#3, which supports a dual-porosity system conceptualization. Although there was much more observed separation between the chloride and bromide responses than predicted, the differences between the PFBA and both halide responses are consistent with matrix diffusion. The differences between the chloride

and bromide responses only add uncertainty to the amount of matrix diffusion deduced; they do not rule it out. The estimated matrix diffusion mass transfer parameters fall in between the parameters deduced from the first and second "pathways" in the previous Bullfrog Tuff reactive tracer test.

- Lithium sorption in the Prow Pass system was adequately described by a linear, equilibrium sorption isotherm in the matrix with no sorption in fractures. Kinetic and nonlinear effects were not required to explain the data. It was also confirmed that lithium sorbed by exchange primarily with sodium and calcium ions in the rocks. The deduced lithium sorption parameters ( $K_{DS}$ ) were somewhat higher than laboratory-derived parameters for Prow Pass Tuffs, suggesting that the laboratory data would result in conservative overpredictions of lithium transport in the field. The same conclusion was drawn from the Bullfrog Tuff reactive tracer test.
- The microspheres were highly attenuated relative to the solutes, and their transport behavior over the first 300 hrs of the test was accounted for very well by a linear, first-order filtration model with negligible resuspension/detachment. However, the sporadic late-time response of the spheres suggested a small amount of detachment (possibly enhanced by flow transients) that was not amenable to modeling using a simple first-order attachment-detachment rate model. The filtration coefficients deduced for all microspheres were comparable to those observed in the previous Bullfrog Tuff reactive tracer test, although the late-time responses (tentatively attributed to detachment) were clearly less pronounced than in the Bullfrog test. The yellow microspheres were not recovered at all presumably because they were injected in a solution of  $\sim 0.4$  M ionic strength, which would have tended to destabilize the spheres and make them more susceptible to attachment to rock surfaces.
- The solute tracer responses after the flow interruptions suggest that there may have been some flow into and out of the matrix as a result of pressure transients during the interruptions and/or that there was a wide range of solute diffusion rates in the system.
- The mean residence times and Peclet numbers deduced from the solute breakthrough curves indicate (1) a fracture/flow porosity between 0.0027 and 0.0062 in the system, and (2) a longitudinal dispersivity between 15 and 64 m. Uncertainties in these estimates are discussed below.

We consider our modeling of the tracer tests to be a relatively simple approach to interpreting the data. This approach involves a minimum number of adjustable parameters, which is consistent with our limited knowledge of flow system geometry and heterogeneity. Although we believe that our conclusions are sound, we recognize that there is much room for revisiting the analyses using more sophisticated modeling tools and introducing more system complexity, particularly as more site-specific information becomes available. In the future, we plan to incorporate this information into numerical models that can better account for both physical and chemical heterogeneity in two- and three-dimensions. We also plan to examine other semi-analytical modeling approaches, such as the multi-rate diffusion model of Haggerty and Gorelick (1995), which has been used to interpret tracer tests conducted in a fractured dolomite near Carlsbad, NM for the Waste Isolation Pilot Plant project (Meigs et al., 1998). The tracer responses after flow interruptions suggest multiple rates of diffusion, although the possibility of flow into and out of the matrix as a result of pressure transients during these interruptions cannot be discounted. It is also possible that some of the apparent matrix diffusion in the field experiments was actually diffusion into stagnant water along the rough fracture walls

or within the fractures themselves (occurring as a result of tracers diffusing out of high flow rate channels and into low flow zones), rather than into the matrix proper. These possibilities have important implications for saturated zone performance assessments and merit further study because, if valid, they would suggest that matrix diffusion might be overestimated in short-duration tracer experiments.

### 5.App Method of Estimating Hydrodynamic Dispersion from Observed Dispersion in a Recirculating Tracer Test

Dispersion can be thought of as a measure of the variance in travel times (or travel distances) in a flow system relative to the mean groundwater travel time (or distance). If local perturbations are assumed to be random, then the following equation holds for the variance in travel distance regardless of what type of statistical distribution is assumed for the random perturbations (Bear 1972, pp. 589-592):

$$\sigma_i^2 = 2D\tau \quad (5.8)$$

where,  $\sigma_i^2$  = variance in travel distances,  $L^2$

$D$  = dispersion coefficient,  $L^2/T$

$\tau$  = mean travel time,  $T$ .

All that is required for equation (5.8) to hold is that the local perturbations must occur over length scales much smaller than the scale of measurement. To convert this expression to a variance in travel times, we simply divide both sides of equation (5.8) by the mean velocity squared:

$$\sigma^2 = \frac{\sigma_i^2}{V^2} = \frac{2D\tau}{V^2} \quad (5.9)$$

where,  $\sigma^2$  = variance in travel times,  $T^2$

$V$  = mean velocity,  $L/T$ .

Recognizing that  $D = \alpha V$  ( $\alpha$  = dispersivity) and  $\tau = L/V$ , equation (5.9) can be shown to be equivalent to:

$$\sigma^2 = \frac{2\alpha V \tau^3}{L^2} = \frac{2\alpha \tau^2}{L} \quad (5.10)$$

Substitution of  $Pe = L/\alpha$  into equation (5.10) yields the following expression:

$$\sigma^2 = 2 \frac{\tau^2}{Pe} \quad (5.4)$$

This equation can be used to obtain estimates of  $\sigma^2$  from  $Pe$  (or vice-versa) from the analysis of a breakthrough curve. In the development outlined in Section 5.4, the variance in travel times was

estimated from the RELAP simulations by inserting the mean residence times and Peclet numbers from RELAP into equation (5.4).

It is well known that the variance of a process that is the sum of two independent (uncorrelated) processes is equal to the sum of the variances of the processes (Walpole and Myers 1985, p. 98):

$$\text{If } A = X + Y \Rightarrow \sigma_A^2 = \sigma_X^2 + \sigma_Y^2 \quad (5.11)$$

We now make the assumption that the observed dispersion in the Prow Pass tracer test was the sum of the dispersion due to the flow field and dispersion due to "true hydrodynamic dispersion" in the system. The latter dispersion is the only type of dispersion that would theoretically be observed under nonrecirculating flow conditions. Bear (1972, p. 637) describes a similar assumption made by researchers analyzing dispersion in radially-divergent flow fields in the late 1950's, although in that case, it was assumed that the standard deviations were additive, not the variances. We have chosen to use the variance, which is more consistent with long-accepted statistical theory and can be rigorously proven.

Given these assumptions, if the total system variance and the variance due to the flow field are known, then the variance due to true hydrodynamic dispersion can be estimated from:

$$\sigma_{HD}^2 = \sigma_{Tot}^2 - \sigma_{Flow}^2 \quad (5.12)$$

where,  $\sigma_{HD}^2$  = travel time variance due to hydrodynamic dispersion,  $T^2$

$\sigma_{Tot}^2$  = total observed travel time variance,  $T^2$

$\sigma_{Flow}^2$  = travel time variance due to flow field,  $T^2$

$\sigma_{Tot}^2$  in equation (5.12) can then be obtained from equation (5.4) (with Pe given by the RELAP simulations) and  $\sigma_{Flow}^2$  can be determined from the 2WELLS\_2D simulations assuming a homogeneous, isotropic medium. The resulting  $\sigma_{HD}^2$  is then converted to a Peclet number by inserting the variance into equation (5.4) and rearranging to solve for Pe.

The method described above was tested by conducting a number of stochastic transport simulations using 2WELLS\_2D. In these simulations, it was assumed that the local dispersivity was identical to that obtained from equation (5.12). Although there is some uncertainty associated with estimating means and variances from a finite ensemble of particle travel times that have an inherently large variance, it was found that the total variance obtained from the 2WELLS\_2D simulations was in good agreement with the "theoretical" total variance obtained by summing the flow field variance (determined from 2WELLS\_2D simulations without local dispersion) and the variance due to hydrodynamic dispersion assumed in the simulations.

One of the uncertainties associated with the method described above is that the 2WELLS\_2D simulations assume a homogeneous, isotropic medium. It is undoubtedly true that the Prow Pass flow system is neither homogeneous or isotropic. However, because we do not know the true nature of the flow system, we resort to this simplifying assumption to make it possible to estimate the contribution of the recirculating flow field to the observed dispersion. Another uncertainty in the method is that the length scale of the "local" perturbations in the Prow Pass system is not known. This length scale could, in fact, be approaching the scale of the tracer tests, as the deduced dispersivities are similar in magnitude to the distance between the injection

and production wells (see Table 5-7). Our analysis assumes that the observed hydrodynamic dispersion is the result of a relatively large number of large perturbations occurring over scales much shorter than the distance between wells C#2 and C#3. The 2WELLS\_2D simulations confirm that this assumption results in predictions consistent with the observed transport behavior, although they do not necessarily imply that the assumption is correct.

## Section 5.0 References

- Bear, J. 1972. *Dynamics of Fluids in Porous Media*. New York, Dover Publications, pp. 589-592, p. 637. TIC Catalog # 217568.
- Becker, M. W. 1996. *Tracer Tests in a Fractured Rock and Their First Passage Time Mathematical Models*, Ph.D. Dissertation, University of Texas, Austin, TX, pp. 110-115 and 119-131. TIC Catalog # 236855.
- Draper, N. R. and H. Smith. 1981. *Applied Regression Analysis*, 2nd ed. New York: John Wiley and Sons, pp. 93-96, pp. 472-473. TIC Catalog # 231231.
- Haggerty, R. and S. M. Gorelick. 1995. "Multiple-Rate Mass Transfer for Modeling Diffusion and Surface Reactions in a Media with Pore-Scale Heterogeneity." *Water Resour. Res.*, 31(10), 2383-2400. (Submitted to RIS for Accession # 5/21/99.)
- Jenson, V. G. and G. V. Jeffreys. 1977. *Mathematical Models in Chemical Engineering*, 2nd ed., London, Academic Press, pp. 169-170. (Submitted to RIS for Accession # 5/21/99.)
- Maloszewski, P. and A. Zuber. 1983. "Interpretation of Artificial and Environmental Tracers in Fissured Rocks with a Porous Matrix." In *Isotope Hydrology*, pp. 635-651. Vienna, Austria: International Atomic Energy Agency (IAEA). (Submitted to RIS for Accession # 5/21/99.)
- Maloszewski, P. and A. Zuber. 1985. "On the Theory of Tracer Experiments in Fissured Rocks with a Porous Matrix." *J. Hydrology*, 79, 333-358. TIC Catalog # 222390.
- Maloszewski, P. and A. Zuber. 1991. "Influence of Matrix Diffusion and Exchange Reactions on Radiocarbon Ages in Fissured Carbonate Aquifers." *Water Resour. Res.*, 27(8), 1937-1945. (Submitted to RIS for Accession # 5/21/99.)
- Meigs, L. C., R.L. Beuheim, J.T. McCord, Y.W. Tsang, and R. Haggerty. 1998. "Design, Modeling, and Current Interpretations of the H-19 and H-11 Tracer Tests at the WIPP Site." In *Field Tracer Transport Experiments: Role in the Prediction of Radionuclide Migration*, Synthesis and proceeding an NEA/EC GEOTRAP Workshop, Cologne, Germany, August 28-30, 1996, pp. 157-169. (Submitted to RIS for Accession # 5/21/99.)
- Moench, A. F. 1995. "Convergent Radial Dispersion in a Double-Porosity Aquifer with Fracture Skin: Analytical Solution and Application to a Field Experiment in Fractured Chalk." *Water Resour. Res.*, 31(8), 1823-1835. TIC Catalog # 233132.

- National Research Council. 1996. *Rock Fractures and Fluid Flow: Contemporary Understanding and Applications*. Washington, D.C: National Academy Press, pp. 252-259. TIC Catalog # 235913.
- Neuman, S. P. 1990. "Universal Scaling of Hydraulic Conductivities and Dispersivities in Geologic Media." *Water Resour. Res.*, 26(8), 1749-1758. TIC Catalog # 237977. RIS Accession # NNA.19920320.0021.
- Newman, J. S. 1973. *Electrochemical Systems*. Englewood Cliffs, New Jersey: Prentice-Hall, pp. 229-230. TIC Catalog # 210201.
- Reimus, P. W., and Z. V. Dash. 1998. *Models and Methods Summary for the Reactive Transport Application*. Yucca Mountain Site Characterization Project Milestone Report SP32E1M4. Los Alamos, New Mexico: Los Alamos National Laboratory, all pages. (Submitted to RIS for Accession # 5/21/99.)
- Reimus, P. W. 1995. *Predictions of Tracer Transport in Interwell Tracer Tests at the C-Hole Complex*. LA-13160-MS, Los Alamos, New Mexico: Los Alamos National Laboratory, pp. 12-29. TIC Catalog # 225894.
- Robinson, B. A. 1994. "A Strategy for Validating a Conceptual Model for Radionuclide Migration in the Saturated Zone beneath Yucca Mountain." *Rad. Waste Mgmt. & Env. Restor.*, 19, 73-96. TIC Catalog # 222513.
- Tang, D. H., E. O. Frind, and E. A. Sudicky. "Contaminant Transport in a Fractured Porous Media: Analytical Solution for a Single Fracture." *Water Resour. Res.*, 17(3), 555-564. TIC Catalog # 225368. RIS Accession # NNA.19900711.0084.
- Walpole, R. E. and R. H. Myers. 1985. *Probability and Statistics for Engineers and Scientists*. New York. MacMillan Publishing Co., p. 98. (Submitted to RIS for Accession # 5/21/99.)

## Section 5.0 Tables

Table 5-1. Summary of tracer injections for the Prow Pass reactive tracer test. Both injections involved injecting ~6000 liters of J-13 water into C#3 over ~18 hrs at ~5.7 L/min. (DTN LAPR831231AQ99.001)

Injection starting 9/23/98, 3:30 pm:

Tracer	Injection Amount	Injection Concentration
0.64- $\mu\text{m}$ CML microspheres (blue)	$3.0 \times 10^{14}$ spheres	$5.1 \times 10^{10}$ spheres/L
0.28- $\mu\text{m}$ CML microspheres (orange)	$2.1 \times 10^{14}$ spheres	$3.5 \times 10^{10}$ spheres/L

Injection starting 9/25/98, 3:00 pm:

Tracer	Injection Amount	Injection Concentration
Lithium Ion*	15.97 kg	2660 mg/L
Bromide Ion*	30.62 kg	5100 mg/L
Chloride Ion*	67.98 kg	11,330 mg/L
Pentafluorbenzoic Acid (PFBA)	11.99 kg	2000 mg/L
0.28- $\mu\text{m}$ CML microspheres (yellow)	$2.1 \times 10^{14}$ spheres	$3.5 \times 10^{10}$ spheres/L

\*Lithium, bromide, and chloride injected as 33.28 kg LiBr and 81.29 kg LiCl.

Table 5-2. Times and durations of flow interruptions in the Prow Pass reactive tracer test. (DTN LAPR831231AQ99.001)

Interruption	Flow Shut Off	Flow Turned On	Duration
1	11/14/98, ~9:00 am	11/14/98, ~11:00 pm	~14 hrs
2	11/23/98, ~9:00 am	11/30/98, ~4:00 pm	~175 hrs
3	12/21/98, ~9:00 am	1/4/99, ~11:00 pm	~337 hrs

Table 5-3. Estimated tracer recoveries in the Prow Pass reactive tracer test through Jan. 30, 1999, 6:00 am (microspheres through Jan. 27, 1999, 10:30 am). (Based on data from DTN LAPR831231AQ99.001)

Tracer	Fraction Recovered at C#2	Fraction ReInjected into C#3 <sup>(1)</sup>	Fraction Remaining in C#3 on 11/2/98 <sup>(2)</sup>
Lithium Ion	0.185	0.053	0.005
Bromide Ion	0.433	0.124	0.006
Chloride Ion	0.488	0.139	0.006
Pentafluorbenzoic Acid (PFBA)	0.518	0.148	0.006
0.64- $\mu\text{m}$ CML microspheres (blue)	0.0033	0.00095	0.0035
0.28- $\mu\text{m}$ CML microspheres (orange)	0.0012	0.00034	0.006
0.28- $\mu\text{m}$ CML microspheres (yellow)	unquantifiable	Nil	0.006

<sup>(1)</sup> These numbers are approximately 30% of the fraction recovered at C#2, based on ~30% recirculation.

<sup>(2)</sup> Based on samples collected during mixing of C#3 on Nov. 2, 1998.

Table 5-4. Parameters obtained from simultaneous RELAP fits to the PFBA, bromide, and lithium responses in the Prow Pass and Bullfrog reactive tracer tests. (DTN LAPR831231AN99.001 [Prow Pass] and DTN LAPR831231AQ99.002 [Bullfrog])

Parameter	Prow Pass Test	Bullfrog Test Pathway 1	Bullfrog Test Pathway 2
f, mass fraction	0.75	0.12	0.59
$\tau$ , linear flow, hr	1230	37	995
Pe, linear flow	0.9	6	1.7
$\tau$ , radial flow, hr	620	31	640
Pe, radial flow	1.9	9	3
Bromide (PFBA) $\frac{\phi}{b} \sqrt{D_m}$ , sec <sup>-1/2</sup>	0.000968 (0.000559)	0.00158 (0.000912)	0.000458 (0.000264)
Lithium fracture retardation factor	1	1	~5*
Lithium matrix retardation factor	12	7*	~18*

\*See Appendix C for a discussion of how these parameters were obtained and also for a discussion of alternative parameter estimates.

Table 5-5. Parameters obtained from simultaneous RELAP fits to the PFBA, chloride, and lithium responses in the Prow Pass reactive tracer test. (DTN LAPR831231AN99.001)

Parameter	Parameter Value
f, mass fraction	0.60
$\tau$ , linear flow, hr	960
P <sub>e</sub> , linear flow	1.2
$\tau$ , radial flow, hr	540
P <sub>e</sub> , radial flow	2.3
Chloride (PFBA) $\frac{\phi}{b} \sqrt{D_m}$ , sec <sup>-1/2</sup>	0.000612 (0.000354)
Lithium fracture retardation factor	1
Lithium matrix retardation factor	23

Table 5-6. Comparison of lithium sorption parameters deduced from field and laboratory experiments in Prow Pass and Bullfrog Tuffs from the C-holes. (DTN LAPR831231AQ98.001 [lab data], and DTN LAPR831231AQ99.002 and DTN LAPR831231AN99.001 [field test interpretations])

Parameter	Field K <sub>D</sub>	Laboratory K <sub>D</sub> <sup>(1)</sup>
Prow Pass matrix K <sub>D</sub> assuming Central Prow Pass Tuff	0.66 (1.33) <sup>(2)</sup>	0.13 (0.26 at infinite dilution)
Prow Pass matrix K <sub>D</sub> assuming Lower Prow Pass Tuff	1.68 (3.36) <sup>(2)</sup>	0.084 (0.44 at infinite dilution)
Bullfrog matrix K <sub>D</sub> in Pathway 1 assuming Central Bullfrog Tuff <sup>(3)</sup>	0.24	0.19 (0.44 at infinite dilution)
Bullfrog matrix K <sub>D</sub> in Pathway 1 assuming Lower Bullfrog Tuff <sup>(3)</sup>	0.97	0.32 (1.64 at infinite dilution)
Bullfrog matrix K <sub>D</sub> in Pathway 2 assuming Central Bullfrog Tuff <sup>(3)</sup>	0.67	0.19 (0.44 at infinite dilution)
Bullfrog matrix K <sub>D</sub> in Pathway 2 assuming Lower Bullfrog Tuff <sup>(3)</sup>	2.75	0.32 (1.64 at infinite dilution)

<sup>(1)</sup>Values at "infinite dilution" obtained from slopes of Langmuir isotherm fits to the data (asymptotic slope at very low concentrations; i.e., K<sub>L</sub>S<sub>max</sub>). Other values obtained from a simple linear fit to the entire range of data.

<sup>(2)</sup>Values in parentheses obtained from PFBA-Cl-Li RELAP fits. Others obtained from PFBA-Br-Li fits.

<sup>(3)</sup>"Pathway 1" refers to pathways that resulted in the first tracer peak in the Bullfrog reactive tracer test, and "Pathway 2" refers to pathways that resulted in the second peak in this test. K<sub>D</sub> values were calculated from the smallest matrix retardation factors obtained from alternative interpretations of the test (see Appendix C).

Table 5-7. Estimated microsphere filtration rate constants and filtration coefficients in the Prow Pass reactive tracer test. (DTN LAPR831231AN99.001)

Parameter*	Microsphere		
	0.64-μm Blue	0.28-μm Orange	0.28-μm Yellow
k <sub>filt</sub> , 1/hr	0.043	0.07	0.2
λ, 1/cm	0.00143	0.00233	0.00667
k <sub>res</sub> , 1/cm-hr	0	0	0

\*k<sub>filt</sub> = filtration rate constant

\*λ = filtration coefficient = k<sub>filt</sub>/V, where V = average linear velocity.

\*k<sub>res</sub> = resuspension rate constant.

Table 5-8. Fitted RELAP parameters used in the RETRAN simulations to predict the effects of flow interruptions on the tracer responses. (DTN LAPR831231AN99.001)

Parameter	Parameter Value
τ, linear flow, hr	1240
P <sub>e</sub> , linear flow	1.0
Bromide (PFBA) $\frac{\phi}{b} \sqrt{D_m}$ , sec <sup>-1/2</sup>	0.000968 (0.000559)
Lithium matrix retardation factor	11

Table 5-9. Estimated Peclet numbers and dispersivities corresponding to true hydrodynamic dispersion in the Prow Pass flow system after removing dispersion due to the recirculating flow field. (DTN LAPR831231AQ99.002 and DTN LAPR831231AN99.001)

Simulation Case	Peclet Number	Dispersivity, m*
PFBA-Br Fit	1.26	23.8
PFBA-Cl Fit	1.94	15.5

\*Assumes a travel distance of 30 m (separation distance between wells).

Table 5-10. Ranges of physical parameter values derived from the interpretations of the Prow Pass and Bullfrog reactive tracer tests. See Section 5.6 and Appendix C for discussion. (DTN LAPR831231AN99.001 [Prow Pass Data] and DTN LAPR831231AQ99.002 [Bullfrog Data])

Parameter	Prow Pass		Bullfrog	
	Lower Bound	Upper Bound	Lower Bound	Upper Bound
Dispersivity, m	15	64	3.3	59
Flow porosity	0.0027	0.0062	0.0037	0.12*
Fracture aperture, cm	0.18	1.64	0.084	1.26
Fracture spacing, cm	2.8	infinite	4	infinite
$B_r \text{ or } C_l \frac{\phi}{b} \sqrt{D_m}, \text{ sec}^{-1/2}$	0.000612	0.000968	0.000458	0.00158

\*This value is based on the analysis of the second set of tracer peaks in the Bullfrog test assuming that the entire production rate in the Bullfrog test moved through the entire interval thickness. This assumption very likely results in erroneously high estimates of flow porosity.

## Section 5.0 Figures

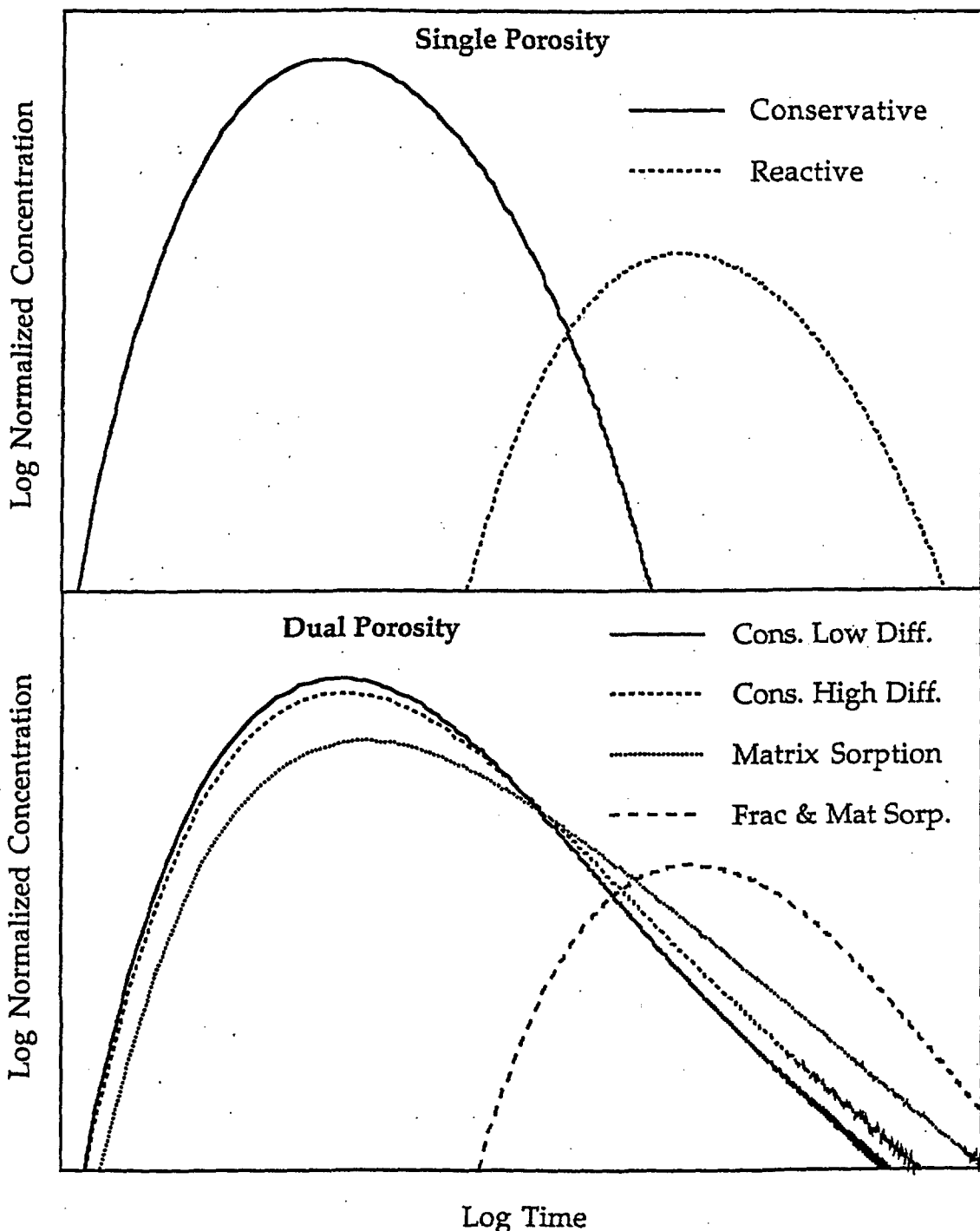


Figure 5-1. Generic predicted tracer responses in field tests in single- and dual- porosity media. Units are arbitrary. "Cons. Low Diff." means nonsorbing solute with small diffusion coefficient, "Cons. High Diff." means nonsorbing solute with large diffusion coefficient, "Matrix Sorption" means sorption only in the matrix, and "Frac & Mat Sorp." means sorption in both fractures and matrix.

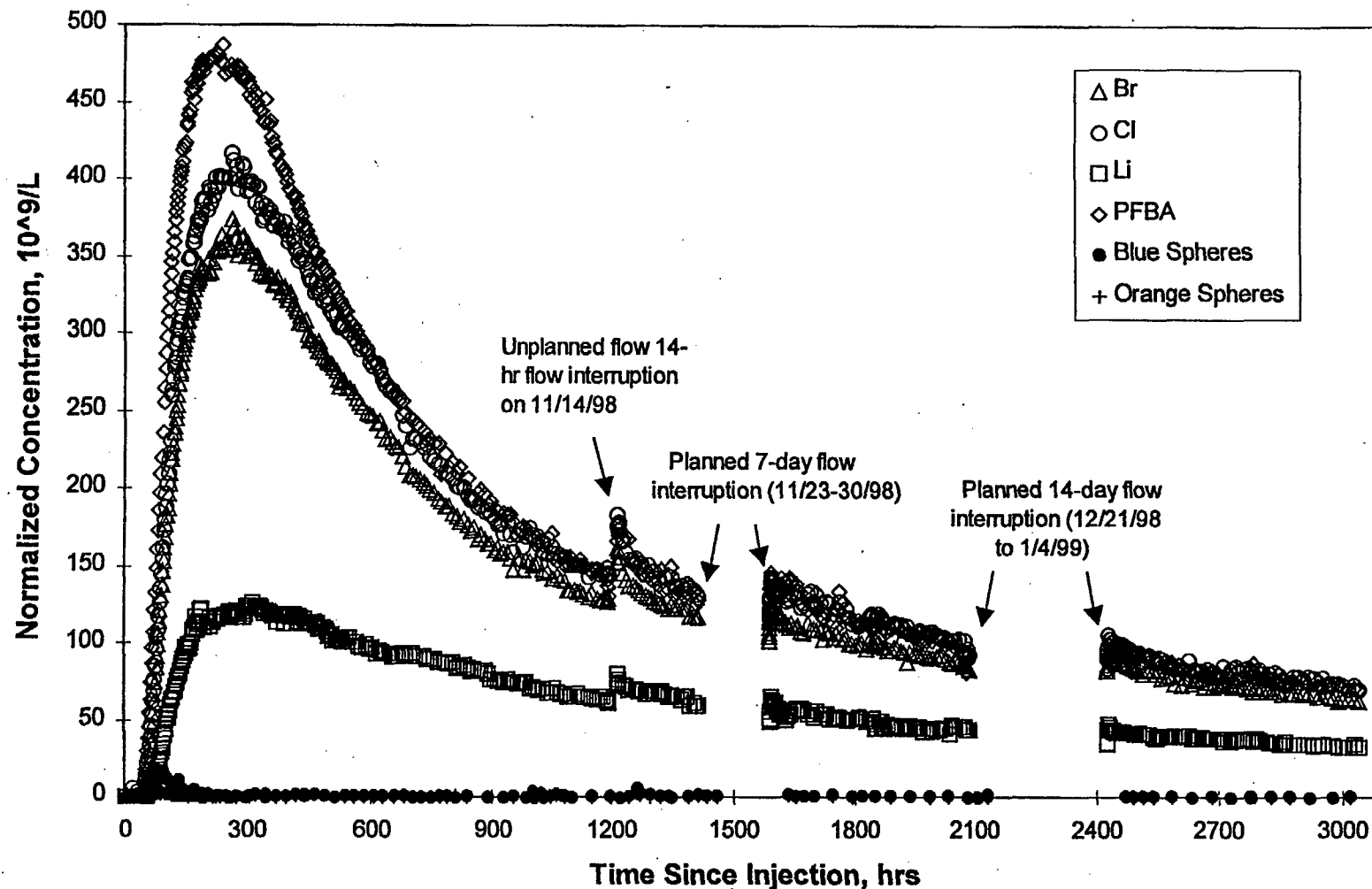


Figure 5-2. Tracer responses in the Prow Pass reactive tracer test. All concentrations are normalized to injection mass ( $\times 10^9$ ). (DTN LAPR831231AQ99.001)

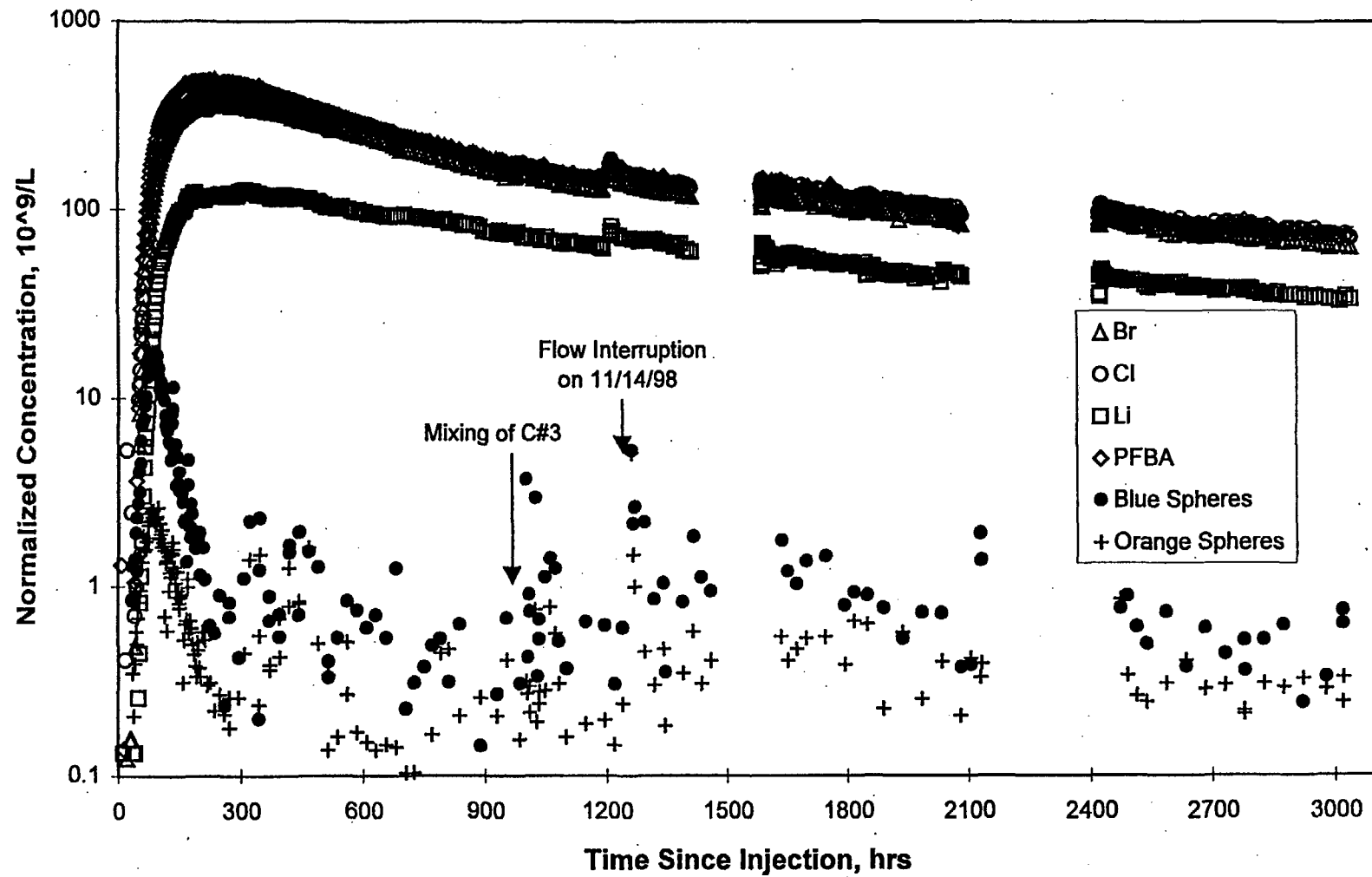


Figure 5-3. Log<sub>10</sub> normalized tracer concentrations in the Prow Pass reactive tracer test. (DTN LAPR831231AQ99.001)

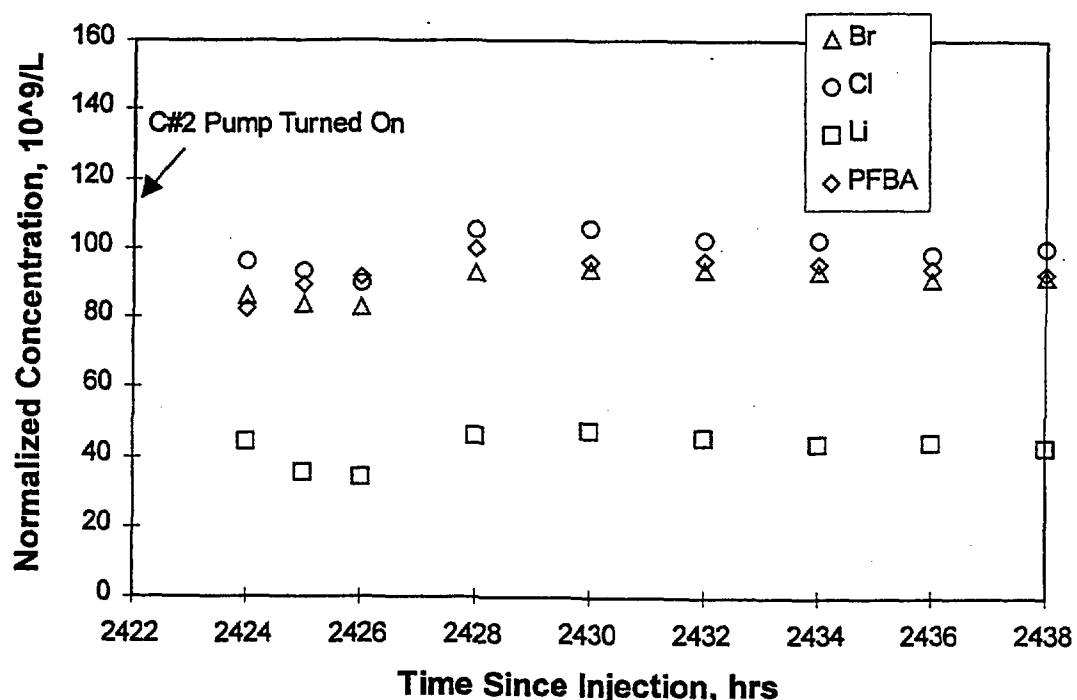
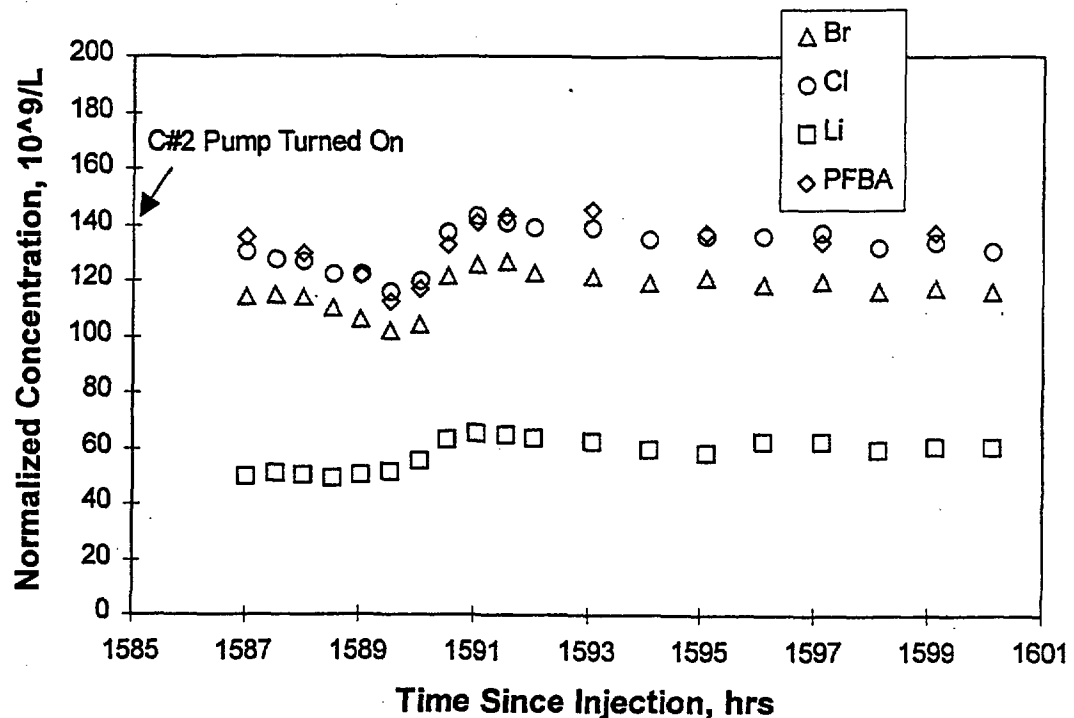


Figure 5-4. Solute tracer responses after the second (upper plot) and third (lower plot) flow interruptions (first 16 hrs after resumption of C#2 pumping). (DTN LAPR831231AQ99.001)

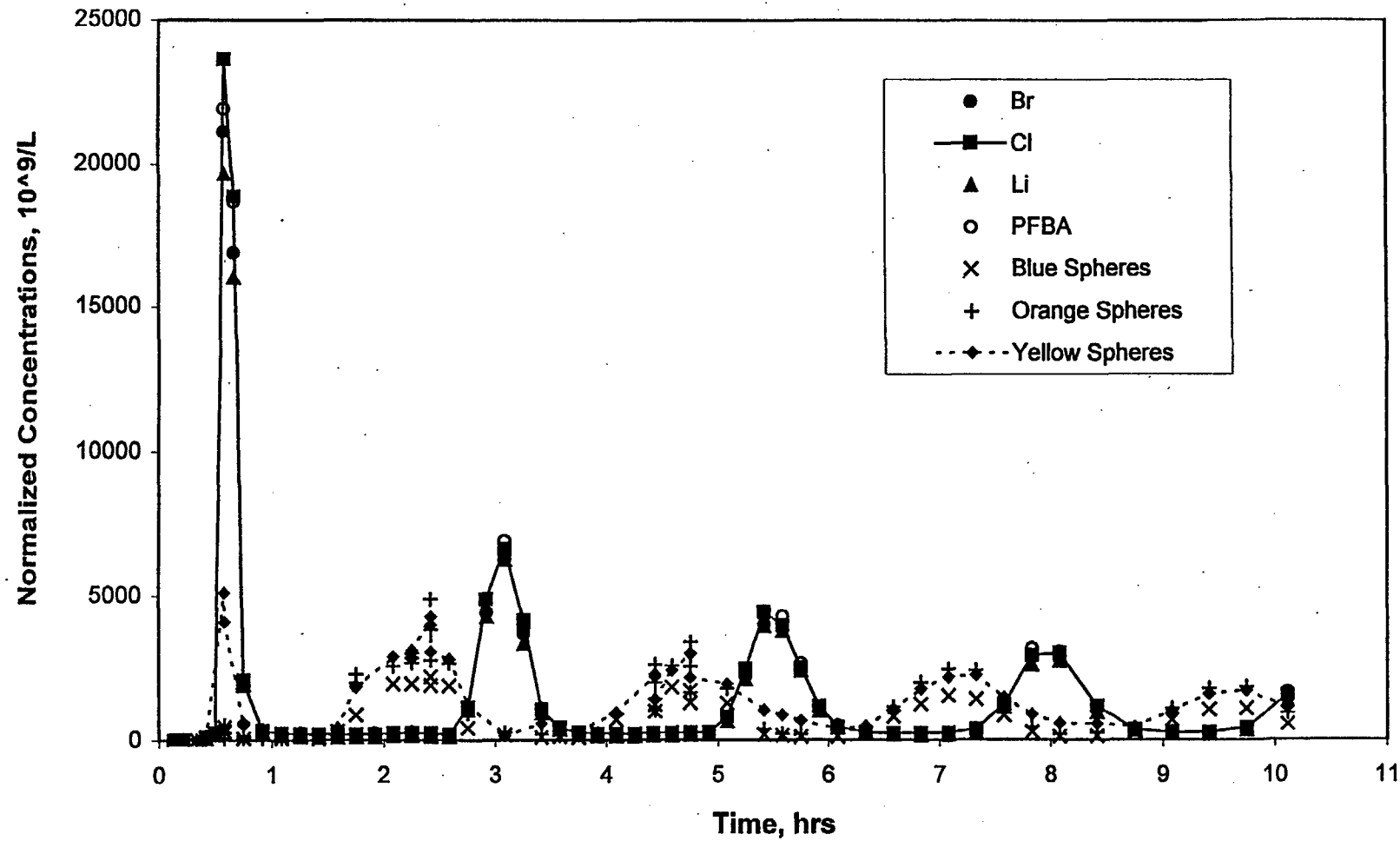


Figure 5-5. Normalized tracer concentrations measured in samples taken from the C#3 mixing loop on Nov. 2, 1998. (DTN LAPR831231AQ99.001)

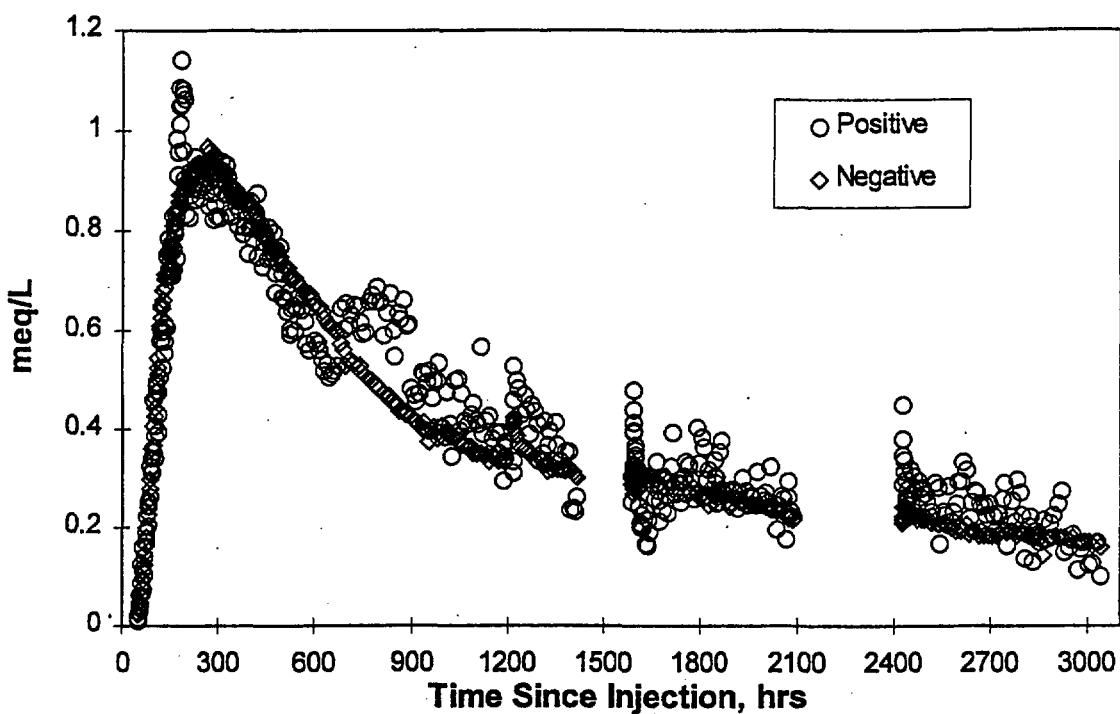


Figure 5-6. Overall charge balance (above background) during the Prow Pass reactive tracer test. (DTN LAPR831231AQ99.001)

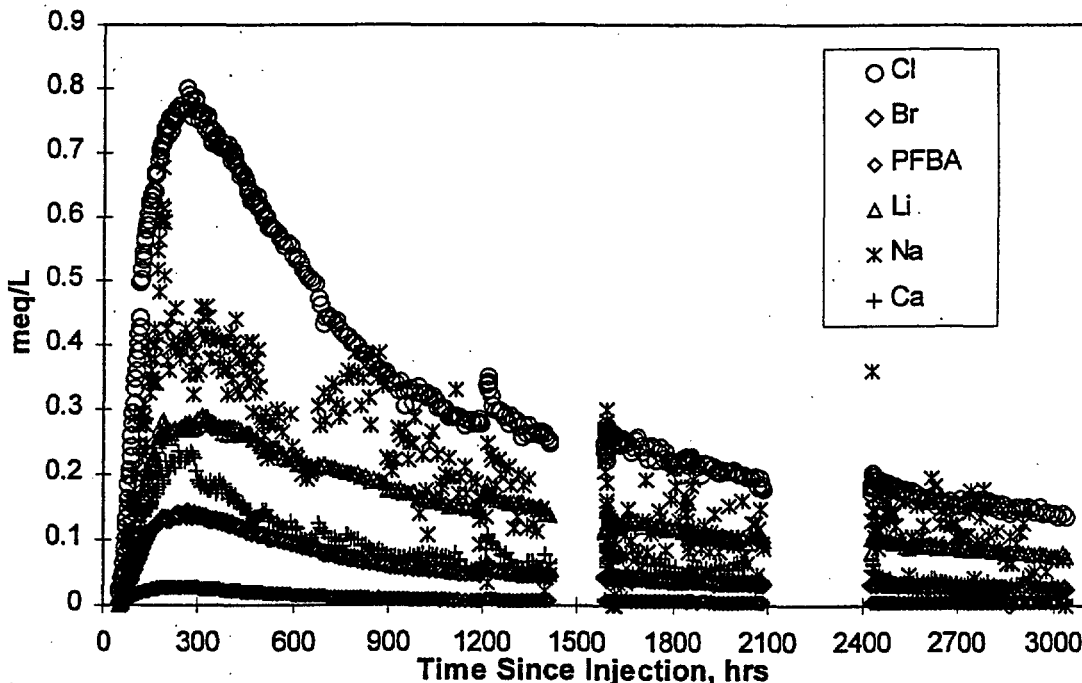


Figure 5-7. Concentrations (meq/L) of individual ions (above background) during the Prow Pass reactive tracer test. (DTN LAPR831231AQ99.001)

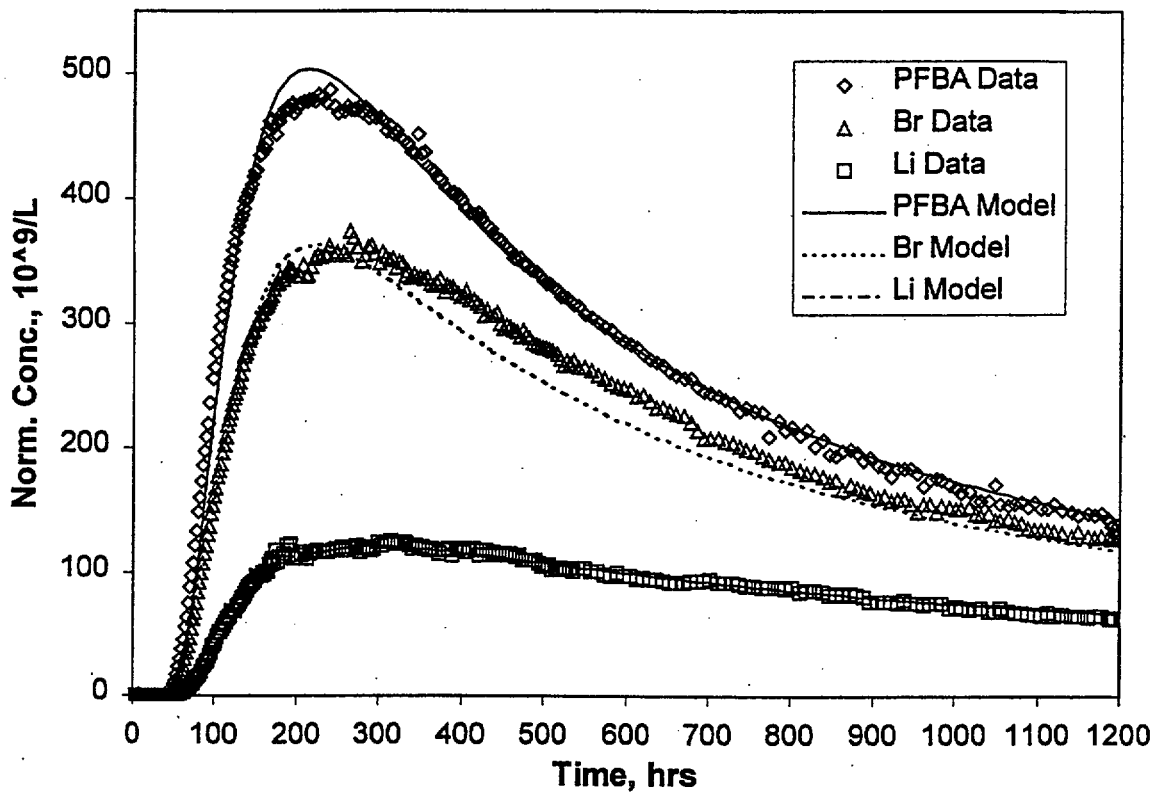


Figure 5-9. Simultaneous RELAP fits to the PFBA, bromide, and lithium data (see Table 5-4 for model parameters resulting in the best fits). (DTN LAPR831231AQ99.001 [data] and DTN LAPR831231AN99.001 [model fits]).

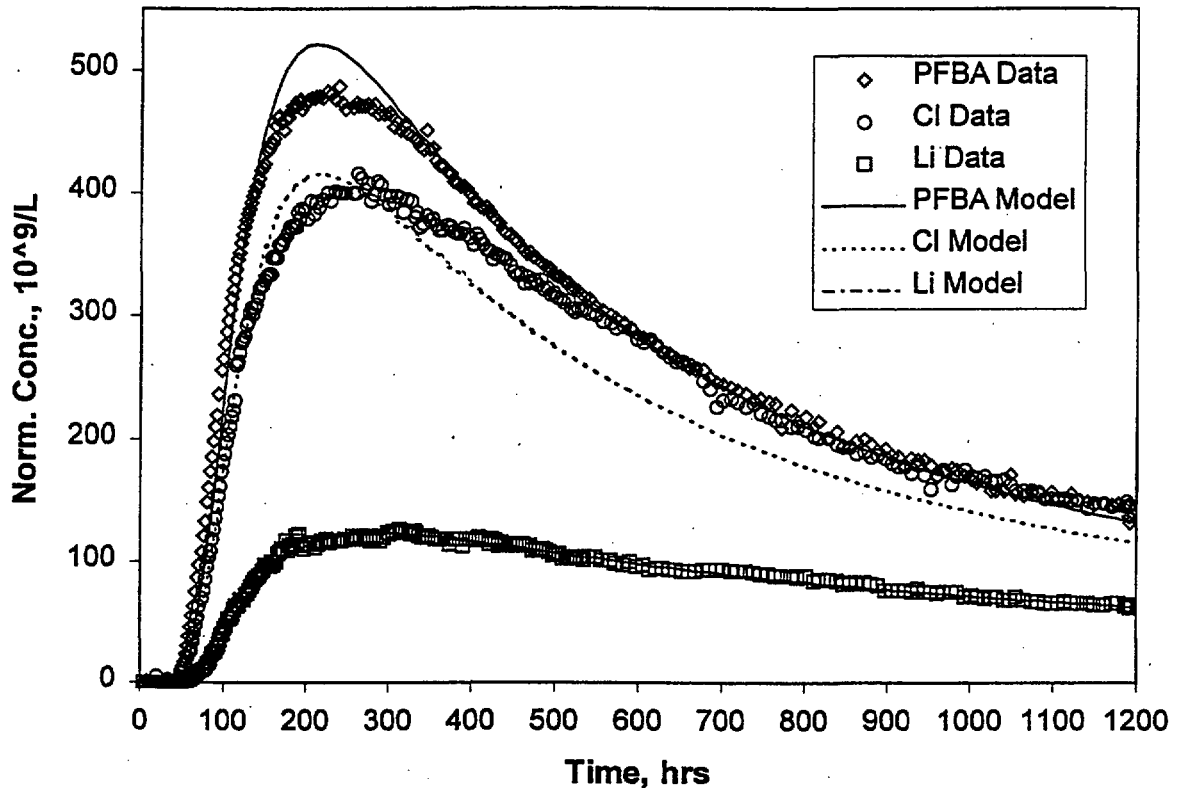


Figure 5-10. Simultaneous RELAP fits to the PFBA, chloride, and lithium data (see Table 5-5 for model parameters resulting in the best fits). (DTN LAPR831231AQ99.001 [data] and DTN LAPR831231AN99.001 [model fits]).

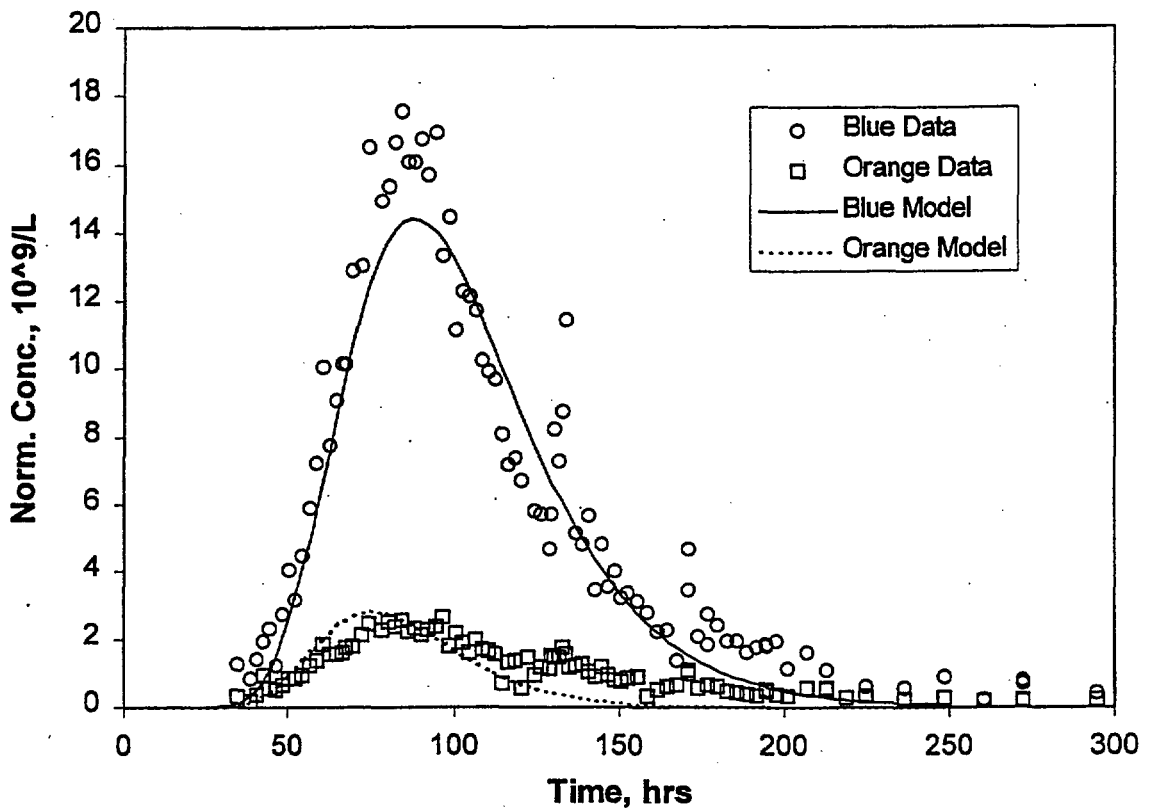


Figure 5-11. RELAP fits to the early blue and orange microsphere data. (DTN LAPR831231AQ99.001 [data] and DTN LAPR831231AN99.001 [model fits]).

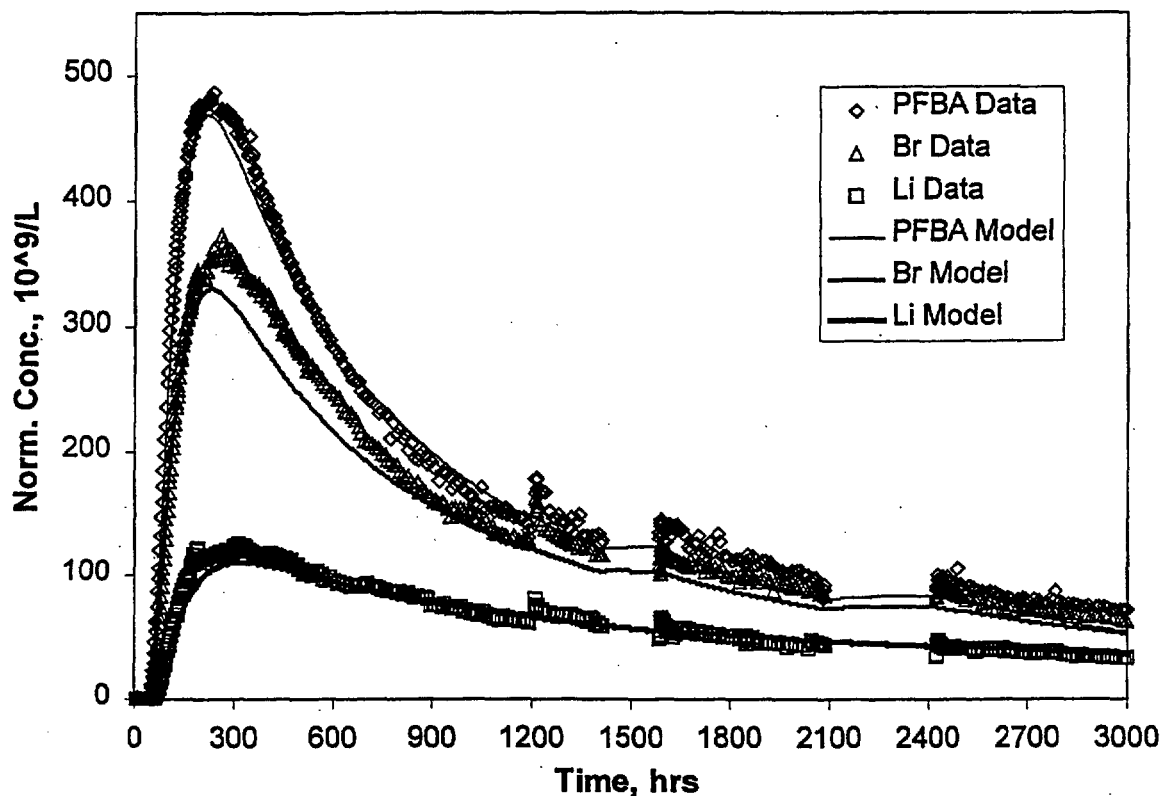


Figure 5-12. Comparison of actual solute responses and RETRAN-simulated responses over the entire duration of the reactive tracer test. (DTN LAPR831231AQ99.001 [data] and DTN LAPR831231AN99.001 [model fits]).

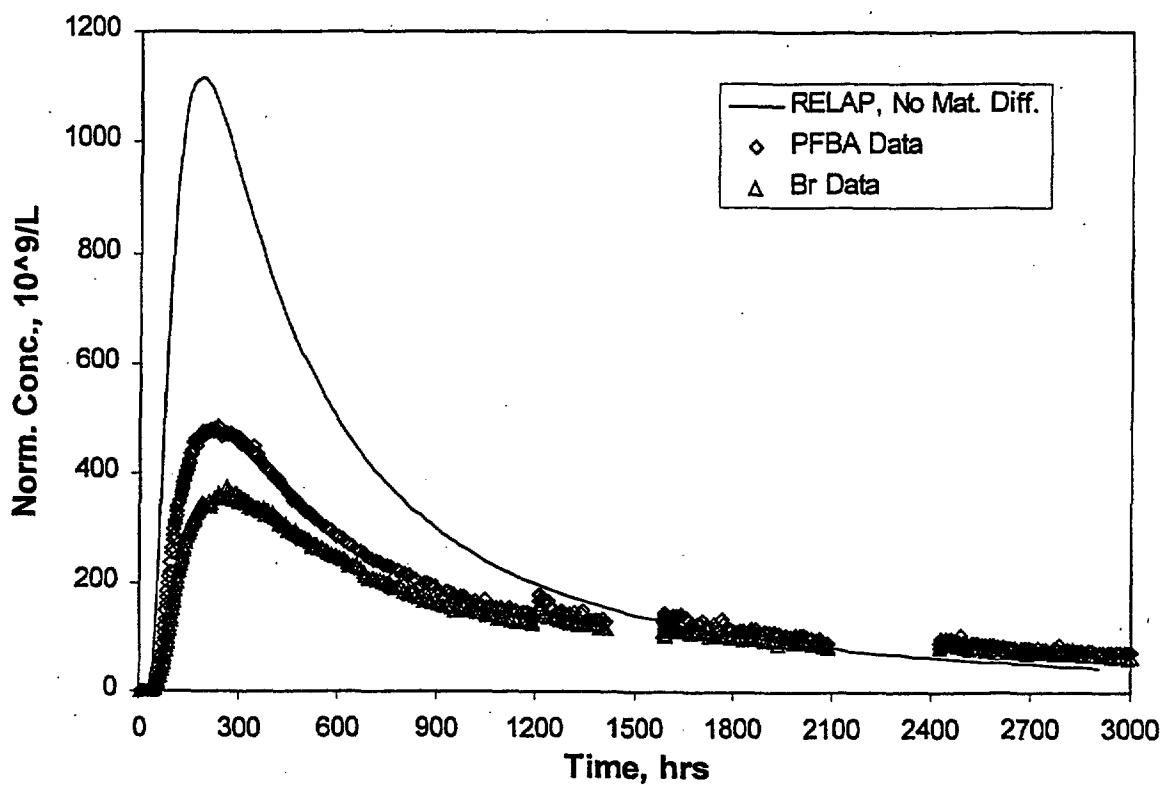


Figure 5-13. RELAP simulation without matrix diffusion or sorption (PFBA and bromide data shown for comparison). (DTN LAPR831231AQ99.001 [data] and DTN LAPR831231AN99.001 [model]).

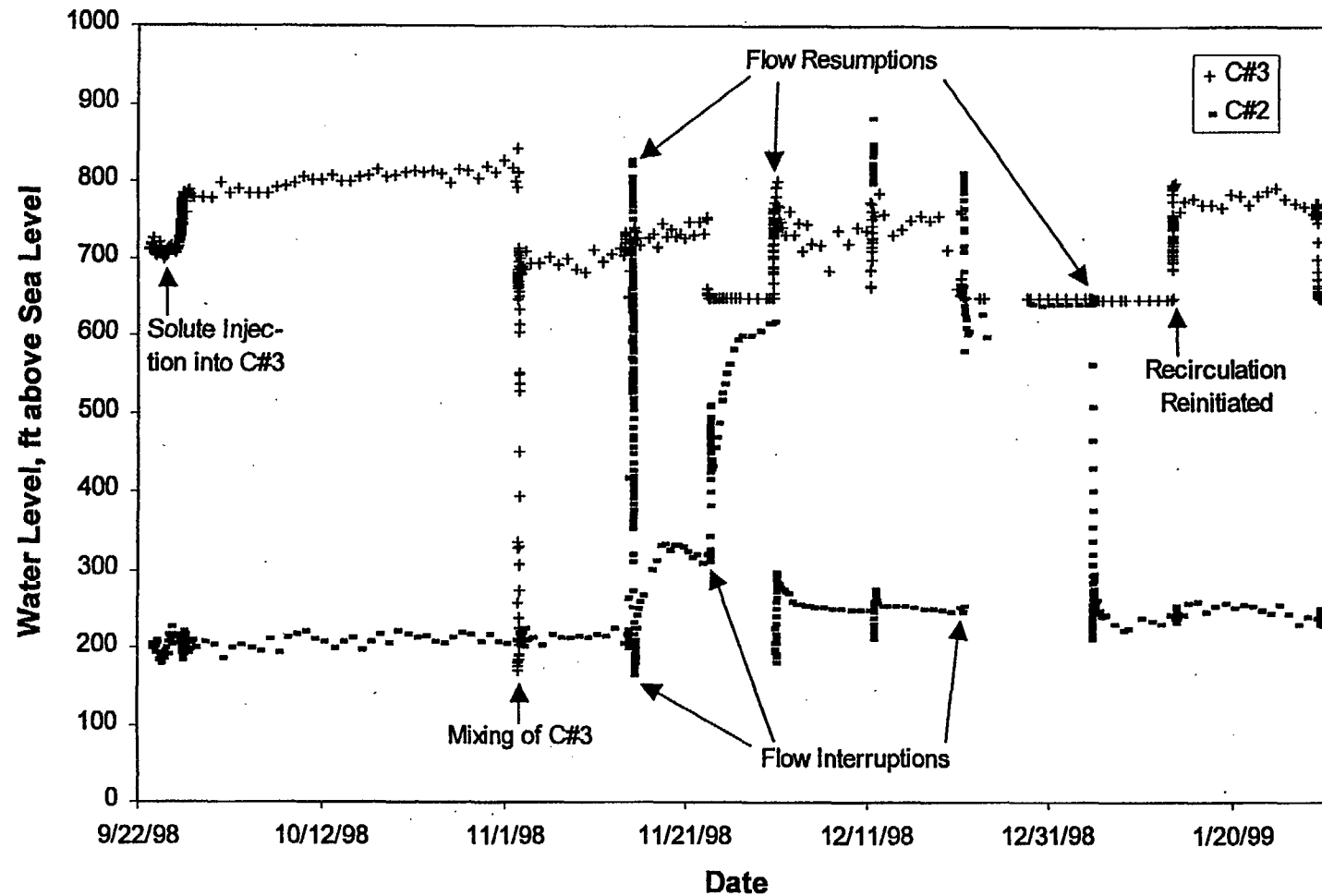


Figure 5-14. Pressures (expressed as water levels) in C#2 and C#3 during the Prow Pass reactive tracer test. (DTN GS990408312315.002).

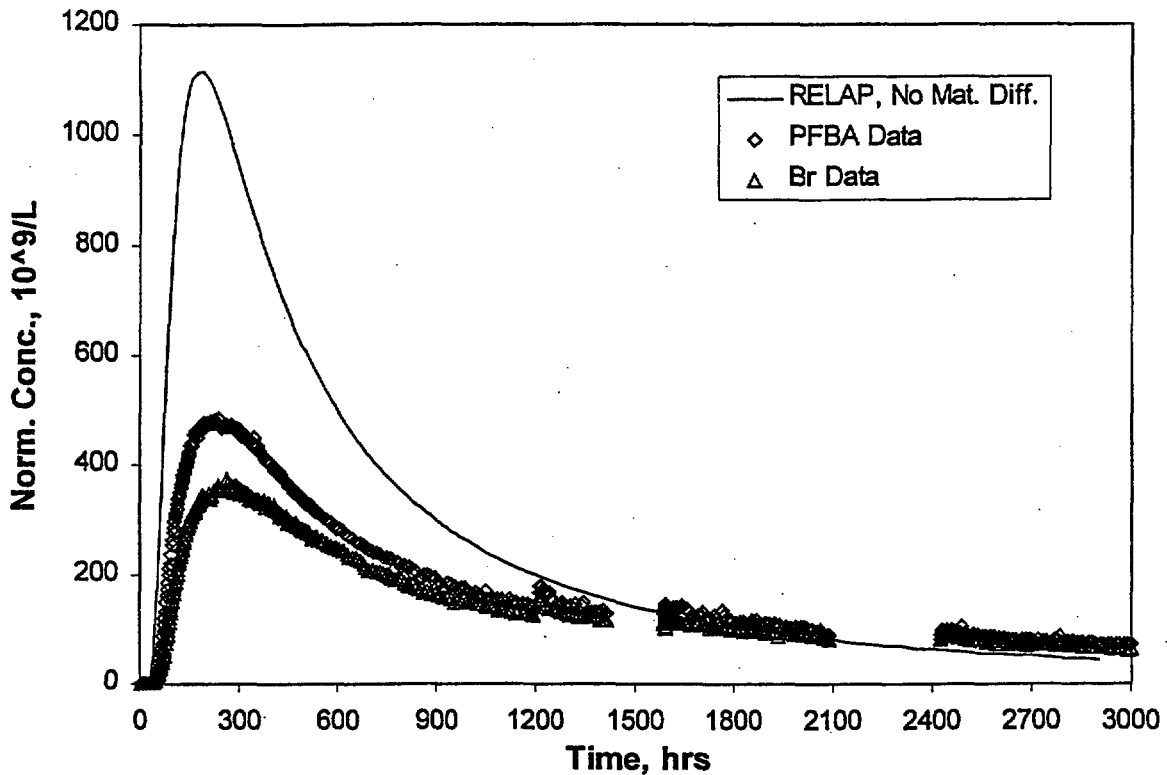


Figure 5-15. RETRAN-simulated response assuming a matrix diffusion mass transfer coefficient,  $\frac{\phi}{b} \sqrt{D_m}$ , 2.5 times larger than the best-fitting value for bromide (bromide data also shown for comparison). The mean residence time for this simulation was 170 hrs and the Peclet number was 20. (DTN LAPR831231AQ99.001 [data] and DTN LAPR831231AN99.001 [model]).

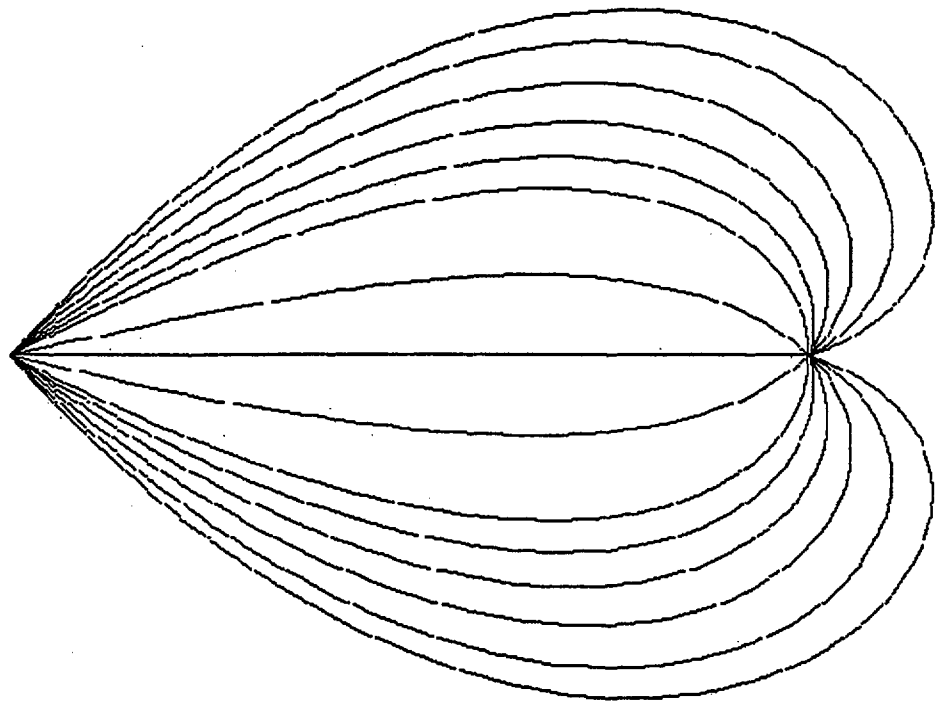


Figure 5-16. Flow streamlines in a 30% recirculation 2-D flow field (generated by the 2WELLS\_2D code). (DTN LAPR831231AN99.001).

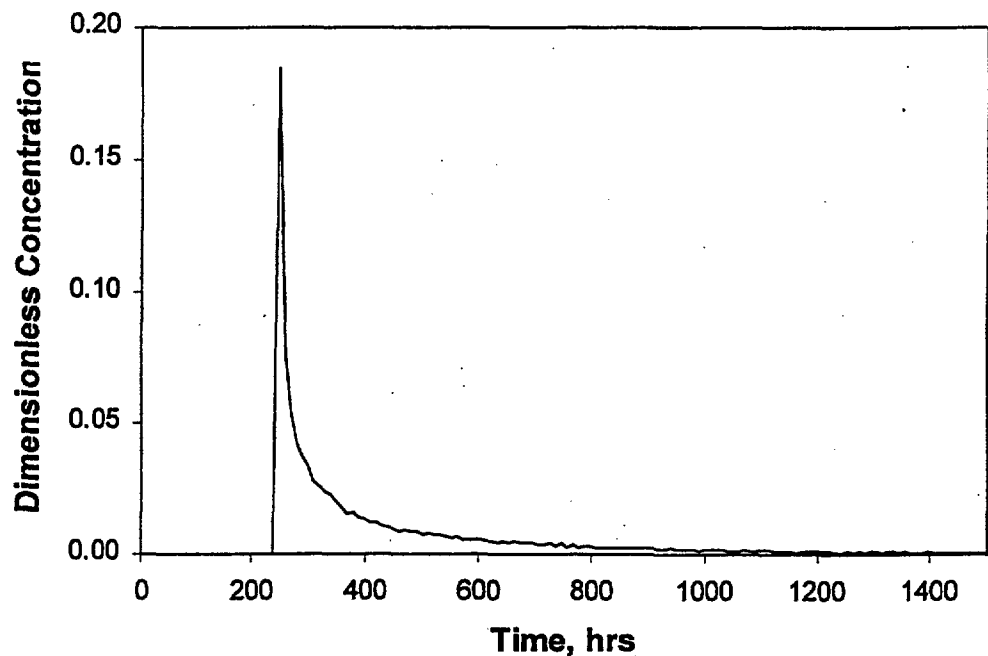


Figure 5-17. Breakthrough curve simulated by 2WELLS\_2D for the 30% recirculation flow field shown in Fig. 5-16. The curve was generated by particle-tracking methods assuming no local dispersion; i.e., all dispersion was due to the flow field. (DTN LAPR831231AN99.001).

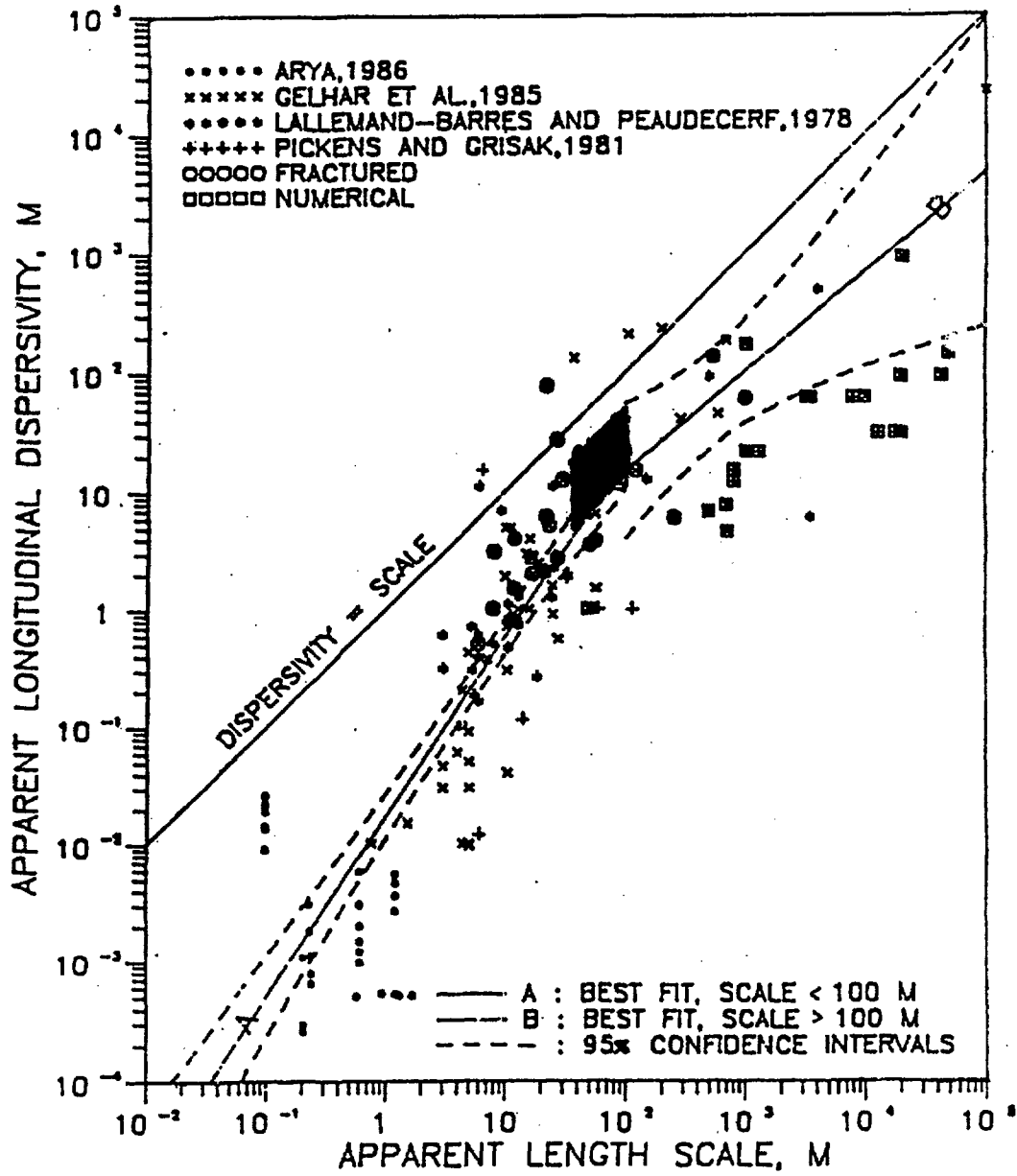


Figure 5-18. Plot of dispersivity vs. length scale showing range of C-holes values derived from interpretations of the Prow Pass and Bullfrog reactive tracer tests (darkened box). Plot taken from Neuman (1990). (DTN LAPR831231AQ99.002, DTN LAPR831231AN99.001 and notebook LA-CST-CW-NBK-98-011).

## 6.0 Batch Measurements of Lithium Sorption to C-Holes Tuffs

### 6.1 Materials and Methods

Batch sorption experiments were conducted in a manner similar to that described by Reimus and Turin (1997, Appendix A), who reported results of batch sorption experiments of lithium ion onto central Bullfrog tuff. The following steps were common features of all experiments:

- C-holes core from a stratigraphic unit of interest was crushed, pulverized, and passed through a 500- $\mu\text{m}$  sieve but retained on a 75- $\mu\text{m}$  sieve.
- A specified amount of crushed tuff was added to polycarbonate (polyallomer) Oak Ridge centrifuge tubes. In some experiments, the tuff and centrifuge tubes were autoclaved prior to contacting the tuff with the lithium solution.
- The tuff was preconditioned with filter-sterilized (0.2- $\mu\text{m}$  filter) J-13 water.
- A specified amount of tracer-bearing water (either from well J-13 or well C#3) was added to the preconditioned tuff, and the mixture was continuously shaken for 24 to 72 hrs at either 25°C or 38°C to achieve equilibration between solid and solution.
- After equilibration, the tubes were centrifuged and a portion of the supernate was filtered (0.2- or 0.4- $\mu\text{m}$  filter) for tracer analysis to determine the tracer concentration remaining in solution. Lithium was analyzed by inductively-coupled plasma-atomic emission spectrometry (ICP-AES).
- The mass of tracer sorbed to the tuff was determined by mass balance, with corrections, if necessary, to account for sorption to the container walls, which was measured in control experiments in which tuff was omitted.
- All measurements were made in duplicate.

Isotherms were determined under several different experimental conditions: 1:1 solution:solid ratio in J-13 water at 25°C, 1:1 solution:solid ratio in J-13 water at 38°C, 2:1 solution:solid ratio in J-13 water at 25°C, 4:1 solution:solid ratio in C-3 water at 38°C, 4:1 solution:solid ratio in J-13 water at 25°C, and 4:1 solution:solid ratio in J-13 water at 38°C. The two temperatures were intended to span the range of conditions under which sorption would occur in either the laboratory or the field (the average groundwater temperature in the Bullfrog Tuff at the C-holes is about 38°C).

At the time of these studies, groundwater from the C-holes complex was not consistently available, so groundwater from well J-13, located 4 km southeast of the C-holes complex, was used as a surrogate in most tests. J-13 water is well-characterized and has become a *de facto* standard groundwater for use in Yucca Mountain sorption studies (Harrar et al. 1990, pp. 6.6-6.7; Triay et al. 1997, pp. 11, 16, 45). A comparison of J-13 and C-holes groundwater chemistry shows that the two waters are both sodium bicarbonate dominated and in all regards quite similar (Table 6-1). Lithium solutions for sorption tests were prepared by dissolving reagent grade lithium bromide in either C#3 or J-13 water. All solutions were filter-sterilized before use.

A few tests were conducted in a sodium bicarbonate solution having the same ionic strength as J-13 water but without the calcium and other cations present in J-13 water (Reimus et al. 1997, pp. 3-5). Lithium sorption in this solution was noticeably greater than in J-13 water,

presumably because of the absence of cations that compete with lithium for sorption sites (primarily calcium). The results of these experiments are not reported here.

Ion-exchange theory suggests that the actual ion exchange process is rapid and will reach equilibrium quickly; in natural systems apparent equilibration rates are limited by diffusion of ions through the solution to the mineral surface (Bolt et al., 1978, pp. 54-90). In a well-mixed system such as a shaken centrifuge tube, diffusion is not limiting, and equilibration should be achieved quickly. A previous study of lithium sorption to the Prow Pass Member of the Crater Flat Tuff found that sorption equilibrium was reached within 1 h, confirming this hypothesis (Newman et al., 1991). For consistency with other sorption studies and for scheduling convenience, a minimum equilibration period of 24 h was adopted for these studies.

Tuffs from seven different lithologies were tested, including two samples of the same unit (the central Bullfrog Tuff) from two different holes (C#1 and C#2) to allow an assessment of spatial heterogeneity in lithium sorption parameters. The experimental matrix of tuffs, groundwaters, temperatures, and solid-solution ratios is summarized in Table 6-2. Fig. 6-1 shows the sampling locations of the C-holes core used in the experiments. Core from these same locations were also used in the experiments described in Sections 7.0 and 8.0 of this report.

The mineralogy of the tuffs used in the batch sorption experiments is listed in Table 6-3. The mineralogy was determined from x-ray diffraction (XRD) analyses. The tuffs differ primarily in their smectite and zeolite (clinoptilolite and mordenite) content, both of which have high cation exchange capacities and would be expected to sorb lithium quite strongly compared to other minerals present in the rocks. Fig. 6-2 provides a graphical depiction of the smectite and zeolite content of the tuffs used in the batch sorption experiments.

The cation exchange capacities of most of the tuffs used in batch sorption experiments were measured according to the following procedure:

- The tuff samples were crushed and wet-sieved with J-13 water to a particle size range between 75-500  $\mu\text{m}$ .
- 5g of each tuff was weighed into a 50 mL centrifuge Teflon tube.
- Samples were saturated three times with 30 mL of 1N LiBr-LiOAc solution to ensure replacement of cations present on mineral surface sites with Li. The pH of the solution was maintained at ~8.2 to prevent dissolution of calcite. After each LiBr addition, the tubes were sonified to disperse the centrifuged sediment, and then the samples were shaken for 30 min.
- Samples were centrifuged at 10000 rpm for 15 min and aliquots were pipetted out and analyzed for major cations such as Na, K, Ca, and Mg. The remaining solution in the tubes was dispensed into the same volumetric flask to determine the cation sorption after all three combined steps of Li sorption.
- After the Li sorption steps, the tuff present in the centrifuge tube was washed three times with 30mL 1N CsCl to remove the sorbed Li. The aliquots extracted after centrifuging were analyzed for Li, Na, Ca, K, and Mg. Cs has more affinity for zeolites, and it should therefore displace more cations than Li. In many cases, Cs sorption gives a measure of the total cation exchange capacity (Li measurements of the aliquots give the CEC for Li-Cs exchange).
- It should be noted that analcime (a Na-exchangeable zeolite) is discussed in the literature as having more affinity for Na and less for Li or Cs (Sherry, 1969, pp. 89-123). Ming and Mumpton (1989, pp. 873-911) have stated that the relatively large ionic radius of Cs may

prevent it from penetrating the small pores/channels in analcime. It is possible that the ionic radius of hydrated Li is large enough that it will also not sorb internally.

The experimental cation exchange capacities are listed in Table 6-4. By comparing this table and Fig. 6-2, it is apparent that the cation exchange capacities are highly correlated with the smectite and zeolite content of the rocks.

## 6.2 Results and Discussion

During the course of the experiments, it became apparent that lithium sorption was essentially independent of solution:solid ratio, temperature, and water composition (J-13 or C#3) over the range of conditions studied. Therefore, the data sets for a given tuff lithology were combined to estimate sorption parameters. Three common isotherm models, defined as follows, were fitted to the data for each tuff:

**Linear Isotherm:**

$$S = K_D C \quad (6.1)$$

where S = equilibrium sorbed concentration ( $\mu\text{g/g}$ ); C = equilibrium solution concentration ( $\mu\text{g/mL}$ ); and  $K_D$  = linear distribution coefficient ( $\text{mL/g}$ ).

**Freundlich Isotherm:**

$$S = K_F C^n \quad (6.2)$$

where  $K_F$  = Freundlich coefficient ( $\text{mL}/(\mu\text{g})^n$ ) ( $\mu\text{g/g}$ ) and n = Freundlich exponent (dimensionless).

**Langmuir Isotherm:**

$$S = \frac{K_L S_{\max} C}{(1 + K_L C)} \quad (6.3)$$

where  $K_L$  = Langmuir coefficient ( $\text{mL}/\mu\text{g}$ ) and  $S_{\max}$  = Maximum solid sorption capacity ( $\mu\text{g/g}$ ).

Figs. 6-3 to 6-9 show the experimental data for each tuff plotted as log equilibrium sorbed concentration ( $\mu\text{g/g}$ ) vs. log solution concentration ( $\mu\text{g/ml}$ ). A Langmuir isotherm consistently yielded better visual fits to the data than the other isotherms, so a fitted Langmuir isotherm is also shown in each figure. The Langmuir isotherm is the only isotherm that captures the curvature of the data when graphed on log-log axes. Furthermore, only the Langmuir isotherm recognizes the finite sorptive capacity of the solid matrix; the other models imply potential infinite sorption. A previous study of lithium sorption to the Prow Pass Member of the Crater Flat Tuff also revealed Langmuir behavior (Newman et al., 1991). The Langmuir, Freundlich, and linear isotherm parameters associated with the data in Figs. 6-3 to 6-9 are given in Table 6-5. We conclude that a Langmuir isotherm provides the best representation of lithium sorption onto C-holes Tuffs. However, a detailed statistical analysis to quantify how much better this representation is relative to the other isotherms (or whether it is statistically better) was not conducted. We also did not conduct statistical analyses to determine whether there were significant isotherm differences as a

function of temperature, solid-solution ratio, or core taken from different locations in the same lithological unit (i.e., the central Bullfrog Tuff from C#1 or C#2). However, it appears from Figs. 6-3 to 6-9 that any of these differences should have been minimal. These analyses will be the subject of future studies.

The error bounds shown in Figs. 6-3 to 6-9 reflect uncertainty due to analytical errors in determining lithium concentrations in solution. The error bounds were calculated assuming a 5% relative standard deviation in the lithium concentration measurements (typical for ICP-AES analyses). Errors increase as concentrations increase because there is a lower percentage of lithium sorbing at higher concentrations and hence a smaller relative difference between measured initial and final solution concentrations. It is apparent that the scatter in the data sets often exceeds the analytical error bounds, suggesting other sources of error besides analytical errors. These other potential sources of error have not been systematically identified.

The fitted Langmuir isotherms corresponding to all seven C-Holes tuff lithologies are plotted together in Fig. 6-10. By comparing Fig. 6-10 to Fig. 6-2 and Tables 3-2 and 3-4, it is apparent that the two tuffs demonstrating the greatest affinity for lithium (Bedded Prow Pass and Lower Bullfrog) are also the tuffs that have the greatest smectite and/or zeolite content as well as the highest cation exchange capacities. Thus, as expected, the lithium sorption capacity is highly correlated to the smectite/zeolite content and the cation exchange capacity of the tuffs.

Batch sorption experiments were also conducted to determine whether PFBA and bromide sorbed to C-holes tuffs. The bromide experiments were actually conducted simultaneously with the lithium experiments, as lithium was added to the solutions as lithium bromide. The starting bromide concentrations ranged from ~10 ppm to ~1000 ppm. The PFBA experiments were conducted at a single concentration (1 ppm). These experiments were conducted on each rock type at 25°C. There was no measureable sorption of PFBA or bromide on any of the tuffs.

## Section 6.0 References

- Bolt, G. H., M. G. M. Bruggenwert and A. Kamphorst. 1978. "Adsorption of Cations by Soil." *Soil Chemistry, A: Basic Elements*, G. H. Bolt and M. G. M. Bruggenwert. Amsterdam, Elsevier: pp. 54-90. (Submitted to RIS for Accession # 5/21/99.)
- Fuentes, H. R., W. L. Polzer, E. H. Essington, and B. D. Newman. 1989. *Characterization Reactive Tracers for C-Wells Field Experiment I: Electrostatic Sorption Mechanism, Lithium*. LA-11691-MS. Los Alamos, New Mexico: Los Alamos National Laboratory, p. 15. TIC Catalog # 202389.
- Harrar, J. E., J. F. Carley, W. F. Isherwood and E. Raber. 1990. *Report of the Committee to Review the Use of J-13 Well Water in Nevada Nuclear Waste Storage Investigations*. Report # UCID21867. Livermore, California: Lawrence Livermore National Laboratory, pp. 6.6-6.7. TIC Catalog # 209096. RIS Accession # NNA.19910131.0274.
- Ming, D.W., and F. A. Mumpton. 1989. *Zeolites in Soils, Minerals in Soil Environments*. Soil Science Society of America Book Series No. 1, pp. 873-911. (Submitted to RIS for Accession # 5/21/99.)
- Newman, B. D., H. R. Fuentes, and W. L. Polzer. 1991. "An Evaluation of Lithium Sorption Isotherms and Their Application to Ground-Water Transport." *Ground Water*, 29(6), 818-824. TIC Catalog # 203790. RIS Accession # 19930921.0012.
- Reimus, P. W., and H. J. Turin. 1997. *Draft Report of Results of Hydraulic and Tracer Tests at the C-Holes Complex*. Yucca Mountain Site Characterization Project Milestone Report SP32APMD. Los Alamos, New Mexico: Los Alamos National Laboratory, Appendix A. (Submitted to RIS for Accession # 5/21/99.)
- Reimus, P. W., T. Callahan, M. Haga, H. J. Turin, D. Frostenson, K. Vought, and D. Counce. 1997. *Results of Laboratory Characterization of Reactive Tracer Sorption to Prow Pass Tuff*. YMP Milestone Report SP2379M4. Los Alamos, New Mexico: Los Alamos National Laboratory, pp. 3-5. (Submitted to RIS for Accession # 5/21/99.)
- Sherry, H.S., (1969) The ion-exchange properties of zeolites. In *Ion Exchange*, 2, J.A. Marinsky, Ed. Marcel Dekker, Inc., N.Y., pp. 89-133. TIC Catalog # 218693.
- Triay, I. R., A. Meijer, J. L. Conca, K. S. Kung, R. S. Rundberg E. A. Strietelmeier, C. D. Tait, D. L. Clark, M. P. Neu, and D. E. Hobart. 1997. *Summary and Synthesis Report on Radionuclide Retardation for the Yucca Mountain Site Characterization Project*, Yucca Mountain Project Milestone Report 3784, LA-13262-MS, Los Alamos National Laboratory, pp. 11, 16, 45. TIC Catalog # 229826. MOL.19971210.0177.

## Section 6.0 Tables

Table 6-1. Comparison of J-13 and C-holes groundwater chemistry. All analyses (except pH) in  $\mu\text{g/mL}$  (Fuentes et al. 1989, p. 15). Note: These data were taken directly from the Fuentes et al. report; because of their vintage (pre-1990), they do not have an assigned DTN number.

	<i>J-13</i>	<i>C-Holes</i>
Al	<0.03	
B	0.13	
Ba	<0.001	
Ca	11.3	11
Cl	7	7
Fe	0.02	
K	5	2
Li	0.040	0.11
Mg	<0.010	0.38
Mn	0.01	
Na	44	55
Si	30	25
Sr	0.040	0.044
$\text{PO}_4$	<2.5	
$\text{SO}_4$	19	22
$\text{HCO}_3$	124	142
pH	7.2	7.8

Table 6-2. Summary of experimental test matrix (DTN LAPR831231AQ98.001).

Tuff <sup>(1)</sup>	Water	Solution:Solid (ml:g)	Temp. (°C)
Central Bullfrog, C#1, 715 m (1)	J-13	2:1	25
	J-13	2:1	38
Central Bullfrog, C#2, 734 m (2)	J-13	1:1	25
	J-13	1:1	38
	C#3	4:1	38
Lower Bullfrog, C#1, 795 m (3)	J-13	4:1	25
	J-13	4:1	38
	J-13	2:1	25
Upper Prow Pass, C#2, 533 m (4)	J-13	4:1	25
	J-13	4:1	38
	J-13	2:1	25
Central Prow Pass, C#2, 553 m (5)	J-13	4:1	25
	J-13	4:1	38
	J-13	2:1	25
Lower Prow Pass, C#1, 573 m (6)	J-13	4:1	25
	J-13	4:1	38
	J-13	2:1	25
Bedded Prow Pass, C#2, 643 m (7)	J-13	4:1	25
	J-13	4:1	38
	J-13	2:1	25
Upper Tram, C#2, 839 m (8)	J-13	4:1	25
	J-13	4:1	38
	J-13	2:1	25

<sup>(1)</sup>Lithology, borehole, and depth from land surface in meters. Numbers in parentheses correspond to numbers in Fig. 6-1 (which show locations where core was collected from the C-holes).

Table 6-3. X-ray Diffraction results\* for tuffs from Prow Pass, Bullfrog and Tram units. Only the main sorptive fractions are listed; the balance of the tuffs was mostly quartz and feldspar with small amounts of hematite, mica/illite, and/or kaolinite (DTN LAPR831231AQ99.003).

Tuff	Depth, m	Smectite	Clinoptilolite	Mordenite	Analcime	Calcite
Central Bullfrog, C#1	715	2±1	-	-	-	2±1
Central Bullfrog, C#2	734	5±2	NR	NR	NR	NR
Lower Bullfrog, C#1	795	9±3	4±1	3±1	12±1	4±1
Upper Prow Pass, C#2	533	-	-	-	-	Trc.
Central Prow Pass, C#2	553	2±1	-	-	-	2±1
Lower Prow Pass, C#1	573	2±1	-	-	-	-
Bedded Prow Pass, C#2	643	-	-	20±4	39±2	-
Upper Tram, C#2	839	1±1	-	-	-	-

\* = weight %

Trc. = trace abundance of < 0.5 wt%

Table 6-4. Cation exchange capacities of C-holes tuffs (DTN LAPR831231AQ99.003).

Tuff Unit	Estimated Average CEC, (meq/100g)	Std. Dev.
Central Bullfrog, C#1	3.65	0.12
Lower Bullfrog, C#1	17.97	0.19
Upper Prow Pass, C#2	1.99	0.49
Central Prow Pass, C#2	4.32	0.14
Lower Prow Pass, C#1	3.19	0.38
Bedded Prow Pass, C#2	21.25	0.13
Upper Tram, C#2	1.93	0.12

Note: CEC of "Central Bullfrog, C#2" was not measured.

Table 6-5. Lithium sorption isotherm parameters associated with the different C-holes tuffs (DTN LAPR831231AN99.001).

Unit	Langmuir Params.		Freundlich Params.		Linear Params.
	K <sub>L</sub> , L/mg	Smax, µg/g	K <sub>F</sub>	N	K <sub>d</sub> , mL/g
Central Bullfrog, C#1 + C#2 <sup>(1)</sup>	0.014	31.4	0.69	0.79	0.186
Lower Bullfrog, C#1	0.0070	233.9	2.26	0.75	0.321
Upper Prow Pass, C#2	0.00094	53.1	0.075	1.03	0.068
Central Prow Pass, C#2	0.0031	83.3	0.48	0.80	0.131
Lower Prow Pass, C#1	0.011	39.8	0.48	0.78	0.084
Bedded Prow Pass, C#2	0.012	254.9	4.17	0.69	0.383
Upper Tram, C#2	0.0026	59.8	0.27	0.78	0.072

<sup>(1)</sup>Sorption data from C#1 and C#2 tuffs lumped together to obtain parameter estimates.

## Section 6.0 Figures

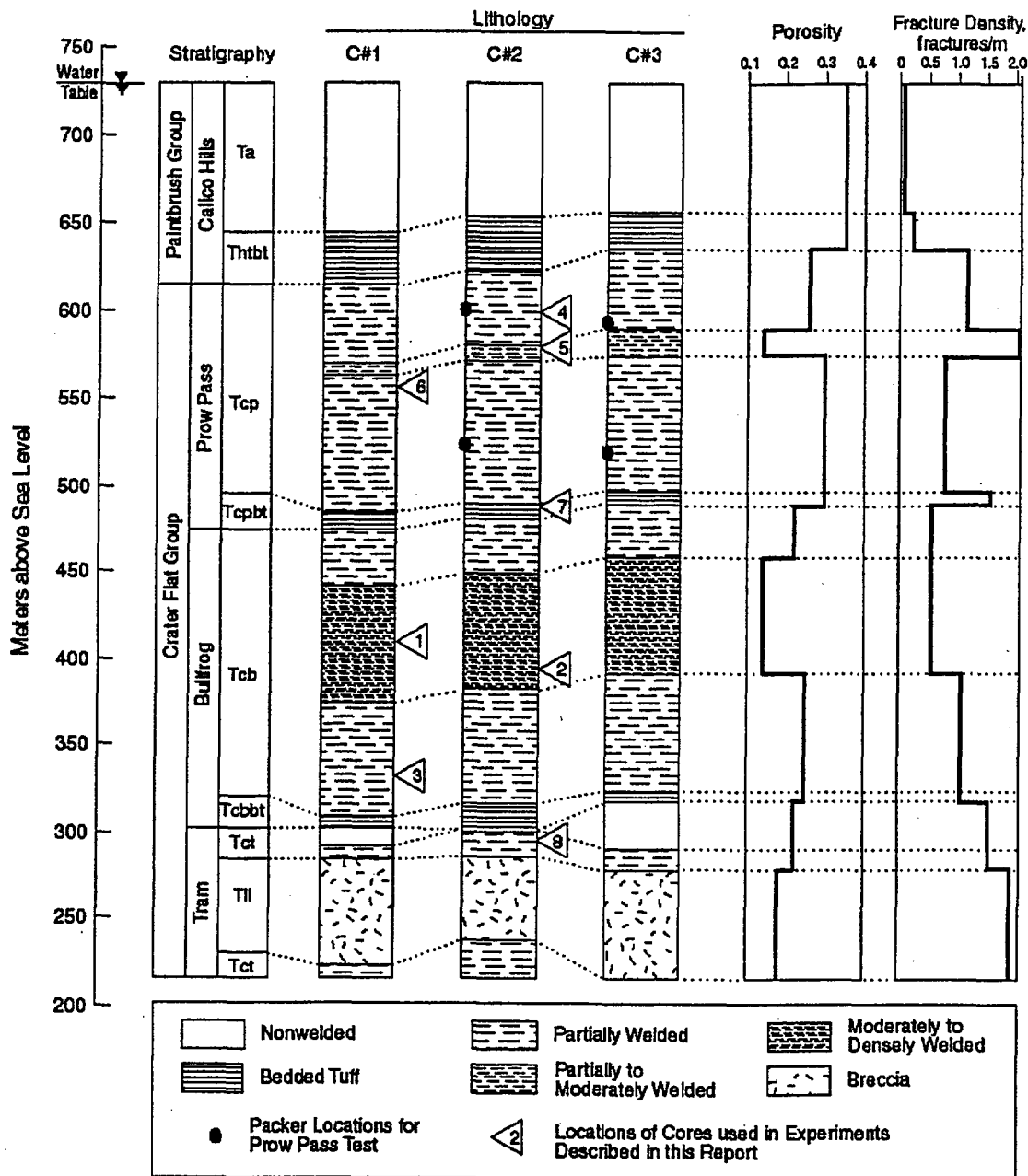


Figure 6-1. C-holes hydrogeology showing sampling locations of all core used in the laboratory experiments described in Sections 6.0, 7.0, and 8.0 of this report. Numbers correspond to numbers in Table 6-2. Also shown are approximate locations of packers for the reactive tracer test in the Prow Pass Tuff. (DTN GS970708312314.007 and DTN GS990408312315.002.)

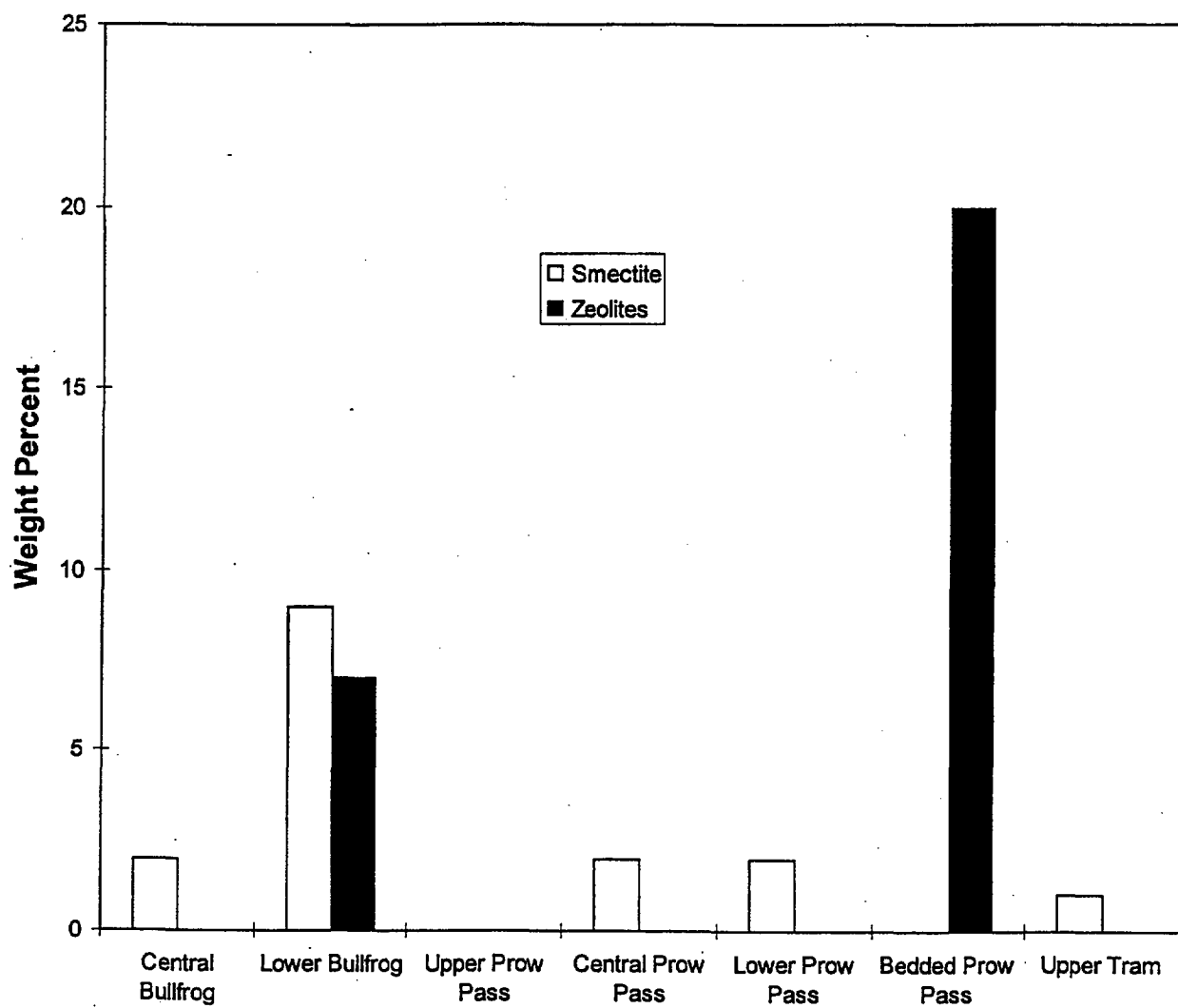


Figure 6-2. Smectite and zeolite weight percentages of the C-holes tuffs used in the batch sorption experiments (DTN LAPR831231AQ99.003).

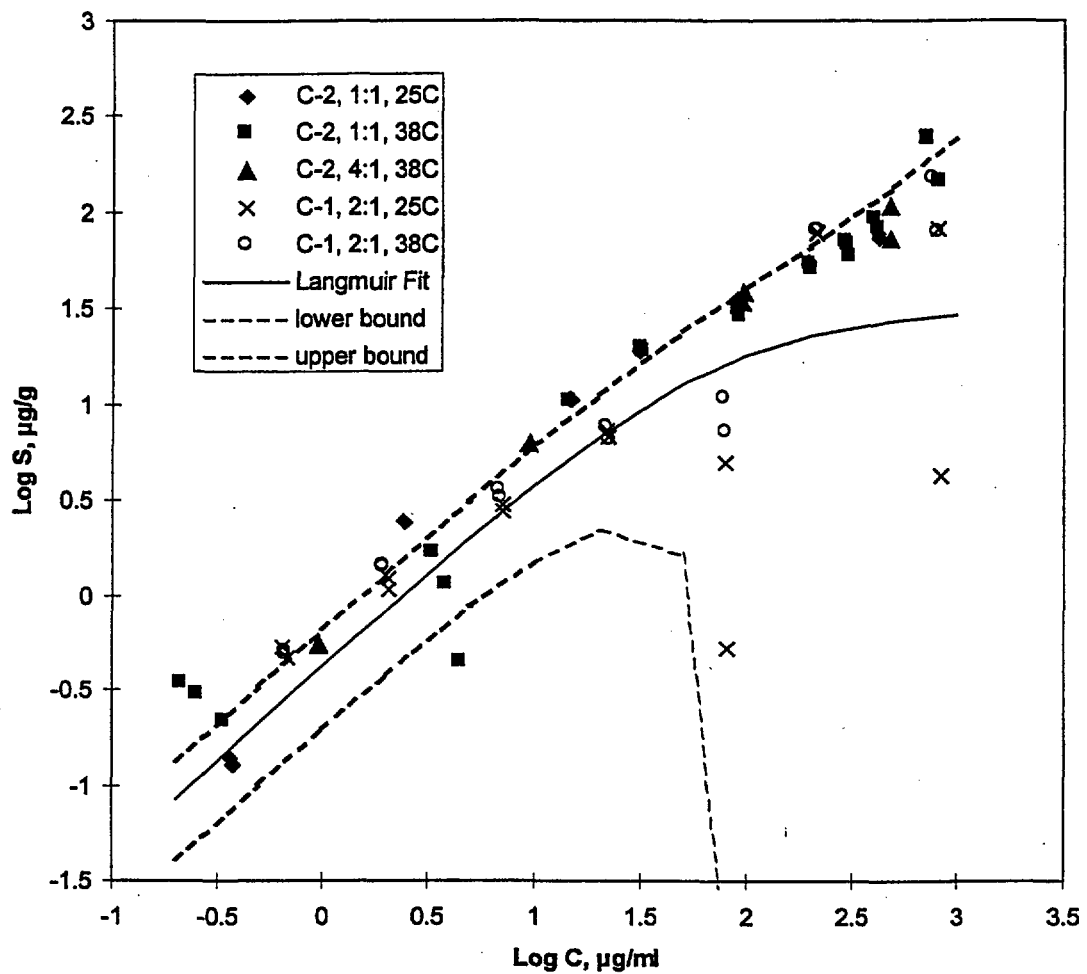


Figure 6-3. Lithium sorption data and fitted Langmuir isotherm for the central Bullfrog Tuff. The legend indicates the borehole (C#1 or C#2) from which the tuff came, the solution:solid ratio (ml:g), and the temperature of the experiments. The dashed lines are error bars associated with 5% analytical measurement error. J-13 water was used in all experiments except for "C-2, 4:1, 38C." Water from C#3 was used for "C-2, 4:1, 38C." The lithium concentration range in the Bullfrog Tuff field test spanned from less than 0.1 µg/ml up to 1200 µg/ml. (DTN LAPR831231AQ98.001 and DTN LAPR831231AN99.001).

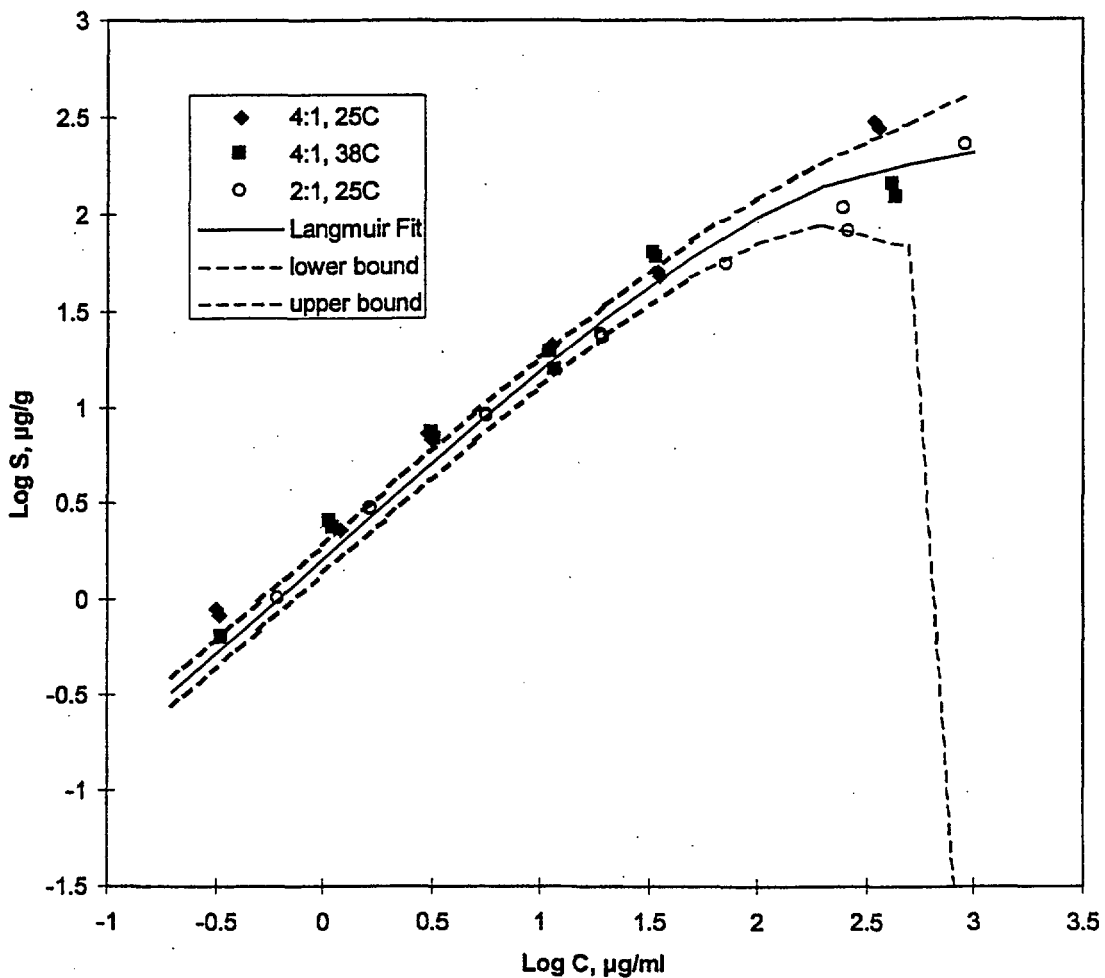


Figure 6-4. Lithium sorption data and fitted Langmuir isotherm for the lower Bullfrog Tuff. The legend indicates the solution:solid ratio (ml:g) and the temperature of the experiments. The dashed lines are error bars associated with 5% analytical measurement error. J-13 water was used in all experiments. The lithium concentration range in the Bullfrog Tuff field test spanned from less than 0.1  $\mu\text{g/ml}$  up to 1200  $\mu\text{g/ml}$ . (DTN LAPR831231AQ98.001 and DTN LAPR831231AN99.001).

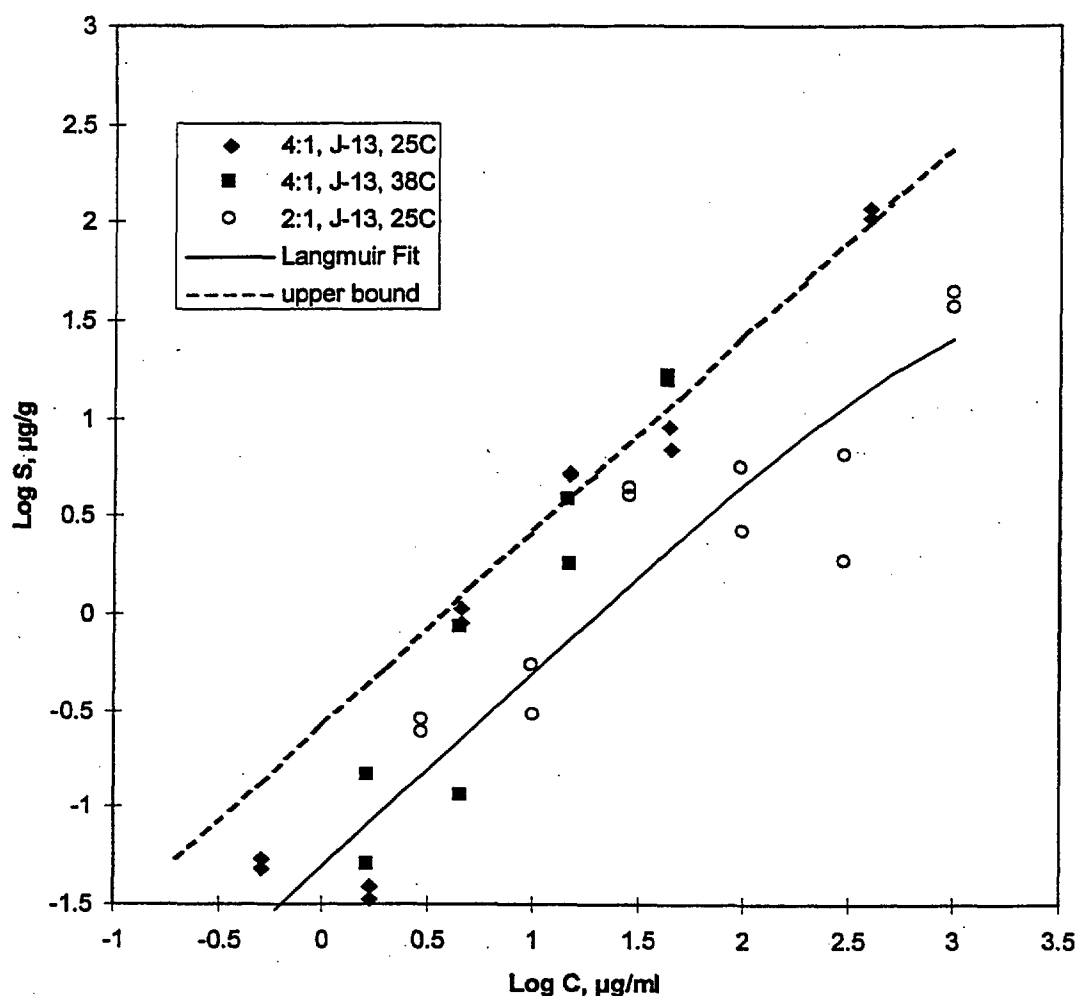


Figure 6-5. Lithium sorption data and fitted Langmuir isotherm for the upper Prow Pass Tuff. The legend indicates the solution:solid ratio (ml:g) and the temperature of the experiments. The dashed lines are error bars associated with 5% analytical measurement error (lower error bound is off-scale over entire range of data). J-13 water was used in all experiments. The lithium concentration in the Prow Pass Tuff field test ranged from less than 0.1 µg/ml up to 2500 µg/ml. (DTN LAPR831231AQ98.001 and DTN LAPR831231AN99.001).

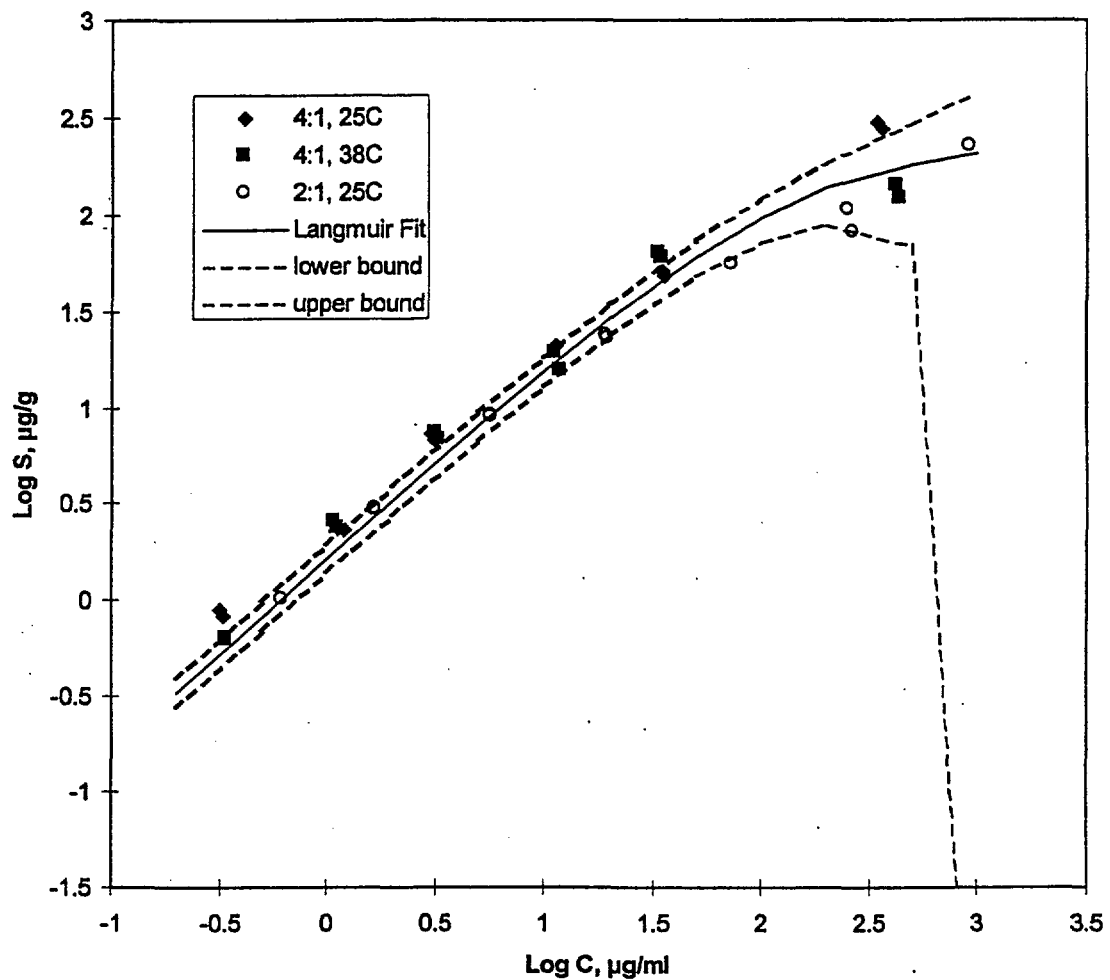


Figure 6-4. Lithium sorption data and fitted Langmuir isotherm for the lower Bullfrog Tuff. The legend indicates the solution:solid ratio (ml:g) and the temperature of the experiments. The dashed lines are error bars associated with 5% analytical measurement error. J-13 water was used in all experiments. The lithium concentration range in the Bullfrog Tuff field test spanned from less than 0.1  $\mu\text{g/ml}$  up to 1200  $\mu\text{g/ml}$ . (DTN LAPR831231AQ98.001 and DTN LAPR831231AN99.001).

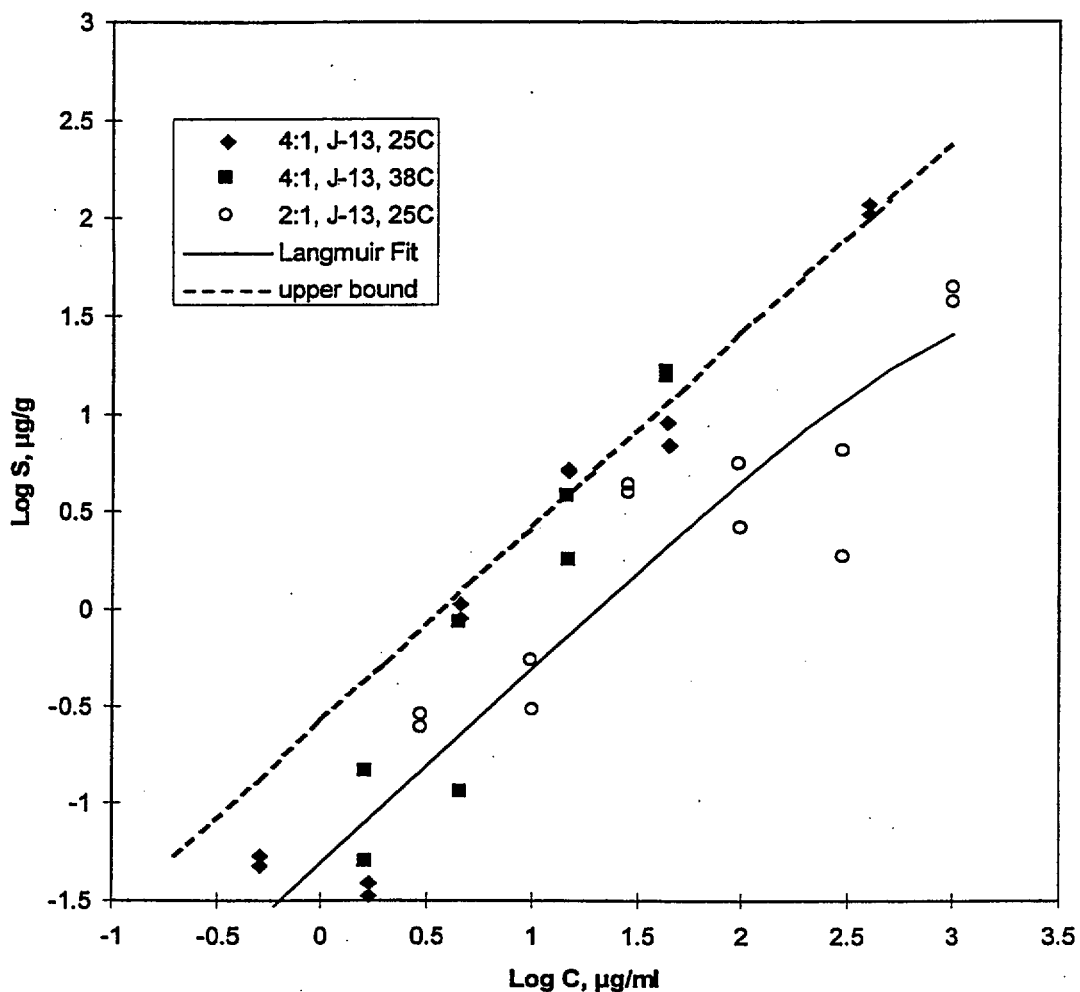


Figure 6-5. Lithium sorption data and fitted Langmuir isotherm for the upper Prow Pass Tuff. The legend indicates the solution:solid ratio (ml:g) and the temperature of the experiments. The dashed lines are error bars associated with 5% analytical measurement error (lower error bound is off-scale over entire range of data). J-13 water was used in all experiments. The lithium concentration in the Prow Pass Tuff field test ranged from less than 0.1  $\mu\text{g}/\text{ml}$  up to 2500  $\mu\text{g}/\text{ml}$ . (DTN LAPR831231AQ98.001 and DTN LAPR831231AN99.001).

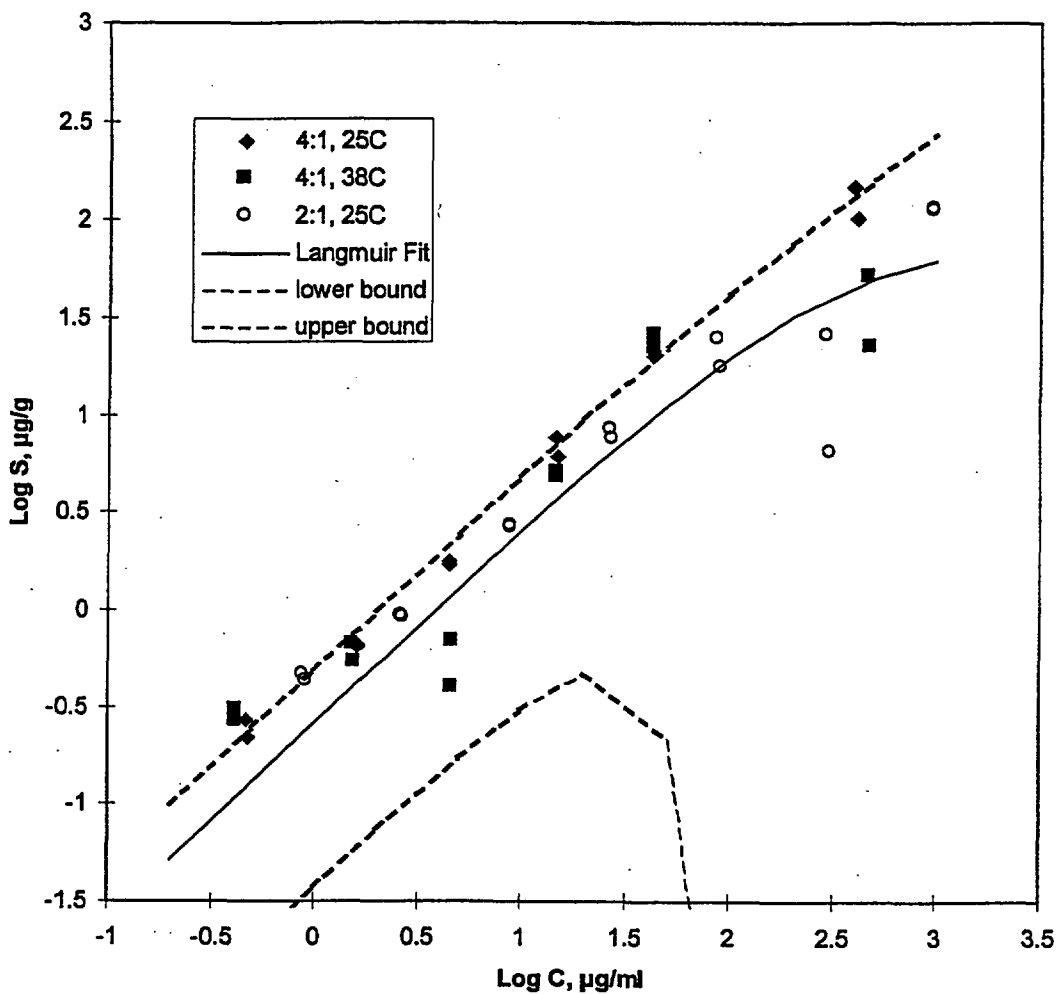


Figure 6-6. Lithium sorption data and fitted Langmuir isotherm for the central Prow Pass Tuff. The legend indicates the solution:solid ratio (ml:g) and the temperature of the experiments. The dashed lines are error bars associated with 5% analytical measurement error. J-13 water was used in all experiments. The lithium concentration in the Prow Pass Tuff field test ranged from less than 0.1  $\mu\text{g}/\text{ml}$  up to 2500  $\mu\text{g}/\text{ml}$ . (DTN LAPR831231AQ98.001 and DTN LAPR831231AN99.001).

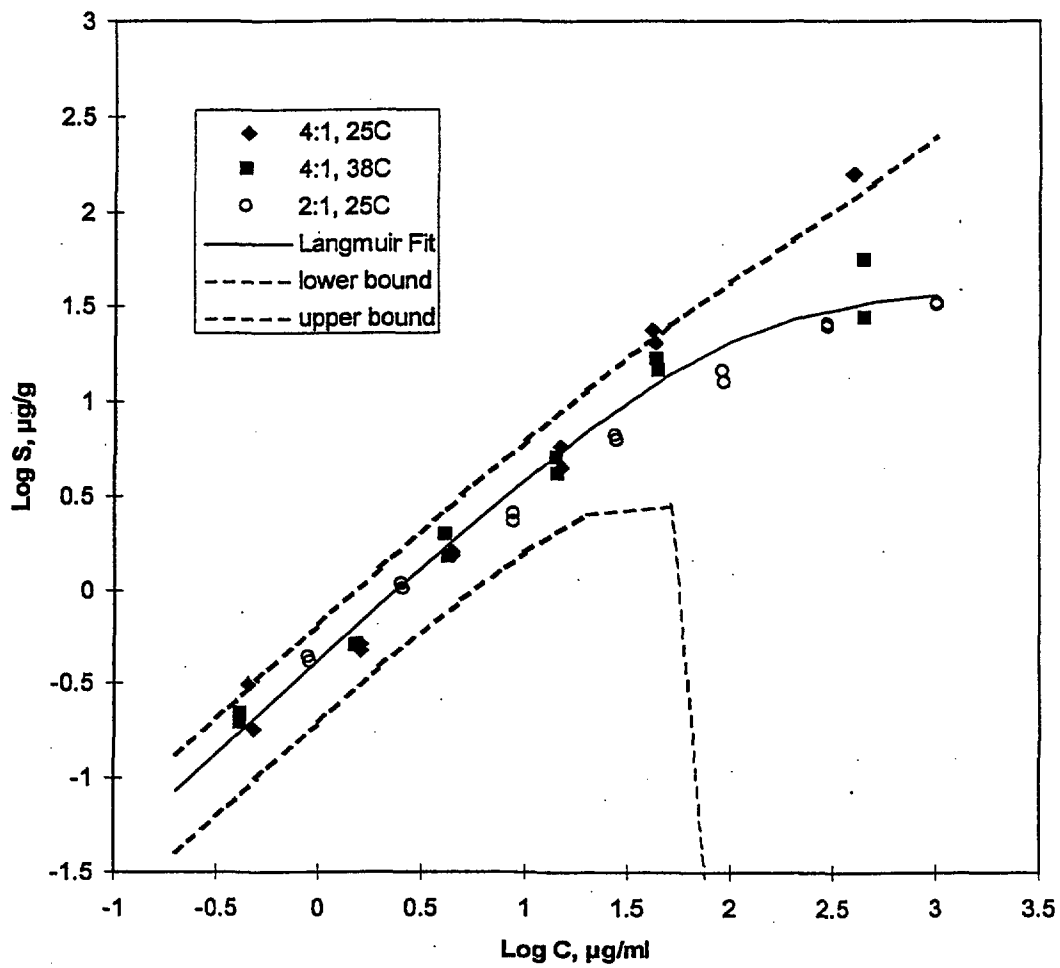


Figure 6-7. Lithium sorption data and fitted Langmuir isotherm for the lower Prow Pass Tuff. The legend indicates the solution:solid ratio (ml:g) and the temperature of the experiments. The dashed lines are error bars associated with 5% analytical measurement error. J-13 water was used in all experiments. The lithium concentration in the Prow Pass Tuff field test ranged from less than 0.1  $\mu\text{g/ml}$  up to 2500  $\mu\text{g/ml}$ . (DTN LAPR831231AQ98.001 and DTN LAPR831231AN99.001).

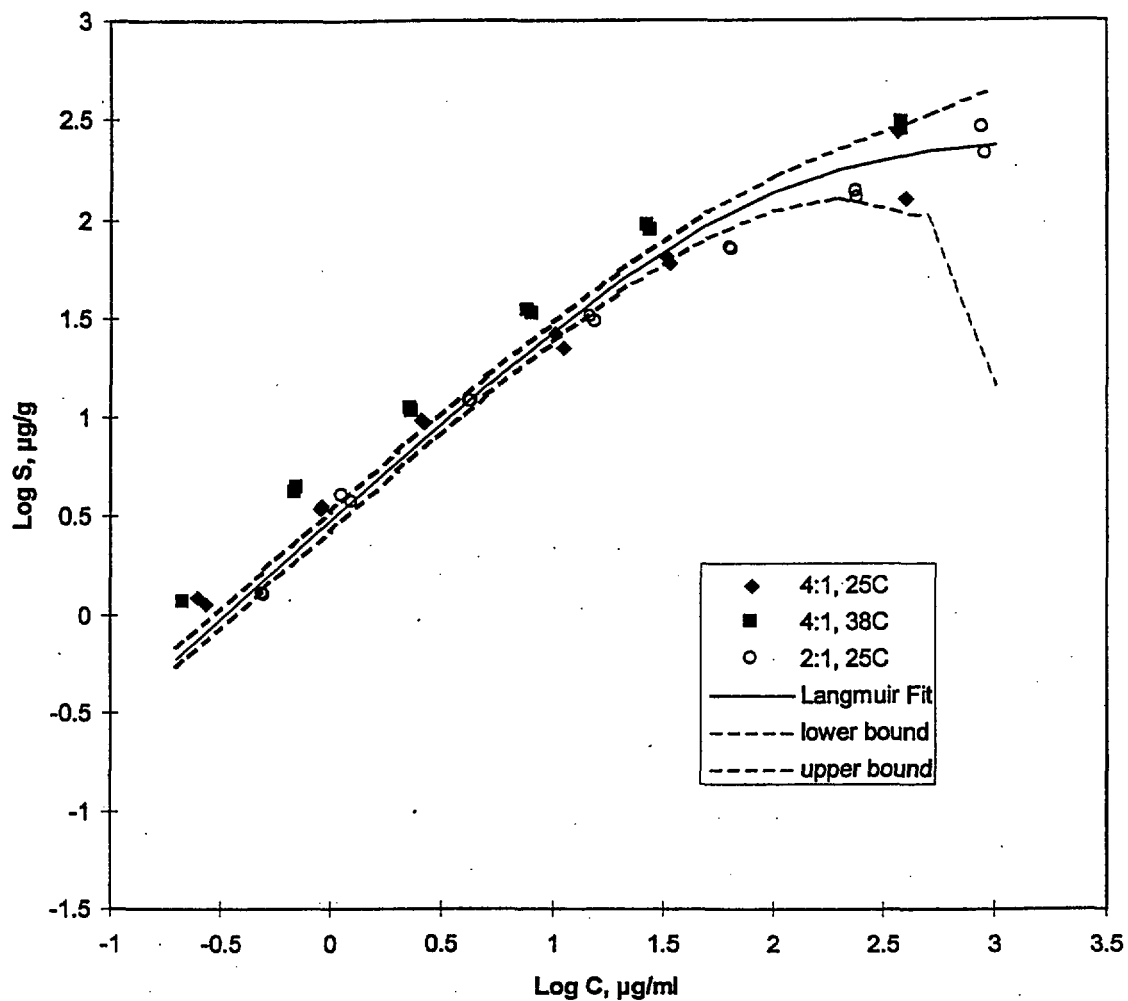
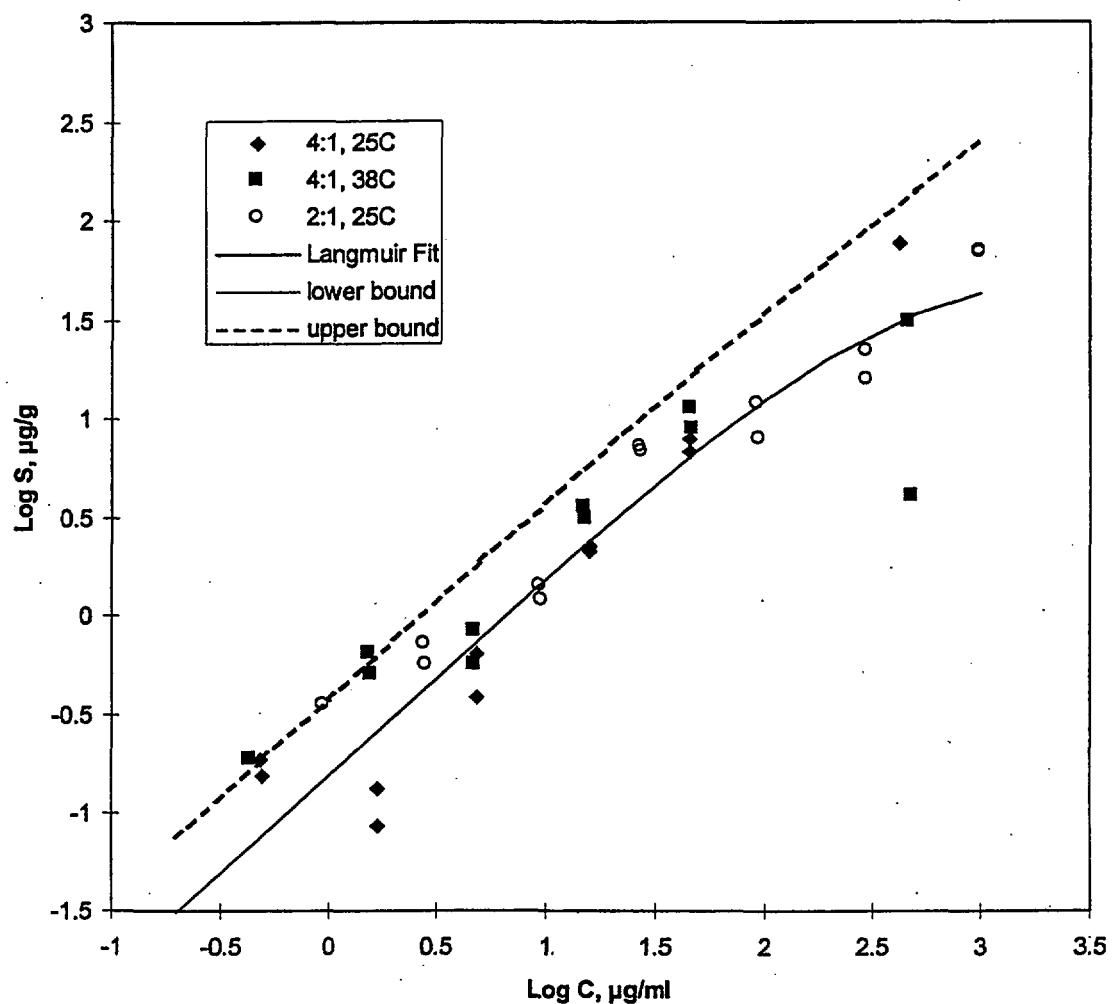


Figure 6-8. Lithium sorption data and fitted Langmuir isotherm for the bedded Prow Pass Tuff. The legend indicates the solution:solid ratio (ml:g) and the temperature of the experiments. The dashed lines are error bars associated with 5% analytical measurement error. J-13 water was used in all experiments. (DTN LAPR831231AQ98.001 and DTN LAPR831231AN99.001).



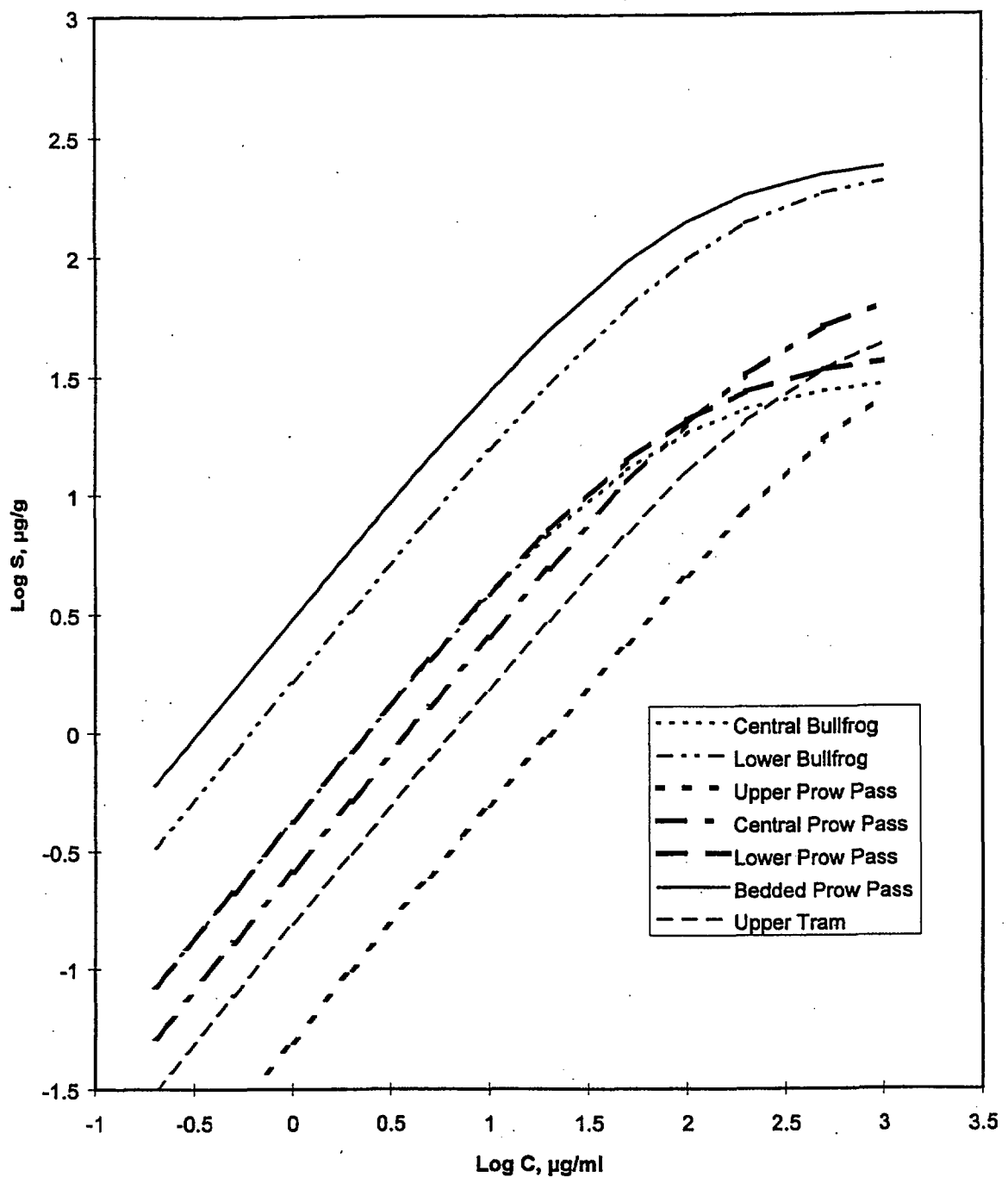


Figure 6-10. Fitted Langmuir isotherms for the seven C-holes tuffs. The lithium concentration range in the field test in the central and lower Bullfrog Tuff spanned from less than 0.1  $\mu\text{g}/\text{ml}$  up to 1200  $\mu\text{g}/\text{ml}$ . The concentration range in the Prow Pass Tuff field test ranged from less than 0.1  $\mu\text{g}/\text{ml}$  up to 1200  $\mu\text{g}/\text{ml}$ . (DTN LAPR831231AN99.001).

## 7.0 Dynamic Laboratory Transport Experiments

Several dynamic laboratory transport experiments involving lithium ion were conducted to study sorbing tracer transport under flowing conditions in both crushed tuff columns and fractured C-holes cores. The crushed tuff column experiments were conducted to determine lithium sorption rate parameters under flowing conditions, and to study the effects of sorption nonlinearity under dynamic conditions. The fractured core experiments were conducted to study lithium transport under more realistic fracture flow conditions where matrix diffusion and sorption in the matrix should influence transport. The crushed tuff experiments are described in Section 7.1, and the fractured core experiments are described in Section 7.2.

### 7.1 Crushed Tuff Columns

#### Experimental Methods

A series of transport experiments was conducted in Plexiglas columns 91.44 cm in length and 0.62 cm in diameter. The columns were packed with crushed central Bullfrog Tuff (the same material that is identified in Section 6.0 as central Bullfrog Tuff from C#2 [location number 2 in Fig. 6-1]) using a wet slurry technique that minimizes layering, but also eliminates particles less than roughly 70  $\mu\text{m}$  in size. With the crushed tuff, approximately 40-50% of the sample was not retained in the column. Column porosity was measured at 57% and dry bulk density was calculated at 1.14 g/mL by assuming a mineral density of 2.65 g/mL, typical values for columns prepared in this fashion (e.g. Treher and Raybold, 1982, pp. 8-9; Thompson, 1989). Three columns were prepared identically. The column apparatus included a constant-rate pump, a valve to switch between a reservoir containing J-13 "background" water and a solution of lithium bromide in J-13 water, and an automatic fraction collector at the downstream end of the column. Each experiment began by pumping approximately 180 mL (roughly 12 pore volumes) of J-13 water through the column at a specified flow rate to equilibrate the tuff with groundwater chemistry. The input was then switched to the lithium bromide solution. Effluent samples were analyzed for lithium and bromide concentration by ion chromatography. In these tests, bromide was assumed to behave as an ideal nonsorbing tracer, in contrast to lithium, a reactive tracer.

Experiments were conducted with two tracer concentrations (approximately 5 mg/L and 20 mg/L) and two flow rates (1.6 and 2.2 mL/h); a 20 mg/L test was also performed at 9.73 mL/h. The different concentrations were intended to quantify effects of sorption nonlinearity, while the different flow rates were intended to reveal kinetically-controlled effects such as sorption nonequilibrium or diffusion-limited sorption. All tests were conducted at 25°C.

#### Results and Discussion

Results of the columns tests are presented in Table 7-1; breakthrough curves (BTCs) for the experiments are shown in Figs. 7-1 through 7-5. The first step in the analysis was the determination of the individual column's transport behavior by fitting a one-dimensional advection-dispersion equation to the bromide BTC, using RELAP, a one-dimensional semi-analytic code based on a LaPlace transform inversion method (Appendix D). All five bromide BTCs were fit very well, suggesting near ideal behavior. RELAP can work with a system of

dimensionless variables, in which hydrodynamic dispersion is represented by the Peclet number,  $P_e$ , defined as  $L/\alpha$ , where  $L$  is the column length and  $\alpha$  the dispersivity. The Peclet numbers shown in Table 7-1 correspond to dispersivities of 0.2 - 0.3 cm, similar in scale to the column radius.

We then analyzed the lithium BTC for each experiment by holding the column's mean residence time and Peclet number fixed at the values determined for bromide, and varying the sorption behavior. RELAP's semi-analytic nature limits its sorption capabilities to a linear isotherm, so its numerical sister-code, RETRAN (Appendix D) was used to simulate Langmuir sorption behavior. Using the Langmuir sorption parameters resulting from the batch sorption studies to the central Bullfrog Tuff from well C#2 (Table 7-2; these represent a subset of the data shown in Fig. 6-3) and assuming local sorption equilibrium, we obtained curve (iv) in Fig. 7-1. Notice that this simulation matches the observed time of breakthrough very closely, but significantly overestimates the slope of the BTC. The observed lower slope (increased apparent dispersion) is symptomatic of kinetic effects (Valocchi, 1985); to explore this possibility, we relaxed the local equilibrium assumption and used RETRAN to better fit the observed BTC. RETRAN includes kinetic effects in terms of the dimensionless Damkohler number,  $Da$ , defined as  $k\tau$ , where  $k$  is a first order reaction rate constant and  $\tau$  is the mean residence time in the column. The observed lithium BTC was well fit by setting  $Da$  to 18 [curve (v) in Fig. 7-1], corresponding to a forward rate constant of  $2.2 \text{ hr}^{-1}$ . This relatively rapid reaction rate is consistent with both ion-exchange theory and measurements of lithium sorption to Prow Pass Tuff (Fuentes et al., 1989, p. 37), as discussed in Section 6.0.

Note that the rate constants shown in Table 7-1 reflect an effective rate constant for the entire sorption process, including both diffusion from the bulk liquid to the exchange site and the actual exchange process. While the latter should be a function only of the solution and medium, the former may depend on flow geometry, in turn a function of column packing. This sensitivity to column packing may explain why Table 7-1 shows that repeated tests in the same column give similar rate constants, but column 2 yielded consistently lower rate constants than the other two columns.

Isotherm nonlinearity can affect BTCs in two related but different ways. The first effect of nonlinear sorption on a BTC reflects the fact that in the solute front itself, a distribution of concentrations occurs, ranging from background (in our case, close to 0 mg/L) to the peak influent concentration (here, 5 or 20 mg/L). Changes in retardation as a function of concentration will alter the shape of the breakthrough curve; specifically, decreased sorption and higher transport velocity at high concentration will sharpen the leading edge of the solute front. We look for this effect by comparing the shape of the observed BTC to simulations assuming linear and nonlinear sorption.

This sharpening effect will be most pronounced in a high-concentration test, in which the leading edge of the front contains the widest range of concentrations. To determine whether sorption nonlinearity has affected the shape of the BTC, RELAP was used to attempt a linear sorption fit to the lithium BTC in Fig. 7-1. Both equilibrium and nonequilibrium fits are shown in the figure; the linear sorption simulations yield results virtually indistinguishable from the Langmuir simulations. This implies that for the concentrations and conditions of the column studies, the nonlinearity of the sorption isotherm had no observable effect on the shape of the BTC. This is probably due in large part to the relatively low lithium concentrations injected into the columns. Sorption nonlinearity in the batch sorption experiments (Section 6.0) was not very pronounced until concentrations exceeded about 100 mg/L. Also, the low dispersivity of the

laboratory columns probably kept the solute front very sharp, and the concentration at any point in the column therefore jumped from background to peak very rapidly. In this case, there is only a very small volume of intermediate concentration liquid in the column. In a higher-dispersion system where a larger portion of the column would contain solutions of varying concentration, nonlinear sorption would be more apparent. Because under the conditions of our tests, nonlinear sorption played no significant role in BTC shape; the rest of the column studies were analyzed assuming linear sorption, leading to the results presented in Table 7-1 and in Figs. 7-2 through 7-5.

The second effect on nonlinearity arises because behind the solute front, solute concentrations are relatively constant and nonlinearity makes the ratio between dissolved and sorbed concentrations a function of dissolved concentration. This ratio controls the velocity of the solute front through the column, through its influence on the retardation factor ( $R_F$ ), the ratio of average groundwater velocity to the velocity of the tracer front. This effect changes the position of the BTC as a function of concentration; decreased sorption at higher concentration will move the BTC earlier in time. We look for this effect by comparing measured  $R_F$ s for different solution concentrations.

Table 4-1 shows that  $R_F$ s for the 5 mg/L tests ranged from 2.2 to 2.3, with a mean of 2.25;  $R_F$ s for the 20 mg/L tests ranged from 1.7 to 2.0, with a mean of 1.87. The observed decreased retardation at higher concentration qualitatively fits our prediction of the effect of nonlinear sorption. We now compare these results to quantitative predictions of nonlinear effects on  $R_F$ . For the Langmuir isotherm, the  $R_F$  can be shown to be (Fetter, 1993, pp. 122-123):

$$R_F = 1 + \frac{\rho_B}{\theta} \left( \frac{K_L S_{\max}}{(1 + K_L C)^2} \right) \quad (7.1)$$

where  $\rho_B$  is the dry bulk density of the medium (g/mL) and  $\theta$  is the volumetric moisture content, or porosity for a saturated medium.

By solving Eq. (7.1) with our batch Langmuir parameters and column values for  $\rho_B$  and  $\theta$  values, we obtain retardation factor predictions of 2.11 for the 5 mg/L tests and 1.95 for the 20 mg/L tests. Overall these predictions match the observations very well, differing by 7% or less for both concentration levels. However, the observed difference in  $R_F$  at the two concentration levels somewhat exceeds that predicted by the model. This may reflect simple experimental variability due to the small number of tests conducted, or may indicate further physical complexities. Additional column studies covering a wider range of concentrations would help settle this question.

We conclude that under our experimental conditions, sorption nonlinearity has a relatively minor effect on the overall retardation of lithium, and the shapes of the breakthrough curves are dominated by kinetic rather than nonlinear effects. This result implies that we can model transport under these conditions using a simple  $K_D$  linear sorption model and assuming rate-limited sorption. The  $K_D$  value should be adjusted as a function of lithium concentration in the inlet solution. Comparison of Eqs. (6.1) and (6.3) shows that at low concentrations ( $C \rightarrow 0$ ), the Langmuir model approaches the linear model with a  $K_D$  value equal to  $S_{\max} \cdot K_L$ , or approximately 0.6 mL/g in the case of the central Bullfrog Tuff from C#2.

## 7.2 Fractured Core Columns

Laboratory-scale fractured tuff column transport experiments were conducted in two different induced fractures to provide more realistic experimental depictions of field-scale transport in fractured tuffs than can be achieved in crushed rock columns. These experiments also allow more detailed investigations of saturated zone transport processes than can be achieved in field experiments, where testing times, complexities, and costs are all considerably higher than in the laboratory (field tests also involve environmental permitting considerations that are not an issue with laboratory experiments). An additional objective of the fractured tuff column experiments was to obtain laboratory data under fracture flow conditions that would support more refined predictions of tracer transport in the Prow Pass member of the Crater Flat Tuff, where a reactive tracer test will be initiated in FY 1998.

### Experimental Methods

Axial fractures were induced in intact C-Holes cores from the upper and central Prow Pass lithologies by striking them with a chisel and hammer. The cores were taken from location numbers 4 and 5 in Fig. 6-1, respectively (C#2, 533 m; and C#2 553 m). Perpendicular cuts were then made on both ends of the fractured cores using a rock saw. After cutting, the cores were approximately 16-cm and 17-cm long, respectively for the upper and central Prow Pass fractures, and both fractures were about 9.5-cm wide (the diameter of the core). Each core was pre-saturated under water and under reduced pressure (vacuum), and then encapsulated within a flow system, as shown in Fig. 7-6 (see also Ware and Triay, 1995, pp. 7-9). The procedure for constructing the flow apparatus was as follows:

- Two end caps, each containing a narrow flow channel that fit exactly over the fracture trace at the ends of the cores, were machined out of Plexiglas stock. Three threaded access ports were drilled from the unmachined side of the end caps into the channel to allow introduction and withdrawal of solutions to/from the channel(s).
- After fixing one cap to an end of the core (using a silastic glue), the fracture trace along the sides of the core was coated with a silastic material, and then the entire side of the core was sealed by pouring a clear epoxy into the annulus formed between the core and a Plexiglas tube surrounding the core.
- The cores were then saturated under water and under strong reduced pressure until air bubbles no longer evolved.
- The remaining open ends of the cores were then fitted with the remaining end cap, and the cores were again saturated under water/reduced pressure.
- The flow apparatus was leak tested by placing several feet of head (of water) on one of the ends with the other end closed off.
- After ensuring there were no leaks, the hydraulic conductivity/aperture of the fractures were estimated by measuring the flow rate through the cores as a function of head difference across them. During these tests, the cores were visually inspected for flow bypass through the annular region and for leakage of water out of the flow channels

under the end caps. The hydraulic apertures were estimated to be 0.0141 cm and 0.0134 cm for the upper and central Prow Pass fractures, respectively.

After determining that the flow systems were satisfactory for further testing, tracer tests were conducted as follows:

- Flow of initially tracer-free J-13 water through the fracture was induced using a precision syringe pump.
- Flow was briefly interrupted, and tracer-bearing J-13 water was introduced in place of the tracer-free solution using a separate syringe pump.
- After a specified period of time (or volume of tracer solution), the inlet solution was switched back over to the tracer-free water, thus creating a finite-duration injection pulse of tracer solution to the fractured core.
- Effluent from the fractured core was collected in test tubes using an automatic fraction collector.
- The fractions were analyzed for tracers to establish tracer breakthrough curves. Iodide was analyzed by ion-selective electrode, PFBA and bromide were analyzed by ion chromatography, and lithium was analyzed by ICP-AES.

To date, five separate tracer experiments have been conducted in the upper Prow Pass Tuff core, and four experiments have been conducted in the central Prow Pass Tuff core. The experimental details in these tests are summarized in Tables 7-3 to 7-7. We first discuss the experiments in the upper Prow Pass core.

Three of the tests in the upper Prow Pass core involved the introduction of a sodium iodide pulse at three different flow rates (2.22 mL/hr, 8.65 mL/hr, and 19.76 mL/hr), with the objectives being to (1) determine tracer residence times so that additional experiments with other tracers could be optimized and (2) determine matrix diffusion parameters by comparing the breakthrough curves at the three different flow rates. The expectation was that iodide peak concentration and recovery would be lower as flow rates decreased because there would be more time for diffusion of iodide out of the fracture and into the stagnant water in the porous matrix at these lower rates. Testing at a single flow rate would not allow unambiguous estimation of matrix diffusion parameters because of the inability to distinguish between the effects of matrix diffusion and flow dispersion in the system. With three flow rates in the same fracture, it can be assumed that the effects of dispersion are approximately the same at each flow rate, and the difference in tracer responses can be attributed to differing amounts of matrix diffusion at the different residence times.

The other two experiments in the upper Prow Pass fracture involved injecting pulses of a solution containing PFBA and LiBr into the core at flow rates of 8.44 mL/hr and 6.33 mL/hr. The second PFBA/LiBr experiment was conducted because (1) an inadvertent flow interruption occurred during the first experiment when tracer concentrations were at their peaks, and (2) it was suspected that the volume of the flow system in the first experiment was different than in all the iodide experiments (see below). The flow volume in the second PFBA/LiBr experiment was more consistent with those in the iodide experiments, which allowed less ambiguous comparisons between the breakthrough curves in the different experiments.

The PFBA/LiBr experiments also featured intentional flow interruptions during the tails of the breakthrough curves. These flow interruptions provided an additional means of evaluating matrix diffusion in the cores; the concentrations of the solute tracers were expected to rebound during the flow interruptions because tracers should diffuse back into the fracture from the matrix.

There were several objectives of the PFBA/LiBr experiments:

- (1) Determine if the PFBA and bromide breakthrough curves were consistent with the factor of ~3 difference in the matrix diffusion coefficients measured in diffusion cells (see Section 8.0). PFBA was expected to have a higher peak normalized concentration than bromide because of its smaller diffusion coefficient.
- (2) Determine if the lithium breakthrough curve, relative to PFBA and bromide, was consistent with the batch sorption and diffusion cell data.
- (3) Determine if the normalized PFBA and bromide breakthrough curves were consistent with the iodide breakthrough curves from the earlier experiments. The bromide breakthrough curve was expected to be similar to that for iodide at a comparable flow rate because bromide and iodide have similar diffusion coefficients (Newman, 1973, pp. 229-230).

If consistency were found for items (1) and (2), it would lend credibility to the hypothesis that the diffusion cell and batch sorption experiments provide estimates of transport parameters that can be reliably used to predict and interpret transport behavior in fractured systems. This consistency would further imply that it is valid to use laboratory estimates of transport parameters to refine and reduce uncertainty in the interpretations of field-scale transport tests, and ultimately to predict transport over long time and distance scales in the field.

The experiments conducted in the central Prow Pass Tuff core had the same objectives and followed a very similar sequence to the experiments in the upper Prow Pass core. These experiments included three tests using iodide at three different flow rates (11.48, 19.73, and 49.44 mL/hr), and one test involving the simultaneous injection of PFBA and LiBr. Compared to the tracer responses in the upper Prow Pass fracture, we expected to see less flow rate dependence of iodide transport and smaller differences in the breakthrough curves of bromide and PFBA because the central Prow Pass tuff was considerably less porous than the upper Prow Pass tuff ( $\phi = 0.14$  and  $0.27$  respectively). Also, the diffusion coefficients of bromide and PFBA, as measured in the diffusion cell experiments (Section 8.0), were much lower in the central Prow Pass tuff than in the upper Prow Pass tuff. The results of the tracer tests in both cores are presented in the "Results and Discussion" subsection below.

### **Interpretative Methods**

The computer models RELAP and RETRAN (Appendix D) were used to interpret all tracer breakthrough curves obtained in the fractured cores. The tracer experiments were initially simulated using the parameter-fitting features of RELAP, which allow specified transport parameters to be systematically varied to obtain a best least-squares fit to one or more data sets (see Appendix D). A simultaneous fit to the iodide breakthrough curves in each core was obtained by adjusting the mean residence time, Peclet number ( $LV/D$ , where  $L$  = length of

column,  $V$  = linear flow velocity through column, and  $D$  = dispersion coefficient in column), and the lumped parameter  $\frac{\phi}{b} \sqrt{D_m}$  (where  $\phi$  = matrix porosity,  $b$  = fracture half aperture, cm, and  $D_m$  = diffusion coefficient in the matrix,  $\text{cm}^2/\text{sec}$ ) to achieve a best fit. After a fit was obtained, average fracture apertures ( $2b$ ) were calculated by (1) dividing the fitted mean fluid residence time by the known volumetric flow rate through the fracture to obtain an estimate of the fracture volume, and then (2) dividing this volume by the product of the length and width of the fracture to obtain an aperture estimate. This aperture estimate assumes that the fracture is a parallel-plate flow channel. Matrix porosities ( $\phi$ ) were independently measured as part of the diffusion cell experiments (Section 8.0), so the fitted value of the lumped parameter  $\frac{\phi}{b} \sqrt{D_m}$  effectively yielded a direct estimate of the matrix diffusion coefficient,  $D_m$ , because independent estimates of  $b$  and  $\phi$  were already made. For any given set of iodide simulations, the mean residence times in the fracture were constrained to differ by the inverse of the ratio of the flow rates in the experiments, and the Peclet numbers and matrix diffusion coefficients were constrained to be identical (since the flow system and tracer were the same in each experiment).

This exercise was repeated for the PFBA and bromide data sets, except that in this case, the mean residence times and Peclet numbers were constrained to be identical (since the tracers were introduced simultaneously), and the matrix diffusion coefficients were constrained to differ by a factor of 3 (with bromide being larger, to be consistent with the diffusion cell data). After the column transport parameters were determined from the nonsorbing tracer data, one of two methods were used to fit the lithium breakthrough curve. Either RELAP was used to fit the lithium breakthrough curve by adjusting the fracture and matrix retardation coefficients (as appropriate), or the transport parameters calculated from the simultaneous PFBA and bromide fits were used in RETRAN to fit the lithium curve. In this case, the  $K_D$  value used to fit the lithium data was constrained to be similar to that obtained from the batch sorption experiments (Section 6.0). As in the field tracer test interpretations (Section 5.0 and Appendix C), the lithium diffusion coefficient was assumed to be two-thirds that of bromide (Newman, 1973, pp. 229-230).

Because the lithium isotherm was known from batch sorption experiments to be nonlinear, we also attempted to fit the lithium breakthrough curves by assuming nonlinear Langmuir sorption behavior and adjusting isotherm parameters using RETRAN. Again, the sorption parameters in RETRAN were constrained to be similar to the parameters measured in batch sorption experiments (Section 6.0). All other model parameters in the RETRAN simulations (mean residence time, Peclet number, and matrix diffusion mass transfer coefficients) were set equal to those determined from the RELAP analyses of the nonsorbing tracer responses, except that the lithium diffusion coefficient was adjusted to be two-thirds of the bromide diffusion coefficient, as described above. If the nonlinear isotherm fits to the lithium data offered a significant improvement over the linear isotherm fit provided by RELAP, it would be taken as a strong indication that nonlinear sorption behavior was influencing lithium transport in the fractures.

In all tests featuring flow interruptions, RELAP was used to simulate the tracer breakthrough curves up until the time of the flow interruption (the first interruption if there were more than one). Predictions of tracer responses after flow interruptions were then made using RETRAN, which is capable of simulating flow rate changes. (Because of its Laplace transform

approach, RELAP is not capable of simulating such flow transients.) In these cases, the transport parameters determined from RELAP simulations up until the time of the flow interruption were used in RETRAN to effectively extend the simulations to the end of the experiment(s).

## Results and Discussion

The three normalized iodide breakthrough curves in the upper Prow Pass Tuff fracture and the best simultaneous fits to the three data sets are shown as a function of volume eluted from the fracture in Fig. 7-7. The experimental and model parameters corresponding to the best fits are given in Table 7-3. The quality of the fits was not very sensitive to the value assumed for the iodide matrix diffusion coefficient. That is, changing the iodide matrix diffusion coefficient by as much as a factor of 2 did not significantly hinder the ability to fit the data as long as the mean residence time and Peclet number were allowed to vary.

Fig. 7-8 shows the PFBA, bromide, and lithium breakthrough curves in the first PFBA/LiBr experiment in the upper Prow Pass Tuff fracture along with the best simultaneous fits to these data under the modeling constraints discussed in the previous section. The experimental and model parameters corresponding to this experiment are given in Table 7-4. The breakthrough curves from the first PFBA/LiBr experiment in the upper Prow Pass Tuff fracture may have been affected by an increase in the volume of the fracture or in the end caps of the flow system, as there was a significant delay in the arrival of all tracers and greater apparent tracer dispersion in this experiment compared to the iodide experiments in this fracture (Reimus et al. 1997, pp. 12-13). The apparent increase in volume could have resulted from an expansion of the flow apparatus (due to epoxy shrinkage, for instance), which would have resulted in an increase in fracture aperture (note the calculated mean fracture apertures in Tables 7-3 and 7-4). Another possible explanation is that there was some additional dead volume in the end caps during the first PFBA/LiBr experiment that was not present in the other experiments. This explanation is supported by the observation of a large air bubble (exact volume unknown) under the entrance end cap during all of the experiments except for the first PFBA/LiBr experiment (in which the end cap was almost completely filled with water). If there were communication between the column inlet and this volume (when filled with water), the effective volume of the flow system could have been significantly increased, thus resulting in longer tracer travel times and greater apparent dispersion. Table 7-4 gives the parameters that resulted in good fits to the data assuming different residence times/dead volumes in the entrance end cap (assumed to be well-mixed and modeled in exactly the same way in RELAP as injection wellbore volumes). Despite the fact that there is considerable variability in the mean residence times for the experiment depending on what end cap dead volume was assumed, the fitted Peclet numbers and matrix diffusion coefficients of bromide and PFBA are in relatively good agreement in all cases. The diffusion coefficients also agree within a factor of two with the matrix diffusion coefficients deduced for these tracers in the other experiments in this fracture, and the bromide diffusion coefficient agrees quite well with that of iodide (Table 7-3), which is expected because these two anions are similar in size (Newman, 1973, pp. 229-230). The relatively good agreement between the iodide and bromide matrix diffusion coefficients deduced from the different experiments suggests that changes in the flow system did not preclude reasonable estimates of matrix diffusion coefficients.

Fig. 7-9 is a plot of the breakthrough curve data for the second PFBA/LiBr test. Table 7-5 lists the experimental and numerical parameters for this experiment. As was seen in the first

PFBA/LiBr experiment, numerical fits of the bromide and PFBA data for the second test resulted in a larger fracture aperture than was obtained from the simultaneous iodide fits. However, the difference in apparent aperture was not as great as it was for the first PFBA/LiBr experiment. Because there was an air bubble in the inlet flow manifold for the second PFBA/LiBr experiment, the end cap volume should have been similar to that in the iodide tests. We are currently exploring another hypothesis that might help explain apparent discrepancies in deduced fracture apertures/volumes. This hypothesis involves the sensitivity of the mean fluid residence time parameter to the solute first arrival during each experiment. The first iodide experiment in the upper Prow Pass fractured core resulted in an inordinately early first arrival, which may have caused the numerical solution algorithms to calculate an erroneously short residence time value for the core using the iodide data. There are several ways to check this possibility; the most obvious is to discount the suspect data and use RELAP to recalculate the transport parameters. This analysis are in progress.

Figs. 7-10 and 7-11 show the iodide breakthrough curves and the PFBA/LiBr breakthrough curves, respectively, in the central Prow Pass Tuff fracture, along with RELAP/RETRAN fits to these data. Tables 7-6 and 7-7 list the model parameters corresponding to the best fits shown in Figs. 7-10 and 7-11, respectively. It is apparent that the agreement between the iodide and PFBA/LiBr experiments is much better in the central Prow Pass Tuff fracture than it was in the upper Prow Pass Tuff fracture. For instance, there is very good agreement between the Peclet numbers and fracture apertures deduced from the two sets of experiments. It is also apparent that there is somewhat less matrix diffusion in the central Prow Pass Tuff fracture than in the upper Prow Pass Tuff fracture, as evidenced by the larger matrix diffusion coefficients in the latter core. This result is consistent with the results of the diffusion cell experiments discussed in Section 8.0.

Figs. 7-8, 7-9 and 7-11 show that despite the relatively good agreement between the model and data for the PFBA and LiBr breakthrough curves in each fracture, the rebound in tracer concentrations following flow interruptions in the tails of the breakthrough curves is underpredicted by the RETRAN simulations for the upper Prow Pass core in both tests. This result is unexplained at this time. For the central Prow Pass PFBA/LiBr experiment, RETRAN accurately predicts the experimental data collected during this planned flow interruption. One possible explanation for the upper Prow Pass core results is that there could be some advective flow out of the matrix and into the fractures during the shut-in period. Unfortunately, we have no direct evidence of such an advective flow. Another possible explanation is that we are seeing the influence of multiple rates of diffusion, as suggested by Haggerty and Gorelick (1995), although it is not immediately clear why the remainder of the tracer breakthrough curves can be adequately explained/predicted without invoking multiple diffusion rates. It is also not clear why one rock type would reflect this possible physical phenomenon and another rock type would not. It may be that such results are related in some way to the porosity or the tortuosity of the rock matrix. We will continue to study all these possibilities by conducting more flow interruptions in future fractured core experiments and in other rock types.

Of particular interest in the analysis of the fractured core experiments is the comparison of transport parameters deduced from these experiments with parameters deduced from the batch sorption and diffusion cell experiments. The matrix diffusion coefficients of bromide and PFBA in the upper Prow Pass Tuff diffusion cell experiments (see Section 8.0) were estimated to be about twice those deduced in the fractured core tests in this lithology. This discrepancy can be explained by recognizing that flow through the fracture was most likely channelized to some

degree, and therefore, the effective aperture in the flow pathways was probably larger than the average aperture obtained by assuming a parallel-plate fracture (as described above). For every twofold increase in the effective half-aperture,  $b$ , the diffusion coefficient,  $D_m$ , must increase by a factor of four to maintain the same value of the lumped parameter,  $\frac{\phi}{b} \sqrt{D_m}$ . Thus, the factor of two discrepancy will disappear if it is assumed that the planar area through which flow occurred in the fracture was a factor of  $\sqrt{2}$  less than the entire planar area of the fracture. This amount of channeling is not unexpected; channeling to a greater degree was, in fact, deduced previously in fractured cores from the C-Holes (Reimus 1995, pp. 73-94). Qualitative fracture channeling has been visualized at the laboratory-scale by others as well (Brown et al., 1998; Thompson, 1991).

Diffusion coefficients measured in diffusion cell experiments in the central Prow Pass Tuff were considerably smaller than those deduced from the fractured core tests in this lithology. This result may indicate that much of the diffusive mass transfer observed in the fractured core experiments occurred in stagnant zones within the fracture (near the fracture walls or in low flow regions within the fracture) rather than into the matrix proper. In this case, apparent diffusion coefficients would be expected to be much larger than those measured in the matrix.

Although we found that the fits to the lithium breakthrough curves could be slightly improved by assuming nonlinear Langmuir sorption, the fits obtained assuming a linear sorption isotherm were consistently quite satisfactory. We concluded that lithium sorption in the rock cores could be adequately approximated using a linear isotherm. This assumption is more justifiable for the experiments in which the lithium injection concentration was relatively low. The fitted linear distribution coefficient,  $K_D$ , obtained for lithium in the fractured core experiments was in relatively good agreement with the  $K_D$ s deduced in the batch sorption tests (see Section 6.0). The  $K_D$  value in the fractured core experiments was obtained by either goodness of fit using RETRAN or by dividing the product of the lithium matrix diffusion coefficient and matrix retardation coefficient (the lumped parameter determined in the RELAP simulations) by a diffusion coefficient that was assumed to be two-thirds of the bromide diffusion coefficient observed in the core experiments. Equation (5.1) was then used to calculate a  $K_D$  value from the fitted retardation coefficient.

An important point to note is the lack of agreement for the  $K_D$  value obtained for the two PFBA/LiBr tests in the upper Prow Pass core. In the first test, the lithium injection concentration was five times higher than in the second test. Thus, lithium transport in the first test should have been influenced more by nonlinear sorption than in the second. Analysis of this difference shows the opposite effect; that is, a greater difference between the bromide and lithium breakthrough curves was expected in the second test than in the first because of the higher expected degree of lithium sorption. The lower apparent sorption in the second test was perhaps due to some small amount of lithium remaining on sorption sites in the first test due to irreversible sorption, thus decreasing the available sorption sites in the second test (the lithium recovery in the first test was not complete). Chemical analysis of the other major cations (e.g.,  $\text{Na}^+$ ,  $\text{Ca}^{2+}$ , and  $\text{K}^+$ ) may help elucidate this hypothesis. If the transport behavior of these cations is different for the two experiments, then some amount of lithium may have remained sorbed to the matrix.

In all of the RELAP and RETRAN simulations, sorption was assumed to occur only in the matrix, with no sorption to fracture surfaces. This assumption is consistent with the fact that the fractures were artificially induced in an intact core (so there should have been no sorptive

mineral coatings). The relatively good agreement between the lithium  $K_D$  values deduced from the batch sorption tests and the fractured core experiments lends validity to the practice of using sorption parameters deduced from simple laboratory experiments to predict sorbing solute transport in fractured media. This is one of the main goals of the Los Alamos C-holes testing effort.

## Section 7.0 References

- Brown, S., A. Caprihan, and R. Hardy. 1998. "Experimental Observation of Fluid Flow Channels in a Single Fracture." *J. Geophys. Res.*, 103(B3), 5125-5132. (Submitted to RIS for Accession # 5/21/99.)
- Fetter, C. W. 1993. *Contaminant Hydrogeology*. New York: Macmillan Publishing Company, pp. 122-123. TIC Catalog # 240691.
- Fuentes, H. R., W. L. Polzer, E. H. Essington, and B. D. Newman. 1989. *Characterization Reactive Tracers for C-Well Field Experiment I: Electrostatic Sorption Mechanism, Lithium*. LA-11691-MS. Los Alamos, New Mexico: Los Alamos National Laboratory, p. 37. TIC Catalog # 202389.
- Haggerty, R., and S. M. Gorelick. 1995. "Multiple-Rate Mass Transfer for Modeling Diffusion and Surface Reactions in a Media with Pore-Scale Heterogeneity." *Water Resour. Res.*, 31(10), 2383-2400. (Submitted to RIS for Accession # 5/21/99.)
- Newman, J. S. 1973. *Electrochemical Systems*. Englewood Cliffs, New Jersey: Prentice-Hall, pp. 229-230. TIC Catalog # 210201.
- Reimus, P. W., T. Callahan, M. Haga, H. J. Turin, D. Frostenson, K. Vought, and D. Counce. 1997. *Results of Laboratory Characterization of Reactive Tracer Sorption to Pore Pass Tuff*. YMP Milestone Report SP2379M4. Los Alamos, New Mexico: Los Alamos National Laboratory, pp. 12-13. (Submitted to RIS for Accession # 5/21/99.)
- Reimus, P. W. 1995. *The Use of Synthetic Colloids in Tracer Transport Experiments in Saturated Rock Fractures*. LA-13004-T (also PhD Dissertation, University of New Mexico). Los Alamos, New Mexico: Los Alamos National Laboratory, pp. 73-94. TIC Catalog # 219271.
- Thompson, J. L. 1989. "Actinide Behavior on Crushed Rock Columns." *J. Radioanal. Nucl. Chem.*, 130(2), 353-364. RIS Accession # NNA.19920131.0401.
- Thompson, M. E. 1991. "Numerical Simulation of Solute Transport in Rough Fractures." *J. Geophys. Res.*, 96(B3), 4157-4166. RIS Accession # NNA.19910812.0005.

Treher, E. N., and N. A. Raybold. 1982. *The Elution of Radionuclides through Columns of Crushed Rock from the Nevada Test Site*. LA-9329-MS. Los Alamos, New Mexico: Los Alamos National Laboratory, pp. 8-9. TIC Catalog # 202338. RIS Accession # HQS.19880517.2892.

Valocchi, A. J. 1985. "Validity of the Local Equilibrium Assumption for Modeling Sorbing Solute Transport through Homogeneous Soils." *Water Resour. Res.*, 21(6), 808-820. TIC Catalog # 223203. RIS Accession # NNA.19890918.0541.

Ware, S. D., and I. R. Triay. 1995. *Transport of Radionuclides through Natural Fractures under Saturated Conditions*. Yucca Mountain Site Characterization Project Milestone Report #3063. Los Alamos, New Mexico: Los Alamos National Laboratory, pp. 7-9. RIS Accession # MOL.19971105.0646.

## Section 7.0 Tables

Table 7-1. Results of crushed tuff column studies. Refer to text for notation.  
(LAPR831231AQ98.001 and LAPR831231AN99.001).

Column	Figure	Flow Rate (mL/hr)	Li Conc. (mg/L)	$\tau$ (hr)	P <sub>e</sub>	R <sub>f</sub>	k <sub>f</sub> (hr <sup>-1</sup> )	D <sub>a</sub>
1	4-1	2.2	20	8.2	300	2.0	2.2	18
1	4-2	1.6	20	11	300	1.9	3.6	40
1	4-3	9.7	20	1.9	400	1.7	14	27
2	4-4	2.2	5	8.0	400	2.3	18	140
2	4-5	1.6	5	11	400	2.2	14	160

Table 7-2. Lithium isotherm parameters derived from batch sorption studies to central Bullfrog Tuff from C#2 (0.5 - 500  $\mu\text{g}/\text{mL}$  concentration range). Note that these data represent a subset of the data shown in Fig. 6-3. (LAPR831231AQ98.001 and notebook LA-CST-CW-NBK-98-011).

<u>Linear</u>	
K <sub>D</sub>	0.21 mL/g
<u>Freundlich</u>	
K <sub>F</sub>	$0.76 (\text{mL}/\mu\text{g})^{0.82} \mu\text{g}/\text{g}$
n	0.82
<u>Langmuir</u>	
K <sub>L</sub>	$5.3 \times 10^{-3} \text{ mL}/\mu\text{g}$
S <sub>max</sub>	110 $\mu\text{g}/\text{g}$

Table 7-3. Summary of experimental and numerically deduced parameters from the NaI tests in the upper Prow Pass fractured core (16.1 cm long by 9.5 cm diameter). (DTN LAPR831231AQ98.001 and DTN LAPR831231AN99.002).

<i>Parameter</i>	<i>First I Test</i>	<i>Second I Test</i>	<i>Third I Test</i>
<b>Experimental Parameters</b>			
Hydraulic aperture (cm)	0.0141	0.0141	0.0141
Injection flow rate (mL/hr)	2.22	19.76	8.65
Injection duration (hr)	31.00	2.95	7.03
Injection concentration (mg/L)	1000.	999.3	1000.
Flush flow rate (mL/hr)	2.00	20.16	8.29
Flow interruption, hrs into test (duration, hr)	None	None	None
<b>Modeling Best-fit Parameters</b>			
Mean fluid residence time (hr)	4.10	0.46	1.05
Average fracture aperture (cm)	0.060	0.060	0.060
Peclet number	33.	33.	33.
Dispersivity (cm)	0.49	0.49	0.49
Matrix diffusion coefficient ( $\times 10^{-6}$ cm $^2$ s $^{-1}$ )	3.6	3.6	3.6

Table 7-4. Summary of experimental and numerically deduced parameters from the first PFBA/LiBr test (1997) in the upper Prow Pass fractured core (16.1 cm long by 9.5 cm diameter). (DTN LAPR831231AQ98.001 and DTN LAPR831231AN99.002).

Parameter	Experimental Parameters			
Hydraulic aperture (cm)	0.0141			
Injection flow rate (mL/hr)	8.44			
Injection duration (hr)	19.2			
Injection concentration (mg/L)	278 (PFBA) 11400 (Br) 1010 (Li <sup>+</sup> )			
Flush flow rate (mL/hr)	8.03			
Flow interruption, hrs into test (duration, hr)	19.2 (1.35) 50.4 (14.25)			
Modeling Best-fit Parameters				
End cap residence time (hr)	0	0.67	1.5	2
Mean fluid residence time (hr)	4.4	3.8	3.0	2.2
Average fracture aperture (cm)	0.233	0.202	0.159	0.117
Peclet number	5.2	4.0	3.5	4.0
Dispersivity (cm)	3.1	4.0	4.57	4.0
Matrix diffusion coefficient (x10 <sup>-6</sup> cm <sup>2</sup> s <sup>-1</sup> )	1.2 (FBA) 3.5 (Br) 2.2 (Li <sup>+</sup> ) <sup>a</sup>	1.1 (FBA) 3.3 (Br) 2.1 (Li <sup>+</sup> ) <sup>a</sup>	1.4 (FBA) 4.1 (Br) 2.6 (Li <sup>+</sup> ) <sup>a</sup>	1.3 (FBA) 3.9 (Br) 2.5 (Li <sup>+</sup> ) <sup>a</sup>
Lithium matrix retardation coefficient <sup>b</sup>	3	3	3	3
Lithium matrix K <sub>D</sub> (L kg <sup>-1</sup> ) <sup>c</sup>	0.28	0.28	0.28	0.28

<sup>a</sup>Assumed to be two-thirds the bromide matrix diffusivity.

<sup>b</sup>Obtained from RELAP fit to rising portion of breakthrough curve.

<sup>c</sup>Calculated from the retardation coefficient using equation (5.3).

Table 7-5. Summary of experimental and numerically deduced parameters from the second PFBA/LiBr test (1998) in the upper Prow Pass fractured core (16.1 cm long by 9.5 cm diameter). (DTN LAPR831231AQ98.001 and DTN LAPR831231AN99.002).

Parameter	PFBA/LiBr Test
	Experimental Parameters
Hydraulic aperture (cm)	0.0141
Injection flow rate (mL/hr)	6.33
Injection duration (hr)	11.21
Injection concentration (mg/L)	766 (PFBA) 2528 (Br) 216 (Li <sup>+</sup> )
Flush flow rate (mL/hr)	6.42
Flow interruption, hrs into test (duration, hr)	43.58 (20.00)
	Modeling Best-fit Parameters
Mean fluid residence time (hr)	3.00
Average fracture aperture (cm)	0.100
Peclet number	6.5
Dispersivity (cm)	2.5
Matrix diffusion coefficient ( $\times 10^{-6}$ cm <sup>2</sup> s <sup>-1</sup> )	1.60 (PFBA) 4.80 (Br) 3.20 (Li <sup>+</sup> ) <sup>a</sup>
Lithium matrix retardation coefficient <sup>b</sup>	0.05
Lithium matrix K <sub>D</sub> (L kg <sup>-1</sup> ) <sup>c</sup>	1.35

<sup>a</sup>Assumed to be two-thirds the bromide matrix diffusivity.

<sup>b</sup>Parameter estimated in RETRAN corresponding to batch sorption data.

<sup>c</sup>Calculated from the retardation coefficient using equation (5.3).

Table 7-6. Summary of experimental and numerically deduced parameters from the NaI tests in the central Prow Pass fractured core (17.3 cm long by 9.5 cm diameter). (DTN LAPR831231AQ98.001 and DTN LAPR831231AN99.002).

Parameter	First I Test	Second I Test	Third I Test
<b>Experimental Parameters</b>			
Hydraulic aperture (cm)	0.0134	0.0134	0.0134
Injection flow rate (mL/hr)	19.73	49.44	11.48
Injection duration (hr)	4.09	1.56	6.37
Injection concentration (mg/L)	1000.	1000.	1000.
Flush flow rate (mL/hr)	20.07	49.60	11.78
Flow interruption, hrs into test (duration, hr)	None	None	None
<b>Modeling Best-fit Parameters</b>			
Mean fluid residence time (hr)	0.55	0.22	0.95
Average fracture aperture (cm)	0.066	0.066	0.066
Peclet number	31.	31.	31.
Dispersivity (cm)	0.56	0.56	0.56
Matrix diffusion coefficient ( $\times 10^{-6}$ $\text{cm}^2 \text{s}^{-1}$ )	2.60	2.60	2.60

Table 7-7. Summary of experimental and numerically deduced parameters from the PFBA/LiBr test in the central Prow Pass fractured core (17.3 cm long by 9.5 cm diameter). (DTN LAPR831231AQ98.001 and DTN LAPR831231AQ99.002).

<i>Parameter</i>	<i>PFBA/LiBr Test</i>
	<b>Experimental Parameters</b>
Hydraulic aperture (cm)	0.0134
Injection flow rate (mL/hr)	5.92
Injection duration (hr)	11.97
	766 (PFBA)
Injection concentration (mg/L)	2528 (Br <sup>-</sup> ) 216 (Li <sup>+</sup> )
Flush flow rate (mL/hr)	5.98
Flow interruption, hrs into test (duration, hr)	42.60 (20.00)
	<b>Modeling Best-fit Parameters</b>
Mean fluid residence time (hr)	1.89
Average fracture aperture (cm)	0.068
Peclet number	28.
Dispersivity (cm)	0.62
	0.60 (PFBA)
Matrix diffusion coefficient ( $\times 10^{-6}$ cm <sup>2</sup> s <sup>-1</sup> )	1.80 (Br <sup>-</sup> ) 1.07 (Li <sup>+</sup> ) <sup>a</sup>
Lithium matrix retardation coefficient <sup>b</sup>	4.5
Lithium matrix K <sub>D</sub> (L kg <sup>-1</sup> ) <sup>c</sup>	0.25

<sup>a</sup>Assumed to be two-thirds the bromide matrix diffusivity.

<sup>b</sup>Parameter estimated in RETRAN corresponding to batch sorption data.

<sup>c</sup>Calculated from the retardation coefficient using equation (5.3).

## Section 7.0 Figures

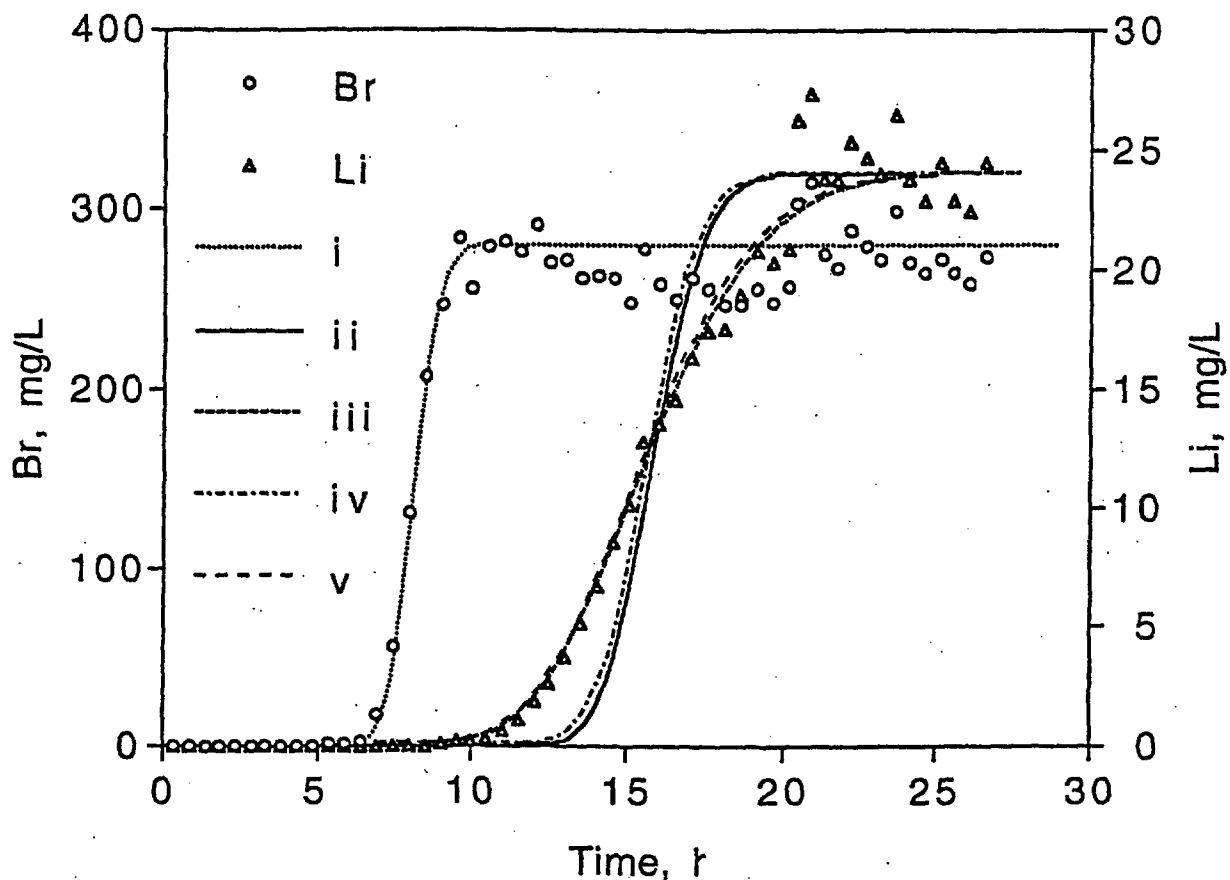


Figure 7-1. Bromide and lithium breakthrough curves in Column 1 at a flow rate of 2.2 mL/hr, and corresponding fits to data. (i) Fit to bromide data with a Peclet number of 300, (ii) fit to lithium data assuming linear isotherm ( $R_F = 2.0$ ) with equilibrium sorption, (iii) fit to lithium data assuming linear isotherm with a forward rate constant of  $2.2 \text{ h}^{-1}$ , (iv) fit to lithium data assuming a Langmuir isotherm with equilibrium sorption, and (v) fit to lithium data assuming a Langmuir isotherm with a forward rate constant of  $2.2 \text{ h}^{-1}$ . Langmuir isotherm parameters:  $K_L = 0.0053 \text{ mL}/\mu\text{g}$  and  $S_{max} = 110 \mu\text{g/g}$  (batch isotherm values obtained for lithium on central Bullfrog Tuff from C#2). (DTN LAPR831231AQ98.001 and DTN LAPR831231AN99.001).

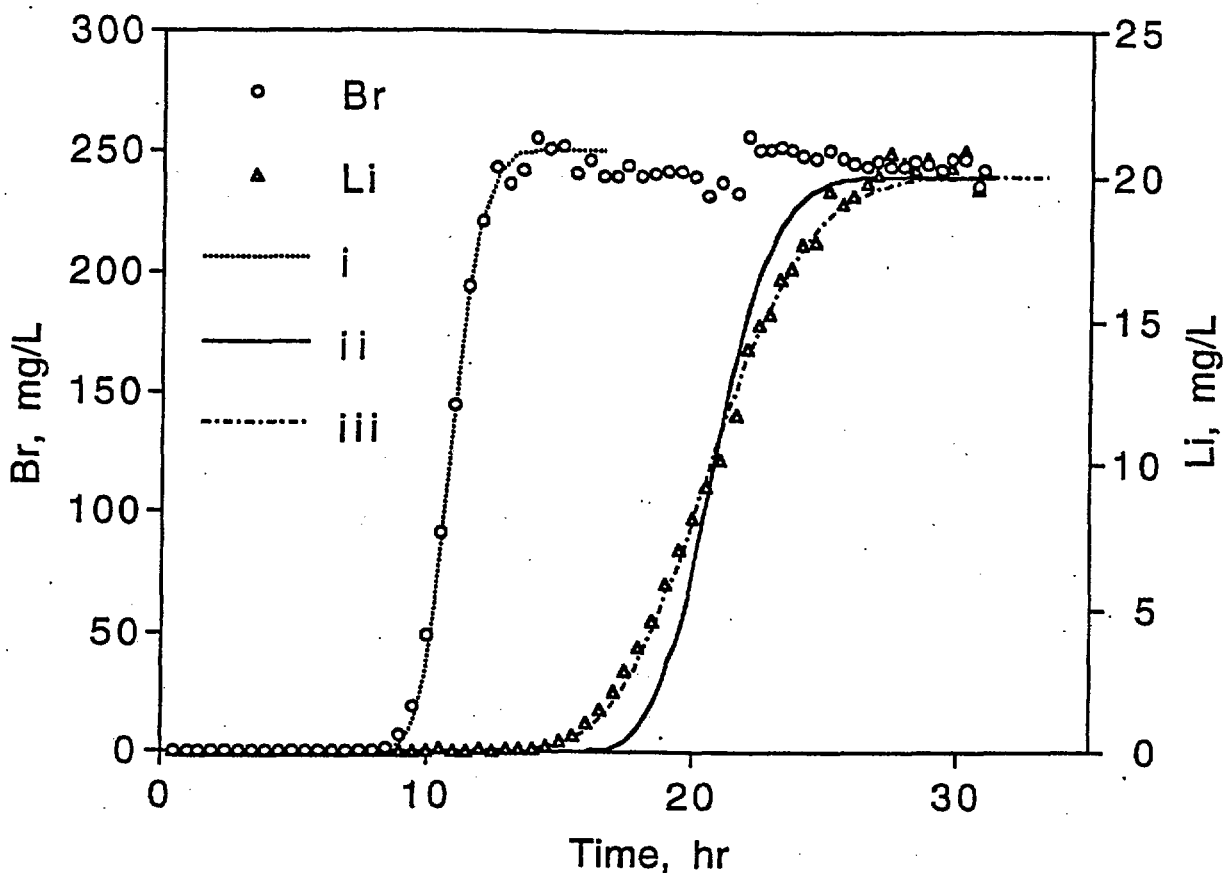


Figure 7-2. Bromide and lithium breakthrough curves in Column 1 at a flow rate of 1.6 mL/hr, and corresponding fits to data. (i) Fit to bromide data with a Peclet number of 300, (ii) fit to lithium data assuming linear isotherm ( $R_F = 1.9$ ) with equilibrium sorption, and (iii) fit to lithium data assuming linear isotherm with a forward rate constant of  $3.6 \text{ h}^{-1}$ . (DTN LAPR831231AQ98.001 and DTN LAPR831231AN99.001).

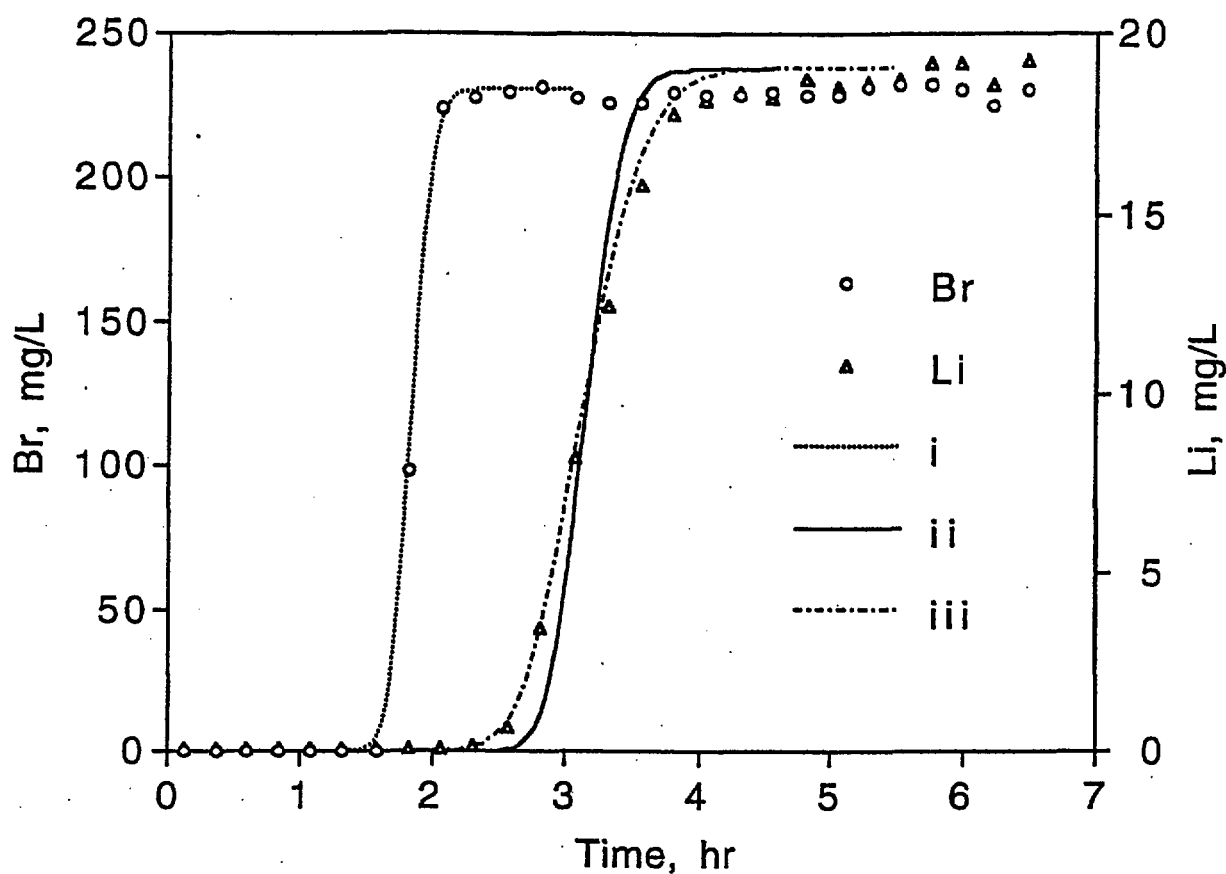


Figure 7-3. Bromide and lithium breakthrough curves in Column 2 at a flow rate of 9.7 mL/hr, and corresponding fits to data. (i) Fit to bromide data with a Peclet number of 400, (ii) fit to lithium data assuming linear isotherm ( $R_F = 1.7$ ) with equilibrium sorption, and (iii) fit to lithium data assuming linear isotherm with a forward rate constant of  $14 \text{ h}^{-1}$ . (DTN LAPR831231AQ98.001 and DTN LAPR831231AN99.001).

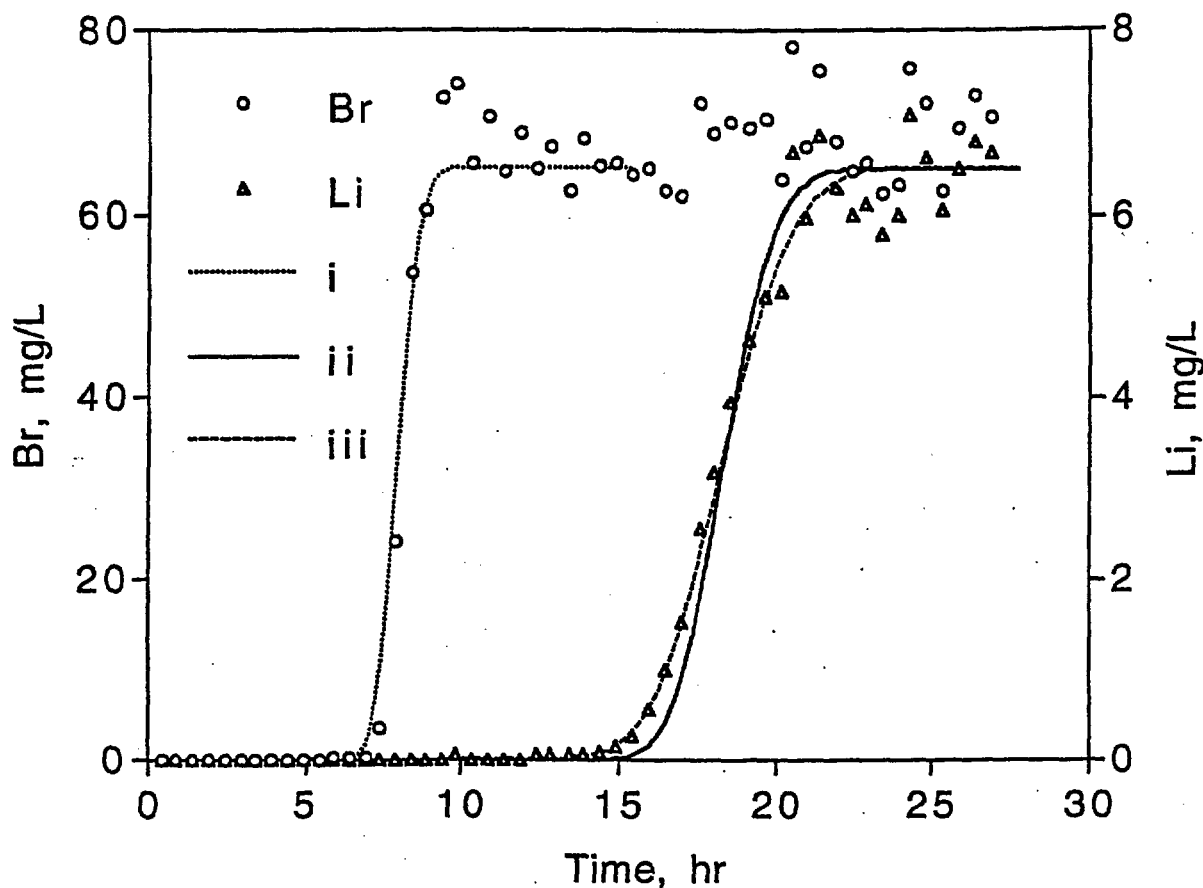


Figure 7-4. Bromide and lithium breakthrough curves in Column 3 at a flow rate of 2.2 mL/hr, and corresponding fits to data. (i) Fit to bromide data with a Peclet number of 400, (ii) fit to lithium data assuming linear isotherm ( $R_F = 2.3$ ) with equilibrium sorption, and (iii) fit to lithium data assuming linear isotherm with a forward rate constant of  $18 \text{ h}^{-1}$ . (DTN LAPR831231AQ98.001 and DTN LAPR831231AN99.001).

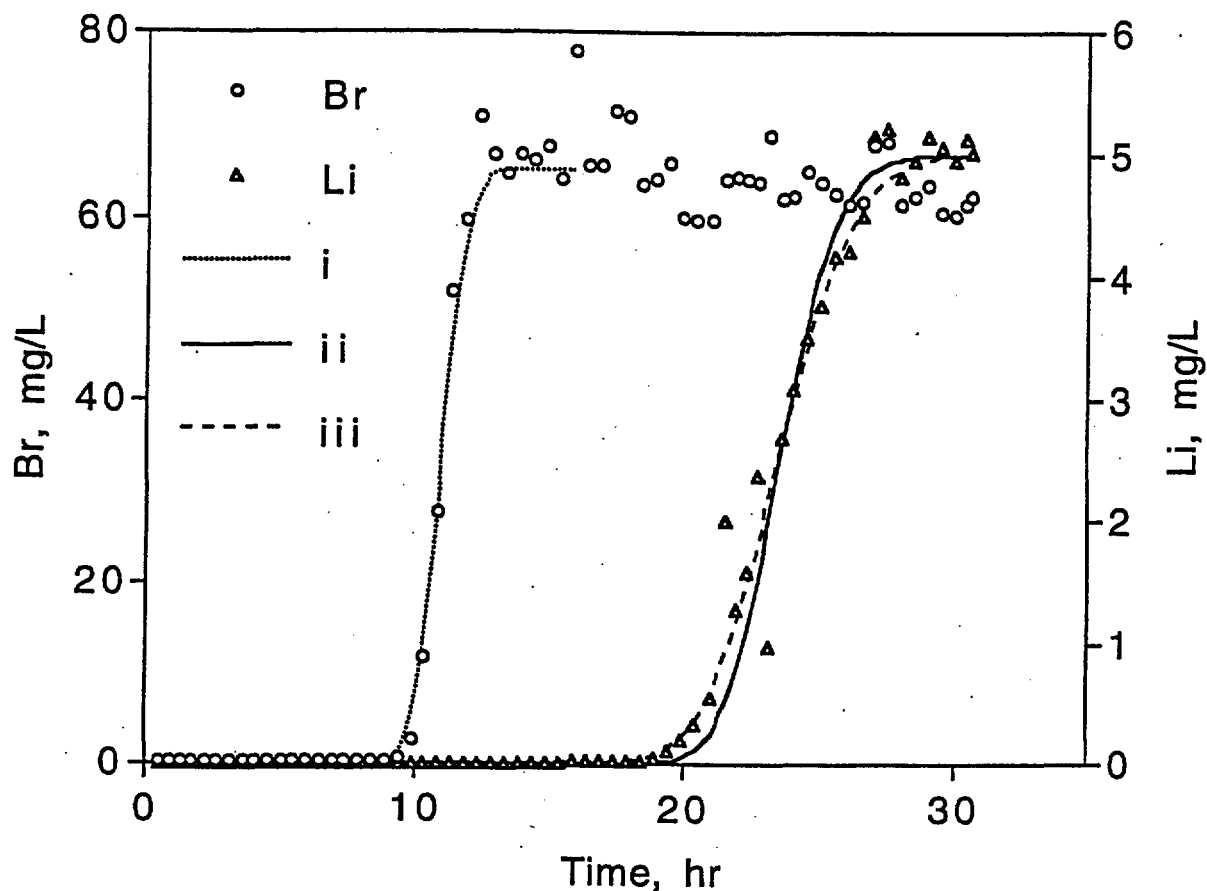
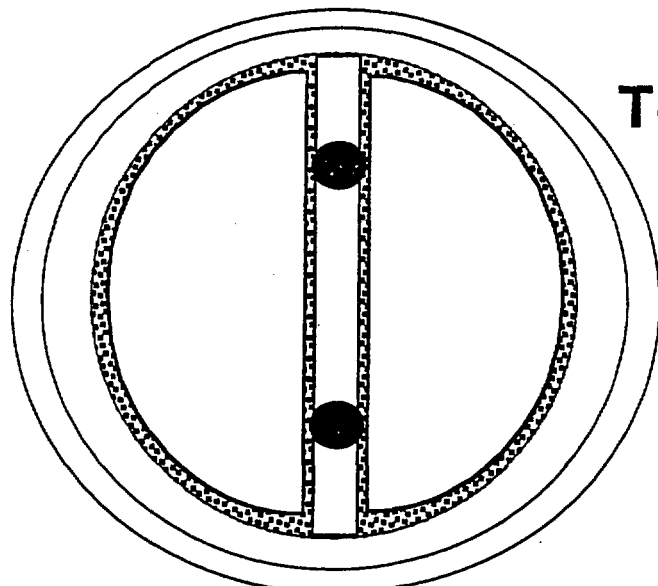
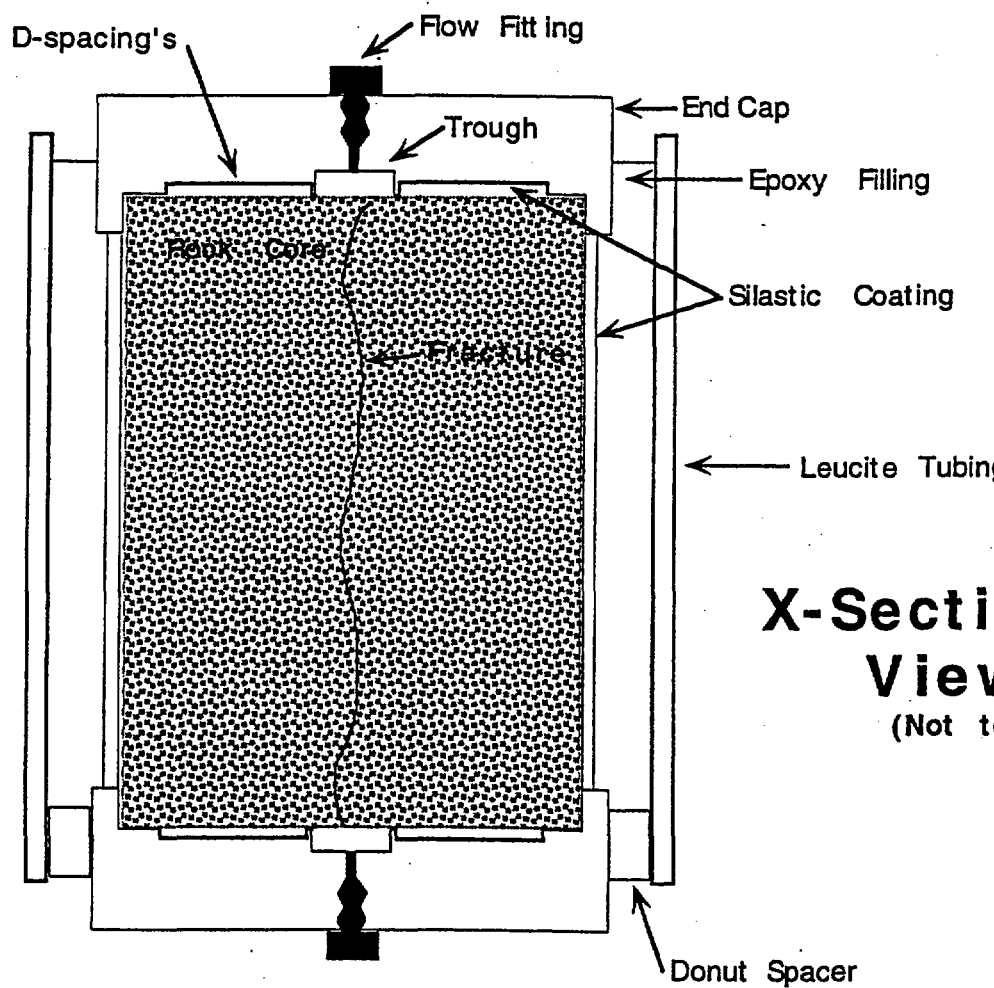


Figure 7-5. Bromide and lithium breakthrough curves in Column 3 at a flow rate of 1.6 mL/hr, and corresponding fits to data. (i) Fit to bromide data with a Peclet number of 400, (ii) fit to lithium data assuming linear isotherm ( $R_F = 2.2$ ) with equilibrium sorption, and (iii) fit to lithium data assuming linear isotherm with a forward rate constant of  $14 \text{ h}^{-1}$ . (DTN LAPR831231AQ98.001 and DTN LAPR831231AN99.001).



**Top View**  
(Not to Scale)



**X-Sectional  
View**  
(Not to Scale)

Figure 7-6. Schematic drawing of fractured core column apparatus.

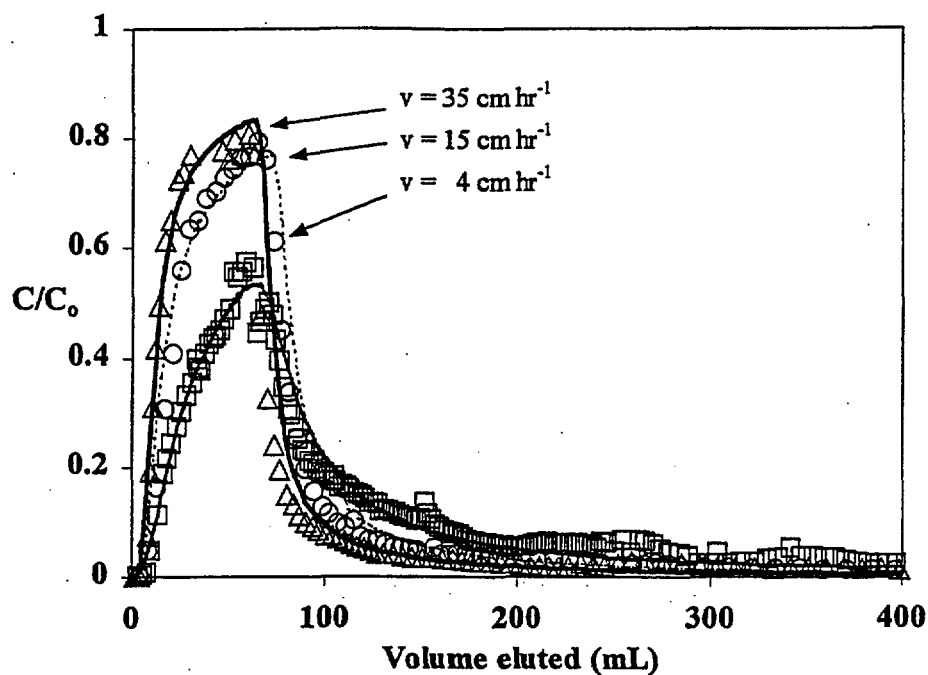


Fig. 7-7. Breakthrough curves and RETRAN fits for the NaI tests in the upper flow zone fractured core sample of the Prow Pass Tuff. (DTN LAPR831231AQ98.001 and DTN LAPR831231AQ99.002).

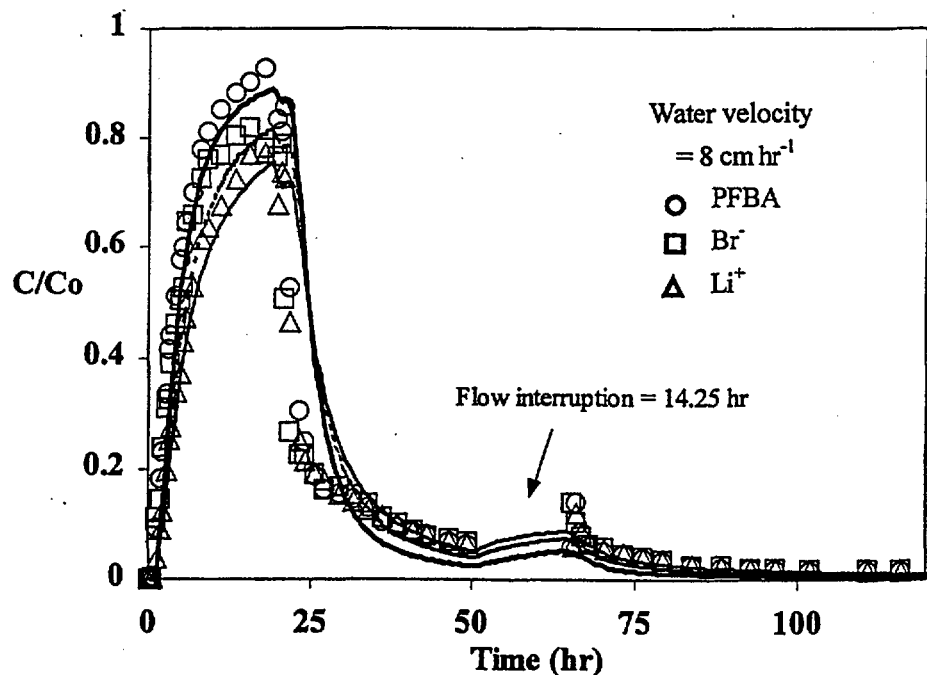


Fig. 7-8. Breakthrough curves and RETRAN fits for the first PFBA/LiBr test in the upper flow zone fractured core sample of the Prow Pass Tuff. (DTN LAPR831231AQ98.001 and DTN LAPR831231AQ99.002).

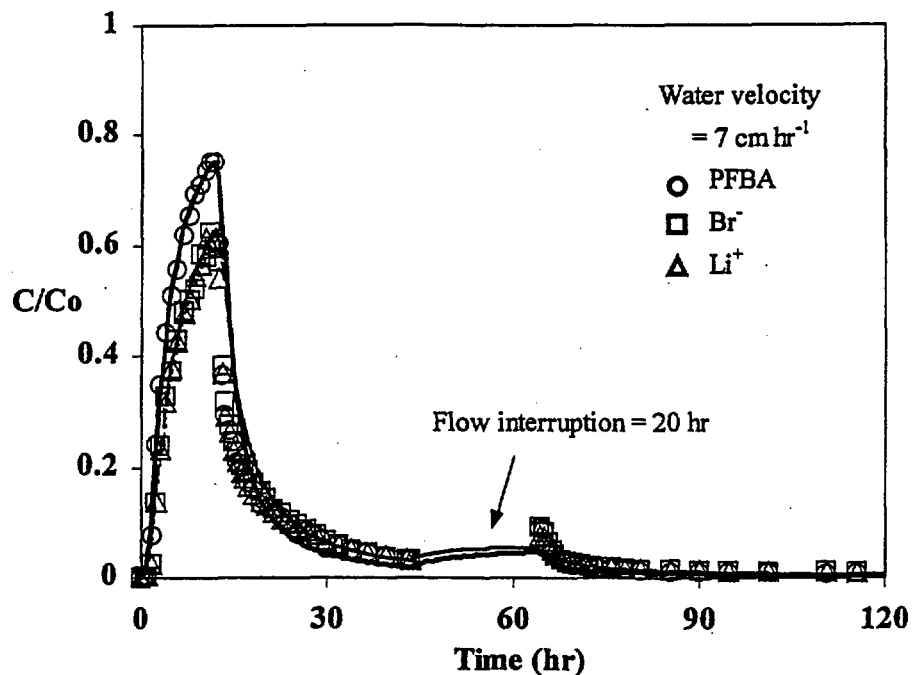


Fig. 7-9. Breakthrough curves and RETRAN fits for the second PFBA/LiBr test in the upper flow zone fractured core sample of the Prow Pass Tuff. (DTN LAPR831231AQ98.001 and DTN LAPR831231AQ99.002).

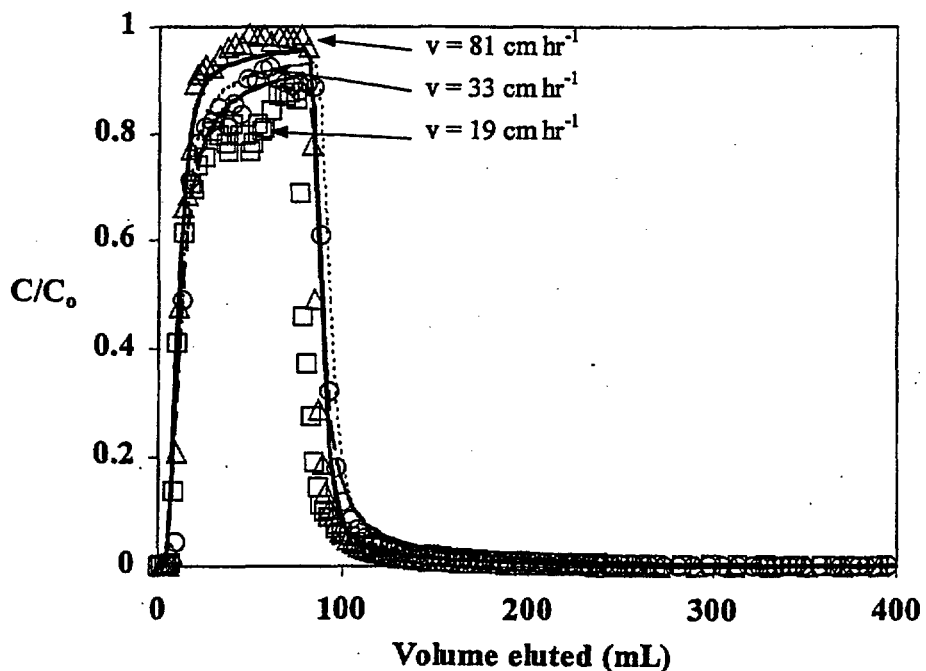


Fig. 7-10. Breakthrough curves and RETRAN fits for the NaI tests in the central flow zone fractured core sample of the Prow Pass Tuff. (DTN LAPR831231AQ98.001 and DTN LAPR831231AQ99.002).

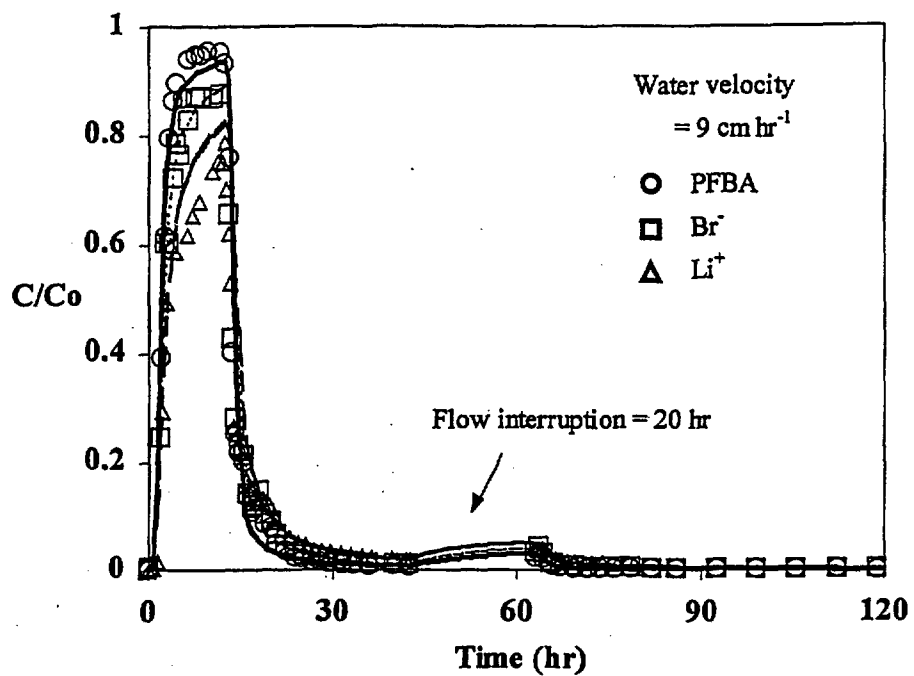


Fig. 7-11. Breakthrough curves and RETRAN fits for the PFBA/LiBr test in the central flow zone fractured core sample of the Prow Pass Tuff. (DTN LAPR831231AQ98.001 and DTN LAPR831231AQ99.002).

## 8.0 Diffusion Cell Experiments

### 8.1 Materials and Methods

Six diffusion cell experiments were conducted to determine diffusion coefficients of PFBA and bromide ion in five different C-holes tuff matrices. Estimates of matrix diffusion coefficients are important because they can greatly reduce uncertainty in interpreting and predicting both field-scale and laboratory-scale tracer experiments. One of the tests was a repeat experiment using a different core from the same interval as another test (the lower Prow Pass Tuff). This test was conducted to determine the reproducibility and variability of the experiments. The five different intervals tested in the diffusion cell experiments represented all of the major lithologies in either the previously-conducted Bullfrog field tracer test or the upcoming Prow Pass reactive tracer test.

A schematic drawing of the experimental diffusion cell apparatus is illustrated in Fig. 8-1. The apparatus consists of two plexiglass reservoirs, one large and one small, separated by a "pellet" of tuff, which is cut/cored from C-holes core and incorporated into either a flat epoxy cast or an RTV silicone cast of the same thickness as the pellet. After saturating the tuff, experiments were initiated by carefully pouring a solution containing PFBA and LiBr into the large reservoir and tracer-free solution into the small reservoir. The pressures in the two reservoirs were kept approximately equal to minimize advective flow through the tuff, thus ensuring that tracer movement through the tuff was by diffusion only. The small reservoir was kept well mixed with a magnetic stir bar and flushed continuously at a relatively low flow rate. The flush water was collected in an automatic fraction collector, and fractions were analyzed for tracers to establish breakthrough curves through the tuff from which diffusion coefficients could be estimated. As in the other laboratory experiments, PFBA and bromide were analyzed by ion chromatography, and lithium was analyzed by inductively-coupled plasma-atomic emission spectrometry (ICP-AES). Filtered J-13 water or synthetic J-13 water (a sodium/calcium bicarbonate solution having the same ionic strength as J-13 water) were used in all experiments.

The porosities of the tuffs were measured by subtracting dry weights from saturated weights of intact tuff samples and dividing by the volumes of the samples (measured by water displacement). Porosity measurements were used to obtain unambiguous estimates of diffusion coefficients in the tuff matrices (see equations below). Hydraulic conductivities/permeabilities of the tuffs were also measured by imposing a known pressure difference across the tuff pellets either before or after a diffusion experiment was conducted. The flow through the pellets at the imposed pressure difference was measured by weighing the water that flowed through the pellet over a specified amount of time. Hydraulic conductivities were then calculated from the following equation:

$$K = -\frac{Q L}{A \Delta H} \quad (8.1)$$

where,  $K$  = hydraulic conductivity, cm/sec

$\Delta H$  = water height (head) difference across pellet, cm

$A$  = surface area of pellet,  $\text{cm}^2$

$Q$  = volumetric flow rate through pellet, ml/sec  
 $L$  = thickness of pellet, cm.

Permeabilities (in millidarcys) were calculated from hydraulic conductivities using the following well-known formula (Freeze and Cherry, 1979, pp. 26-30)

$$k = \left( 1.013 \times 10^{11} \frac{mD}{cm^2} \right) \frac{K \mu}{\rho g} \quad (8.2)$$

where,  $k$  = permeability, millidarcys  
 $\mu$  = water viscosity, g/cm-sec  
 $\rho$  = water density, g/cm<sup>3</sup>  
 $g$  = acceleration due to gravity, cm/sec<sup>2</sup>.

To estimate diffusion coefficients, it was assumed that the tracers moved according to one-dimensional diffusive transport through the tuff pellets. The one-dimensional diffusion equation is:

$$\frac{\partial c}{\partial t} = \frac{D}{R} \frac{\partial^2 c}{\partial x^2} \quad (8.3)$$

where,  $c$  = tracer concentration,  $\mu\text{g/mL}$   
 $D$  = diffusion coefficient,  $\text{cm}^2/\text{sec}$   
 $R$  = retardation factor (1 for nonsorbing solutes),  
 $x$  = distance, cm  
 $t$  = time, sec.

Although analytical solutions to this simple partial differential equation exist for simple boundary conditions (Jenson and Jeffreys 1977, pp. 291-295), the time-dependent concentration boundary conditions at the inlet and outlet reservoirs in the diffusion cell experiments demand a numerical solution. Thus, equation (8.3) was solved using an implicit finite-difference technique. The equations describing the tracer concentrations in the inlet and the outlet reservoirs (the first and last finite difference nodes), respectively, were:

$$\frac{\partial c_i}{\partial t} = \frac{\phi \pi r^2 D}{V_i} \frac{\partial c}{\partial x} \Big|_{x=0} \quad (8.4)$$

$$\frac{\partial c_o}{\partial t} = - \frac{\phi \pi r^2 D}{V_o} \frac{\partial c}{\partial x} \Big|_{x=L} - \frac{Q}{V_o} c_o \quad (8.5)$$

where,  $c_i$  = tracer concentration in inlet reservoir,  $\mu\text{g/mL}$   
 $c_o$  = tracer concentration in outlet reservoir,  $\mu\text{g/mL}$   
 $V_i$  = volume of inlet reservoir, mL

$V_o$  = volume of outlet reservoir, mL  
 $Q$  = flush rate of outlet reservoir, mL/sec  
 $\phi$  = porosity of tuff  
 $r$  = radius of tuff "pellet", cm  
 $L$  = thickness of tuff "pellet", cm.

The numerical solution of equations (8.3), (8.4), and (8.5) was obtained using a modified version of the RETRAN computer code called DIFCEL. DIFCEL allows the user to specify changes in the flush rate,  $Q$ , with time, which was necessary to simulate the manner in which the experiments were conducted.

## 8.2 Results and Discussion

Figs. 8-2 through 8-7 show the breakthrough curves of the bromide and PFBA in each of the six diffusion cells along with "fits" to the data obtained using DIFCEL. The "fits" are not actual least-squares fits; rather, they were obtained by manual adjustment of the diffusion coefficients until a reasonable match to the data was obtained. The apparent discontinuities in some of the data sets and the corresponding model predictions are a consequence of changes in the flush rate through the outlet reservoirs. A decrease in concentration occurs when the flush rate is increased and vice-versa.

The resulting estimates of tracer diffusion coefficients in each diffusion cell are given in Table 8-1 (measured tuff porosities, pellet thicknesses, and tuff permeabilities are also listed in this table). It is apparent that there is about an order of magnitude range of diffusion coefficients in the various tuff lithologies. Figs. 8-8 and 8-9 show the bromide diffusion coefficients in the tuff matrices as a function of porosity and permeability, respectively, for the five different C-holes tuffs. Although the diffusion coefficients are not well correlated with porosity, they are quite well correlated with permeability (on a log-log scale). This result suggests that permeability may be a good predictor of matrix diffusion coefficients. Such correlations could prove useful for estimating matrix diffusion coefficients, as diffusion coefficients are typically more difficult to measure than matrix properties such as permeabilities.

Table 8-1 shows that excellent agreement was obtained between the two diffusion cell experiments conducted in the same lithology (the lower Prow Pass Tuff). This result suggests that the experiments have reasonably good reproducibility, although certainly more experiments should be conducted in the same lithologies before measurement uncertainty and tuff variability can be properly assessed.

It is interesting that although the PFBA and bromide diffusion coefficients are significantly different in the different tuffs, the ratios of the diffusion coefficients are approximately the same in each tuff. This result suggests that we successfully eliminated advection through the tuff pellets, as any advection would result in different ratios in different tests. The factor of ~3 difference in the diffusion coefficients of the PFBA and bromide is greater than the factor of 2 difference assumed by Reimus and Turin (1997, p. 4) in their analyses of the Bullfrog Tuff reactive tracer field test data, which is one of the reasons the Bullfrog test data are reinterpreted in this report.

## References for Section 8.0

- Freeze, R. A. and J. A. Cherry. 1979. *Groundwater*. Englewood Cliffs, New Jersey: Prentice Hall, pp. 26-30. TIC Catalog #217571.
- Jenson, V. G., and G. V. Jeffreys. 1977. *Mathematical Models in Chemical Engineering*, 2nd ed., London, Academic Press, pp. 291-295. (Submitted to RIS for Accession # 5/21/99.)
- Reimus, P. W. and H. J. Turin. 1997. *Draft Report of Results of Hydraulic and Tracer Tests at the C-Holes Complex*. Yucca Mountain Site Characterization Project Milestone Report SP32APMD. Los Alamos, New Mexico: Los Alamos National Laboratory, p. 4. (Submitted to RIS for Accession # 5/ 21/ 99.)

## Section 8.0 Table

Table 8-1. Measured matrix diffusion coefficients of bromide and PFBA in C-holes tuffs. Measured tuff porosities and permeabilities are also reported. Synthetic J-13 water was used for the experiments involving the first 3 tuffs. Filtered J-13 water was used in the other 3 experiments. (DTN LAPR831231AQ98.001 and DTN LAPR831231AN99.001).

Tuff <sup>(1)</sup>	Porosity	Permeability,					Matrix Diff. Coef., cm <sup>2</sup> /s X 10 <sup>6</sup>
		mDarcy	L, cm <sup>(2)</sup>	Br	PFBA	Br/PFBA	
Central Bullfrog (1)	0.094	0.00107	1.16	0.45	0.13	3.46	
Lower Bullfrog (3)	0.298	0.0949	0.84	1.0	0.35	2.86	
Upper Prow (4)	0.272	4.72	0.91	6.0	1.9	3.16	
Central Prow (5)	0.138	0.000786	1.23	0.4	0.13	3.08	
Lower Prow-1 (6)	0.288	0.455	2.27	3.0	1.1	2.73	
Lower Prow-2 (6)	0.288	0.455	1.82	3.0	1.0	3.0	

<sup>(1)</sup>Numbers in parentheses correspond to numbers in Fig. 6-1 (which shows locations where core was collected from the C-holes) and in Table 6-2 (which lists actual depths associated with the cores).

<sup>(2)</sup>L = thickness of tuff wafer.

## Figures for Section 8.0

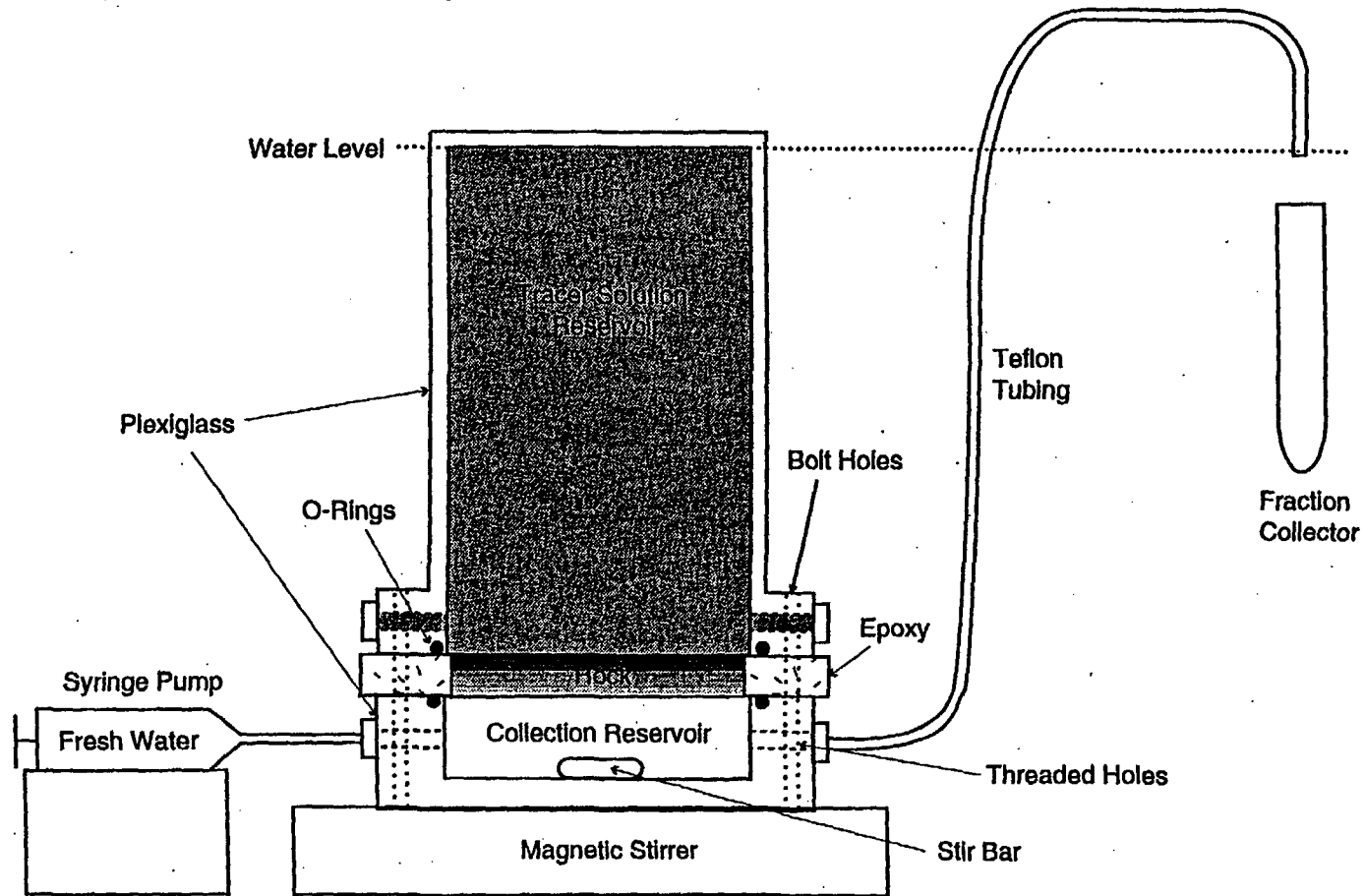


Figure 8-1. Schematic drawing of diffusion cell apparatus. Collection reservoir is continuously flushed by syringe pump, allowing automatic collection of samples. Diffusion cells were actually tipped on their sides in some experiments to avoid introducing pressure gradients (and hence advection) through the rock pellets.

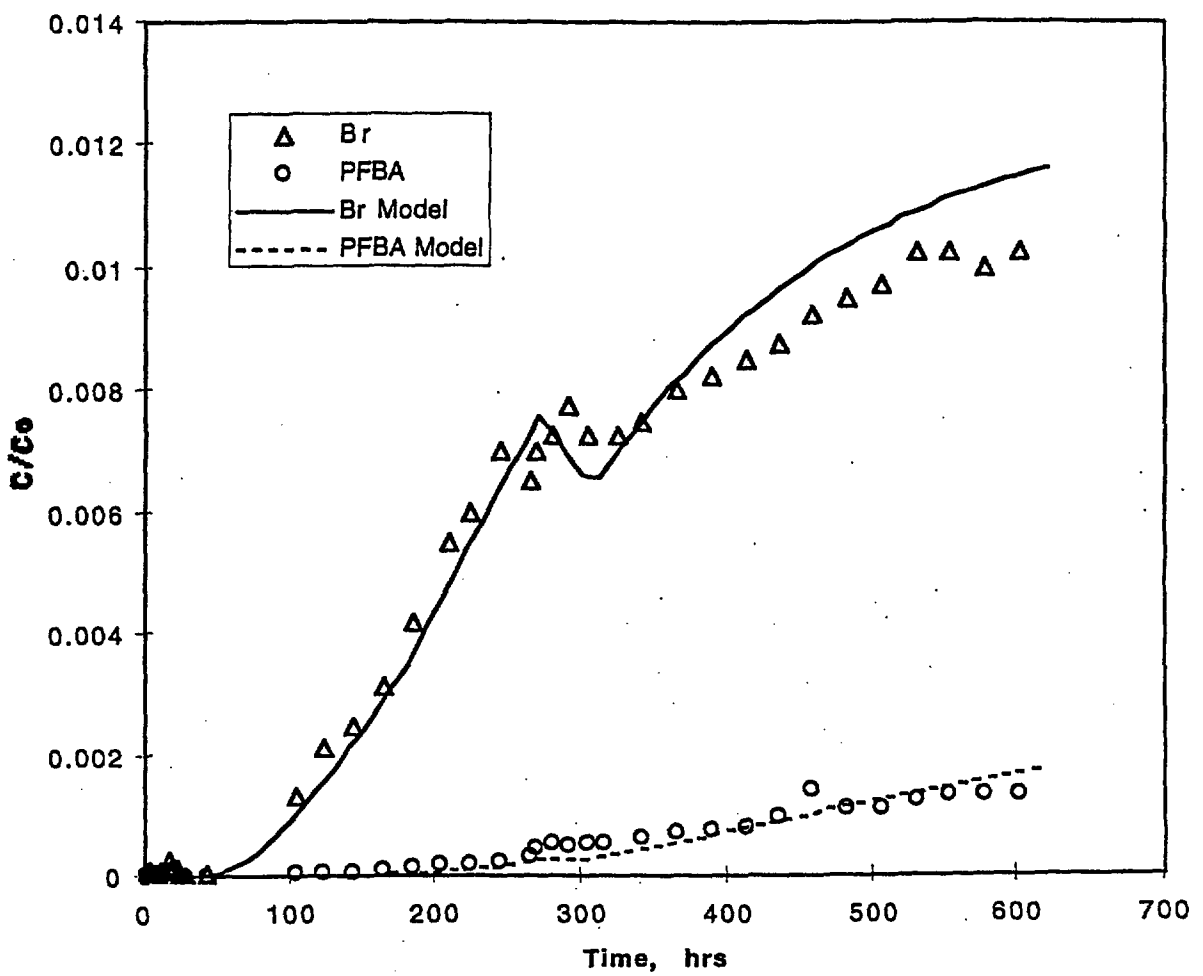


Figure 8-2. Diffusion cell data and DIFCEL model fits for bromide and PFBA in the central Bullfrog Tuff. Diffusion coefficients are given in Table 8-1. (DTN LAPR831231AQ98.001 and DTN LAPR831231AN99.001).

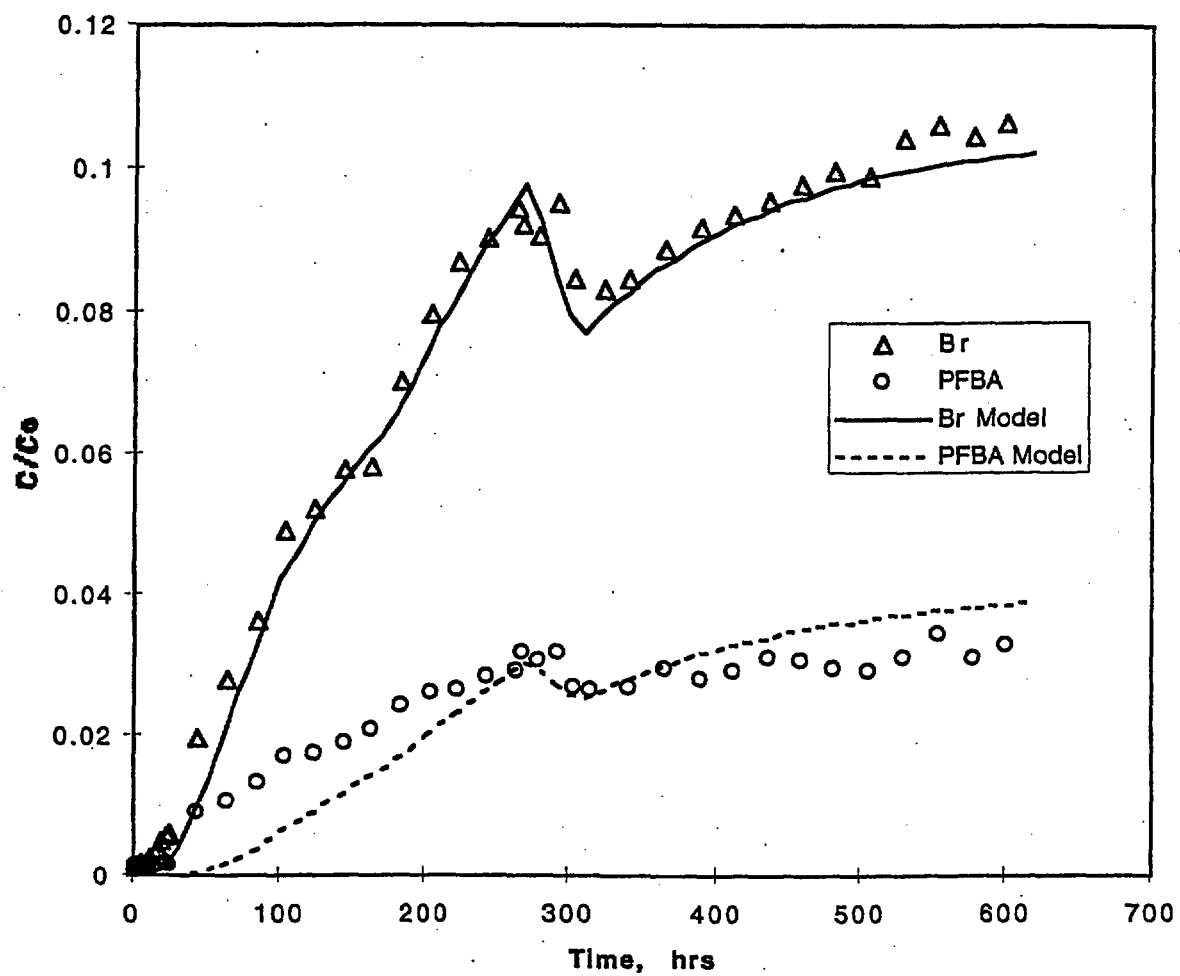


Figure 8-3. Diffusion cell data and DIFCEL model fits for bromide and PFBA in the lower Bullfrog Tuff. Diffusion coefficients are given in Table 8-1. (DTN LAPR831231AQ98.001 and DTN LAPR831231AN99.001).

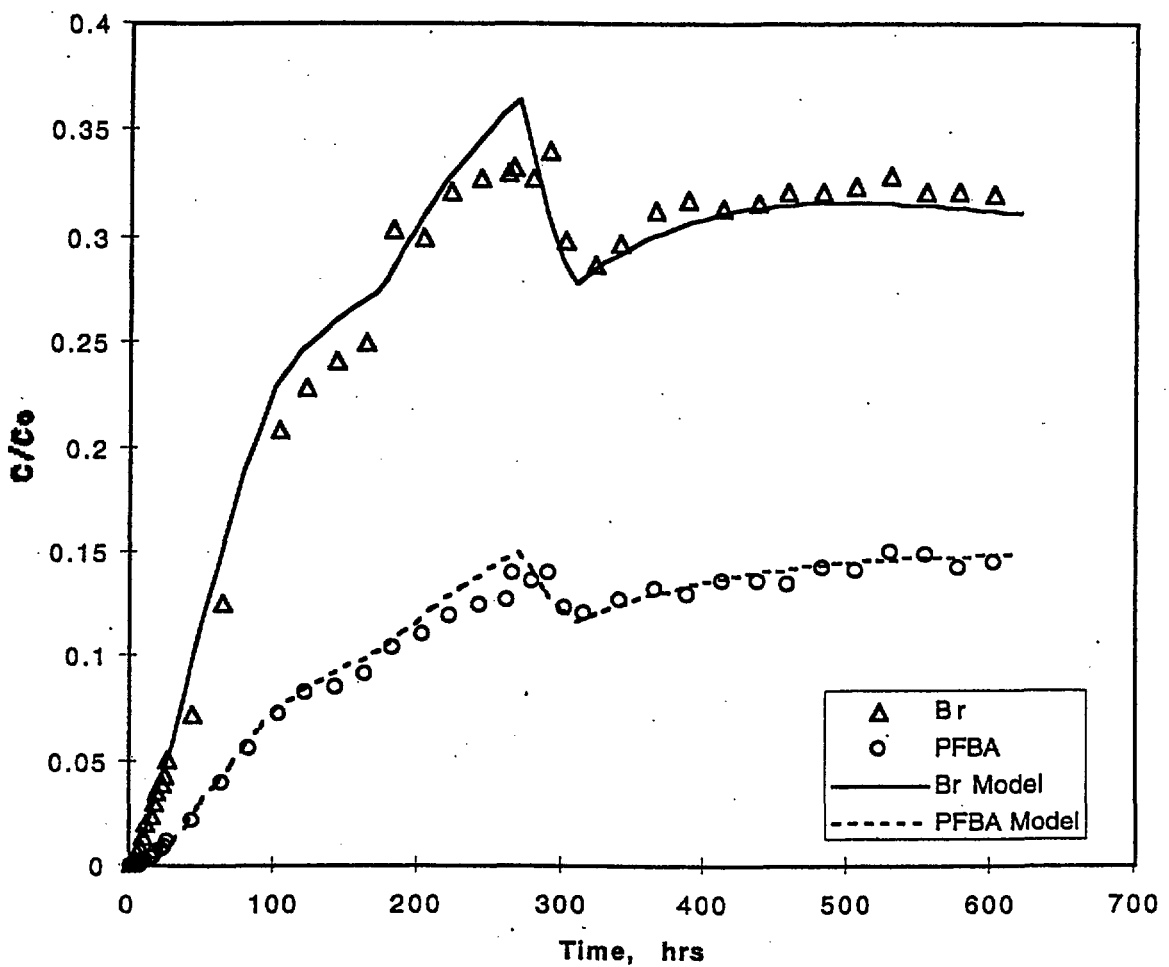


Figure 8-4. Diffusion cell data and DIFCEL model fits for bromide and PFBA in the upper Prow Pass Tuff. Diffusion coefficients are given in Table 8-1. (DTN LAPR831231AQ98.001 and DTN LAPR831231AN99.001).

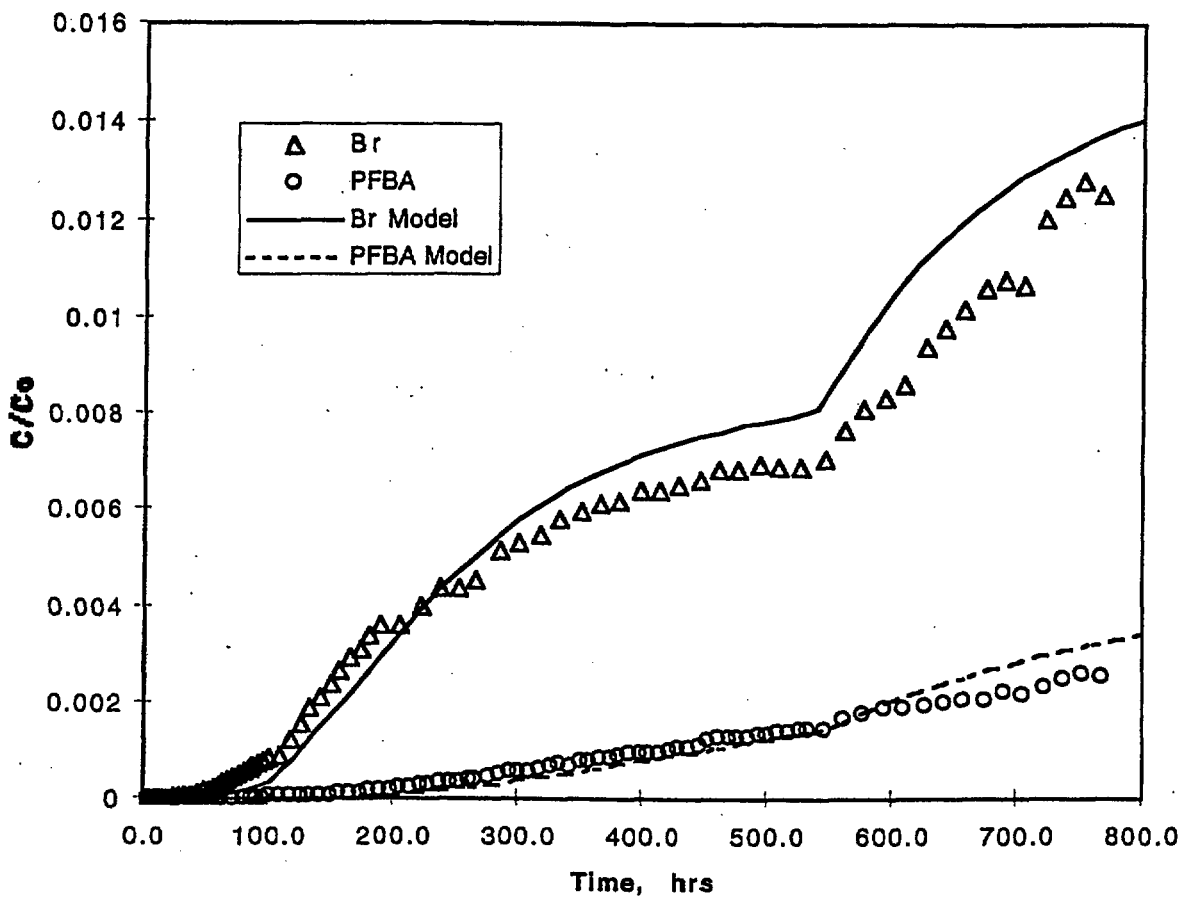


Figure 8-5. Diffusion cell data and DIFCEL model fits for bromide and PFBA in the central Prow Pass Tuff. Diffusion coefficients are given in Table 8-1. (DTN LAPR831231AQ98.001 and DTN LAPR831231AN99.001).

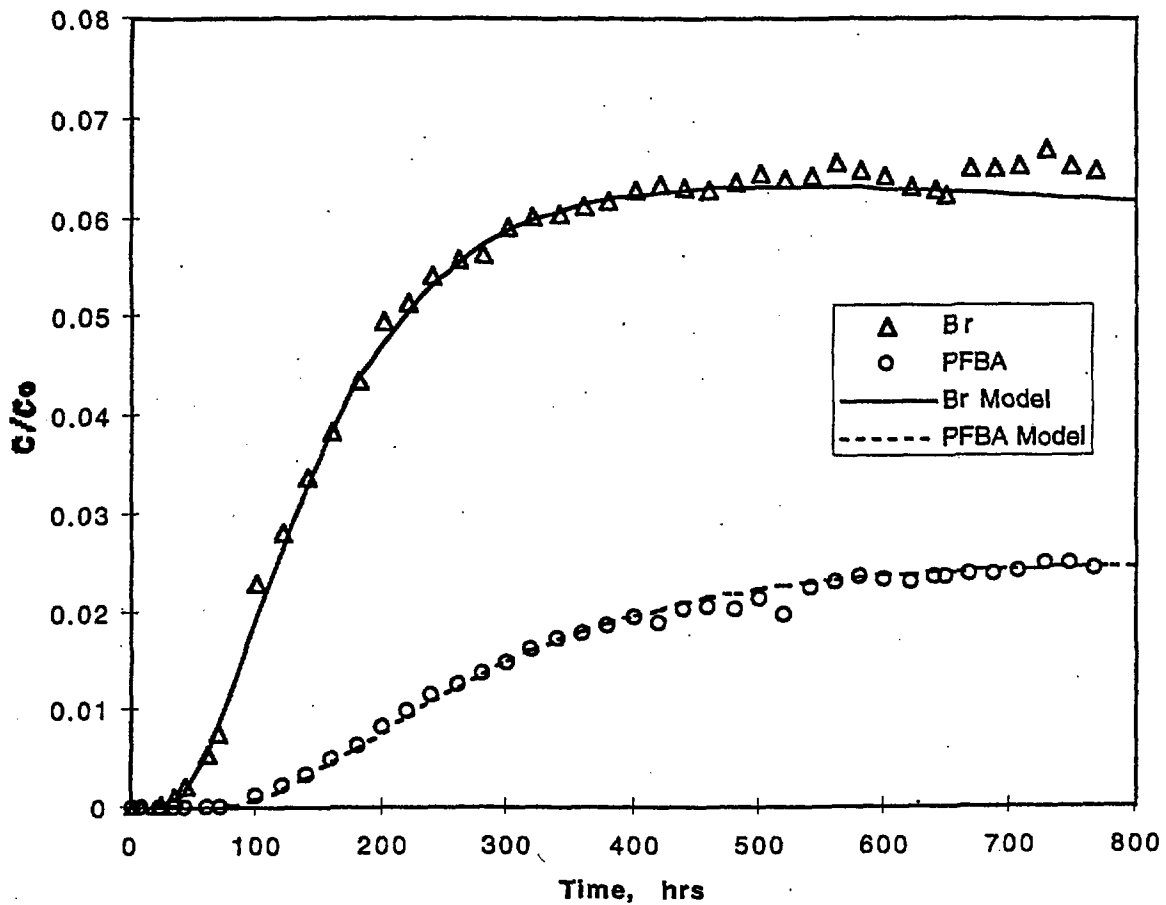


Figure 8-6. Diffusion cell data and DIFCEL model fits for bromide and PFBA in the lower Prow Pass Tuff (first diffusion cell). Diffusion coefficients are given in Table 8-1. (DTN LAPR831231AQ98.001 and DTN LAPR831231AN99.001).

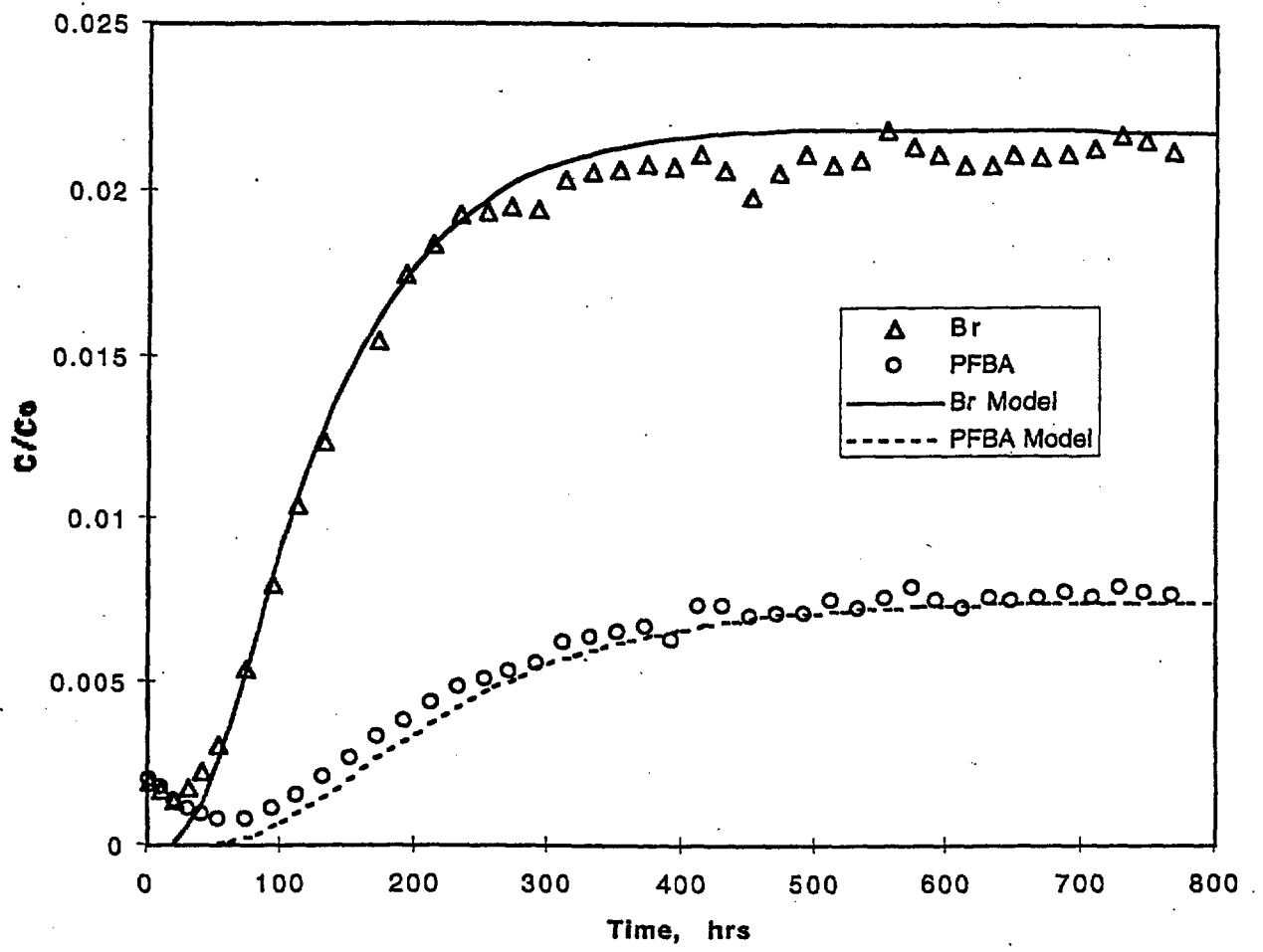


Figure 8-7. Diffusion cell data and DIFCEL model fits for bromide and PFBA in the lower Prow Pass Tuff (second diffusion cell). Diffusion coefficients are given in Table 8-1. (DTN LAPR831231AQ98.001 and DTN LAPR831231AN99.001).

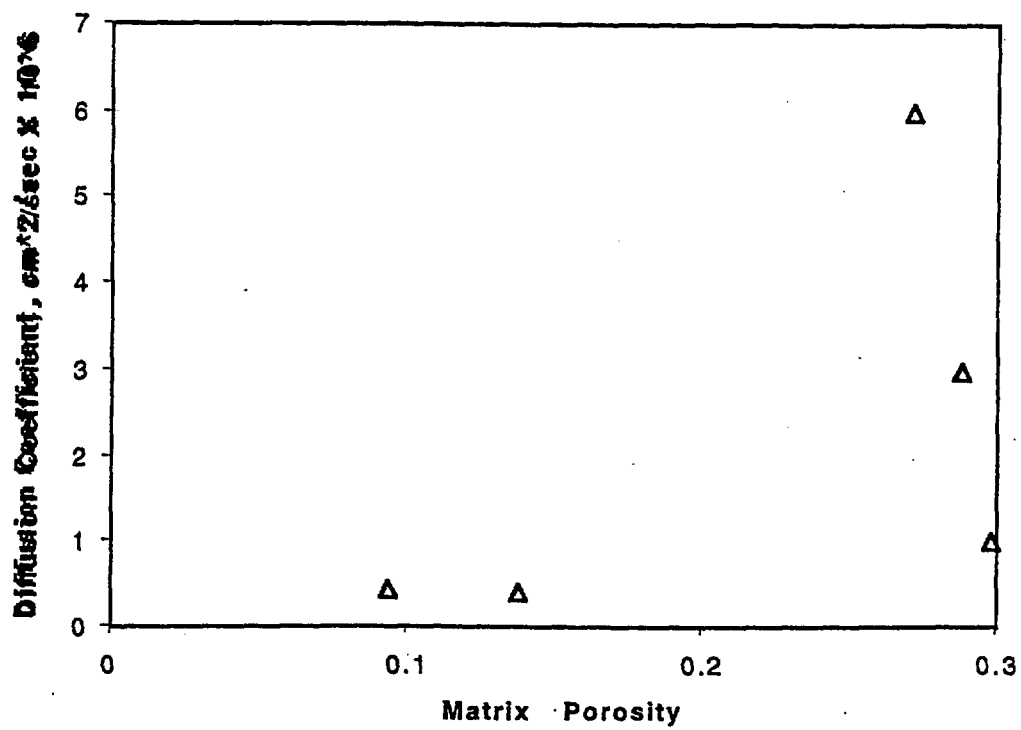


Figure 8-8. Bromide diffusion coefficients vs. tuff porosity for all diffusion cell experiments.  
(DTN LAPR831231AQ98.001).

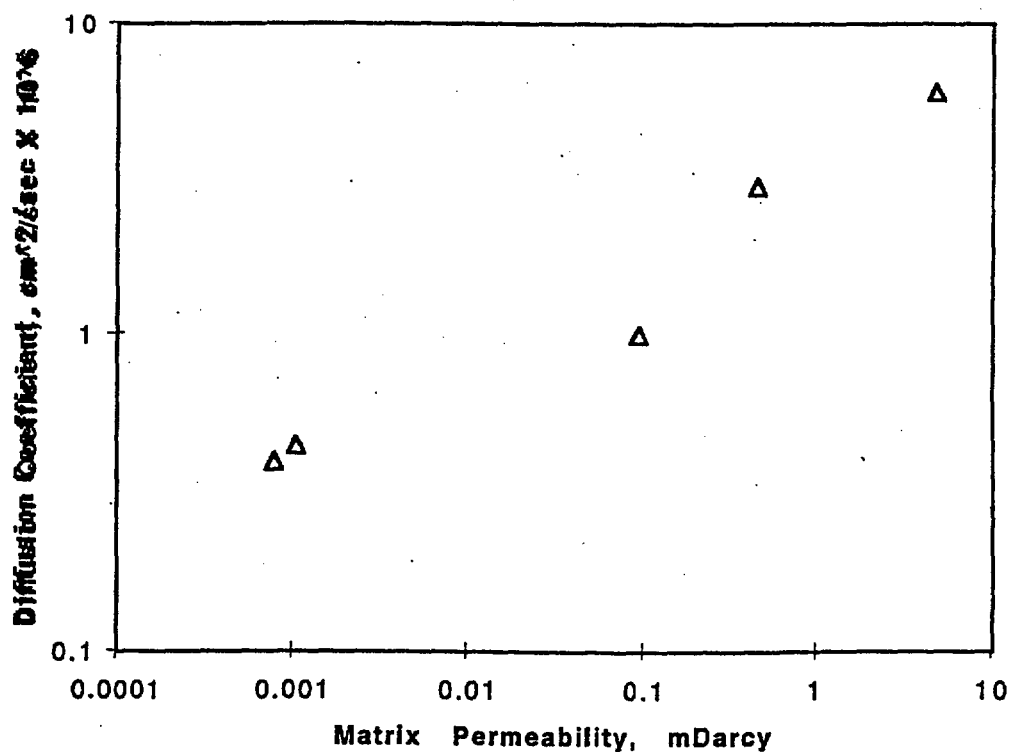


Figure 8-9. Bromide diffusion coefficients vs. tuff permeability for all diffusion cell experiments.  
(DTN LAPR831231AQ98.001).

## 9.0 Discussion of Differences in Conservative and Reactive Tracer Test Interpretations

The differences between the transport parameter estimates derived from the conservative and reactive tracer tests can be attributed to differences in both the approaches taken and the assumptions made in the analyses. The models themselves (the Moench model and the RELAP model) are very similar in that they both solve semi-analytically the dual-porosity transport equations using Laplace transform methods. For the exact same approach and same input assumptions, the two models should yield only slightly different parameter values (principally, mean residence times or flow porosities; dispersivities; and matrix diffusion parameters). Differences can be attributed to slight differences in the model equations and in the built-in matrix block geometry assumptions and boundary conditions in the two models (e.g., spherical matrix blocks vs. rectangular blocks). In a limited number of unreported test cases, the Moench and RELAP model predictions were in good agreement when input parameters were consistent.

For interpretation of the conservative tracer test, the Moench model was matched to the 2,4,5-TFBA and iodide breakthrough curves normalized to their peak concentrations (i.e., maximum normalized concentration was 1.0 for both tracers). With this type of normalization, only the shapes of the breakthrough curves are matched; the differences in peak concentrations and mass recoveries of different tracers are not used. This interpretive approach has been advocated by Moench (1989, 1995), and it works by analyzing the differences in the timing of the tracer peak concentrations and the time lags in the tails of the breakthrough curves to determine different tracer matrix diffusion characteristics. Because the breakthrough curves of the 2,4,5-TFBA and iodide are similar in shape and have almost the same peak arrival time, the responses of these tracers can be matched effectively assuming very little or no matrix diffusion (i.e., single-porosity solution or very low storage porosity). However, there is enough time lag in the falling limbs of the two normalized breakthrough curves to estimate a ratio of the matrix diffusion coefficients of the two tracers comparable to the ratio of their free-water diffusion coefficients.

In contrast, the interpretation of the reactive tracer test involved fitting the reactive tracer responses normalized to injection mass rather than peak concentration. With this type of normalization, the peak heights and mass recoveries of the tracers are significantly different, which forces the RELAP model to adjust matrix diffusion parameters to explain the differences. Although it is not straightforward to make direct comparisons between matrix diffusion parameters obtained from the Moench model and RELAP (because of different geometric assumptions and parameterizations), back-of-the-envelope calculations suggest that the matrix diffusion parameters used in the Moench model were generally much smaller than those obtained from RELAP fits (with the possible exception of the case of a storage porosity of 0.01 in the Moench model).

Significant differences in dispersivity estimates derived from the two tracer tests probably resulted from different assumptions made about injection wellbore mixing in the two tests. In both cases, the wellbores were assumed to be well-mixed volumes, but a much larger mean residence time was assumed in the injection wellbore for the conservative tracer test than in the reactive tracer test. The relatively large assumed mixing length (~30 m), combined with the implicit assumption in the Moench model that

tracers exit the injection well at a rate dictated by flow induced by pumping the production well, results in a long residence time assumption for the conservative tracer test analysis. Injection wellbore residence times that are long relative to tracer travel times in the formation can result in very long-tailed breakthrough curves even if there is not much dispersion in the formation (because of the slow exponential decay of tracer from the injection wellbore). The mean wellbore residence time associated with an assumed mixing length of ~30 m is calculated to be 514 hours, which is over a factor of two larger than the time to peak tracer concentrations. The fact that a 3-fold larger formation dispersivity was obtained from the Moench model when wellbore mixing was dramatically reduced (resulting in a 5-6 hr wellbore residence time) shows how the assumed wellbore residence time affects the solution. -The match in this case, employing the Moench single-porosity solution (no matrix diffusion), was only to the rising limb of the conservative tracer breakthrough curves because the shape of the rising limb is primarily affected by the longitudinal dispersivity and only minimally affected—if at all—by matrix diffusion. Although not reported here, the formation dispersivity increased more when the match of the single-porosity Moench solution was extended to include the tails of the breakthrough curves (to the point where it was approaching the reactive tracer test dispersivity estimates). However, when the single-porosity solution is matched to the entire curve, including the tail, the shape of the falling limb is attributed entirely to longitudinal dispersivity, even though matrix diffusion also affects the shape of the falling limb. It should be noted that large assumed wellbore residence times also tend to depress estimates of matrix diffusion (in addition to dispersivity) because wellbore mixing has the effect of adding dispersion to the predicted responses.

Relatively short wellbore residence times (~9 hr) were assumed in all reactive tracer test interpretations because the wellbore was assumed to be flushed quickly by the recirculation flow through the wellbore. When wellbore residence times are small compared to the tracer arrival times, the effect of wellbore mixing is minimized.

The foregoing discussion is not intended to endorse one analysis method or set of assumptions over another. To the contrary, the use of different methods and assumptions, provided they are reasonable, can yield valuable insights into parameter uncertainties. The fact that the wellbores were not actively mixed during the tracer tests, suggests that it is reasonable to assume large wellbore residence times to assess the impact of inefficient flushing of tracer from the injection borehole. The different modeling approaches involving different normalizations of tracer responses also provide insights into the sensitivities and uncertainties associated with analysis methodologies. Overall, it can be concluded that the different transport parameters obtained for the conservative and reactive tracer tests are consistent with the different approaches and assumptions made in the analyses.

## **10.0 Quality Assurance Status of Data and Interpretations**

All of the data presented in this report were acquired under Project-approved quality assurance procedures. Applicable data tracking numbers (DTNs) are noted in places where the data are presented (table and figure captions primarily). DTN numbers are summarized here as follows:

### **Q Data/Interpretations:**

Stratigraphic contacts in C-holes and locations of packers (Section 1.0 and Fig. 6-1):

DTN GS970708312314.007 and DTN GS990408312315.002.

Prow Pass Hydraulic Test Data, including Water Flow Rates (Section 3.0): DTN GS990408312315.002.

Prow Pass Conservative Tracer Test Data (Section 4.0): DTN GS9908312315.001

Prow Pass Reactive Tracer Test Data (Section 5.0): LAPR831231AQ99.001

All Laboratory Data and Bullfrog Reactive Tracer Test Data (Sections 6.0, 7.0, 8.0, and Appendix C): LAPR831231AQ98.001

Note: Although all laboratory data were acquired under appropriate QA procedures, the C-holes core used in all experiments is currently considered non-Q.

Interpretations of Bullfrog Reactive Tracer Test Data (Appendix C) and Interpretations of Fractured Column Test Data (Section 7.2): LAPR831231AQ99.002

Cation Exchange Capacity and XRD Mineralogy Data (Section 6.1):  
LAPR831231AQ99.003

### **Non-Q or Indeterminate Q Status Interpretations:**

Interpretations of Prow Pass Reactive Tracer Test Data (Section 5.0), Calculations of Sorption Isotherm Parameters (Section 6.0), Interpretations of Crushed Tuff Column Data (Section 7.1), Interpretations of May 1996 PFBA Bullfrog Test Data (Appendix C), Relationships between Radial and Linear Residence Times and Peclet Numbers (Fig. C-8), and Interpretations of Diffusion Cell Experiments (Section 8.0): DTN LAPR831231AN99.001

Interpretations of Prow Pass Hydraulic Test Data (Appendix A) and Prow Pass Conservative Tracer Test Data (Sections 4.0 and Appendix B): No DTNs assigned.

The interpretations of the hydraulic and tracer test data and the laboratory data were conducted using a combination of acquired and developed software. LABVIEW, a graphic-language software package created by National Instruments, Inc., was used to obtain pressure and flow

rate data during field tests and to record data to electronic files. The routine written for this purpose during hydraulic and tracer tests (TEST25.vi) was assigned USGS SID no. ESP 5.34.

Microsoft Excel 97 (USGS SID no. ESP 5.15) was used to convert data in LABVIEW-created files to forms that could be analyzed to calculate hydrologic properties. For example, pressures recorded in LABVIEW-created files were converted to drawdown. Conversions involved simple arithmetic, algebraic equations, or statistical functions (*e.g.*, averaging and linear regression).

Routines written with LABVIEW were used to calculate hydrologic properties from drawdown and water-level rise data. These routines are THEIS.vi (USGS SID no. ESP 5.35), STRLTSVA.vi (USGS SID no. 5.36), and NEUMAN.vi (USGS SID no. ESP 5.37).

The conservative tracer test interpretations were conducted using a FORTRAN code acquired from Allen Moench of the USGS, Menlo Park. This code was embedded within a LABVIEW routine that provided a user-friendly graphical interface and facilitated curve-matching by visual inspection of model output and tracer test data. Neither the FORTRAN code nor the LABVIEW routine are formally qualified for use in quality-affecting activities on the Yucca Mountain Site Characterization Project. As such, the conservative tracer test interpretations must be considered non-Q at this time.

Software input and output files associated with the interpretations of the hydraulic and conservative tracer test data have not been compiled into data packages, and data tracking numbers (DTNs) have not been assigned to these interpretations.

The reactive tracer test interpretations were conducted using the Reactive Transport Application (RELAP and RETRAN, LANL LC-195-146). This package was also used to interpret the laboratory crushed tuff and fractured core column data (Section 7.0). However, the laboratory crushed tuff column experiments were interpreted prior to qualification of the Reactive Transport Application, so the interpretation of these experiments must be considered non-Q. The same situation applies to the alternative interpretations of the May 1996 PFBA tracer test (Appendix C) and the relationships between radial and linear mean residence times and Peclet numbers (also Appendix C). For the Prow Pass field reactive tracer test interpretations, the RELAP code had to be modified slightly to properly account for recirculation (this modification wasn't necessary for the Bullfrog field test interpretations and the fractured column laboratory test interpretations because there was very little or no recirculation in those tests). Thus, the interpretations of the Prow Pass reactive tracer test must be considered non-Q at this time.

All processing of the raw reactive tracer test data (*i.e.*, converting raw concentrations into normalized concentrations, calculating tracer recoveries) was done in Microsoft Excel 97 spreadsheets (see notebook LA-CST-CW-NBK-98-011). The 2WELLS\_2D code used to correct observed field dispersion for the effects of the recirculating flow field is currently not qualified. Therefore, these corrections must be considered non-Q at this time.

The laboratory sorption data (including cation exchange capacity data) reported in Section 6.0 were calculated from raw data in Microsoft Excel 97 spreadsheets. The isotherm parameters were calculated from curve fits of the reduced data within Microsoft Excel 97 spreadsheets. Excel 97 spreadsheets were also used to calculate matrix porosity and permeability estimates (Section 8.0) from raw data and to reduce the raw diffusion cell data to normalized concentrations. Notebook LA-CST-CW-NBK-98-011 lists the names of the spreadsheets that contain these calculations. The DIFCEL code used to interpret the diffusion cell data is currently not qualified. The interpretations of these data must therefore be considered non-Q at this time.

All C-holes core used in the laboratory experiments of Sections 6.0, 7.0, and 8.0 was collected in 1982-1983 before formal quality-assurance procedures were in place to address core collection. As a result, the core used in all the laboratory experiments must be considered unqualified at this time. An independently-funded effort is currently underway to try to qualify core from several boreholes drilled in the 1980s, including the C-holes.

## APPENDIX A - HYDRAULIC TESTS IN THE PROW PASS TUFF, MAY TO SEPTEMBER 1998, YUCCA MOUNTAIN, NYE COUNTY, NEVADA

By Arthur L. Geldon, Amjad M.A. Umari, and James M. Gemmell

Two cross-hole hydraulic tests were conducted with tracer tests by the U.S. Geological Survey at Yucca Mountain, Nev., between June 2 and September 1, 1998. These tests were conducted in the C-holes (fig. 1) as part of ongoing investigations to determine the hydrologic and geologic suitability of Yucca Mountain as a potential site for permanent underground storage of high-level nuclear waste.

The C-hole complex consists of three 914-m-deep boreholes that are 28.6-87.5 m apart at the depth at which the tests were conducted (Depths from Geldon, 1993, p.3; interborehole distances were calculated on the basis of borehole coordinates in Geldon, 1993, table 1 and borehole deviation surveys listed in Geldon, 1996, table 1). The C-holes are completed in fractured, variably welded tuffaceous rocks of Miocene age (Day and others, 1998). Six hydrogeologic intervals occur within the saturated zone in these boreholes - the Calico Hills, Prow Pass, Upper Bullfrog, Lower Bullfrog, Upper Tram, and Lower Tram intervals (Geldon and others, 1998, p. 14-19).

Hydraulic tests in 1998 were conducted in the Prow Pass interval, which is 56-73 m thick (table 1). Dual-mandrel packers were emplaced in the C-holes on 7.3-cm-diameter tubing to isolate the Prow Pass interval from hydrogeologic intervals above and below it. Temperature-compensated pressure transducers were strapped to the 7.3-cm-diameter tubing above, between, and below packers to monitor the Calico Hills, Prow Pass, and combined Bullfrog-Tram intervals in c#2 and c#3. Failure of a transducer prevented monitoring of the Calico Hills interval in c#1, but transducers were installed in this borehole to monitor the Upper and Lower Bullfrog intervals independently of each other and hydrogeologic intervals in the Tram. A multi-stage submersible pump with a capacity of 0.3-1.3 L/s was suspended on the 7.3-cm-diameter tubing in c#2 at the bottom of the Prow Pass interval. A positive-displacement pump placed on the drill pad near c#3 was used to inject water into c#3 during tracer tests. A well screen was opened in the 7.3-cm-diameter tubing in each of the C-holes to enable hydraulic communication with the Prow Pass interval. Instantaneous and cumulative discharge from c#2 and inflow to c#3 were monitored with vortex flowmeters emplaced inline near the top of each well. Pressures and pumping rates were read and written to electronic files by graphic-language software installed on a computer at the C-hole complex.

A constant-rate withdrawal (CRW) test was conducted June 2-11, 1998. Borehole UE-25 c#2 (c#2) was used as the pumping well, and boreholes UE-25 c#1 (c#1), UE-25 c#3 (c#3), and UE-25 ONC#1 (ONC#1) were used as observation wells during this test. Borehole ONC#1 is 875 m northwest of c#2 and 851 m northwest of c#3 (The location, configuration, and stratigraphy of ONC#1 are described in a report by the Nye County Nuclear Waste Repository Project Office, 1995, p. 1-5, 21-29). During the CRW test, c#2 was pumped at an average rate of 0.33 L/s (Calculated from discharge rates in data package DTN GS990408312315.002). This pumping caused 128 m of drawdown in c#2 (Drawdown in all C-hole intervals was calculated from pressures in data package DTN GS990408312315.002). It is estimated that only 1.34 m of the drawdown in c#2 resulted from stressing the Prow Pass interval, and the balance (99 percent) resulted from well losses. Aquifer drawdown as a ratio of total drawdown (the well efficiency)

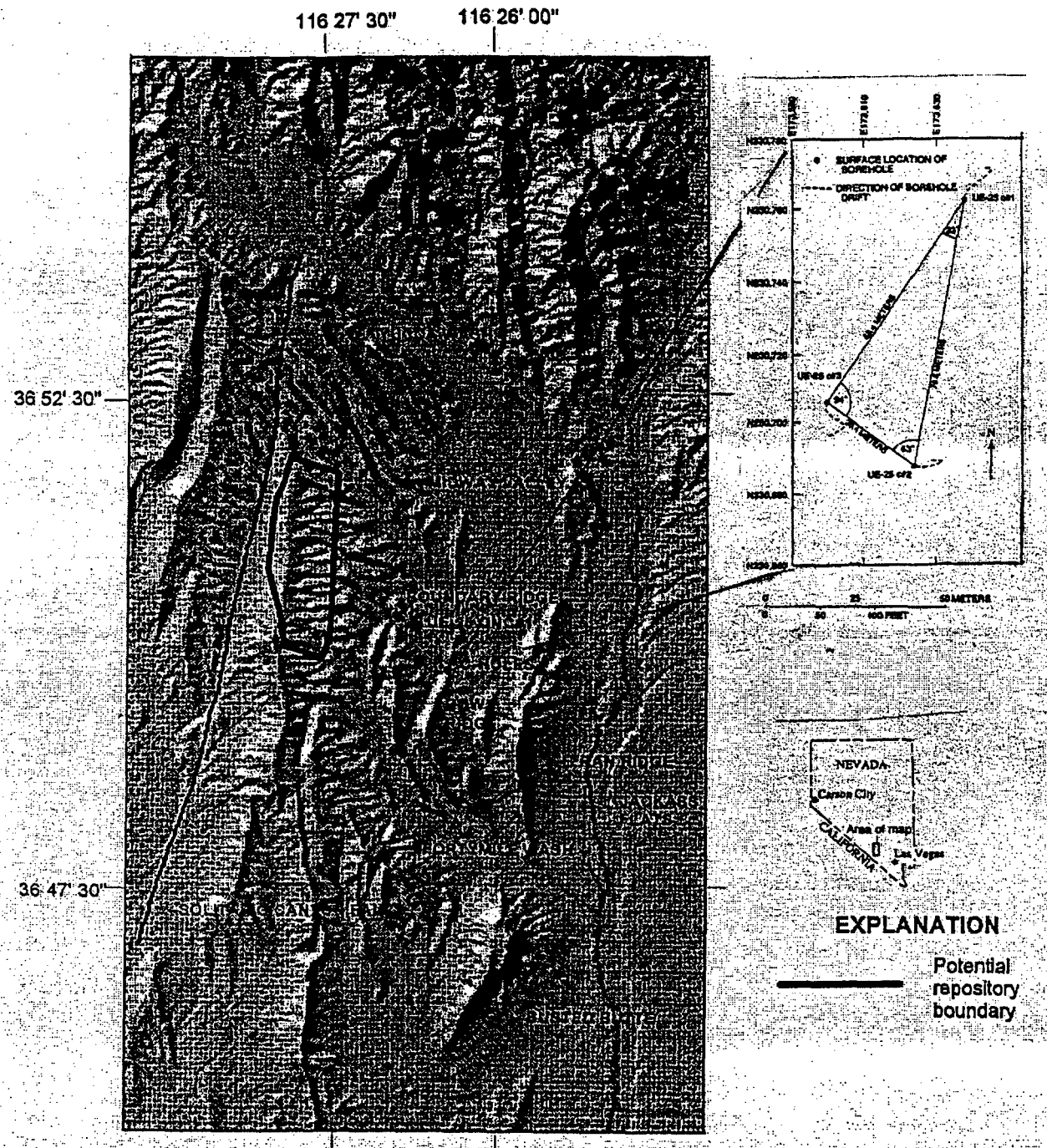


Figure 1—Location of the C-hole complex, boreholes UE-25 c#1, UE-25 c#2, and UE-25 c#3 (C-hole map is referenced to Nevada State Zone 2 coordinates), and borehole UE-25 ONC#1

Table 1 – Prow Pass Test Packer and Transducer Locations (c#2 and c#3 string settings provided by the Nevada Test Site management and operations contractor; c#1 settings from Geldon and others, 1997, tables 2, 4, and 5; ONC#1 settings from Nye County Nuclear Waste Repository Project Office, 1995, p. 21, 27-29; depths in meters below land surface)

Feature	UE-25 c#1	UE-25 c#2	UE-25 c#3	UE-25 ONC#1
Calico Hills				
Top (bottom of casing in C-holes; bottom of packer 13 in ONC#1)	418	416	417	408
Transducer	None	486	472	450
Packer 1 in C-holes; packer 14 in ONC#1 (deflated in tests)	None	488-490	473-475	434-435
Bottom (top of packer 2 in C-holes; top of packer 15 in ONC#1)	547	531	540	450
Prow Pass				
Top (bottom of packer 2; bottom of packer 15 in ONC#1)	549	533	542	452
Upper transducer	552	587	592	458
Lower transducer	None	589	593	Not applicable
Bottom (top of packer 3 in C-holes; bottom of hole in ONC#1)	605	606	610	469
Guard packer (packer 3a)	None	612-614	616-618	Not applicable
Upper Bullfrog				
Top (bottom of packer 3 or 3a)	607	614	618	Not applicable
Transducer	610	616	620	Not applicable
Bottom (top of packer 4 in c#1; bottom of hole in others)	698	910	900	Not applicable
Lower Bullfrog				
Top (bottom of packer 4)	700	Not applicable	Not applicable	Not applicable
Transducer	703	Not applicable	Not applicable	Not applicable
Bottom (top of packer 5)	797	Not applicable	Not applicable	Not applicable

was estimated at different times after pumping started using an equation given by Lohman (1979, p. 52) and hydraulic properties of the Prow Pass (Transmissivity =  $30 \text{ m}^2/\text{d}$ , Storativity = 0.0004) determined from observation-well drawdown in this test and in previous tests (Geldon and others, 1997, table 8). The well efficiency was multiplied by total drawdown to estimate the aquifer drawdown at the end of the CRW test.

Pumping c#2 caused 54 cm of drawdown in the Prow Pass interval of c#3, 12 cm of drawdown in the Prow Pass interval of c#1, and 0.9 cm of drawdown in the Prow Pass interval of ONC#1 (ONC#1 drawdown was calculated from pressures in files downloaded from internet site <http://site206087.primehost.com/index.htm>). The Prow Pass interval in boreholes c#1 and c#3 responded within minutes to the pumping in c#2, but it took about 2 hours for the Prow Pass interval in ONC#1 to show a definite response to this pumping.

Pressures in hydrogeologic intervals above and below the Prow Pass were monitored during the CRW test to determine how well the Prow Pass interval was isolated from these

intervals by packers emplaced in the C-holes. Drawdown in the overlying Calico Hills interval was as much as 19 cm in c#2 and 12 cm in c#3. Leakage from the Calico Hills to the Prow Pass interval during the CRW test is indicated by this drawdown. In contrast, no drawdown was observed below the Prow Pass interval in c#2 and c#3 and below the Upper Bullfrog interval in c#1 during this test. Drawdown in the Upper Bullfrog interval of c#1 was 55 cm. Leakage from the Upper Bullfrog to the Prow Pass interval in c#1 through fractures not present in c#2 and c#3 is indicated by the different responses of the Upper Bullfrog interval in individual C-holes. Monitoring indicated no hydraulic connection between the Prow Pass interval and the underlying, highly permeable Lower Bullfrog interval during the CRW test.

Flow was apportioned among responding intervals to analyze the CRW test by solving analytical equations simultaneously for interval discharge and transmissivity. To make the number of equations equal to the number of unknown variables, it was assumed that 1) transmissivity values for the Calico Hills and Prow Pass intervals in the C-holes are constant; 2) the transmissivity of the Calico Hills is  $5.6 \text{ m}^2/\text{d}$ ; and 3) flow laterally and vertically within the Calico Hills was the same in each of the C-holes during the test. These assumptions were based on analyses and interpretations of previous hydraulic tests, borehole flow surveys, borehole geophysical logs, and other information, that are discussed in reports by Geldon (1996, p. 13-20) and Geldon and others (1997, Hydraulic Tests section, p. 25-30).

The Prow Pass interval contributed 94 percent of the total flow in c#2 and c#3, whereas this interval contributed 24 percent of the total flow in c#1, if assumptions made to calculate interval flows are correct. It seems unlikely, however, that flow from the Prow Pass would be much different in c#1 than in the other boreholes because lithologic and structural factors that might affect flow do not change significantly from one borehole to the next. It is more likely that flow from the Calico Hills interval or the transmissivity of either or both the Prow Pass and Calico Hills intervals is not constant throughout the C-hole complex. A flow survey in the pumping well would have been useful to apportion flow with more certainty, but funding was unavailable for this additional work.

The Prow Pass interval in the C-holes responded to pumping June 2-11, 1998 as a fissure-block aquifer (an aquifer with fracture and rock matrix permeability). Generally, fractures controlled the pumping response for about 200 minutes; delayed yield was evident on plots of drawdown as a function of log time from about 200 to 6,000 minutes; and the fractures and matrix, together, controlled the pumping response from about 6,000 minutes to the end of the test (12,500 minutes after pumping started). Drawdown in the Prow Pass intervals of c#1 and c#3 that was not disturbed by tracer-test operations conformed roughly to type curves of Streletsova-Adams (1978, fig. 13) for  $r/B = 0.05$  and  $\eta=10$  (figs. 2 and 3). Hydraulic properties determined from type curve matches are listed in table 2. Data analyses indicate that the rock matrix and fractures in the Prow Pass interval both contribute water, although proportionately, the matrix permeability is insignificant. The matrix contains 90 percent of the total storativity in this interval. Results of the current testing are supported by a shorter test conducted in June 1995 (table 2).

Drawdown data from ONC#1 plotted alone or with data from c#1 and c#3 as a function of time were inadequate for determining hydraulic properties. However, drawdown data from ONC#1, c#1, and c#3 plotted together as a function of distance from the pumping well 12,500 min after pumping started could be fit to a straight line and analyzed to determine hydraulic properties of the Prow Pass interval in the area between ONC#1 and the C-holes. A least-squares line fit to these data (fig. 4) had a correlation coefficient ( $R^2$ ) of 0.74. Analyzed by the

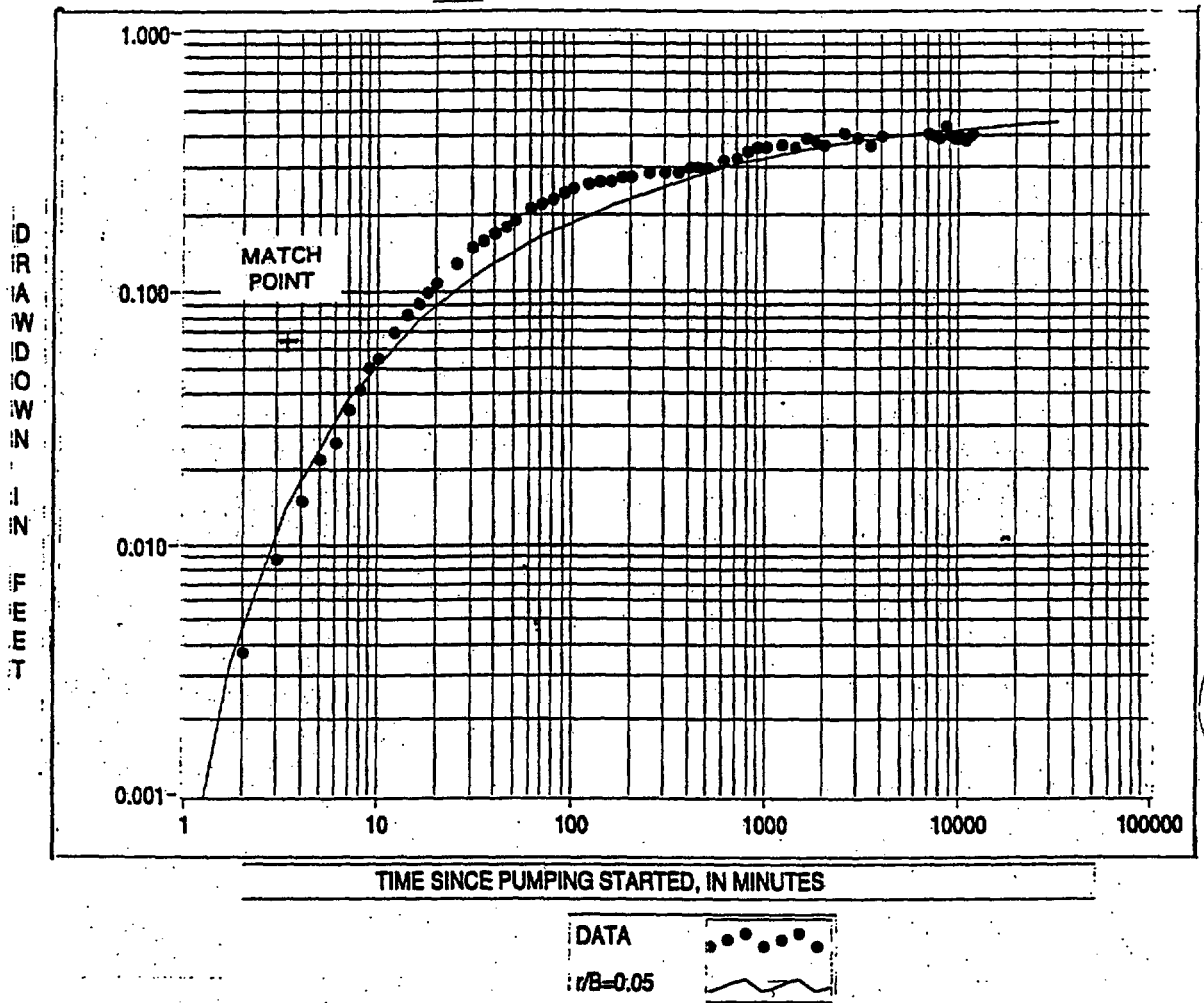


Figure 2 – UE-25 c#1 Prow Pass drawdown June 2-11, 1998 matched to type curves of Streltsova-Adams (1978) for a fissure-block aquifer (1 foot = 0.3048 meters)

method of Cooper and Jacob (1946), the drawdown data indicated transmissivity of  $30 \text{ m}^2/\text{d}$ , hydraulic conductivity of  $1 \text{ m/d}$ , and storativity of  $0.0008$ .

From June 11 to September 1, a period of 118,159 minutes, the effects of injecting water into the Prow Pass interval of c#3 at an average rate of  $0.095 \text{ L/s}$  and injecting tracers into the Prow Pass intervals of c#1 and c#3 were superimposed on the effects of withdrawing water from the Prow Pass interval of c#2 at an average rate of  $0.33 \text{ L/s}$  (Average injection and withdrawal

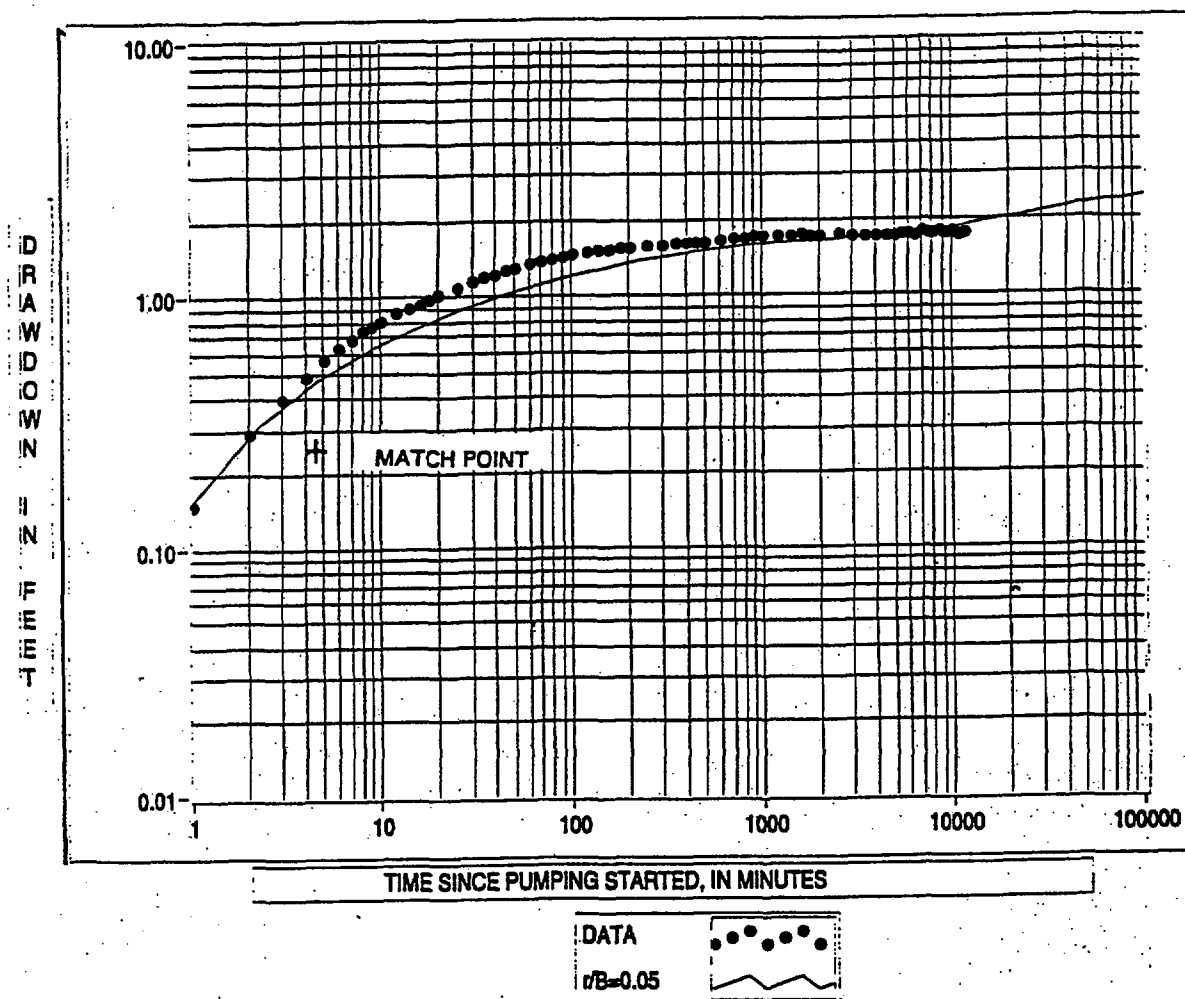


Figure 3 – UE-25 c#3 Prow Pass drawdown June 2-11, 1998 matched to type curves of Streltsova-Adams (1978) for a fissure-block aquifer (1 foot = 0.3048 meters)

rates June 11 to September 1 calculated from discharge values in data package DTN GS990408312315.002). The effects of injecting water into c#3 generally predominated over the effects of withdrawing water from c#2, and water levels in monitored wells generally rose after injection started (Water-level changes in the C-holes June 11 to September 1 calculated from pressures in data package rates June 11 to September 1 calculated from discharge values in data package DTN GS990408312315.002; water-level changes in ONC#1 calculated from pressures in files obtained from internet site <http://site206087.primehost.com/index.htm>).

Injecting water into c#3 caused the discharge from c#2 to oscillate as much as 0.05 L/s between consecutive flowmeter readings (flowmeter and transducer readings generally were

Table 2 - Hydraulic properties of the Prow Pass interval (Data for the 1995 test from Geldon and others, 1997, table 8)

	UE-25 c#1	UE-25 c#1	UE-25 c#2	UE-25 c#3
Borehole				
Test dates	June 12-16, 1995	June 2-11, 1998	June 12-16, 1995	June 2-11, 1998
Period of record (min)	5,800	12,500	5,800	12,500
Analyzed data	Drawdown	Drawdown	Drawdown	Drawdown
Transmissivity ( $m^2/d$ )	60	30	40	30
Hydraulic conductivity, fractures (m/d)	No Data	1	No Data	0.8
Hydraulic conductivity, matrix (m/d)	No Data	0.000003	No Data	0.0002
Hydraulic conductivity (m/d)	3	No Data	2	No Data
Storativity, fractures	No Data	0.00004	No Data	0.00004
Storativity, matrix	No Data	0.0003	No Data	0.0004
Storativity	0.0003	0.0004	0.0004	0.0004

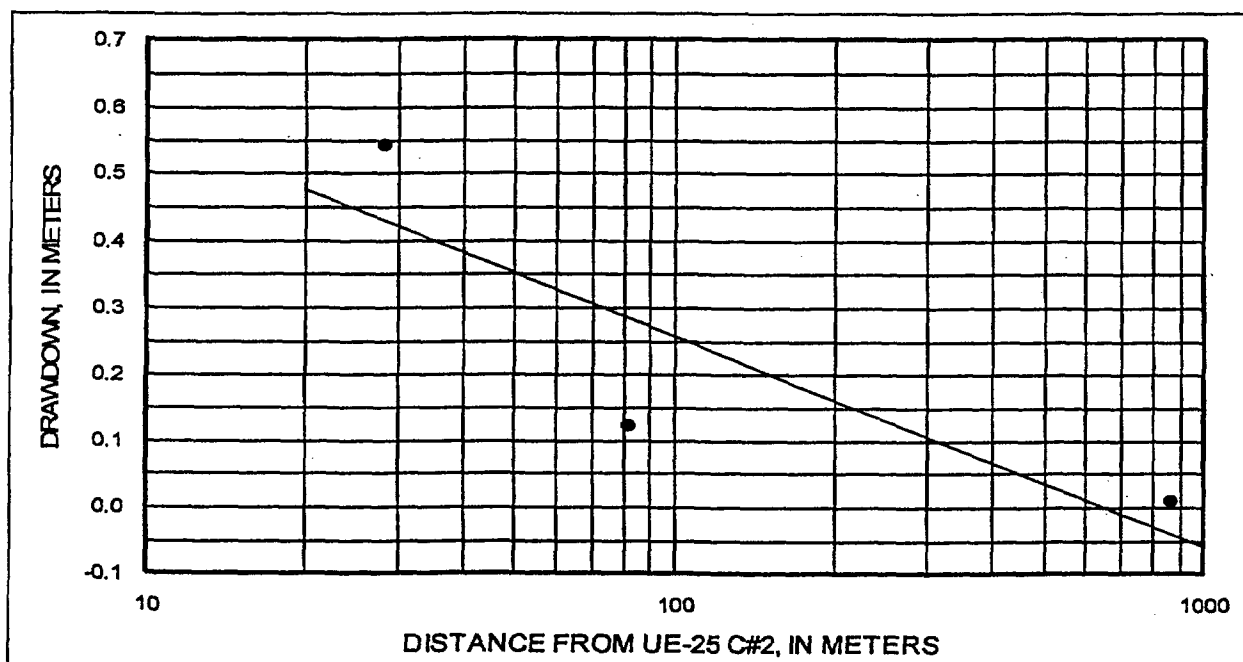


Figure 4 – Relation of drawdown in UE-25 c#1, UE-25 c#3, and UE-25 ONC#1 to distance from the pumping well on June 11, 1998, 12,500 minutes after pumping started.

recorded every 10 minutes). After these discharge fluctuations began, water levels in the Prow Pass interval of c#2 oscillated as much as 10 m between consecutive transducer readings. As water flowed from c#3 to c#2 between June 11 and 22, the water level in the Prow Pass interval of c#2 rose about 13 m. Subsequently, however, drawdown in the Prow Pass interval of c#2

resumed, despite the flux from c#3. Drawdown in this interval (with respect to the pre-pumping water level) was as much as 143 m by September 1.

In contrast to the pumping well, water levels in observation wells rose irregularly during most of the period between June 11 and September 1. Water levels in the Prow Pass interval rose as much as 3,078 cm in c#3, 10 cm in c#1, and 4.4 cm in ONC#1. Injecting fluorinated benzoic acid and iodide tracers into the Prow Pass interval of c#3 on June 17, operating a mixing pump in c#3 on June 18, and injecting a fluorinated benzoic acid tracer into the Prow Pass interval of c#1 on July 31 disturbed the water-level rise in c#3. Injecting tracers into the Prow Pass interval of c#3 on June 17, operating a mixing pump in c#3 on June 18, pulling damaged injection tubing from c#1 on June 26, replacing this tubing on July 13, and injecting a tracer into the Prow Pass interval of c#1 on July 31 disturbed the water-level rise in c#1.

Water-level rises in the C-holes were too irregular and disturbed by tracer-test operations to be analyzed quantitatively. However, the water-level rise in ONC#1 could be analyzed as a constant-rate-injection (CRI) test. Analysis of this water-level rise necessitated removing concurrent drawdown from pumping c#2. Concurrent drawdown was estimated by extrapolating the vaguely defined trend in ONC#1 drawdown prior to the start of injecting water into c#3 (fig. 5) through the period of water injection and subtracting this extrapolated drawdown from the total drawdown.

Matched to the type curve of Streltsova-Adams (1978, fig. 13) for  $r/B=1.0$  and  $\eta=10$  (fig. 6), the water-level rise in ONC#1 as a function of time indicated transmissivity of  $30 \text{ m}^2/\text{d}$ , fracture hydraulic conductivity of  $2 \text{ m/d}$ , matrix hydraulic conductivity of  $0.00001 \text{ m/d}$ , fracture storativity of  $0.0002$ , and matrix storativity of  $0.002$ . Transmissivity and hydraulic conductivity in ONC#1 and the C-holes are identical, but storativity is an order of magnitude larger near ONC#1 than at the C-hole complex. Responses of the Prow Pass interval in ONC#1, c#1, and

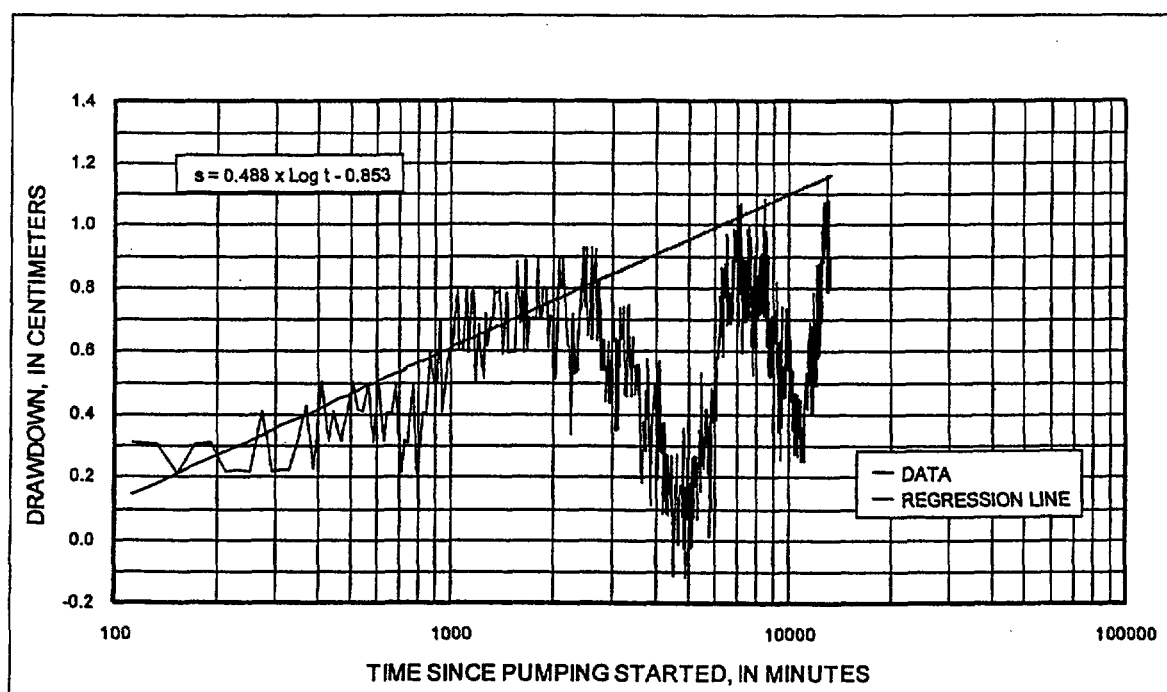


Figure 5 – Drawdown in UE-25 ONC#1 as a function of time. June 2-11, 1998

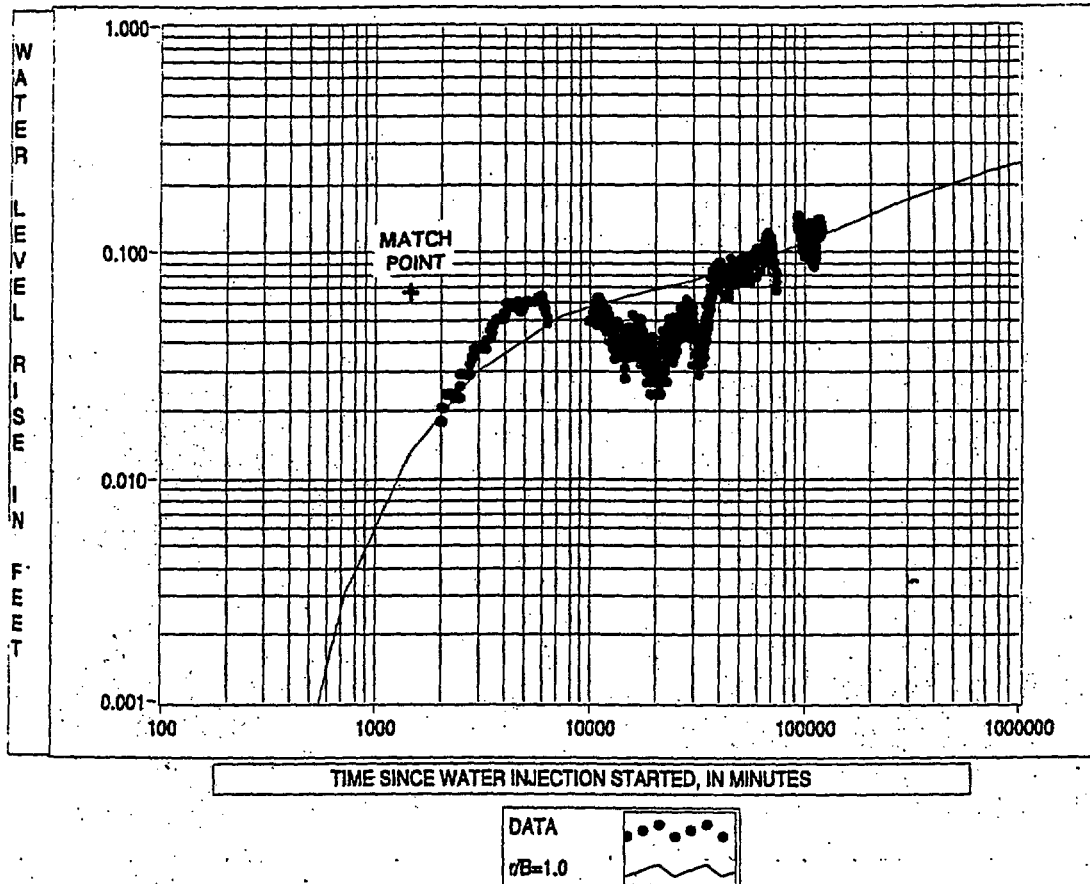


Figure 6 – UE-25 ONC#1 water-level rise, June 11 to September 1, 1998, matched to type curves of Streitsova-Adams (1978) for a fissure-block aquifer (1 foot = 0.3048 meters).

c#3 to hydraulic tests conducted in 1998 indicate that the Prow Pass is a continuous fissure-block aquifer between the C-holes and ONC#1 (across the northern end of Bow Ridge).

Together with a hydraulic test conducted from May 1996 to November 1997 in the highly permeable Lower Bullfrog interval at the C-hole complex (Geldon and others, 1997, Hydraulic Tests section, p. 17-36), the current tests establish a range in hydraulic properties to be expected in typical lithologic and structural settings in the Yucca Mountain area. In an area where the tuffaceous rocks are sparsely fractured and not intersected by major faults, the tuffaceous rocks might be assumed to have hydraulic properties similar to the Prow Pass interval between the C-hole complex and ONC#1. Highly fractured and faulted tuffaceous rocks might be assumed to have hydraulic properties similar to those of the Lower Bullfrog interval in the C-holes. As a

first approximation, transmissivity might be assumed to range from 30 to 1,700 m<sup>2</sup>/d, hydraulic conductivity might be assumed to range from 2 to 50 m/d, and storativity might be assumed to range from 0.0002 to 0.002 in most structural settings where Miocene tuffaceous rocks are present in the saturated zone at Yucca Mountain.

## REFERENCES

- Cooper, H.H., Jr., and Jacob, C.E., 1946, A generalized graphical method for evaluating formation constants and summarizing well-field history: American Geophysical Union Transactions, v. 27, no. 4, p. 526-534 (TIC no. 225279).
- Day, W.C., Dickerson, R.P., Potter, C.J., Sweetkind, D.S., San Juan, C.A., Drake, R.M., II, and Fridrich, C.J., 1998, Bedrock geologic map of the Yucca Mountain area, Nye County, Nevada: U.S. Geological Survey Geologic Investigations Map I-2627, scale 1:24,000 (TIC no. 238732).
- Geldon, A.L., 1993, Preliminary hydrogeologic assessment of boreholes UE-25 c#1, UE-25 c#2, and UE-25 c#3, Yucca Mountain, Nye County, Nevada: U.S. Geological Survey Water-Resources Investigations Report 92-4016, 85 p. (MOL.19960808.0136).
- Geldon, A.L., 1996, Results and interpretation of preliminary aquifer tests in boreholes UE-25 c #1, UE-25c #2, and UE-25c #3, Yucca Mountain, Nye County, Nevada: U.S. Geological Survey Water-Resources Investigations Report 94-4177, 119 p. (MOL.19980724.0389).
- Geldon, A.L., Umari, A.M.A., Fahy, M.F., Earle, J.D., Gemmell, J.M., and Darnell, Jon, 1997, Results of hydraulic and conservative tracer tests in Miocene tuffaceous rocks at the C-hole complex, 1995 to 1997, Yucca Mountain, Nye County, Nevada: U.S. Geological Survey Milestone Report SP23PM3 (to U.S. Department of Energy), various paging (MOL.19980122.0412).
- Geldon, A.L., Umari, A.M.A., Earle, J.D., Fahy, M.F., Gemmell, J.M., and Darnell, Jon, 1998, Analysis of a multiple-well interference test in Miocene tuffaceous rocks at the C-hole complex, May-June 1995, Yucca Mountain, Nevada: U.S. Geological Survey Water-Resources Investigations Report 97-4166, 33 p. (MOL.19980514.0524).
- Lohman, S.W., 1979, Ground-water hydraulics: U.S. Geological Survey Professional Paper 708, 70 p. (TIC no. 237291).
- Nye County Nuclear Waste Repository Project Office, 1995, Borehole UE-25 ONC #1 and USW NRG-4 drilling and instrumentation report, Yucca Mountain, Nevada: Pahrump, Nev., Nye County Nuclear Waste Repository Program, various paging (MOL.19960910.0231).
- Streltsova-Adams, T.D., 1978, Well testing in heterogeneous aquifer formations, in Chow, V.T., ed., Advances in hydroscience: New York, N.Y., Academic Press, v. 11, p. 357-423 (TIC no. 225957).

## **DATA PACKAGES**

DTN, [in review], Transducer, barometer, pressure, and discharge data collected from April 19, 1998 to November 24, 1998 in support of ongoing hydraulic and tracer tests being conducted at the UE-25 C-well complex, Nevada.

## **SOFTWARE**

LABVIEW, graphic-language software created by National Industries, was used to obtain data during field tests and to record data to electronic files. The routine written for this purpose during hydraulic and tracer tests done in 1998 was assigned SID no. ESP 5.34.

Microsoft Excel 97 (SID no. ESP 5.15) was used to convert data in LABVIEW-created files to forms that could be analyzed to calculate hydrologic properties. For example, pressures recorded in LABVIEW-created files were converted to drawdown. Conversions involved simple arithmetic, algebraic equations, or statistical functions (*e.g.*, averaging and linear regression).

Routines written with LABVIEW were used to calculate hydrologic properties from drawdown and water-level rise data. These routines are THEIS.vi (SID no. ESP 5.35), STRLTSVA.vi (SID no. 5.36), and NEUMAN.vi (SID no. ESP 5.37).

Microsoft Word 97 (SID no. ESP 5.40) was used to write this report.

## **APPENDIX B - TRACER TESTS IN THE PROW PASS TUFF, JUNE TO SEPTEMBER 1998, YUCCA MOUNTAIN, NYE COUNTY, NEVADA**

By Amjad M.A. Umari, Michael F. Fahy, and John D. Earle

A tracer test was conducted by the U.S. Geological Survey in the Prow Pass tuff at Yucca Mountain, Nev., from June 17, 1998 to February 25, 1999. This report describes this test and presents interpretations of data obtained between June 17 and September 1, 1998. This test was conducted in the C-holes (fig. 1) as part of ongoing investigations to determine the hydrologic and geologic suitability of Yucca Mountain as a potential site for permanent underground storage of high-level nuclear waste.

The C-hole complex consists of three 914-meter deep boreholes that are 28.6 to 87.5 meters apart at the depth at which the tests were conducted. The C-holes are completed in fractured, variably welded tuffaceous rocks of Miocene age (Day and others, 1998). Six hydrogeologic intervals occur within the saturated zone in these boreholes - the Calico Hills, Prow Pass, Upper Bullfrog, Lower Bullfrog, Upper Tram, and Lower Tram intervals (Geldon and others, 1998). The tracer tests discussed in this report were conducted in the Prow Pass interval (referred to here as the Prow Pass tuff), which is 56 to 72.5 m thick.

On June 17, 1998, a partial-recirculation conservative tracer test was initiated from UE-25c#3 to UE-25c#2 by injecting approximately 14.83 kilograms of 2,4,5 trifluorobenzoic acid (TFBA) and 12.26 kilograms of iodide (in the form of sodium iodide) into UE-25c#3 while UE-25 c#2 was pumped at the rate of approximately 0.33 liters per second (l/s). The concentration of 2,4,5 TFBA was 14,239 ppm in the injected slug and that of iodide 14,307 ppm. Out of the 0.33 l/s pumped from UE-25c#2, 0.095 l/s were continuously reinjected into the Prow Pass interval of UE-25c#3. Approximately forty hours after the injection, breakthrough of the tracers occurred in water pumped out of UE-25 c#2. The peak for the 2,4,5 TFBA breakthrough curve, with a concentration of approximately 3.8 ppm ( $C_{max}$  for 2,4,5 TFBA), occurred 6.74 days after tracer injection, and the peak for iodide, with a concentration of approximately 2.6 ppm ( $C_{max}$  for iodide), at 7 days (fig. 2). On September 4, 79 days after tracer injection, the concentration of 2,4,5 TFBA had decreased to approximately 0.52 ppm, and that of iodide to approximately 0.357 ppm.

The iodide and 2,4,5 TFBA breakthrough curves were analyzed using the-single- and dual-porosity analytical solutions of the advection-dispersion equation, commonly used to describe the flow of solutes in ground water, as given in Moench (1989, 1995, and 1996). The curves were first analyzed assuming Moench's single-porosity solution. In this case, the aquifer is considered to be an equivalent porous medium made up of a network of fractures, some of them continuous, and some discontinuous with connecting segments of matrix (Fahy, 1997). The porosity of this network of fractures and connecting segments of matrix, through which flow of solutes occurs, is referred to herein as "flow porosity," Fahy (1997).

For the single-porosity solution, two different flow regimes were considered, purely-convergent and partially-recirculating. Although the actual flow regime established for the test was partially recirculating, a purely-convergent flow regime was considered because its analysis

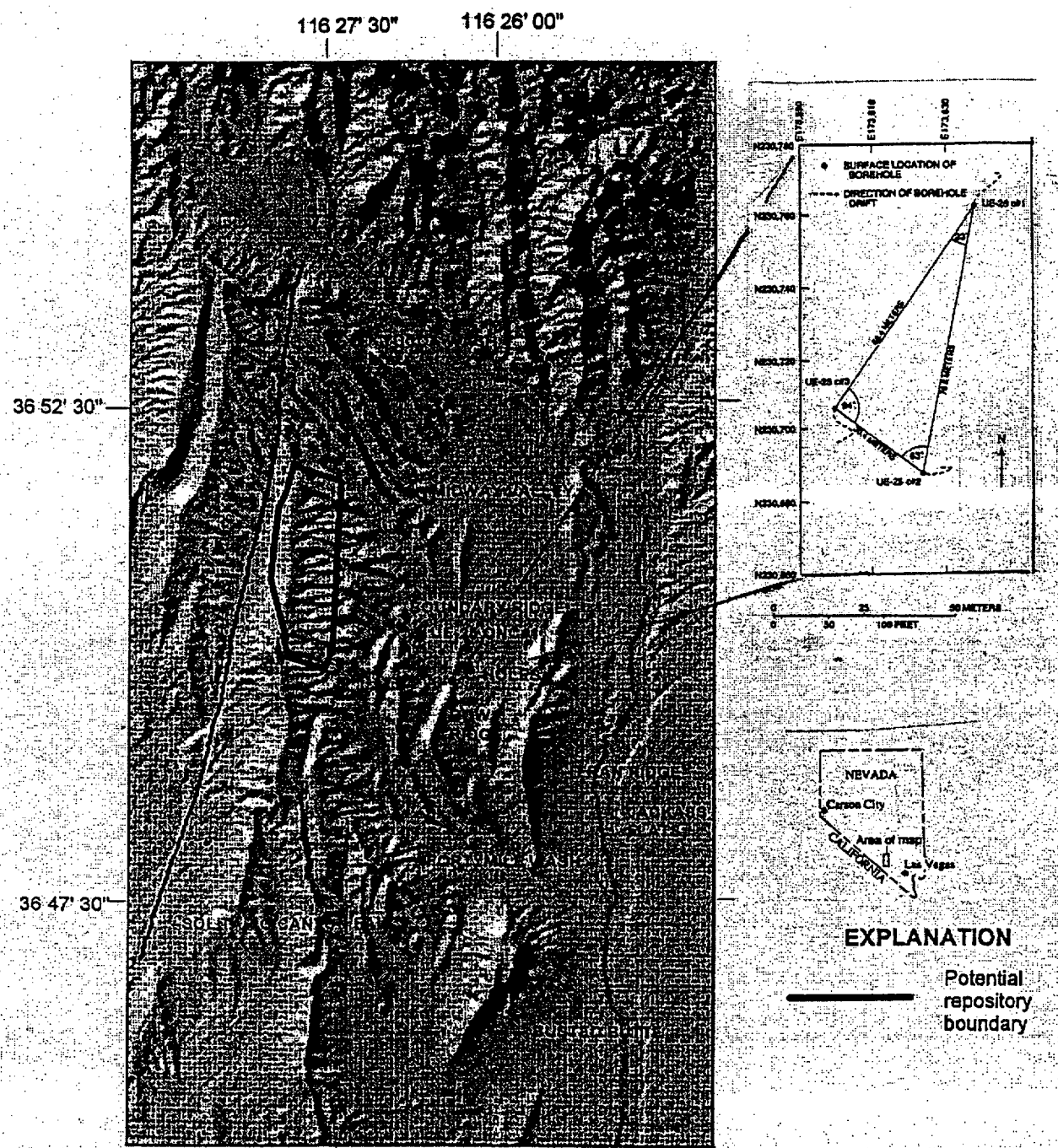


Figure 1—Location of the C-hole complex, boreholes UE-25 c#1, UE-25 c#2, and UE-25 c#3 (C-hole map is referenced to Nevada State Zone 2 coordinates), and borehole UE-25 ONC#1

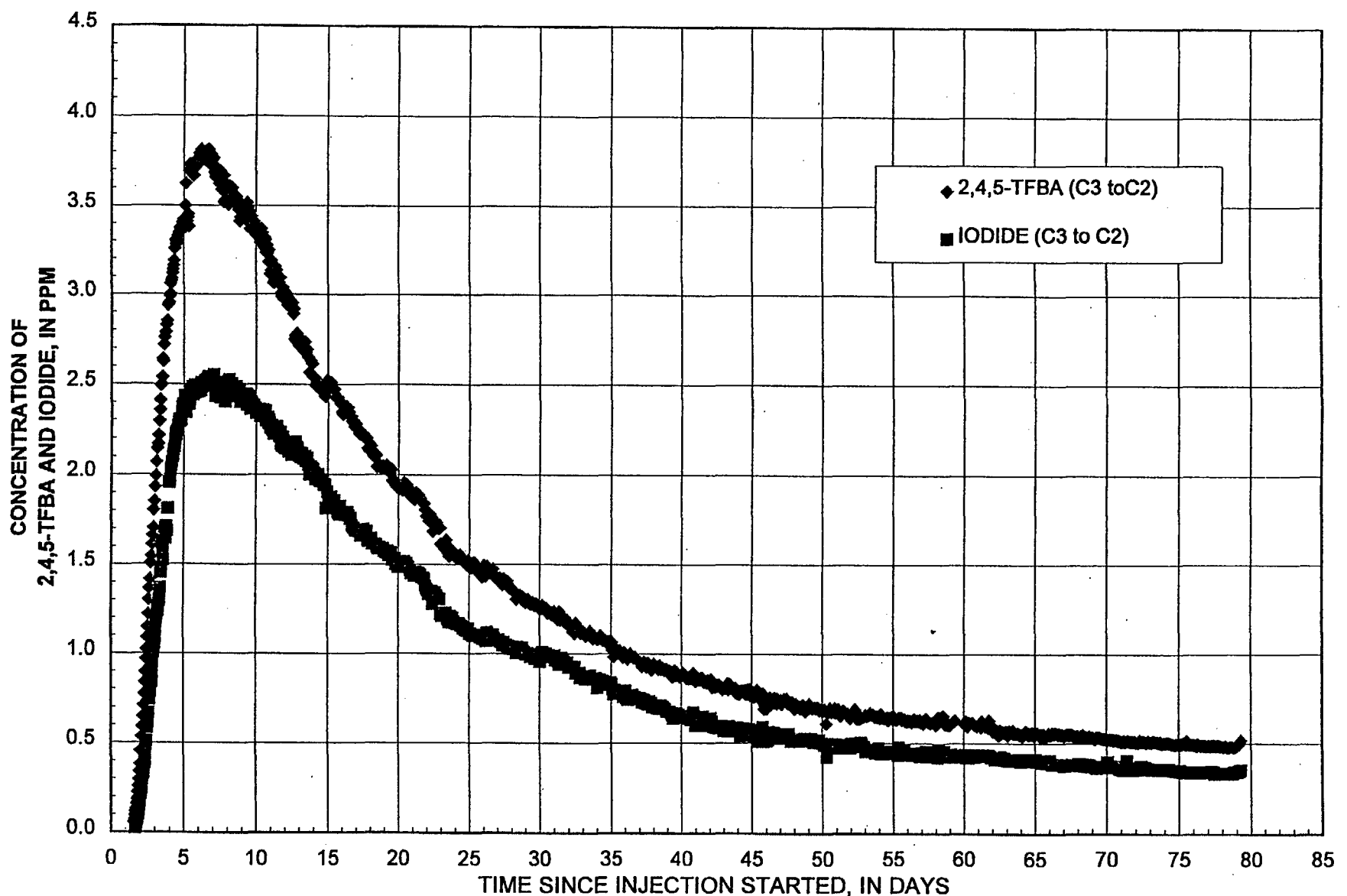


Figure 2. BREAKTHROUGH CURVES FOR 2,4,5 TFBA  
AND IODIDE TRACER TEST



was simpler and provided a stepping stone to the analysis of the more complex, partially-recirculating flow regime.

The single-porosity, purely-convergent solution is obtained directly from the Moench (1995) solution to the advection-dispersion equation. This solution, the output of which is in the form of a breakthrough curve (values of concentration versus time) at the pumped well, requires the following input parameters: pumping rate; aquifer thickness; distance between, and radii of, injection and withdrawal wells; and mixing lengths in the injection and withdrawal wells. In all solutions presented in this report, the following values were used: pumping rate of 3.3 l/s (represents the average rate for the test), aquifer thickness of 61 m (represents the average thickness of the Prow Pass interval between UE-25 c#2 and UE-25 c#3), distance between injection and pumping wells of 29 m (represents the calculated average distance, within the Prow Pass interval, between boreholes UE-25 c#2 and UE-25 c#3), radii of injection and pumping wells of 13.97 cm (nominal value: caliper log shows variations, larger and smaller than 13.97 cm), and borehole mixing length of 30.5 m (assumed: discussed below). Three additional input parameters, the mass and concentration of tracer slug injected, and the duration of slug injection are optional. Because all breakthrough curves were normalized to their own maximum concentrations, the need for specifying the mass and concentration of the injected tracer slug was obviated. The duration of slug injection also was not needed because instantaneous slug injection—rather than the finite-duration slug injection—was assumed in the purely-convergent solution presented. The medium parameters required are the flow porosity, the longitudinal dispersivity, and the retardation coefficient of the tracer specific to the medium. The flow porosity and longitudinal dispersivity are different for each of the solutions presented. The retardation coefficient used for all solutions was 1.0 indicating that iodide and 2,4,5 trifluorobenzoic acid are considered conservative with respect to the Prow Pass tuff.

The single-porosity, purely-convergent solution to the advection-dispersion equation, obtained directly from Moench (1995) for fitted values of 0.07% and 1.45 m corresponding to the flow porosity and longitudinal dispersivity, respectively, is presented in figure 3, along with the iodide and 2,4,5 TFBA breakthrough curves. All breakthrough curves, such as the ones in figure 3, were normalized by dividing the measured concentrations by their own maximum concentration,  $C_{max}$ , rather than by the concentration of the injected mass slug,  $C_0$ . (A discussion on the different representation of the effects of matrix diffusion using the two methods of normalization is presented later in this report when dual-porosity solutions are described.) Longitudinal dispersivity is a measure of the porous medium's ability to disperse a solute along streamlines. Transverse dispersivity, which represents the medium's ability to disperse a solute in a direction perpendicular to streamlines, is not obtainable from this analysis method and flow geometry. The above longitudinal dispersivity of 1.45 m and the 29 m flow length correspond to a Peclet number of 20, where the Peclet number is a dimensionless parameter formed in Moench (1995) by dividing the distance between injection and pumping wells by the longitudinal dispersivity.

The fitted values of longitudinal dispersivity and flow porosity may be sensitive to the mixing lengths assumed for the injection and pumped wells. The mixing lengths represent those lengths within the boreholes through which the tracer enters or exits the aquifer. The 30.5 m mixing length assumed for all solutions in this report is based on the thickness of the transmissive interval within the packed-off

Prow Pass tuff (the transmissive interval within the

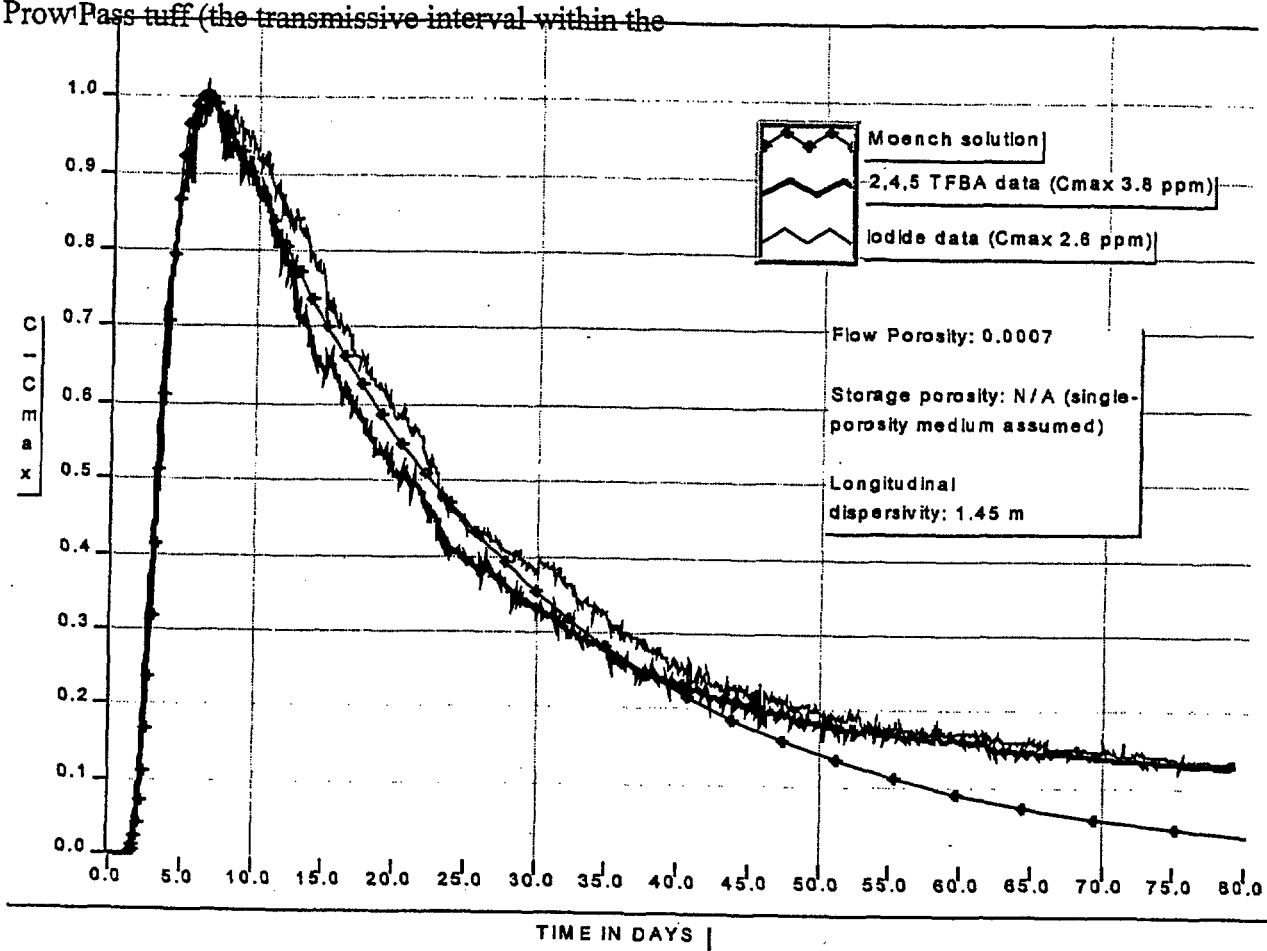


FIGURE 3 . BREAKTHROUGH CURVE FOR 6/17/98 2,4,5 TFBA AND IODIDE TRACER TEST,  
MATCHED BY SINGLE-POROSITY, PURELY CONVERGENT MOENCH (1995) SOLUTION

Prow Pass hydrogeologic interval in UE-25 c#3 is shown in figure 5, p. 9 of Geldon and others, 1998, to be approximately 33.8 m.) That is, the 30.5 m mixing length is consistent with the hydrogeology of the Prow Pass interval.

However, uncertainty accompanies any estimate of the transmissive interval within a borehole. The residence time of the tracer slug within the borehole is directly proportional to the mixing length. To evaluate the effect of the mixing length on the fitted longitudinal dispersivity and flow porosity, the 30.5 m mixing length used for all solutions in this report is considered to be one end member of a range, and the effect of another end member, that of 0.3 m mixing length, on the results of the single-porosity purely-convergent solution, is investigated. In addition to introducing uncertainty as to the length of the transmissive interval, an assumed mixing length of 0.3 m decreases the residence time of the tracer slug in the injection borehole which would simulate the effect of borehole flushing due to partial recirculation. Data collected

during the tracer injection indicate that the borehole was flushed in 8.5 hours (the concentration in the injected interval was measured in the field and found to rise from below detection limit to 2,721 ppm and then back to below detection limit in 8.5 hours. The concentration in the injection interval was measured as 29 ppm, 2721 ppm, 1552 ppm, 557 ppm, and 323 ppm at 5.5 hours; 6.5 hours; 7 hours, 35 minutes; 8 hours, 10 minutes; and 8.5 hours, respectively, after injection.) Because the single-porosity purely-convergent solution is being discussed here, only the borehole-flushing effect of partial recirculation is relevant, which is the same as the effect of a chase fluid in a purely-convergent test. When the mixing length is reduced to 0.3 m and only the rising limb of the actual breakthrough curve (BTC) is matched to the theoretical breakthrough curve (BTC) from Moench (1995) (assuming minimal diffusion during the rising limb), a longitudinal dispersivity value of 4.27 m and a flow porosity value of 0.0016 are obtained as fitting parameters. So, by changing the mixing length from 30.5 m to 0.3 m, a 2- order-of-magnitude change, in both injection and pumping wells to capture uncertainty in transmissive interval length in the two wells and represent flushing the injection well, the estimates of longitudinal dispersivity and flow porosity change from 1.45 m and 0.0007 in the case of 30.5 m mixing length to 4.3 m and 0.0016 in the case of 0.3 m mixing length. This is a 3-fold change in the estimate of longitudinal dispersivity and a 2-fold change in the estimate of flow porosity, both less than an order-of-magnitude change. The estimated parameters, therefore, are not very sensitive to the mixing length.

The above porosity value of 0.07% is in the range of 0.001% to 1% cited in the literature to represent fracture porosity (see, for example, Freeze and Cherry, 1979, p. 408). This implies that the flow network for this test is composed predominately of fractures.

When the purely-convergent flow field of figure 3 is replaced by a partially-recirculating flow field, the resulting solution to the advection-dispersion equation changes from the curve labeled "Moench solution" in figure 3 to the curve labeled "Modified Moench solution" shown in figure 4. The difference between the two solutions reflects the difference in flow field representation, and in the fitted values of longitudinal dispersivity and flow porosity used (or implied) for each solution. Two elements of partial-recirculation are represented in this solution. First, the flow field is different from that of purely-convergent flow. Rather than straight converging rays into the pumped well, the partially-recirculating flow field streamlines that are within the capture zone of the pumped well emanate from the injection well and curve towards the pumped well (fig. 5a). The streamlines shown in figure 5a are lines of equal stream function values, where the stream function of the partial recirculation field is calculated as the sum of the stream functions of a 0.33 l/s sink and a 0.095 l/s source, 29 m apart. The volume of rock between pairs of these curved streamlines constitute distinct pathways for the solute (tracer) to take from the injection to the pumped well. Three such inter-streamline pathways (fig. 5a) are assumed for the partial-recirculation analysis in this report. The Moench (1995) single-porosity, purely-convergent solution is viewed as the solution of the advection-dispersion equation along a single straight pathway, that represented by the rock between the pair of bounding streamlines from the injection to the pumped well (fig. 5b). This solution, for a particular longitudinal dispersivity value and an initial value of flow porosity, is then applied to each of the above three distinct pathways with a proper delay factor to account for the differences in lengths, or swept volumes, of these pathways relative to the straight purely-convergent pathway from injection to pumped well. The significance of using the designation "initial value" for the flow porosity used

for the three pathways will be explained later in the report.

The above three solutions from Moench (1995), for a particular longitudinal dispersivity value and an initial value of flow porosity, and with appropriate delay factors, assuming an instantaneous-slug-injection, are then superimposed to obtain what is considered to be the

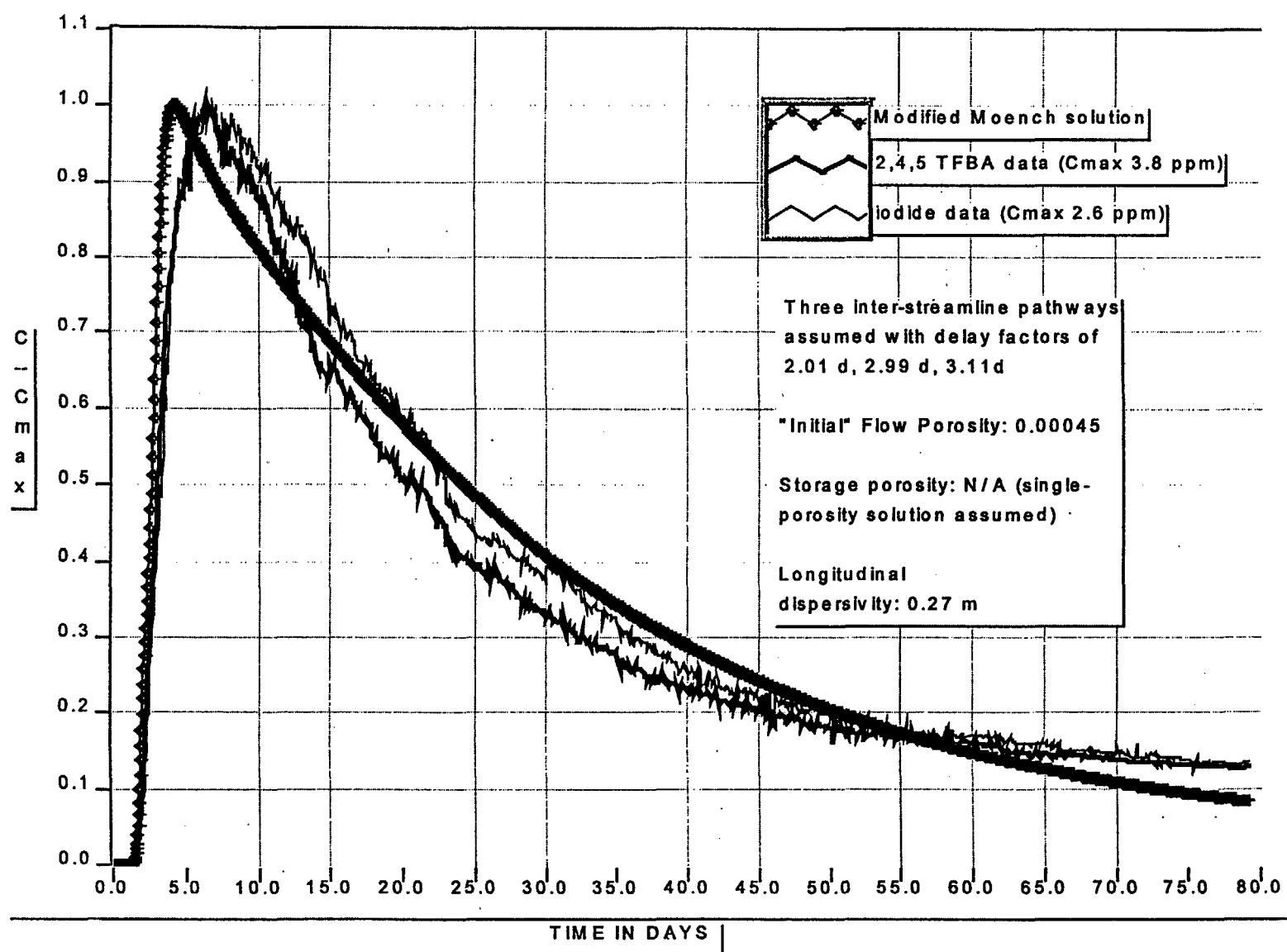


FIGURE 4 . BREAKTHROUGH CURVE FOR 6/17/98 2,4,5 TFBA AND IODIDE TRACER TEST, MATCHED BY SINGLE-POROSITY, PARTIAL-RECIRCULATION SOLUTION DERIVED FROM MOENCH (1995)

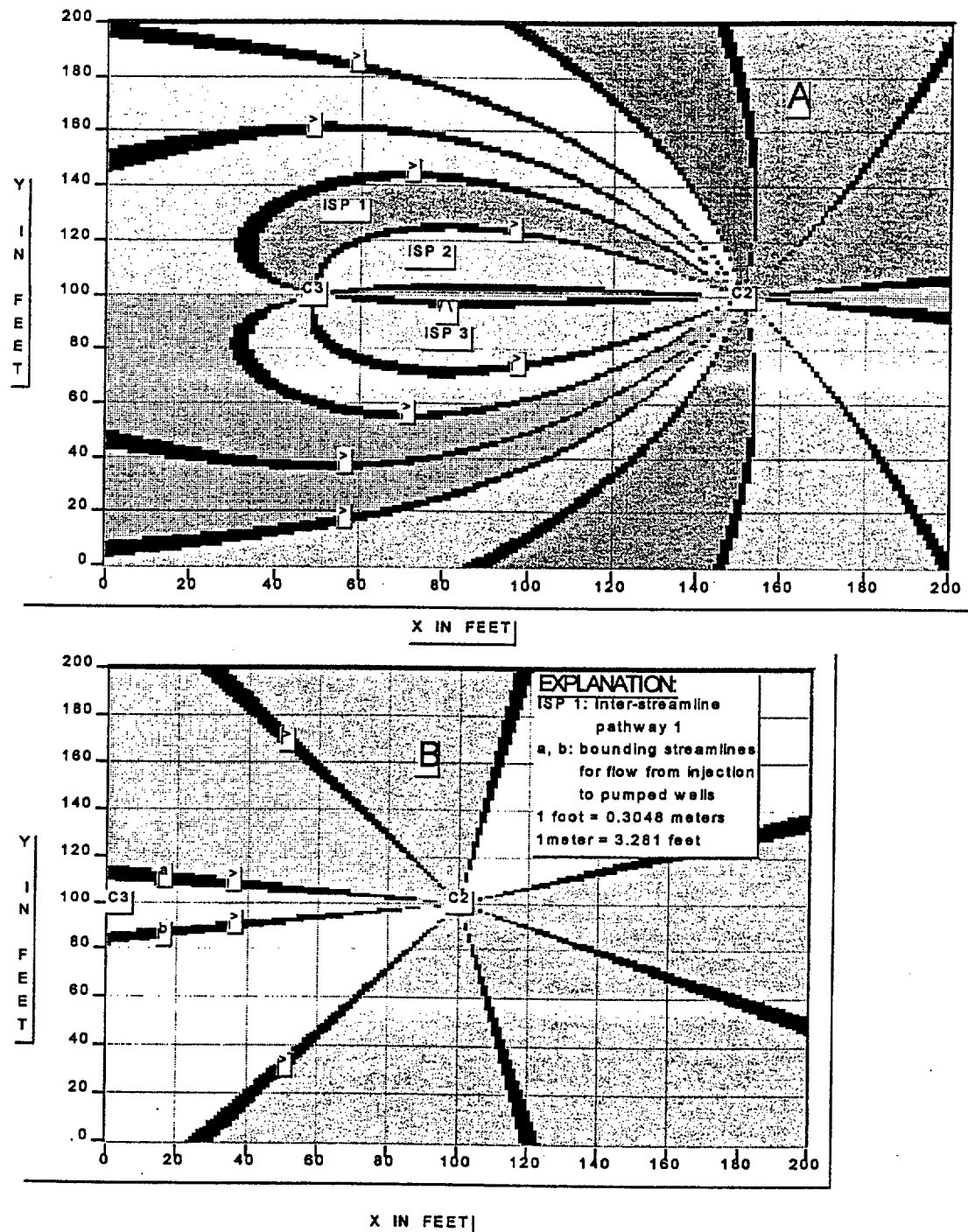


FIGURE 5. STREAMLINES: A) FOR PARTIAL-RECIRCULATION FLOW FIELD;  
B) FOR PURELY-CONVERGENT FLOW FIELD

system's unit response function. The summed curve represents what is seen at the pumped well in response to an instantaneous input function at the injection well in a partial-recirculation flow field.

The second element of partial recirculation is that the reinjected water contains a concentration of the tracer, and so the tracer is continuously reintroduced into the aquifer. In order to represent this, it was assumed that the concentration of reinjected tracer as a function of time, the injection concentration curve, was the same as the breakthrough curve of the tracer at the pumped well, but lagged by a certain duration, due to travel through surface plumbing. This lag represents the length of time it would take the tracer to be recirculated from the discharge/sampling point of the pumped well at the surface to the downhole point in the injection well where it enters the aquifer. For the calculations presented here, it was assumed that this lag duration is approximately 1 hour. The injection concentration curve was padded at the beginning by 2 hours of very high concentrations representing the "top hat" finite-duration slug injection that preceded the concentrations resulting from the recirculated tracer.

The injection concentration curve is then convolved (Levenspiel, 1972) with the unit response function to produce the calculated partial-recirculation breakthrough curve at the pumped well. The parameter fitting process performed here involves the visual comparison of actual and calculated partial-recirculation curves for a set of input parameters (longitudinal dispersivity, initial flow porosity, and the three inter-streamline pathway delay factors) and the trial-and-error selection of the set of parameters that minimizes the difference between these two curves.

Employing the parameter fitting process above, a longitudinal dispersivity of 0.27 m and an initial flow porosity of 0.00045, which result in the calculated partial-recirculation breakthrough curve presented in figure 4, were selected as "optimal" for the single-porosity, partial-recirculation, case. The delay factors for the three inter-streamline pathways, inherent in the calculation of the breakthrough curve of figure 4, were initially assumed to be 1.83 days for the first pathway, 3.5 days for the second, and 7.5 days for the third. (Each delay factor is calculated by multiplying the volume of the corresponding inter-streamline pathway by the initial flow porosity of 0.00045, and then dividing the result by the flow rate that is carried by the inter-streamline pathway, which is equal to the difference in the stream function values of the bounding streamlines.) However, use of these delay factors produced a calculated breakthrough curve that did not fit the actual breakthrough curve very well. The fit was substantially improved by changing the delay factors to 2.01 days, 2.99 days, and 3.11 days, which resulted in the calculated breakthrough curve of figure 4. Because these three delay factors are not the ones indicated by the volumes of rock calculated for the three inter-streamline pathways, they are interpreted to represent the uncertainty in either the initial, single, flow porosity value or in the assumed streamline pattern and resulting rock volumes. In the first approach, the volumes of rock calculated for the three inter-streamline pathways is considered correct, in which case the deviation of optimal delay factors from those calculated with the single initial porosity value is interpreted to imply that the three pathways in fact have varying flow porosities (hence the "initial porosity" designation.) Given the rock volumes for the three pathways, the optimal delay factors of 2.01 days, 2.99 days, and 3.11 days represent flow porosities of 0.0005, 0.0004, and 0.0002 for the three pathways. This reflects uncertainty in the assumption of a homogeneous medium with one flow porosity value. In the second approach, the initial flow porosity is considered correct and the deviation of the optimal delay factors from those calculated with the

rock volumes of figure 5a is interpreted to reflect the uncertainty in the calculated pathway rock volumes. But because the rock volumes were calculated assuming the streamline pattern of a homogeneous medium, this in turn represents uncertainty in the underlying homogeneity assumption—the same conclusion as the one reached from the first approach. The above modified delay factors were used in all partial-recirculation solutions in this report.

The results shown in figures 3 and 4 indicate that if the breakthrough curves of 2,4,5 TFBA and iodide are analyzed as if they result from a purely-convergent flow field, ignoring that the real flow field is partially recirculating, some error in the derived parameters occurs. A longitudinal dispersivity of 1.45 m is obtained when purely-convergent conditions are assumed, 5 times the 0.27 m obtained when the partial- recirculation flow field is recognized. The flow porosity of 0.0007 obtained for purely-convergent conditions is 56% higher than the initial flow porosity of 0.00045 obtained for partial-recirculation.

Note that although the purely-convergent solution in figure 3 matches the data on the rising limb better than the partial-recirculation solution in figure 4, the latter matches the data on the falling limb better, especially in the tail of the breakthrough curve. The solution in figure 4 attempts to capture all the elements of partial recirculation, whereas the solution in figure 3 doesn't. The fact that the partial-recirculation solution in figure 4 doesn't match the data any better than it does indicates that, although it attempts to incorporate all elements of partial recirculation, it does not capture everything that in fact takes place in the field. For example, one element that has not been incorporated into the partial recirculation solution in figure 4 is the effect on the flow field of the natural gradient. Incorporating the natural gradient would alter the streamline pattern of figure 5a to some extent and lead to different inter streamline pathway volumes and resulting delay factors. Also, representation of the effects of partial recirculation can be improved by using more than three inter-streamline pathways. In the dual-porosity case, the medium is assumed to be comprised of flow and storage components. Advection and hydrodynamic dispersion, as represented by the advection/dispersion equation, occur in the "flow" component. Matrix diffusion is represented as a source/sink term in the advection/dispersion equation and occurs in the storage component. The flow component is conceptualized as a flow network of 1) continuous fractures and 2) discontinuous fractures with interconnecting segments of matrix. The porosity of the flow component of the medium is referred to as the "flow porosity" in this report (same as for the single-porosity case.) The storage component is assumed to consist of dead-end fractures and the part of the matrix not contributing to the flow network. The porosity of the storage component of the medium is referred to as the "storage porosity" in this report.) The flow network is represented by a longitudinal dispersivity and a flow porosity, and the storage component by a storage porosity and a dimensionless matrix diffusion coefficient.

The calculated dual-porosity solution is predicated upon the single-porosity, partial- recirculation solution presented earlier, i.e. a longitudinal dispersivity of 0.27 m and an initial flow porosity of 0.00045. The same process of superimposing three purely-convergent solutions with delay factors—representing either the flow porosities, or the uncertainty in the streamline pattern and resulting rock volumes, of the three inter-streamline pathways—to obtain the medium's unit response function, followed by the latter's convolution with the delayed input concentration curve, is employed. However, the starting purely-convergent solution used is the dual-porosity—rather than the single-porosity—Moench (1995) solution, and it requires, in

addition to the input parameters presented earlier for the single-porosity solution, the medium's storage porosity and dimensionless matrix diffusion coefficient (the latter defined below). Two calculated breakthrough curves obtained this way, for a storage porosity of 0.001 and two dimensionless matrix diffusion coefficients (gamma), namely 0.0001 and 0.001, are presented in figure 6, along with the actual breakthrough curves of 2,4,5 TFBA and iodide.

The free-water molecular diffusion coefficients of 2,4,5 TFBA and iodide are  $8.0 \times 10^{-6}$  cm<sup>2</sup>/sec and  $18.0 \times 10^{-6}$  cm<sup>2</sup>/sec, respectively (Bowman, 1984; Skagius and Neretnieks, 1986). When a solution is placed in a porous medium and it diffuses into the matrix, the extent of matrix diffusion is represented by the dimensionless matrix diffusion parameter, gamma, defined in table 1, p. 1826, of Moench (1995). This parameter represents the extent of matrix diffusion, i.e. the matrix diffusion flux and resulting effect on the breakthrough curve. For a specific distance between injection and pumping wells, test interval thickness, and assumed representative matrix block dimension, the dimensionless diffusion coefficient is directly proportional to the product of the porosity of the matrix (the storage porosity) and the free-water diffusion coefficient of the solute, and inversely proportional to the flow rate. This implies that, for a certain flow rate, the larger the storage porosity, the greater the effect on matrix diffusion resulting from a specific change in the free-water diffusion coefficient of a tracer. The above relationships will be evident from the effects of changing the storage porosity and free-water diffusion coefficient on the calculated breakthrough curves, as shown below.

Figure 6 shows the effects on matrix diffusion—as represented by two calculated breakthrough curves—of changing the free-water diffusion coefficient by a factor of 10, for fixed storage porosity, 0.001, and fixed flow rate. (A gamma change of 0.001 to 0.0001 implies a change in the free-water diffusion coefficient by a ratio of 10 to 1, because the storage porosity and flow rate are held constant.) Figure 7, shows that when the storage porosity is increased from 0.001 to 0.01, the effect on matrix diffusion of the same change in the free-water diffusion coefficient as that in figure 6 is markedly larger. The calculated breakthrough curve with the higher free-water diffusion coefficient (corresponding to a gamma of 0.001) is more retarded, relative to that with the lower coefficient, in figure 7 than it is in figure 6. It should be noted here that the effects of matrix diffusion on a breakthrough curve (BTC) are seen as a reduction in peak if the BTC is normalized by the mass injected, and a delay if it is normalized by its maximum concentration. Figures 6 and 7 use the latter method. The 10 to 1 ratio of the free-water diffusion coefficient used for the two calculated BTCs shown in figures 6 and 7 is larger than the ratio of 18 to 8 (i.e. 2.25 to 1) of the free-water diffusion coefficient of iodide relative to that of 2,4,5 TFBA.

When the ratio in free-water diffusion coefficients of the two calculated BTCs is fixed at that of iodide and 2,4,5 TFBA, i.e. 2.25 to 1 (gamma ratio of 0.001 to 0.000444), the results shown in figures 8 and 9 are obtained. Figure 8 shows the two calculated BTCs, with gamma values of 0.001 and 0.000444 for a storage porosity of 0.001, and figure 9 shows the two BTCs with the same gamma values for a storage porosity of 0.01. As in figures 6 and 7, the effects of matrix diffusion increase with increasing storage porosity for the same change in the water-diffusion coefficient, or in gamma. In contrast to figures 6 and 7, the calculated BTCs in figures 8 and 9 show less effects of matrix diffusion for a particular storage porosity, because of the smaller ratio in the free-water diffusion coefficient, or in gamma, used for the two curves.

The separation between calculated BTCs in figure 9 is similar to that between the actual 2,4,5 TFBA and iodide curves, which would suggest a storage porosity value of approximately

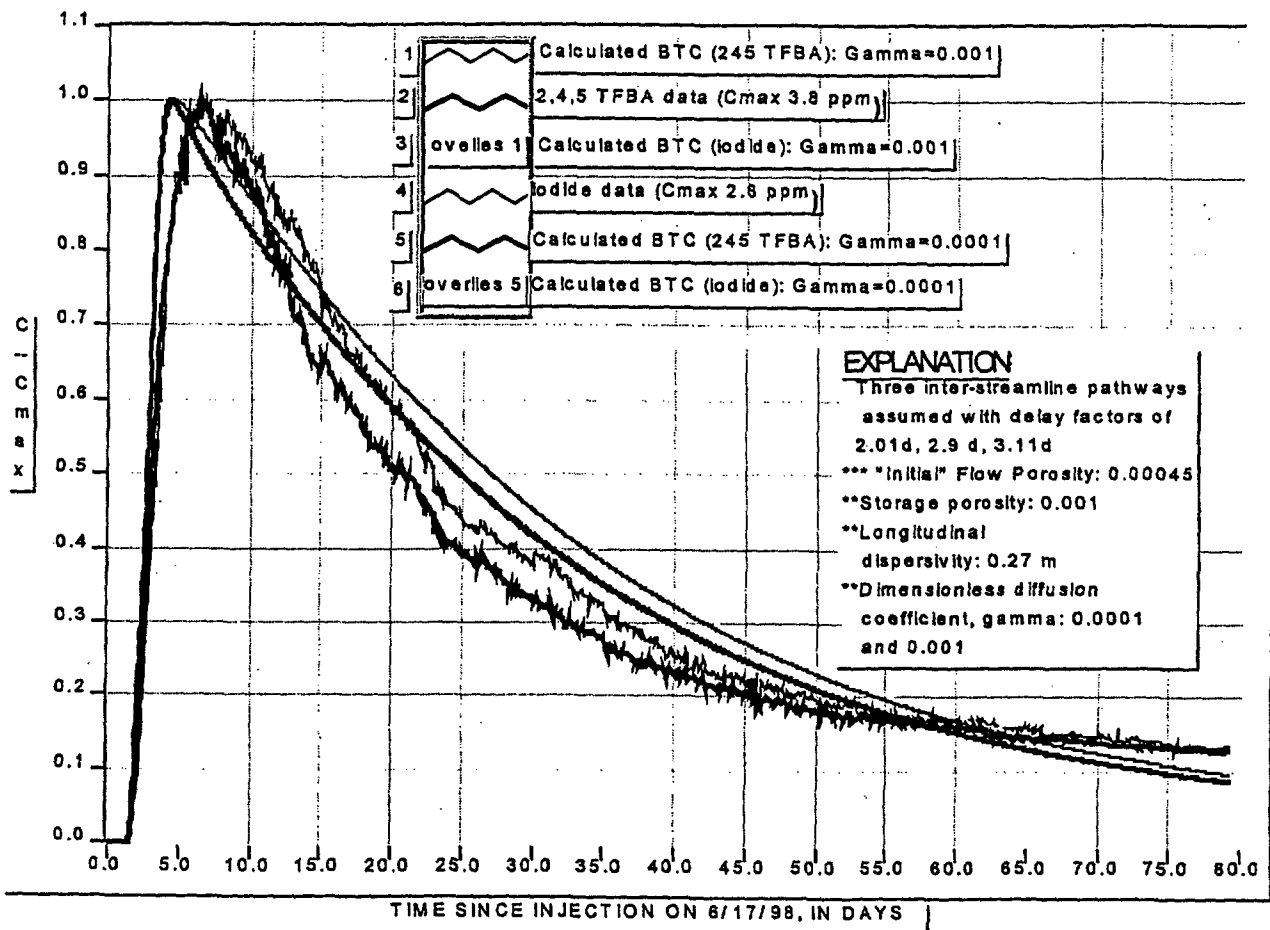


FIGURE 6 . BREAKTHROUGH CURVE FOR 8/17/98 2,4,5 TFBA AND IODIDE TRACER TEST, MATCHED BY DUAL-POROSITY, PARTIAL-RECIRCULATION SOLUTION DERIVED FROM MOENCH (1995), WITH STORAGE POROSITY OF 0.001 AND DIMENSIONLESS DIFFUSION COEFFICIENTS, GAMMA, OF 0.0001 AND 0.001

0.01. This result is combined with earlier ones to indicate a dual-porosity medium with an initial flow porosity of 0.00045 (which may represent three inter-streamline pathways of flow porosities ranging from 0.0002 to 0.0005), a storage porosity of 0.01, and a longitudinal dispersivity of 0.27 m. The flow porosity and longitudinal dispersivity characterize a flow network within this medium comprised of 1) continuous fractures and 2) discontinuous fractures with interconnecting segments of matrix. The storage porosity characterizes a storage component of the conceptualized dual-porosity medium consisting of dead-end fractures and the part of the matrix not contributing to the flow network.

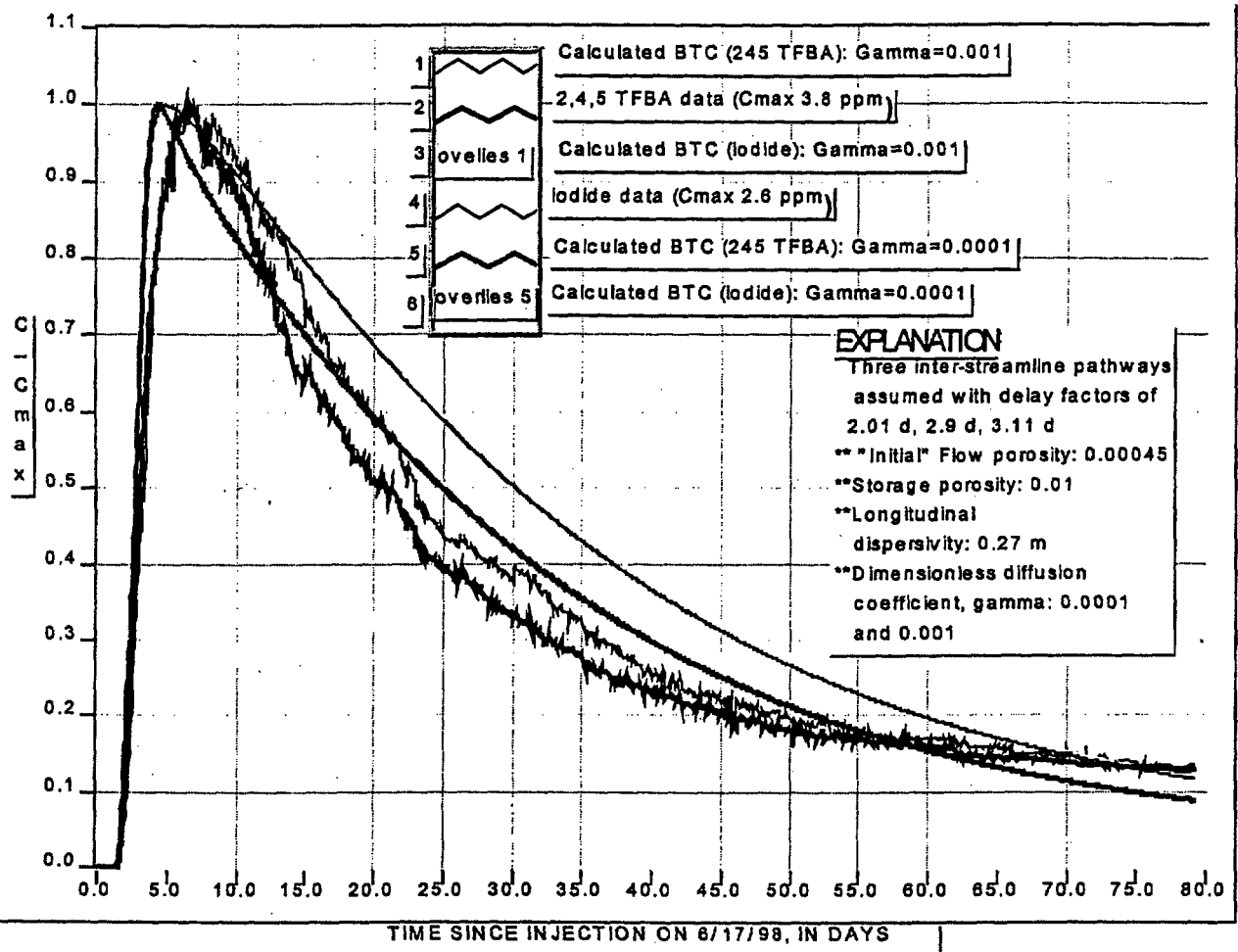


FIGURE 7. BREAKTHROUGH CURVE FOR 6/17/98 2,4,5 TFBA AND IODIDE TRACER TEST, MATCHED BY DUAL-POROSITY, PARTIAL-RECIRCULATION SOLUTION DERIVED FROM MOENCH (1995), WITH STORAGE POROSITY OF 0.01 AND DIMENSIONLESS DIFFUSION COEFFICIENTS, GAMMA, OF 0.0001 AND 0.001

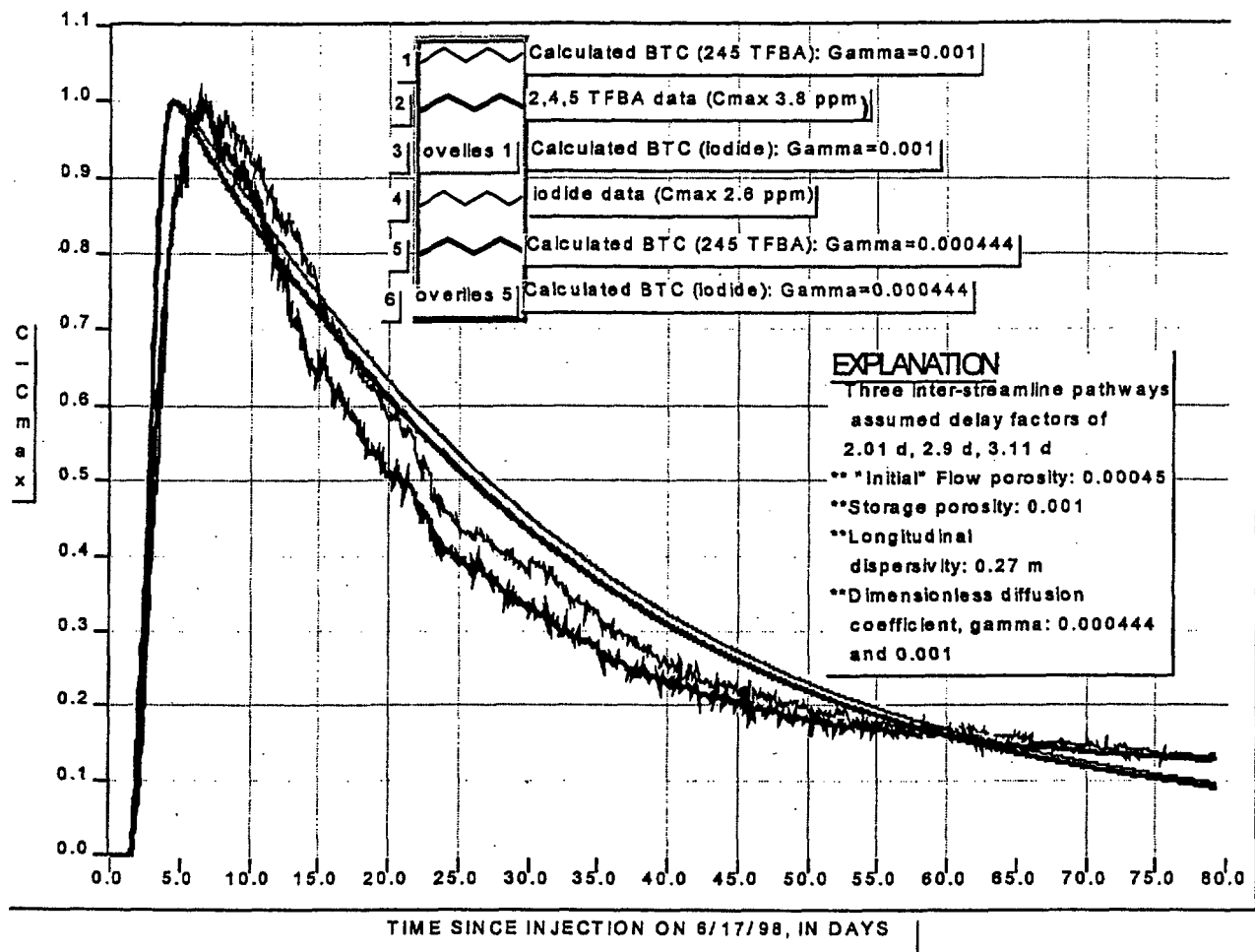


FIGURE 8 . BREAKTHROUGH CURVE FOR 6/17/98 2,4,5 TFBA AND IODIDE TRACER TEST, MATCHED BY DUAL-POROSITY, PARTIAL-RECIRCULATION SOLUTION DERIVED FROM MOENCH (1995), WITH STORAGE POROSITY OF 0.001 AND DIMENSIONLESS DIFFUSION COEFFICIENTS, GAMMA, OF 0.000444 AND 0.001

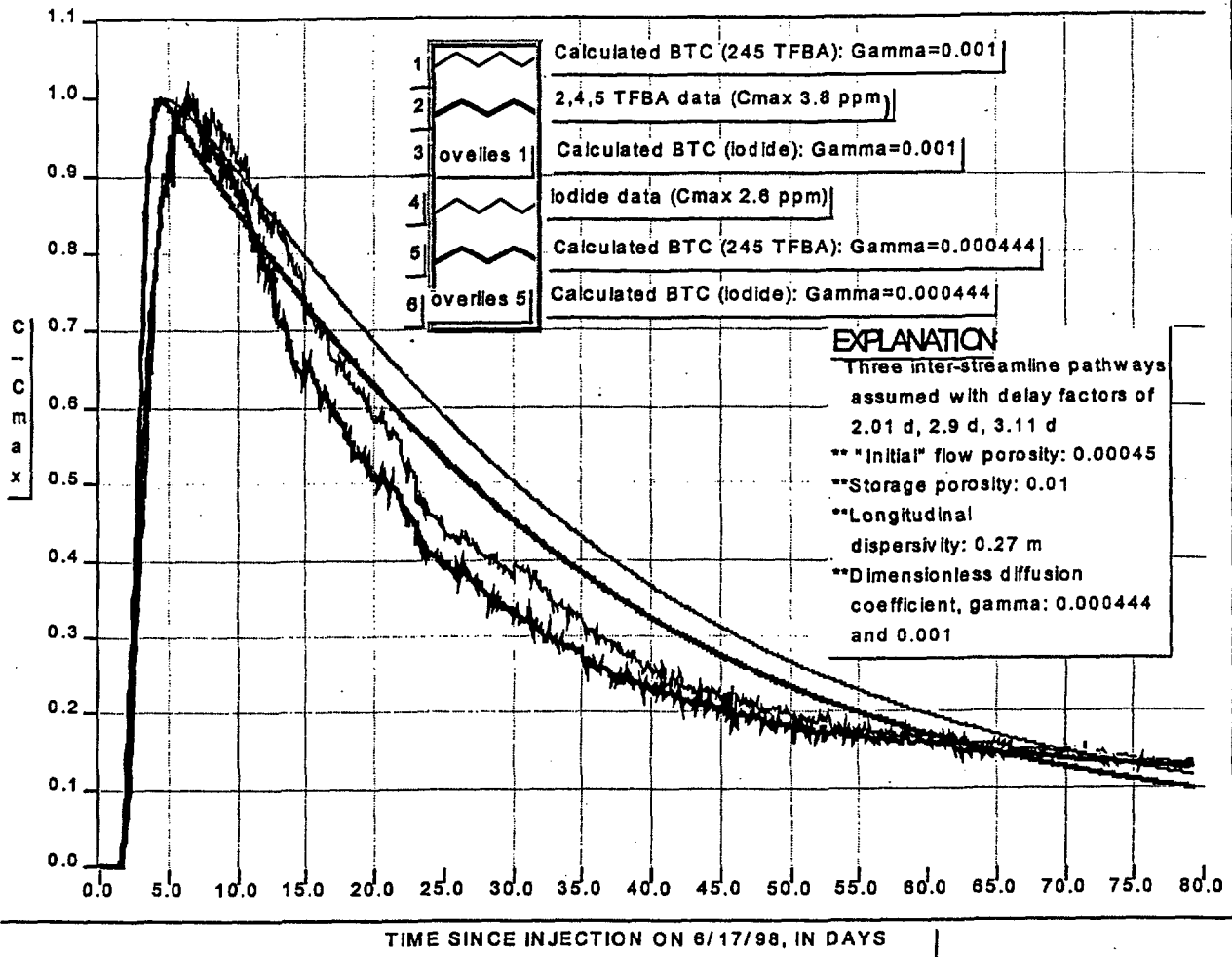


FIGURE 9 . BREAKTHROUGH CURVE FOR 6/17/98 2,4,5 TFBA AND IODIDE TRACER TEST, MATCHED BY DUAL-POROSITY, PARTIAL-RECIRCULATION SOLUTION DERIVED FROM MOENCH (1995), WITH STORAGE POROSITY OF 0.01 AND DIMENSIONLESS DIFFUSION COEFFICIENTS, GAMMA, OF 0.000444 AND 0.001

## REFERENCES

Bowman, R.S., 1984, Evaluation of some new tracers for soil water studies, *Journal of the Soil Science Society of America*, v. 48, p. 987-993. (Submitted to RIS for Accession # 5/21/99.)

Day, W.C., Dickerson, R.P., Potter, C.J., Sweetkind, D.S., San Juan, C.A., Drake, R.M., II, and Fridrich, C.J., 1998, Bedrock geologic map of the Yucca Mountain area, Nye County, Nevada: *U.S. Geological Survey Geologic Investigations Map I-2627*, scale 1:24,000. TIC Catalog # 238732.

Fahy, M.F., 1997, Dual-porosity analysis of conservative tracer testing in saturated volcanic rocks at Yucca Mountain in Nye County, Nevada: *International Journal of rock mechanics and mining science*, v.34, No.3/4, Paper 074. TIC Catalog # 237601.

Freeze, R.A., and Cherry, J.A., 1979, *Groundwater*: Englewood Cliffs, N.J., Prentice-Hall, 604 p. TIC Catalog # 217571.

Geldon, A.L., Umari, A.M.A., Earle, J.D., Fahy, M.F., Gemmell, J.M., and Darnell, Jon, 1998, Analysis of a multiple-well interference test in Miocene Tuffaceous rocks at the C-hole complex, May-June 1995, Yucca Mountain, Nevada: *U.S. Geological Survey Water-Resources Investigations Report 97-4166*, 33 p. MOL.19980514.0524.

Levenspiel, O., 1972, *Chemical reaction engineering*, second edition, New York, John Wiley and Sons. NNA.19910207.0115.

Moench, A.F., 1989, Convergent radial dispersion: a Laplace transform solution for aquifer tracer testing: *Water Resources Research*, v.25, no.3, p. 439-447. TIC Catalog # 238281.

Moench, A.F., 1995, Convergent radial dispersion in a double-porosity aquifer with fracture skin: Analytical solution and application to a field experiment in fractured chalk: *Water Resources Research*, v.31, no.8, p.1823-1835. TIC Catalog # 233132.

Moench, A.F., 1996, Correction to "Convergent radial dispersion: a Laplace transform solution for aquifer tracer testing": *Water Resources Research*, v.32, no.5, p. 1475. (Submitted to RIS for Accession # 5/21/99.)

Skagius, K., and Neretnieks, I., 1986, Porosities and diffusivities of some nonsorbing species in crystalline rocks: *Water Resources Research*, v. 22, no. 3, p. 389-398. TIC Catalog # 225291.

## Appendix C: Reactive Tracer Testing in the Bullfrog Tuff

### C.1 Test Strategy

Tracer testing in the Bullfrog Tuff at the C-holes was conducted with the multiple objectives of (1) testing/validating conceptual models of radionuclide transport through a dual-porosity system, (2) obtaining estimates of key transport parameters in the Bullfrog Tuff, and (3) assessing the applicability of laboratory-derived sorption parameters to field-scale transport predictions. To accomplish all of the test objectives in a reasonable time, we chose to conduct a forced-gradient, cross-hole tracer test involving the simultaneous injection of four tracers having different physical and chemical properties. By simultaneously introducing the tracers (in a single solution), we ensured that they all experienced the same flow field and hence followed identical flow pathways through the system. The test interpretation could then be based on comparing the responses of the different tracers in addition to analyzing the individual responses of the tracers. The tracers used were (1) pentafluorobenzoate (PFBA), (2) bromide ion, (3) lithium ion, and (4) ~360-nm diameter carboxylate-modified-latex polystyrene microspheres (Interfacial Dynamics, Inc.). Lithium bromide salt was used as the source of lithium and bromide. PFBA and bromide were analyzed by high-pressure liquid chromatography with a UV absorbance detector, lithium was analyzed by inductively coupled plasma-atomic emission spectrometry (ICP-AES), and the microspheres were analyzed by flow cytometry (Steinkamp et al., 1991; Becker et al., 1999).

The bromide and PFBA served as nonsorbing solutes with matrix diffusion coefficients differing by about a factor of three (as determined from diffusion cell experiments discussed in Section 8.0). Batch sorption experiments have established the nonreactivity of both bromide and PFBA in with C-holes tuffs (Section 6.0). Both tracers are monovalent anions in groundwater, which has a pH of about 8. A comparison of the responses of these two tracers was expected to yield information about matrix diffusion, as the smaller bromide ion would be expected to diffuse more readily into the matrix than the larger PFBA. Robinson (1994) has shown that in a dual-porosity system, a higher diffusivity tracer is expected to have a breakthrough curve with a lower, slightly delayed peak and a longer tail relative to a lower diffusivity tracer. However, in a single-porosity system (i.e., a classic porous medium) two such tracers should behave identically. Thus, if bromide appeared attenuated relative to PFBA, it would indicate that a dual-porosity system conceptualization was valid. By simultaneously analyzing the breakthrough curves of the two tracers, we planned to obtain quantitative estimates of parameters describing both flow field dispersion and matrix diffusion in the system.

Lithium ion served as a weakly-sorbing solute tracer. Its response was to be interpreted by comparing with the responses of the PFBA and bromide. The diffusion coefficient of lithium is expected to be intermediate between PFBA and bromide (about two-thirds of the bromide diffusion coefficient; Newman, 1973, pp. 229-230), so in the absence of sorption, its response would be expected to fall between that of PFBA and bromide. Therefore, any attenuation of lithium relative to bromide, manifested as either a lower peak, a delayed peak, or both, could be attributed to sorption. In generic calculations (not location specific), we have predicted lithium transport relative to nonsorbing solutes in field tests assuming both single- and dual-porosity media. Breakthrough curve predictions for lithium and for two different nonsorbing solutes with different matrix diffusion coefficients (e.g., PFBA and bromide) are shown in Fig. C-1. It is apparent from this figure that, in a dual-porosity system with no sorption in fractures ("Matrix Sorption" curve in upper half of Fig. C-1), the lithium response is predicted to have a lower peak

concentration than the nonsorbing solutes, but its peak is not significantly delayed in time relative to the nonsorbing solutes. The two nonsorbing solutes have different responses because the more diffusive tracer moves more readily out of fractures and into the matrix than the less diffusive tracer (see discussion above). In a single-porosity system (bottom half of Fig. C-1), the lithium response is predicted to be much lower in peak concentration and much later in time relative to the nonsorbing solutes (which have identical curves because there is no matrix diffusion). This type of behavior is also predicted in a dual-porosity system with significant sorption in fractures ("Frac and Mat Sorp." curve in upper half of Fig. C-1), although the peak lithium concentration in this case is predicted to be slightly lower and the tail of the response slightly longer than in the single-porosity case because of lithium diffusion into the matrix. These generic predictions form the basis for qualitatively determining whether transport at the C-holes is governed by dual-porosity or single-porosity transport behavior. That is, we look for the "hallmarks" of matrix diffusion and sorption, as shown in Fig. C-1, to determine whether a single- or dual-porosity flow/transport conceptualization is appropriate based on the field tracer test data.

We planned to deduce quantitative lithium sorption parameters in the system using the models described in Appendix D to fit the lithium breakthrough curve under the constraint that the dispersion and matrix diffusion parameters deduced from the simultaneous analysis of the bromide and PFBA responses must apply to the lithium as well. Thus, the only adjustable parameters in the lithium fitting exercise would be sorption parameters.

The polystyrene microspheres were introduced into the test for two purposes: (1) they served as colloid tracers to provide insights into the potential for colloidal radionuclide transport in the saturated zone near Yucca Mountain, and (2) they served as large, low diffusivity tracers that should be excluded from the matrix and hence provide an indication of true fracture flow in the system without the effects of matrix diffusion. Carboxylate-modified-latex (CML) polystyrene microspheres with fluorescent dye tags were used because these microspheres had previously been shown to have less tendency for attenuation/filtration in fractured systems than other synthetic colloids that we considered (Reimus, 1995, pp. 49-50). The spheres have a density of 1.055 g/cm<sup>3</sup>, which minimizes their tendency to settle in groundwater. The fluorescent dye tags allowed the spheres to be discriminated from natural colloidal material and to be quantified at concentrations as low as ~100/mL using flow cytometry (Steinkamp et al., 1991; Becker et al., 1999). The CML spheres have carboxyl functional groups on their surfaces, which give them a negative surface charge at pHs greater than about 5; and unlike most other polystyrene microspheres, they also have hydrophilic surfaces (Wan and Wilson, 1994). Both of these features tend to minimize attractive interactions with rock surfaces (Reimus, 1995, pp. 49-50), and they make the spheres very stable against flocculation, even at relatively high ionic strengths, which is important if the spheres are to be injected simultaneously with solutes in a relatively concentrated solution. However, despite these measures, we still expected significant attenuation of the spheres based on previous experience in both laboratory- and field-scale fractured systems (Becker et al., 1999). We used 360-nm-diameter spheres because we found in previous work that larger spheres were more attenuated in fractured systems, possibly due to more rapid settling of the larger particles (Becker et al., 1999). Also, the flow cytometer that we had access to had a lower size detection limit of about 250-nm diameter, although this does not represent a fundamental limitation of the technique.

## C.2 Test Procedure

Because of the considerable investment associated with conducting a test involving multiple tracers, we first conducted two single-tracer pilot tests to determine nonsorbing tracer travel times and recoveries from wells c#1 and c#2 to well c#3. Well c#3 was used as the production well in all tests because it has the largest open-hole transmissivity of the three C-holes (Geldon, 1996, pp. 70-71). The pilot tests allowed us to (1) determine which hole, c#1 or c#2, offered a faster, higher peak concentration response and would therefore be the preferred injection hole for a test involving a reactive tracer, (2) estimate tracer masses required for the multiple tracer test, and (3) plan sampling frequencies for the multiple tracer test. Although c#2 is much closer to c#3 than c#1 (~30 m vs. ~80 m at depth), it was not taken for granted that c#2 would have a better tracer response because (1) local fracture strikes tend to be oriented more in the direction of c#1-to- c#2, (2) c#1 had approximately the same magnitude pressure response as c#2 when pumping c#3, and (3) the natural gradient is believed to be approximately in the direction from c#3 to c#2 (Geldon, 1993, pp. 43-50; Geldon et al. 1997, p. Hydraulic Tests-16). We were particularly concerned that if we didn't inject enough lithium bromide (which is only ~8% lithium by mass) into the system, we would not observe any lithium at the production well. This concern stemmed from the uncertainty in the expected lithium attenuation due to sorption and also because of the relatively high lithium background concentration, ~65 µg/L, in the groundwater. Additionally, environmental permitting dictated that we minimize, within reason, tracer masses injected.

The packed-off zone in c#3 (Fig. 1-2) was pumped continuously at about 575 L/min in each test. The first pilot tracer test involved the injection of approximately 10 kg of PFBA into well c#2 on May 15, 1996. The PFBA was dissolved in ~1000 L of groundwater. The test was conducted under partial recirculation conditions with about 20 L/min of the water produced from c#3 (~3.5% of production rate) being continuously reinjected into c#2. The recirculation was initiated approximately 24 hr before tracer injection to establish a steady flow field, and it was continued for 23 days after injection. The tracer solution was plumbed into the recirculation loop such that there were no flow interruptions during injection.

The second pilot test involved the injection of about 12.7 kg of iodide (~15 kg of sodium iodide dissolved in ~1000 L of groundwater) into c#1. It was conducted in a manner very similar to the PFBA pilot test and was initiated on June 18, 1996. The recirculation rate in this test was about 15 L/min (~2.6% of production rate), and recirculation continued for 16 days after injection.

The results of these two pilot tests clearly indicated that c#2 was the preferred injection hole for the multiple tracer test, as the PFBA recovery from the May injection was about 73% and the iodide recovery from the June injection was estimated between 6 and 10%. The May PFBA response from c#2 was previously reported by Reimus and Turin (1996, pp. 9-26) (also shown in Figs. C-4 and C-6 of this report), and the iodide response from c#1 is shown in Fig. C-2. Based on these results, a tracer test involving the simultaneous injection of ~12 kg PFBA, ~180 kg of lithium bromide (14.5 kg lithium, 165.5 kg bromide), and ~7 g of microspheres (~3.5 x 10<sup>14</sup> spheres) into c#2 was initiated on October 9, 1996. Because of the much greater tracer mass in this test than in the pilot tests, and the desire to minimize solute concentrations to prevent microsphere flocculation, the tracers were dissolved in ~12,000 L of groundwater instead of the ~1000 L used in the pilot tests. The greater volume kept the density contrast between

tracer solution and the downhole groundwater about the same as in the pilot tests. The microspheres were actually introduced to the tracer mixture after about one-third of the solution had been injected, which corresponded to about one injection interval volume. The test was carried out under partial recirculation conditions with a recirculation rate of about 20 L/min that was continued for 40 days. Steady flow conditions were established by starting recirculation ~36 hr prior to tracer injection.

### C.3 Test Results

The breakthrough curves (normalized to mass injected) of the four tracers in the multiple-tracer test are shown on a log-log plot in Fig. C-3. This test was conducted for ~8200 hrs, and the tracer recoveries at the end of the test were estimated to be ~69% for PFBA, ~69% for bromide, ~39% for lithium, and ~15% for the microspheres (at ~6900 hr into the test). Microsphere concentrations dropped below quantifiable levels (<50/ml) after 6900 hrs, so results were not reported after that time, although the spheres were still detectable in the production water. PFBA concentrations also dropped below quantifiable levels (<4 µg/L) after about 7500 hr into the test. This fact, coupled with the uncertainty in how much PFBA from the May 1996 pilot test was still contributing to the PFBA response in the multiple-tracer test, introduced considerable uncertainty into estimates of PFBA concentrations and recoveries from the October 1996 injection, particularly at late times. The PFBA response shown in Fig. C-3 represents the lower bound case for PFBA concentrations from the October injection. This lower bound was obtained by subtracting 10 µg/L (the residual PFBA concentration in the system at the beginning of the reactive tracer test) from the measured concentrations. Although this assumption may seem unrealistic, it is supported by the fact that the PFBA concentrations from the May injection remained essentially constant at 10-14 µg/L for the last 6-7 weeks prior to the October injection. PFBA concentrations were also calculated by subtracting (from the measured concentrations) an exponentially-decaying function with a decay constant determined by a linear least-squares fit to the tail of the May breakthrough curve on a log-log plot. We found that the PFBA response up to 2000 hrs after injection was insensitive to which assumption was made about residual PFBA concentrations. However, because the measured concentrations after 2000 hrs declined to the point where assumed residual concentrations became a significant fraction of the measured values, the tail of the PFBA curve assuming an exponential decay became noticeably higher than the tail of the PFBA curve shown in Fig. C-3.

This uncertainty in residual PFBA concentrations significantly affects calculated PFBA recoveries; the recoveries associated with the two cases described above were 63% for the first case and 74% for the exponential decay case. We give more weight to the exponential decay case at late times because if the assumptions associated with the first case are accepted, then the PFBA concentrations from the October injection actually become negative after about 6000 hrs because the measured PFBA concentration decreases to less than 10 µg/L at this time. Because negative concentrations are a physical impossibility, we conclude that concentrations from the May injection must have continued to decline after the October injection, although probably not as fast as the exponential decay assumed for the upper curve in Fig. C-3. We therefore consider 69% to be reasonable estimate of the PFBA recovery from the October injection given the uncertainties and lines of reasoning discussed above.

The most striking feature of the breakthrough curves in Fig. C-3 is their bimodal (double-peaked) behavior, discussed below. The PFBA and bromide responses show clear qualitative

evidence of matrix diffusion, as the normalized PFBA concentrations are higher than the normalized bromide concentrations at both peaks, and the second bromide peak is somewhat delayed relative to the PFBA with a tail that appears to cross over the PFBA at long times. As discussed above, these are all hallmarks of matrix diffusion in a dual-porosity system. The lithium response shows obvious attenuation relative to the nonsorbing tracers, providing clear evidence of lithium sorption. It is interesting that the attenuation of the first peak is almost exclusively a lowering of the peak with little or no time delay, while the attenuation of the second peak involves a clear time delay along with a dramatic lowering of concentration. Explanations for this behavior are offered in the test interpretation section.

The microsphere breakthrough curve, which is corrected for the ~3.5-hr delay in their injection time relative to the solutes, is clearly attenuated compared to the solutes. However, it is interesting that their first arrival preceded the solutes, although if the delay in their injection is not accounted for, the first arrival time is very close to the first solute arrival time. The early microsphere arrival behavior has been observed in other field and laboratory tests in fractured systems (Reimus, 1995, p. 51; Becker et al., 1999), and it may be attributed to a small fraction of the spheres moving rapidly through high-velocity streamlines in fractures without having the opportunity to diffuse into low-velocity or stagnant water. The majority of the microspheres may have been attenuated by filtration mechanisms, possibly gravitational settling, as proposed by Becker et al. (1999). It is also interesting that while the first microsphere peak occurs earlier than the solutes, the second peak occurs later than the solutes. A quantitative interpretation of the microsphere response is discussed in Section C.5.

The response to the May PFBA injection into c#2 was significantly different than the response in October. The first 1800 hrs of the normalized PFBA breakthrough curves in the two tests are shown in Fig. C-4 (with linear axes). The May breakthrough curve is a more conventional single mode response. PFBA concentrations from the May injection were monitored for just over 3000 hr with a total recovery of ~73%, and the total recovery at 3000 hr in the October test was ~58%; i.e., a higher recovery in the May test than in the October test at the same point in time.

We offer the following explanation for the different responses in May and October. Because of the lack of mixing in the injection interval, the tracer solutions, which were injected directly below the top packer and were ~2% more dense than the groundwater in each test, probably sank rapidly to the bottom of the interval in each test. The tests were conducted in an identical manner in every respect except that only ~1000 L of tracer solution was injected in May, while ~12,000 L was injected in October. (The duration of recirculation was also different, 23 vs. 40 days, but all significant differences occurred prior to 23 days.) The injection interval volume was ~4300 L, so in the May test, only one-quarter of an interval volume was injected, and it is very possible that only flow pathways in the lower part of the interval conducted tracers out of the borehole. In contrast, in the October test, approximately three interval volumes of tracer solution were injected, so the volume between the packers should have completely filled with tracer solution and tracers would have accessed flow pathways throughout the entire length of the interval. We suspect that the first peak in October was the result of a small percentage (~13%) of the injected tracer mass entering a flow pathway (or set of pathways) in the upper part of the borehole that was not accessed in May. The flow survey information depicted in Fig. 1-2 certainly suggests that the zone of highest flow in well c#2 occurs in the upper half of the interval, although one cannot necessarily conclude that there is a cross-hole connection originating from these pathways. Much of the remaining mass then presumably followed

pathways that were also accessed in May and resulted in the second peak occurring at the same time as the May peak (Fig. C-4). However, because the shapes of the May and second October peaks are different, and the total PFBA recovery was actually lower in October despite the early peak, we also suspect that a considerable fraction of the mass injected in October followed other pathways that were not accessed in May and were slower, in general, than those accessed in May.

Although we have no direct proof to support this hypothesis, we conducted some simple laboratory experiments involving the injection of dyed salt solutions into a ~2-m-long, ~1.5-cm ID, clear plastic tube with a tee about 1 m from the top of the tube to serve as a pathway out of the borehole. The dyed solution had approximately the same density as the solutions injected in the field experiments, and it was injected at the same rate, relative to the diameter of the tube, as in the field. We found that even though the tee was the only exit point for flow out of the tube, most of the dyed solution sank below the tee and remained in the lower part of the tube

(unpublished data). However, it must be recognized that the Reynolds number,  $\frac{DV\rho}{\mu}$ , where D = borehole diameter, V = fluid velocity,  $\rho$  = fluid density, and  $\mu$  = fluid viscosity (Reynolds number is a measure of turbulence - Bird et al., 1960) was drastically different in the laboratory than in the field; more turbulence would have been expected in the field.

We view the bimodal response in October and the single-peak response in May as serendipitous good fortune. First, the two peaks allow us to objectively conclude that there are at least two separate sets of flow pathways that contributed to the October tracer responses. This allows us to estimate a different set of transport parameters for each set of pathways, meaning that we effectively conducted "two tests in one."

#### C.4 Quantitative Interpretation of Solute Responses

The solute tracer responses were interpreted by simultaneously fitting the breakthrough curves using a semi-analytical, dual-porosity transport model, RELAP, which is described in detail in Appendix D and briefly summarized here (see also, Reimus and Dash, 1998, all pages). The physical, conceptual, and mathematical models assumed for the field transport system are depicted in Fig. C-5. The equations shown at the bottom of Fig. C-5 are Laplace-domain "transfer functions" that describe tracer residence time distributions within each of the system "components." The most important of these is the transfer function for the groundwater system, which is taken from Tang. et. al. (1981). This transfer function assumes 1-dimensional advective-dispersive transport in parallel-plate fractures with 1-dimensional diffusion (perpendicular to fracture flow) into a homogeneous, infinite matrix. It also assumes linear, equilibrium, reversible sorption of a reactive species and a constant flow velocity in the fractures. Model formulations assuming a finite matrix (Maloszewski and Zuber, 1983, 1985), radial flow (Moench, 1995; Becker, 1996) and rate-limited sorption (Maloszewski and Zuber, 1991) are also embodied in RELAP. These were used to evaluate the sensitivity of the derived transport parameters to radial vs. linear flow, infinite vs. finite matrix, and equilibrium vs. rate-limited sorption. A detailed description of the mathematical development of the models embodied in RELAP is provided in Appendix D.

The transfer functions shown in Fig. C-5 were multiplied together to describe transport throughout the system; a multiplication in the Laplace domain is equivalent to a convolution integral in the time domain (Jenson and Jeffreys, 1977, pp. 169-170). Although not shown

explicitly in Fig. C-5, recirculation of the production water from well c#3 into c#2 was also accounted for (see Appendix D). However, the amount of recirculation was so small (~3.3%) that it made virtually no difference whether or not recirculation was accounted for at all. Wellbore storage was accounted for by assuming that the boreholes were well-mixed, with the tracers experiencing an exponential-decay residence time distribution with a time constant slightly greater than the volume of the interval divided by the volumetric flow rate into (injection well) or out of (production well) the interval. Note that an equation for wellbore mixing in the production well is not shown in Fig. C-5 because residence times in this well were very short (less than 10 minutes) due to the high flow rate out of the well (~575 L/m). The Laplace domain solutions were then inverted to the time domain using a Fourier-transform inversion technique (Appendix D). Because the Fourier-transform technique is very efficient (and stable), it could be performed thousands of times per minute on a computer workstation, making it practical to estimate model parameters by systematic, brute-force adjustments of their values to achieve a least-squares fit to the data. The fitting procedure used to quantitatively interpret the October tracer responses is summarized in Table C-1 and discussed in detail in the following two subsections.

#### C.4.1 Nonsorbing Solutes

The first step in the interpretation procedure involved using the transfer function model depicted in Fig. C-5 to simultaneously fit the PFBA and bromide data assuming that all transport parameters except for diffusion coefficients were identical for the two solutes. Bromide matrix diffusion was assumed to be triple that of PFBA based on diffusion cell results presented in Section 8.0. The matrix and fracture retardation factors for these two nonsorbing tracers were set equal to 1. The procedure involved simultaneously fitting the early tracer peak(s) with a single set of model parameters assuming that only a fraction of the tracer mass accounted for the peak. The parameters adjusted to achieve the fit were (1) the mass fraction,  $f$ , (2) the mean fluid residence time,  $\tau$ , (3) the Peclet number,  $Pe = L/\alpha$ , where  $L$  is the distance between wells and  $\alpha$  is the dispersivity, and (4) the lumped parameter,  $\frac{\phi}{b} \sqrt{D_m}$ , which is effectively a mass transfer coefficient for diffusion into stagnant water, assumed to be in the matrix ( $\phi$  is the matrix porosity,  $b$  is the fracture half-aperture, and  $D_m$  is the matrix diffusion coefficient). The matrix porosities and matrix diffusion coefficients measured in laboratory diffusion cell experiments (see Section 8.0) were assumed to apply to the field test; these measurements made it possible to estimate fracture half-apertures in the field test (the only variable in the lumped parameter that could not be independently measured). All other parameters in the transfer function model were fixed according to the manner in which the test was conducted (e.g., the injection concentration, injection duration, and time constants for mixing in the injection and production wellbores).

Although the injection duration was about 10 hrs, we arbitrarily assumed an injection delay time of 4 hr followed by a 6-hr injection when fitting the early tracer response (the first peak). Our rationale for making this assumption was that there was no early response in the May PFBA test (which involved an injection duration of less than one hour), so it seemed logical to assume that the earliest injected tracer solution did not follow the earliest-arriving pathways. We chose a 4-hr delay time because the injected tracer solution volume exceeded the injection interval volume by this time, and we felt that this was a reasonable criteria for when at least a portion of the tracer solution should have begun moving through the earlier-arriving pathways.

Subsequent sensitivity analyses indicated that the best-fitting model parameters were not very sensitive to assumed tracer injection durations ranging from 2 hr to 10 hr, although there was a definite trend toward smaller Peclet numbers (greater dispersion) as the injection duration was shortened. This result is undoubtedly due to the fact that shorter tracer pulses must "spread" more to match the observed breakthrough curve. The injection duration for the second peak was assumed to be the full 10 hrs of injection.

The best fit to the first peak was subtracted from the entire breakthrough curve of each tracer, leaving only a single second peak. The simultaneous fitting procedure was then repeated for the second peak. All of the parameters describing the second peak were adjusted independently of the parameters that offered the best fit to the first peak (except that the sum of the mass fractions in both fits could not exceed 1). This procedure assumed that each peak could be described by a single advection-dispersion equation to account for flow and dispersion in fractures with a single mass transfer coefficient accounting for matrix diffusion. We recognize that the tracer response in reality was probably the result of flow through many pathways in a fracture network, and that these pathways undoubtedly had a distribution of residence times, dispersivities, and matrix diffusion mass transfer coefficients. However, without specific data on the geometry and transport properties of individual pathways, it is difficult to justify assuming more pathways than the number of peaks in the tracer responses. Thus, we initially limited ourselves to two pathways, one for each peak.

It is important to recognize that the simultaneous interpretation of the PFBA and bromide breakthrough curves offers a tremendous advantage over the interpretation of either tracer breakthrough curve individually. In fact, without this simultaneous interpretation, it is not possible to distinguish between the effects of hydrodynamic dispersion and matrix diffusion in a field tracer test. This dilemma is illustrated in Fig. C-6, which shows arguably equally good fits to the May PFBA breakthrough curve obtained using the sets of model parameter values given in Table C-2. It is apparent that, although there is an upper limit to the matrix diffusion mass transfer coefficient that can be assumed in the system (constrained by the fact that the mass fraction of tracer participating in the test cannot exceed 1), a reasonably good fit to the data can be obtained by assuming no matrix diffusion at all (i.e., a single-porosity system). Note that even though the curve with the largest amount of matrix diffusion appears to offer the best fit to the data in Fig. C-6, an equally good fit can be obtained by assuming two overlapping single-porosity pathways with different dispersion parameters or by simply assuming a much longer mean residence time for the tracer solution in the injection borehole. Thus, while the analysis of a single breakthrough curve can offer an upper bound on matrix diffusion and a range of possible values for the dispersion coefficient and mean fluid residence time in the system, it cannot conclusively establish that matrix diffusion is occurring in the system.

We consider fractional mass participation in the tracer tests to be a definite possibility, as the natural gradient is believed to be almost opposite the direction of induced flow from c#2 to c#3 (Fig. 1-2), and some of the tracer mass could have sunk (due to density effects) out of the zone of influence of induced flow. Also, it is possible that at least some of the unaccounted-for tracer mass could have actually moved through the tuff matrix rather than through fractures because the matrix permeability is not zero (as assumed in the dual-porosity model formulation). It can be shown that even with very low matrix permeabilities relative to fracture permeabilities, a significant amount of tracer mass can still move through the matrix if the cross-sectional area available for matrix flow is much greater than that for fracture flow. For instance, if the cross-sectional area for fracture flow is 0.001 times that of the matrix, but the fracture permeability is

1000 times greater than that of the matrix, then equal volumetric flows would be expected through both the fractures and matrix. Given the fracture densities and apertures observed in C-Holes logs, it is not unreasonable to expect some mass flow through the matrix.

Fig. C-7 shows the best fits to the PFBA and bromide breakthrough curves in the reactive tracer test. The transport model parameters used to obtain the fits are given in Table C-3. Note that different mean residence times ( $\tau$ ) and Peclet numbers (Pe) were obtained in each pathway depending on whether linear or radial flow was assumed. In a heterogeneous, confined aquifer, the flow velocity to a single production well is expected to vary between linear and radial (National Research Council, 1996, pp. 252-259). Thus, if we assume that the Bullfrog Tuff is reasonably confined, as suggested by Geldon (1996, p. 71), presenting the two sets of residence times and Peclet numbers in Table C-3 is a way of bounding these parameter estimates as a result of flow field uncertainty. The radial mean residence time is always less than the linear residence time, and the radial Peclet number is always greater than the linear Peclet number. This somewhat confusing result can be qualitatively explained by recognizing that the models implicitly assume that the dispersion coefficient is the product of the dispersivity ( $\alpha$ ) and the fluid velocity. Under this assumption, for a given dispersivity, a solute will tend to experience more dispersion in radial flow than in linear flow because any time the solute disperses ahead of the mean position, it will be subjected to a greater flow rate, and any time it disperses behind the mean position, it will be subjected to a slower flow rate. Thus, leading solute particles will tend to be swept further ahead and lagging solute particles will tend to lag further behind in radial flow than they would be in linear flow. In effect, the radial flow field has an additive effect to the dispersion that would be experienced in a linear flow field. Any breakthrough curve can always be fitted equally well assuming either type of flow field; only the values of the parameters will differ. Fig. C-8 shows the relationships between  $\tau$  and Pe in radial and linear flow as a function of linear Peclet number. These relationships were derived using RELAP to fit a linear response with a radial model.

Table C-3 also indicates that the assumption of a finite matrix with a fracture spacing of 4 cm in the second pathway offered a better fit to the end of the tracer breakthrough curves than an infinite matrix assumption (which resulted in underprediction of the tracer responses). This was the only instance where assuming a finite matrix improved a fit. However, we do not consider this result terribly significant because the data at the ends of the breakthrough curves have considerable scatter due to (1) lower analytical precision at the low concentrations, (2) approach to background concentrations, and (3) in the case of PFBA, uncertainty in the contribution from the May 1996 injection.

Another assumption that resulted in better fits to the PFBA and bromide breakthrough curves was that a portion of the reactive tracer test responses was due to tracers following exactly the same pathways as the PFBA in the May test (since the May peak and the second October peak occurred at the same time). In this case, the second peak can be accounted for almost entirely by the May pathways, and a third set of pathways is then required to fit the long tails of the October responses. This approach was discussed in considerable detail in YMP milestone SP23APMD (Reimus and Turin, 1997, pp. 11-12, 36-37), and it is therefore not discussed further here. Although the three-pathway approach can be readily justified because of the observed May PFBA response, we consider it to be a deviation from our self-imposed constraint of not introducing more "pathways" than the observed number of tracer peaks. Also, the introduction of additional pathways should always result in better fits to tracer responses, so it is not surprising that assuming three pathways results in a better fit than assuming two-pathways.

It is interesting that the lumped matrix diffusion parameters that offered the best fits to the PFBA and bromide data (see Table C-3) suggest that the amount of matrix diffusion in the second set of pathways was significantly less than in the first set of pathways. This result appears to contradict our theory that the first peak was the result of a small amount of tracer mass following pathways that were higher in the injection borehole (see Section C.3). The upper half of the injection interval was in the more densely welded central Bullfrog Tuff lithology, which has about a factor of three lower matrix porosity than the tuff in the lower half of the injection interval (see Section 8.0). Also, laboratory measurements of matrix diffusion coefficients in the central and lower Bullfrog Tuffs indicate that the diffusion coefficients in the poorly-welded lower unit are at least two times higher than those in the central unit (also in Section 8.0). Thus, if the early peak was due to tracers moving through the central Bullfrog Tuff and the later peak was due to tracers moving through the lower Bullfrog Tuff, the expectation would be that the first peak would have smaller matrix diffusion parameters, not larger ones, as determined in the fits. However, it must be kept in mind that (1) we do not know the exact locations of the flow pathways that resulted in the tracer responses (they could have all been in either the central or the lower units), (2) the lumped matrix diffusion parameter includes the average fracture half-aperture, which could have been significantly larger in the pathways that resulted in the later peak, thus resulting in a smaller lumped matrix diffusion parameter for these pathways, and (3) there is undoubtedly some variability in porosity and matrix diffusion coefficients within a given lithology (the samples analyzed for porosity and matrix diffusion coefficients were taken from only a few discrete locations). Given these uncertainties, we do not consider it terribly surprising that the amount of matrix diffusion appeared to be greater in the shorter residence time pathways.

#### C.4.2 Lithium

We proceeded to fit the lithium data using the same mean residence times and Peclet numbers that offered the best simultaneous fit(s) to the PFBA and bromide data. The diffusion coefficient for lithium was assumed to be two-thirds that of bromide and twice that of PFBA (Newman, 1973, pp. 229-230). Fits were obtained by adjusting the fracture and matrix retardation coefficients in the flow system equation of Fig. C-5, which assumes equilibrium, linear, and reversible sorption in homogeneous pathways. Sorption in fractures could be the result of the presence of mineral alteration phases (mineral coatings) with a high cation exchange capacity or the presence of crushed tuff within the fractures, or a combination of both. The retardation coefficient, R, is related to the linear distribution coefficient through the well-known expression,

$$R = 1 + \frac{\rho_B}{\phi} K_D \quad (C.1)$$

where  $\rho_B$  = bulk density, g/cm<sup>3</sup>,

$\phi$  = porosity,

$K_D$  = linear distribution coefficient, cm<sup>3</sup>/g.

Note that the assumption of a linear sorption isotherm is contrary to the nonlinear Langmuir isotherm behavior observed in the lithium laboratory experiments described in Section 6.0. However, the asymptotic, low concentration behavior of a Langmuir isotherm is the same as

a linear isotherm with  $K_D$  equal to  $K_L S_{max}$ , so we felt that assuming linear sorption behavior was a reasonable starting point. Also, the relatively fast sorption kinetics observed in the laboratory column experiments and in earlier batch sorption tests (Fuentes et al., 1989, p. 37) suggested that the assumption of equilibrium sorption should be valid for the tracer arrival times in the October test.

Our initial attempts to fit the first lithium peak (up to about 120 hr into the test) using the physical model parameters deduced from the PFBA and bromide fits were unsatisfactory. We found that assuming linear, equilibrium sorption in the matrix resulted in a peak that occurred later than the actual data with a tail that was much higher than the data. We also found we had to assume no sorption in fractures (i.e.,  $R_f = 1$ ) because any fracture sorption resulted in a peak that occurred much too late to match the data. Note that the absence of fracture sorption does not necessarily mean that lithium wasn't sorbing to fracture surfaces; it simply means that the fractures had very little surface area available for sorption (i.e., without crushed fill or sorptive coatings). Because of the relatively poor fits obtained assuming equilibrium, linear sorption behavior, we proceeded to fit the lithium data assuming (1) rate-limited, linear sorption, (2) equilibrium, nonlinear (Langmuir) sorption, and (3) rate-limited, nonlinear sorption with a rate constant equal to the slowest rate constant measured in the crushed-tuff column experiments described in Section 7.1. RELAP offers the option of using a transfer function expression for rate-limited, linear sorption in a dual-porosity system; and a numerical model, RETRAN, was used to simulate nonlinear sorptive transport through a dual-porosity system (Appendix D; Reimus and Dash, 1998, all pages).

Fig. C-9 shows fits to the first lithium peak obtained for the cases mentioned above, including the equilibrium, linear case. Sorption parameters corresponding to the fits in Fig. C-9 are given in Table C-4. These parameters were calculated assuming that the flow pathways resulting in the first peak were in the central Bullfrog Tuff ( $\rho_B = 2.34 \text{ g/cm}^3$  and  $\phi = 0.1$ ). The  $K_D$  and  $S_{max}$  values would be ~3.5 times higher if it were assumed that the flow pathways were in the lower Bullfrog Tuff ( $\rho_B = 1.90 \text{ g/cm}^3$  and  $\phi = 0.29$ ). The best fit to the data was obtained assuming rate-limited, linear sorption in both the fractures and matrix, although Table C-4 shows that the best-fitting rate constants were over an order of magnitude lower than those observed in the laboratory column experiments. The assumption of equilibrium nonlinear (Langmuir) sorption provided a better fit to the tail of the data than the equilibrium linear fit, but the peak was predicted to occur too early. The assumption of rate-limited nonlinear (Langmuir) sorption using rate constants from the crushed-tuff column experiments (Section 7.1) also resulted in improved fits to the tail of the data, but the peak was again predicted to occur early. Fig. C-10 shows a comparison of the Langmuir isotherms derived from the laboratory data and from the field data assuming both equilibrium and rate-limited sorption. Note that the rate-limited field-derived isotherm is in quite good agreement with the laboratory isotherm.

It should be emphasized that the fits in Fig. C-9 and Table C-4 are not unique; reasonable fits can be obtained for any isotherm ranging from the equilibrium, field-derived Langmuir isotherm shown in Fig. C-10 to a linear isotherm, provided that the sorption rate constants are allowed to vary (slower rate constants result in more linear isotherms). The rate-limited nonlinear fit shown in Fig. C-9 (with corresponding isotherm in Fig. C-10) was selected for presentation because it corresponds to the slowest laboratory-observed sorption rate. It should also be noted that the lithium injection concentration in all RETRAN (nonlinear) simulations was assumed to be 1200 mg/L (the concentration of the injectate), which resulted in the maximum possible effect of isotherm nonlinearity on the resulting fits. The nonlinear "fits" obtained using

RETRAN are not true least-squares fits because RETRAN does not currently offer automated minimization of sums of squares of differences. However, after conducting many RETRAN simulations, we were confident that the nonlinear fits in Fig. C-9 were relatively close to best fits. We found that better nonlinear fits could be obtained by assuming shorter injection pulse durations and correspondingly longer injection delays (we assumed a 6-hr pulse after a 4-hr delay), but we chose to maintain consistency with the assumptions made for the linear cases.

We also considered cases in which physical and chemical heterogeneity were assumed in the pathway(s) that resulted in the first set of tracer peaks. Lithium sorption in both of these cases was assumed to be linear and fast (equilibrium). In each case, the first "pathway" was split into two "pathways" which had either different matrix diffusion mass transfer coefficients (physical heterogeneity) or different lithium sorption parameters (chemical heterogeneity). An important constraint in this pathway-splitting approach was that the PFBA and bromide responses from the two pathways were required to sum to the total observed PFBA and bromide responses in the first 80-100 hrs of the test.

In the physical heterogeneity case, the first pathway was assumed to have a matrix diffusion mass transfer coefficient that was half that in the second pathway. The rationale for this assumption was that higher velocity pathways should tend to have larger average apertures. This has been shown to be the case in numerical simulations of flow and transport in single fractures, where flow is often predicted to be highly channelized in large aperture regions (Moreno et al., 1988; Thompson, 1991; Reimus, 1995, pp. 73-94). The larger average apertures of high-velocity channels give these channels smaller matrix diffusion mass transfer coefficients because the aperture appears in the denominator of the lumped mass transfer coefficient. The larger mass transfer coefficient assumed in the second set of pathways was expected to suppress the tail of the first lithium peak relative to the nonsorbing tracers, which is consistent with the behavior observed in the tracer test. Table C-5 shows the model parameters used to obtain a reasonable fit to the early lithium response assuming physical heterogeneity.

In the chemical heterogeneity case, the mass transfer coefficients in the two pathways were constrained to be identical (equal to the single-pathway fit(s) to the PFBA and bromide data). However, lithium sorption was adjusted such that the first pathway accounted for almost the entire early lithium response, while the second pathway had only a minor contribution to the lithium response. This approach, while admittedly somewhat arbitrary, can be justified by recognizing that fractures often differ significantly in their degree of mineral alteration and fracture fill material as well as in the properties of the surrounding matrix, all of which can significantly affect sorption. It is also logical to assume that the fastest flow pathways may be the most open and least sorptive because of less fill material and possibly less mineral alteration to provide favorable sorption sites for lithium. Table C-6 shows the model parameters used to obtain the best fit to the early lithium response assuming chemical heterogeneity.

An extreme variation of both the physical and chemical heterogeneity cases involved assuming that there was a pathway that had no sorption or matrix diffusion at all. This pathway was assumed to account for all of the first lithium peak and approximately half of the first PFBA and bromide peaks. The remainder of the early PFBA and bromide responses was then accounted for by a second pathway in which a large amount of matrix diffusion (and sorption) was assumed. This case was analyzed to demonstrate that it is possible, however unlikely, to postulate that matrix diffusion is not necessarily occurring in all flow pathways in the system. One would have to speculate the existence of a very large aperture fracture pathway in this case that behaved essentially as a "pipe" to transport a small fraction of the tracers without any matrix

diffusion or sorption. The microsphere data argue against this hypothesis because the microspheres would be expected to move very efficiently through such an open pathway, and this was not the case. Also, one would expect such an open pathway to respond even more quickly and with more tracer mass than was observed. Nevertheless, this case illustrates that it is possible to deduce that a small amount of tracer mass could have moved through the system without being affected by matrix diffusion and sorption. Table C-7 shows the model parameters used to obtain the best fit to the early lithium response for this case.

The lithium fitting exercise was completed by assuming that an additional "pathway" accounted for the late lithium response. This pathway was assumed to have the same physical characteristics (mean residence time, Peclet number, and matrix diffusion mass transfer coefficient) that were deduced from the simultaneous fits to the late PFBA and bromide responses. Lithium sorption parameters were the only parameters adjusted to fit the data. We found that the assumption of equilibrium, linear sorption was adequate to provide good fits to the late lithium response, so rate-limited and nonlinear fits were not attempted. Table C-8 provides lithium sorption parameters that yielded good fits to the late lithium data for the various cases discussed above. Note that the parameters resulting in good fits are all very similar regardless of which assumptions were made to explain the first lithium peak. Fig. C-11 shows examples of a composite fits to the entire lithium response in the reactive tracer test. The fits in this figure assume (1) linear, rate-limited sorption of lithium during the early portion of the test (see Tables C-3, C-4, and C-8 for parameters), and (2) linear, equilibrium sorption of lithium throughout the test, but with chemical heterogeneity in the first pathway (resulting in two sub-pathways, 1A and 1B – see Tables C-3, C-6 and C-8 for parameters). The fits obtained by all other modeling approaches discussed in this section were nearly as good as the ones shown in Fig. C-11.

It should be pointed out that, other than for the early lithium response (which required assuming no sorption in fracture flow pathways in order to obtain a reasonable fit), it was possible to explain the majority of the overall lithium response using a relatively wide range of combinations of fracture and matrix retardation factors. At one extreme, relatively large fracture retardation factors could be used with relatively small matrix retardation factors to obtain reasonable fits. At the other extreme, reasonable fits could also be obtained by assuming no fracture retardation at all, but with relatively large matrix retardation factors. Table C-9 shows selected combinations of fracture and matrix retardation factors in pathways 1b and 2 that offered good fits to the lithium data for the cases discussed above.

While the lithium-fitting exercise points out considerable ambiguity in the interpretation of the lithium data, one must not lose sight of the overall goal of the exercise, which was to determine if laboratory measurements of lithium sorption could be used to predict lithium transport in the field. The field test interval included portions of two major lithologies, the moderately-welded central Bullfrog Tuff and the poorly-welded lower Bullfrog Tuff. Based on laboratory sorption measurements (Section 6.0) and measurements of matrix porosities (Section 8.0), the matrix retardation factors of these two tuffs were predicted to be 12.5 for the central Bullfrog Tuff and 12.0 for the lower Bullfrog Tuff. These retardation factors were calculated using equation (C.1) and assuming that  $K_D$  was equal to the asymptotic slopes of the Langmuir isotherms at low lithium concentrations (i.e.,  $K_D = K_L S_{max}$ , which was 0.43 ml/g for the central Bullfrog Tuff and 1.65 ml/g for the lower Bullfrog Tuff). Note that the lower Bullfrog Tuff has a lower predicted retardation factor than the central Bullfrog Tuff even though it sorbed lithium more strongly in the batch sorption tests. This result can be attributed to the higher porosity of

the lower Bullfrog Tuff; in equation (C.1) the retardation factor is inversely proportional to the porosity, and furthermore, the bulk density is related to porosity by

$$\rho_B = \rho_s(1 - \phi) \quad (C.2)$$

where,  $\rho_s$  = density of pure rock material, g/cm<sup>3</sup>.

Thus, a lower porosity rock will always have a higher predicted retardation factor than a higher porosity rock if the sorption characteristics of the two rocks are similar. In this case, the lower Bullfrog Tuff sorbs lithium about 3 times more strongly than the central Bullfrog Tuff, but the porosity of the lower Bullfrog Tuff is also nearly 3 times higher than the porosity of the central Bullfrog Tuff. Thus, the higher porosity of the lower Bullfrog Tuff offsets its higher sorption capacity, and the end result is that the two rocks are predicted to have almost the same matrix retardation factor.

However, this analysis ignores the fact that retardation factors in reality should be dependent on the ratio of rock surface area to solution volume rather than rock mass to solution volume (as assumed in equation C.1). One can readily verify that the blind application of equation (C.1) to very low porosity rocks will result in completely unrealistic retardation factors. In fact, these retardation factors will approach infinity as the matrix porosity approaches zero. If the higher porosity of the lower Bullfrog Tuff relative to the central Bullfrog Tuff were the result of 3 times as many pores per unit volume of rock, but the pores had the same size distribution in each rock, then the surface area to volume ratios in the two rocks would be about the same. In this case, the lower Bullfrog Tuff would be expected to have a factor of 3 greater retardation factor than the central Bullfrog Tuff because of its factor of ~3 greater lithium  $K_D$  value. Although we have no data on pore size distributions in the tuffs, we believe that this postulated situation is probably closer to reality than the implicit assumption that there is a significantly higher surface area to solution volume ratio in lower porosity rocks.

In light of this discussion, we can conclude that the lithium sorption parameters in Tables C-4 through C-9 are in quite good agreement with the laboratory sorption parameters measured for the central and lower Bullfrog Tuffs (see Section 6.0, and Table 6-5). The field-derived lithium retardation factors are consistently greater than or nearly equal to the retardation factors that would have been predicted from the laboratory measurements. Only in the case of the very early lithium response is the field-derived retardation factor lower than the laboratory-derived factor, and even here the difference (42%) could be readily explained if lithium concentrations in the fractures were high enough that sorption nonlinearity was important (recall that we assumed the asymptotic  $K_D$  at the lowest concentrations [=  $K_{LS\max}$ ], which will always yield lower predicted concentrations). However, we also showed that it is possible to conclude that a small amount of lithium (as much as 5%) could have moved through the system unretarded. The general observation that there was greater lithium retardation in the second set of pathways compared to the first set of pathways is consistent with our deduction that the second set of pathways was more likely to have been in the more strongly sorbing lower Bullfrog Tuff. Given the physical and chemical heterogeneity that was undoubtedly present over the ~30-meter long and ~100-meter thick section of tuff that the field test was conducted in, these results are very encouraging, and they lend validity to the practice of using laboratory-derived sorption data to predict field-scale transport of sorbing solutes. If anything, the use of the laboratory-derived

lithium sorption parameters would have resulted in conservatively high predictions of total lithium transport through the field system.

### C.5 Interpretation of Microsphere Response

As with the solutes, the microsphere response in the multiple tracer test was interpreted using the RELAP code to fit the two peaks. The differential equations used to describe microsphere transport in the fractures were:

$$\frac{\partial C}{\partial t} + V \frac{\partial C}{\partial x} - D \frac{\partial^2 C}{\partial x^2} + k_{\text{filt}} C - k_{\text{res}} S = 0 \quad (\text{C.3})$$

$$\frac{1}{b} \frac{\partial S}{\partial t} - k_{\text{filt}} C + k_{\text{res}} S = 0 \quad (\text{C.4})$$

where,  
 $C$  = colloid concentration in solution, no./L  
 $S$  = colloid concentration on surfaces, no./cm<sup>2</sup>  
 $V$  = flow velocity in fractures, cm/sec  
 $D$  = dispersion coefficient, cm<sup>2</sup>/sec  
 $k_{\text{filt}}$  = filtration rate constant (1/sec) =  $\lambda V$ , where  $\lambda$  = filtration coefficient (1/cm)  
 $k_{\text{res}}$  = resuspension rate constant, 1/cm-sec  
 $x, t$  = independent variables for distance and time, respectively.

Note that these equations are equivalent to equations (D1) and (D2) in Appendix D with  $\left(\frac{P_f}{\eta}\right) = b^{-1}$ ,  $\alpha_f = 1$ , and  $\beta_f = 0$ . Thus, the RELAP semi-analytical model was capable of representing the simple colloid transport model given by equations (C.3) and (C.4).

We assumed that the mass fractions, mean residence times, and Peclet numbers of the two "pathways" that accounted for the nonsorbing solute responses (Sections 2.4.1) also applied to the spheres. However, the lumped matrix diffusion parameter was set equal to zero (i.e., no matrix diffusion) because of the large size and small diffusivity of the microspheres relative to the solutes. The only adjustable parameters in the analysis were a forward first-order filtration rate constant and a first-order reverse filtration rate constant (also called a resuspension or detachment rate constant).

We initially tried to fit the early microsphere response (the first peak) by assuming only irreversible filtration with no resuspension/detachment. We found that while this approach was capable of fitting the timing and normalized concentration of the first microsphere peak, it resulted in a much shorter tail than the data indicated. Therefore, to account for the tail, a small fraction of the filtered microspheres was assumed to detach. A fit to the tail was obtained by adjusting both the fraction of spheres detaching and the detachment rate constant (while keeping the forward filtration rate constant the same as in the fit to the peak).

A fit to the second microsphere peak was obtained in the same manner. However, in this case, we found that the forward filtration rate constant had to be adjusted large enough so that essentially all of the microspheres were filtered as they moved through the system. This was necessary because any microspheres moving through the system without being filtered were

predicted to arrive too early to match the observed response (note that the second microsphere peak occurred after the second nonsorbing solute peaks; see Fig. C-3). Unfiltered spheres moving through the second set of pathways were predicted to arrive at about the same time as the low point in concentration between the two peaks.

Therefore, to account for the second microsphere peak, it was necessary to assume that a substantial fraction of the spheres in the second set of pathways were reversibly filtered. Unlike the first peak, however, we found that it was not possible to fit the entire second peak using a single detachment rate constant. The peak itself was fit by assuming a fraction of the microspheres experienced one detachment rate, and the tail was fit by assuming a separate fraction experienced another detachment rate. The remaining microspheres were assumed to not detach at all. The forward rate constant associated with each of these mass fractions was set equal to the minimum rate constant necessary to ensure that nearly all of the microspheres were filtered before making it through the system.

The resulting fit(s) to the microsphere data are illustrated in Fig. C-12. The "pathways" labelled 1A and 1B represent the non-detaching and detaching fractions, respectively, of the microspheres following the pathway(s) that resulted in the first solute peak. Pathways 2A, 2B, and 2C in Fig. C-12 represent the nondetaching and the two detaching fractions of the microspheres following the pathway(s) that resulted in the second solute peak. The fitted mass fractions and filtration parameters associated with the "subpathways" in Fig. C-12 are given in Table C-10.

Note that the predicted first arrival of microspheres precedes their actual first arrival by 2 to 3 hrs. This result can be attributed to the fact that we did not assume a 4-hr delay in the injection of microspheres into the pathways that resulted in the first tracer peaks (as we did for the solutes). We assumed no delay for the microspheres because the microsphere injection began about 3.5 hrs after the solutes were injected. We reasoned that if the solutes did not begin entering the pathways resulting in the first tracer peaks until after the microspheres were injected, then it was reasonable to assume that the microspheres should have entered those pathways at the same time as the solutes. However, if the microspheres experienced a delay similar to the solutes, then their predicted first arrival would actually be slightly later than the observed first arrival. In fact, in this case, the first arrival would coincide almost exactly with the first arrival of solutes. Thus, the uncertainty associated with when the microspheres actually began entering the flow system causes considerable uncertainty in the predicted first arrival of the microspheres.

It should be pointed out that the interpretation of the microsphere response presented in the preceding paragraphs is by no means unique. First, it is quite likely that there exists a continuous distribution of filtration and detachment rate constants rather than a few discrete ones, as assumed in the above analysis. Such a distribution could arise from a distribution of colloid surface properties and/or physical and chemical heterogeneities in fracture surfaces. It is also possible that colloid filtration and detachment are not linear first-order processes as assumed in equations (C.3) and (C.4). Rather, they might be better described as nonlinear and/or stochastic processes (Dabros and Van de Ven, 1982, 1983). Finally, as mentioned above, the interpretation of the microsphere response relative to the solutes is complicated by the fact that the microsphere injection was started later than the solute injection. In addition to causing uncertainty in when the microspheres actually began moving into flow pathways, the differences in injection times may have resulted in the microspheres not being distributed into flow pathways in exactly the same proportion as the solutes (i.e., a different source term). If different

assumptions were made about the distribution of spheres between the two major sets of pathways, different filtration parameters would be obtained.

Although these uncertainties exist, we believe that the interpretation of the microsphere response presented in Fig. C-12 and Table C-10 is one of the simplest that is consistent with the data. Even if the quantitative aspects of the interpretation are not entirely correct, it is difficult to refute the qualitative conclusions that (1) the microspheres were significantly attenuated relative to the solutes and (2) the microsphere response (specifically the long tailing behavior) can only be explained by assuming that at least a portion of the spheres were reversibly filtered. The latter conclusion implies that colloid detachment, or perhaps some other process that behaves like detachment, is important in predicting microsphere transport through saturated, fractured tuffs near Yucca Mountain.

### C.6 Uncertainties in Test Interpretations

There are several sources of uncertainty associated with the tracer tests and their interpretation. First, there are data uncertainties, which are related to the accuracy and precision of the tracer chemical analyses, including both random and systematic errors. We believe that random errors were small because the breakthrough curve data are not widely scattered and show well-defined trends. The most significant sources of systematic errors would have been day-to-day differences in analytical instrument operation and in analytical standard preparation. However, careful checks with control samples and cross-checking with another analytical laboratory (University of Nevada at Las Vegas, unpublished data) indicated that systematic errors were minimal. Incomplete knowledge of the residual concentration of PFBA in the October test due to the May PFBA injection is an additional source of uncertainty in the October PFBA data (see Section C.3), but this uncertainty can be bounded and shown to have minimal impact on the interpretative analysis.

Uncertainties in the model parameter estimates are related to uncertainties in the data, discussed above, and uncertainties in the uniqueness of the curve fits. Parameter uncertainty due to data scatter can generally be quantified by statistical measures such as "95% confidence intervals" (Draper and Smith, 1981, pp. 93-96, 472-473). For a given set of modeling assumptions, we expect this uncertainty to be relatively small given the smoothness of the breakthrough curve data, but we have left its quantification for future work. It is clear that uniqueness-of-fit uncertainties are lower when several tracer responses are analyzed simultaneously than when only a single response is analyzed (Table C-2) because more constraints are placed on the interpretation. However, a detailed analysis of this uncertainty is also reserved for future work.

We believe that the most important source of uncertainty in the tracer test interpretation is associated with the modeling assumptions made in the curve-fitting procedure. These uncertainties include: (1) not knowing whether the flow field was linear or radial, (2) not knowing the exact duration and timing of the tracer injection that resulted in the first tracer peak, and (3) the possibility that the wellbore source functions could have been significantly different than an exponential decay with a time constant approximately equal to the borehole volume divided by the injection flow rate. The effect of radial vs. linear flow is reflected in Tables C-3 and C-5 through C-7, and the effect of varying the tracer injection duration was found to have only a minor effect on the first peak response and virtually no effect on the second peak response.

The source term uncertainty was investigated by varying the exponential decay time constant by about an order of magnitude, from  $0.13$  to  $1\text{ hr}^{-1}$ . For perspective, the value corresponding to the injection borehole volume divided by the injection rate was  $\sim 0.26\text{ hr}^{-1}$ . Interestingly enough, both the mean residence times and Peclet numbers decreased as the time constant was decreased (i.e., a slower exponential decay). This result suggested that the model was trying to compensate for a slow release from the injection wellbore by speeding up the movement of tracer through the formation and increasing the amount of mass arriving early as a result of dispersion. Because the fits tended to be better with faster decay constants, we used a decay constant of  $1\text{ hr}^{-1}$  to obtain all of the parameter estimates in Tables C-3 through C-10. It should be noted that the value of the decay constant (within the range stated above) had virtually no effect on the interpretation of the latter portion of the breakthrough curves.

### C.7 Discussion

We now consider the implications of the test interpretations associated with these fits. First, it is apparent that regardless of which uncertainties or alternative test interpretations are considered for the solutes (particularly for lithium), it must be concluded that matrix diffusion and sorption are occurring in most, if not all, flow pathways. Second, the lithium sorption parameters deduced from the interpretative fits are in reasonably good agreement with the laboratory sorption data. The agreement between field and laboratory data is especially encouraging given all of the chemical and physical heterogeneity present in the field and the lack thereof in the interpretive models and the laboratory experiments. Furthermore, a comparison of the laboratory- and field-derived sorption parameters suggests that the use of the laboratory data to predict field-scale lithium transport will tend to slightly overestimate field transport rates over long distances and times. (See Section C.4.2 for additional discussion of the implications of the lithium response). We conclude that a dual-porosity conceptualization of the saturated zone near Yucca Mountain is valid, and that the reasonable agreement between field and laboratory lithium sorption parameters lends validity to the practice of using laboratory-derived sorption data to predict field-scale transport behavior. However, this latter conclusion should be applied cautiously to sorbing radionuclides, for which there are no field data in the immediate vicinity of Yucca Mountain.

The microsphere response compared to the solutes indicates that while the majority of the spheres were irreversibly attenuated in the system (filtered or deposited), a significant fraction of them moved through the system quite efficiently (some without any apparent filtration). The response also indicates that a significant fraction of the spheres arriving at the production well experienced both filtration and resuspension/detachment, suggesting that not all filtration is irreversible. The implication is that a nontrivial fraction of groundwater colloids can be expected to travel significant distances over significant times in the saturated zone at rates comparable to or exceeding those of nonsorbing solutes.

Table C-11 provides ranges of physical parameter values derived from the field test interpretations. These ranges are intended to provide performance assessment modelers with lower and upper bounds for use in large-scale, abstracted transport models, although it must be recognized that the values apply strictly to only the central and lower Bullfrog Tuffs at the C-wells. Lithium sorption parameters are not included in Table C-11 because they are not directly relevant to any radionuclides of importance to performance assessment. Although some of the

parameter ranges in Table C-11 seem large, the use of simultaneously-injected multiple tracers significantly reduced the range that would have been reported in a single tracer test.

The longitudinal dispersivity values in Table C-11 were calculated using  $\alpha = L/Pe$ , where the travel distance, L, was assumed to take on minimum and maximum values of 30 and 100 m, corresponding to interborehole distance and the approximate distance between the bottom of one borehole and the top of the other (the maximum possible linear transport distance), respectively. The lower bound was calculated assuming a distance of 30 m and a Peclet number corresponding to the first set of pathways. The upper bound was calculated assuming a distance of 100 m and assuming a Peclet number corresponding to the second set of pathways. To put these dispersivities in perspective, Fig. C-13 shows a box encompassing the entire range of calculated dispersivities superimposed on a plot of dispersivity vs. scale taken from Neuman (1990). It is apparent that the C-holes longitudinal dispersivity is reasonably consistent with other data sets and with existing theories on the scale dependence of dispersion.

The values in Table C-11 for fracture apertures, fracture spacing, effective flow porosity, and effective fracture porosity are all very uncertain and should be used with caution. Fracture aperture values were calculated from the best-fitting lumped matrix diffusion parameters,  $\frac{\phi}{b} \sqrt{D_m}$ , assuming that the matrix diffusion coefficients and matrix porosities measured in diffusion cell experiments (see Section 8.0) applied in the field. The lower bound was calculated using the lumped parameter from the first set of pathways and assuming the matrix porosity and diffusion coefficients measured in the central Bullfrog Tuff. The upper bound was calculated using the lumped parameter from the second set of pathways and assuming the matrix porosity and diffusion coefficients measured in the lower Bullfrog Tuff. The lower bound for fracture spacing was based on fitting the extreme tail of the PFBA and bromide breakthrough curves where there is considerable scatter and uncertainty in the data. The upper bound is infinite because good fits to the early tracer data were obtained assuming an infinite matrix. Flow porosities were calculated using the following equation, which assumes homogeneous, isotropic, radial convergent flow of the entire production flow rate over the entire thickness of the test interval.

$$\eta = \frac{Q \tau}{\pi R^2 L} \quad (C.5)$$

where,  $\eta$  = flow porosity  
 $Q$  = production rate ( $\sim 34.1 \text{ m}^3/\text{hr}$ )  
 $\tau$  = mean residence time, hr  
 $R$  = distance between wells ( $\sim 30 \text{ m}$ )  
 $L$  = formation thickness ( $\sim 100 \text{ m}$ ).

Assuming radial convergent flow in a homogeneous, isotropic medium frequently results in high estimates of flow porosity when the medium is actually quite heterogeneous (unpublished results). Also, the upper bound flow porosity values are derived from the longest residence time pathways, which very likely received much less than 100% of the total production flow rate. The upper bound fracture porosity reported in Table C-11 is distinguished from the upper bound flow porosity in that it is estimated by dividing the maximum fracture half-aperture (0.63 cm) by the half the minimum fracture spacing (4 cm). This upper bound is unrealistically high because it

actually exceeds the highest matrix porosities measured in the laboratory. The lower bound for fracture porosity is zero because reasonable fits to the tracer data were obtained assuming an infinite matrix.

While we considered the tracer tests to be highly successful, we recognize that much work remains to be done. We tested only one formation at one location near Yucca Mountain, and it would not be prudent to base performance assessments of the entire saturated zone on such a limited data set. Thus, we plan to conduct additional tracer tests, possibly in other test configurations such as single-well injection-withdrawal mode, in other hydrogeologic formations, and at other locations near Yucca Mountain. Issues to be addressed in these tests include, but are not necessarily limited to, (1) the time- and distance-scale dependence of the processes of dispersion, matrix diffusion, and sorption, (2) the spatial variation of transport properties in the vicinity of Yucca Mountain, (3) the variation of transport properties in different stratigraphic zones and in different hydrogeologic settings (e.g., faulted vs. unfaulted rock, high conductivity vs. low conductivity rock, high matrix porosity vs. low matrix porosity rock, fractured rock vs. porous medium [e.g., alluvium]), (4) field sorption behavior in different rock types (e.g., mineralogically altered vs. unaltered, high in clays vs. low in clays, welded vs. unwelded, fractured vs. porous medium), and (5) the diameter, water chemistry, and geologic media dependence of microsphere/colloid transport in the saturated zone. We also plan to conduct additional laboratory experiments to (1) characterize the sorption of lithium and other potential reactive tracers onto other rocks likely to be encountered in the saturated zone near Yucca Mountain and (2) measure free-water diffusion coefficients of nonsorbing solutes so that quantitative estimates of tortuosity factors can be obtained from diffusion cell data.

We consider our modeling of the tracer tests to be a relatively simple approach to interpreting the data. This approach involves a minimum number of adjustable parameters, which is consistent with our limited knowledge of flow system geometry and heterogeneity. Although we believe that our conclusions are sound, we recognize that there is much room for revisiting the analyses using more sophisticated modeling tools and introducing more system complexity, particularly as more site-specific information becomes available. In the future, we plan to incorporate this information into numerical models that can better account for both physical and chemical heterogeneity in two- and three-dimensions. We also plan to examine other semi-analytical modeling approaches, such as the multi-rate diffusion model of Haggerty and Gorelick (1995), which has been used to interpret tracer tests conducted in a fractured dolomite near Carlsbad, NM for the Waste Isolation Pilot Plant project (Meigs et al., 1997). The fact that the matrix diffusion mass transfer coefficients in our analyses decreased as pathway residence times increased (Table C-3) and that a finite fracture spacing offered a better fit to the end of the conservative tracer breakthrough curves suggests that multiple diffusion rates and/or finite fracture spacings may be important at long time scales in the groundwater system. It might also suggest that interconnected porosity, and hence diffusion coefficients in the matrix, decrease with distance into the matrix (away from fractures). It is also possible that a small amount of the apparent matrix diffusion in the field experiments was actually diffusion into stagnant water along the rough fracture walls or within the fractures themselves (occurring as a result of tracers diffusing out of high flow rate channels and into low flow zones), rather than into the matrix proper. These possibilities have important implications for saturated zone performance assessments and merit further study because, if valid, they would suggest that matrix diffusion might be overestimated in short-duration tracer experiments.

## Appendix C References

- Becker, M. W. 1996. *Tracer Tests in a Fractured Rock and Their First Passage Time Mathematical Models*, Ph.D. Dissertation, University of Texas, Austin, TX, pp. 110-115 and 119-131. TIC Catalog # 236855. MOL.19980601.17633.
- Bird, R. B., W. E. Stewart, and E. N. Lightfoot. 1960. *Transport Phenomena*. New York: John Wiley and Sons, p. 54. RIS Accession # NNA.19900919.0195.
- Dabros, T., and T. G. Van de Ven. 1982. "Kinetics of Coating by Colloidal Particles." *J. Colloid Interface Sci.*, 89(1), 232-244. RIS Accession # MOL.19950103.0131.
- Dabros, T., and T. G. Van de Ven. 1983. "On the Effects of Blocking and Detachment on Coating Kinetics." *J. Colloid Interface Sci.*, 93(2), 576-579. TIC Catalog # 224944.
- Draper, N. R., and H. Smith. 1981. *Applied Regression Analysis*, 2nd ed. New York: John Wiley and Sons, pp. 93-96, pp. 472-473. TIC Catalog # 231231.
- Fuentes, H. R., W. L. Polzer, E. H. Essington, and B. D. Newman. 1989. *Characterization Reactive Tracers for C-Well Field Experiment I: Electrostatic Sorption Mechanism, Lithium*. LA-11691-MS. Los Alamos, New Mexico: Los Alamos National Laboratory, p. 37. TIC Catalog # 202389.
- Geldon, A. L. 1993. *Preliminary Hydrogeologic Assessment of Boreholes UE-25 c#1, UE-25 c#2, and UE-25 c#3, Yucca Mountain, Nye County, Nevada, 1993*. USGS/WRI-92-4016. Denver, Colorado: U.S. Geological Survey, pp. 43-50. TIC Catalog # 210506. RIS Accession # MOL.19960808.0136.
- Geldon, A. L. 1996. *Results and Interpretation of Preliminary Aquifer Tests in Boreholes UE-25c#1, UE-25c#2, and UE-25c#3, Yucca Mountain, Nye County, Nevada*. Water-Resources Investigations Report 94-W-0412, pp. 70-71. Denver, Colorado: United States Geological Survey. TIC Catalog # 223656
- Geldon, A. L., A. M. A. Umari, M. F. Fahy, J. D. Earle, J. M. Gemmell, and J. Darnell. 1997. *Results of Hydraulic and Conservative Tracer Tests in Miocene Tuffaceous Rocks at the C-Hole Complex, 1995 to 1997, Yucca Mountain, Nye County, Nevada*. Yucca Mountain Project Milestone SP23PM3, United States Geological Survey, Denver, CO, p. Hydraulic Tests-16. MOL.19980122.0412.
- Haggerty, R. and S. M. Gorelick. 1995. "Multiple-Rate Mass Transfer for Modeling Diffusion and Surface Reactions in a Media with Pore-Scale Heterogeneity." *Water Resour. Res.*, 31(10), 2383-2400. (Submitted to RIS for Accession # 5/21/99.)
- Jenson, V. G., and G. V. Jeffreys. 1977. *Mathematical Models in Chemical Engineering*, 2nd ed., London, Academic Press, pp. 169-170. (Submitted to RIS for Accession # 5/21/99.)

- Maloszewski, P., and A. Zuber. 1983. "Interpretation of Artificial and Environmental Tracers in Fissured Rocks with a Porous Matrix." In *Isotope Hydrology*, pp. 635-651. Vienna, Austria: International Atomic Energy Agency (IAEA). (Submitted to RIS for Accession # 5/21/99.)
- Maloszewski, P., and A. Zuber. 1985. "On the Theory of Tracer Experiments in Fissured Rocks with a Porous Matrix." *J. Hydrology*, 79, 333-358. TIC Catalog # 222390.
- Maloszewski, P., and A. Zuber. 1991. "Influence of Matrix Diffusion and Exchange Reactions on Radiocarbon Ages in Fissured Carbonate Aquifers." *Water Resour. Res.*, 27(8), 1937-1945. (Submitted to RIS for Accession # 5/21/99.)
- Meigs, L. C., R.L. Beuheim, J.T. McCord, Y.W. Tsang, and R. Haggerty, R. 1998. "Design, Modeling, and Current Interpretations of the H-19 and H-11 Tracer Tests at the WIPP Site." In *Field Tracer Transport Experiments*, proceedings of the first GEOTRAP Workshop, Cologne, Germany, August 28-30, 1996, pp. (Submitted to RIS for Accession # 5/21/99.)
- Moench, A. F. 1995. "Convergent Radial Dispersion in a Double-Porosity Aquifer with Fracture Skin: Analytical Solution and Application to a Field Experiment in Fractured Chalk." *Water Resour. Res.*, 31(8), 1823-1835. TIC Catalog # 233132.
- Moreno, L., Tsang, Y. W., Tsang, C. F., Hale, F. V., and Neretnieks, I. 1988. "Flow and tracer transport in a single fracture: A stochastic model and its relation to some field observations." *Water Resour. Res.*, 24(12), 2033-2048. TIC Catalog # 224888.
- National Research Council. 1996. *Rock Fractures and Fluid Flow: Contemporary Understanding and Applications*. Washington, D.C: National Academy Press, pp. 252-259. TIC Catalog # 235913.
- Neuman, S. P. 1990. "Universal Scaling of Hydraulic Conductivities and Dispersivities in Geologic Media." *Water Resour. Res.*, 26(8), 1749-1758. TIC Catalog # 237977. RIS Accession # NNA.19920320.0021.
- Newman, J. S. 1973. *Electrochemical Systems*. Englewood Cliffs, New Jersey: Prentice-Hall, pp. 229-230. TIC Catalog # 210201.
- Reimus, P. W., and Z. V. Dash. 1998. *Models and Methods Summary for the Reactive Transport Application*. Yucca Mountain Site Characterization Project Milestone Report SP32E1M4. Los Alamos, New Mexico: Los Alamos National Laboratory, all pages. (Submitted to RIS for Accession # 5/21/99.)
- Reimus, P. W. 1995. *The Use of Synthetic Colloids in Tracer Transport Experiments in Saturated Rock Fractures*. LA-13004-T (also PhD Dissertation, University of New Mexico). Los Alamos, New Mexico: Los Alamos National Laboratory, pp. 49-51, 73-94. TIC Catalog # 219271.

Reimus, P. W. and H. J. Turin. 1997. *Draft Report of Results of Hydraulic and Tracer Tests at the C-Holes Complex*. Yucca Mountain Site Characterization Project Milestone Report SP32APMD. Los Alamos, New Mexico: Los Alamos National Laboratory, pp. 11-12, 36-37. (Submitted to RIS for Accession # 5/21/99.)

Reimus, P. W. and H. J. Turin. 1996. *Results of Reactive Tracer Testing at the C-Holes*. Yucca Mountain Site Characterization Project Milestone Report 4270M. Los Alamos, New Mexico: Los Alamos National Laboratory, pp. 9-26. TIC Catalog # 233146. RIS Accession # LAPR831231AG96.001.

Robinson, B. A. 1994. "A Strategy for Validating a Conceptual Model for Radionuclide Migration in the Saturated Zone beneath Yucca Mountain." *Rad. Waste Mgmt. & Env. Restor.*, 19, 73-96. TIC Catalog # 222513.

Steinkamp, J. A., R. C. Haberset, and R. D. Hiebert. 1991. "Improved Multilaser/Multiparameter Flow Cytometer for Analysis and Sorting of Cells and Particles." *Rev. Sci. Instrum.*, 62(11), 2751-2764. TIC Catalog # 222391.

Tang, D. H., E. O. Frind, and E. A. Sudicky. "Contaminant Transport in a Fractured Porous Media: Analytical Solution for a Single Fracture." *Water Resour. Res.*, 17(3), 555-564. TIC Catalog # 225368. RIS Accession # NNA.19900711.0084.

Thompson, M. E. 1991. "Numerical Simulation of Solute Transport in Rough Fractures." *J. Geophys. Res.*, 96(B3), 4157-4166. RIS Accession # NNA.19910812.0005.

Wan, J. and J. L. Wilson. 1994. "Colloid Transport in Unsaturated Porous Media." *Water Resour. Res.*, 30(4), 857-864. TIC Catalog # 222359.

## Appendix C Tables

Table C-1. Summary of quantitative interpretation procedure for reactive tracer test.

1. Find the values of  $\tau$ , Pe,  $\phi/b$ , and f (with  $R_m$  and  $R_f$  equal to 1) that provide the best simultaneous fit to the first PFBA and bromide peaks.
2. Subtract the fits obtained in step 1 from the PFBA and bromide data sets, and repeat step 1 to fit the resulting second peaks (i.e., second set of pathways).
3. Fit the lithium data sequentially as in steps 1 and 2 by adjusting  $R_m$  and  $R_f$  while using the values of  $\tau$ , Pe,  $\phi/b$ , and f that gave best fits to PFBA and bromide data.
4. If step 3 results in poor fit(s) to the lithium data for any given peak, attempt to obtain a better fit by allowing rate-limited and/or nonlinear sorption or by assuming multiple pathways that have different physical or chemical characteristics.

Table C-2. Parameter values resulting in best fits to the May 1996 PFBA data as a function of assumed matrix diffusion mass transfer coefficient,  $\frac{\phi}{b} \sqrt{D_m}$ . (DTN LAPR831231AN99.001).

$\frac{\phi}{b} \sqrt{D_m}$ , sec <sup>-1/2</sup>	$\tau$ , hr	Pe	Dispersivity, m*	f
0.00346	150	29	1.1	0.99
0.00173	220	16	1.9	0.8
0.000866	310	9	3.4	0.72
0.000346	410	6	5.2	0.65
0 (single-porosity)	470	5	6.2	0.55

\* Assumes a 30-m travel distance (borehole separation).

Table C-3. Parameters obtained from fits to the PFBA and bromide responses in the reactive tracer test ( $R_f$  and  $R_m = 1$ ). (DTN LAPR831231AQ99.002).

Parameter	Pathway 1	Pathway 2
f, fraction mass	0.12	0.59
$\tau$ , linear flow, hr	37	995
Pe, linear flow	6.0	1.7
$\tau$ , radial flow, hr	31	640
Pe, radial flow	9.0	3.0
Bromide $\frac{\phi}{b} \sqrt{D_m}$ , sec <sup>-1/2</sup>	0.00158	0.000458
fracture spacing, cm	$\infty$	4

Note:  $\frac{\phi}{b} \sqrt{D_m}$  for PFBA is 0.577 times that for bromide.

Table C-4. Sorption parameters derived from fits to the first lithium peak (Fig. C-11) assuming that the flow pathways resulting in this peak were in the central Bullfrog Tuff. Other parameters used to obtain the fits were the same as for Pathway 1 in Table C-3 (with  $\frac{\phi}{b} \sqrt{D_m}$  for lithium equal to 0.816 that for bromide). Laboratory Langmuir isotherm parameters for the central Bullfrog Tuff were  $K_L = 0.014 \text{ ml/g}$  and  $S_{\max} = 31.4 \mu\text{g/g}$  (see Section 6.0). The laboratory forward sorption rate constant ranged from 2.2 to 18  $\text{hr}^{-1}$  (see Section 7.1). (DTN LAPR831231AQ99.002).

Parameter	Linear, Equilibrium	Linear, Kinetic	Langmuir, Equilibrium	Langmuir, Kinetic
$R_f$	1 (no sorption)	1.3	1 (no sorption)	(see footnote 5)
$R_m$	7	30	-	-
$k_f^{(1)}$ , $\text{hr}^{-1}$	$\infty$	0.14	$\infty$	2.2
$k_m^{(2)}$ , $\text{hr}^{-1}$	$\infty$	0.16	$\infty$	2.2
$K_D^{(3)}$ , $\text{ml/g}$	0.256	1.24	-	-
$K_L^{(4)}$ , $\text{ml}/\mu\text{g}$	-	-	0.1	0.025
$S_{\max}^{(4)}$ , $\mu\text{g/g}$	-	-	21	35.2

<sup>(1)</sup> Forward rate constant in fractures.

<sup>(2)</sup> Forward rate constant in matrix.

<sup>(3)</sup> Matrix value, calculated from equation (C.1) using fitted  $R_m$  and assuming  $\rho_B = 2.34 \text{ g/cm}^3$  and  $\phi = 0.1$  (laboratory values for central Bullfrog Tuff).  $K_D$  would be ~3.5 times larger if transport were assumed to be in the lower Bullfrog Tuff.  $K_D$  not calculated for fractures because of ambiguity in defining  $\rho_B$  and  $\phi$  in fractures.

<sup>(4)</sup> Matrix value, obtained from RETRAN assuming  $\rho_B = 2.34 \text{ g/cm}^3$  and  $\phi = 0.1$ .  $K_L$  would be ~3.5 times larger if transport were assumed to be in the lower Bullfrog Tuff.

<sup>(5)</sup> Sorption in fractures was assumed to follow a Langmuir isotherm with same  $K_L$  as for matrix but with  $S_{\max} = 125 \mu\text{g/g}$  (to simulate slightly greater sorption capacity to fracture surfaces) and  $\rho_B/\phi = 0.1$  (to simulate a lower surface area to volume ratio in fractures). These assumed values result in an  $R_f$  approximately equal to 1.3, which is the  $R_f$  value obtained for the linear, kinetic fit. RETRAN simulations were not very sensitive to fracture sorption parameters.

Table C-5. Transport parameters resulting in a good fit to the early lithium response assuming two separate "pathways" that have different matrix diffusion mass transfer coefficients (physical heterogeneity) but nearly identical lithium sorption parameters. (DTN LAPR831231AQ99.002).

Parameter	Pathway 1A	Pathway 1B
f, fraction mass	0.04	0.07
$\tau$ , linear flow, hr	22	41
P <sub>e</sub> , linear flow	16	18
$\tau$ , radial flow, hr	20	38
P <sub>e</sub> , radial flow	21	24
Bromide $\frac{\phi}{b} \sqrt{D_m}$ , sec <sup>-1/2</sup>	0.00079	0.00158
R <sub>f</sub> for lithium	1	1
R <sub>m</sub> for lithium	13	18

Table C-6. Transport parameters resulting in a good fit to the early lithium response assuming two separate "pathways" that have the same matrix diffusion mass transfer coefficients but different lithium sorption parameters (chemical heterogeneity). (DTN LAPR831231AQ99.002).

Parameter	Pathway 1A	Pathway 1B
f, fraction mass	0.075	0.037
$\tau$ , linear flow, hr	27	46
P <sub>e</sub> , linear flow	11	19
$\tau$ , radial flow, hr	24	43
P <sub>e</sub> , radial flow	15	25
Bromide $\frac{\phi}{b} \sqrt{D_m}$ , sec <sup>-1/2</sup>	0.00158	0.00158
R <sub>f</sub> for lithium	1	5
R <sub>m</sub> for lithium	6	40

Table C-7. Transport parameters resulting in a good fit to the early lithium response assuming two separate "pathways", one of which has no matrix diffusion or sorption and the other of which has only matrix sorption. (DTN LAPR831231AQ99.002).

Parameter	Pathway 1A	Pathway 1B
f, fraction mass	0.049	0.065
$\tau$ , linear flow, hr	42	30
P <sub>e</sub> , linear flow	6	7
$\tau$ , radial flow, hr	35	25
P <sub>e</sub> , radial flow	8.5	10
Bromide $\frac{\phi}{b} \sqrt{D_m}$ , sec <sup>-1/2</sup>	-0-	0.00354
R <sub>f</sub> for lithium	1	1
R <sub>m</sub> for lithium	1	80

Table C-8. Transport parameters resulting in good fits to the second lithium peak for the various cases presented in Tables C-4 through C-7 (see text also). Other parameters used to obtain the fits were the same as for Pathway 2 in Table C-3 (with  $\frac{\phi}{b} \sqrt{D_m}$  for lithium equal to 0.816 that for bromide). (DTN LAPR831231AQ99.002).

Case	R <sub>f</sub>	R <sub>m</sub>
Rate-limited (see Table 4)	4	26
Physical heterogeneity (see Table 5)	5.5	16
Chemical heterogeneity (see Table 6)	5.5	16
No matrix diffusion or matrix sorption (Table 7)	5.5	20

Table C-9. Combinations of fracture and matrix retardation coefficients resulting in good fits to the late lithium response. Other parameters used to obtain the fits are given in Tables C-8 for Pathway 1B and Table C-3 for Pathway 2 (with  $\frac{\phi}{b} \sqrt{D_m}$  for lithium equal to 0.816 that for bromide in each case). (DTN LAPR831231AQ99.002).

Case	Pathway 1B $R_f, R_m$	Pathway 2 $R_f, R_m$
Rate-limited (see Table C-4)	N/A	1, 78 4, 26
Physical heterogeneity (see Table C-5)	1, 18	1, 120 5.5, 16
Chemical heterogeneity (see Table C-6)	1, 100 3, 70 5, 40	1, 120 5.5, 16
No matrix diffusion or matrix sorption (Table C-7)	1, 80 4, 60 7, 40	1, 130 5.5, 20

Table C-10. Microsphere filtration and resuspension parameters associated with the fit shown in Fig. C-12. Other transport parameters used to obtain the fits are given in Table C-3. Note that subpathways 1A and 1B represent a mass fraction split of Pathway 1 from Table C-3, and subpathways 2A, 2B, and 2C represent a mass fraction split of Pathway 2 from Table C-3. (DTN LAPR831231AQ99.002).

Parameter	Path 1A	Path 1B	Path 2A	Path 2B	Path 2C
f, mass fraction	0.115	0.005	0.423	0.067	0.1
k <sub>filtr</sub> , 1/hr	0.2	0.2	0.04	0.04	0.04-
$\lambda^{(1)}$ , 1/cm	0.00247	0.00247	0.0133	0.0133	0.0133
k <sub>res</sub> , 1/cm-hr	0	3.33	0	0.4	0.008

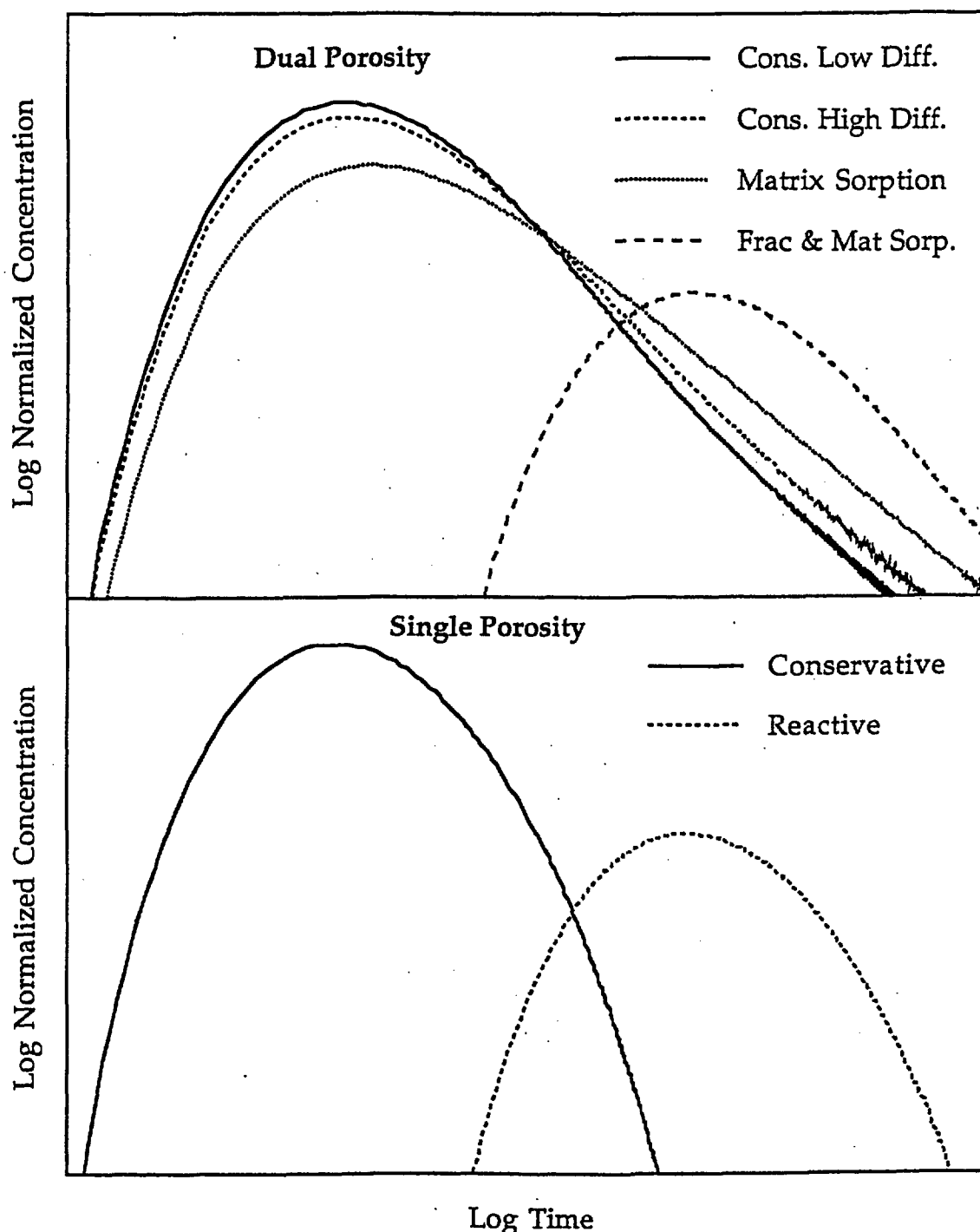
<sup>(1)</sup>λ calculated as  $k_{filtr}/V$ , where V = average linear velocity determined from mean fluid residence time.

Table C-11. Ranges of physical parameters derived from the interpretation(s) of the reactive tracer test. See text for assumptions and discussions of how lower and upper bounds were calculated. (DTN LAPR831231AQ99.002 and notebook LA-CST-CW-NBK-98-011).

Parameter	lower bound	upper bound
longitudinal dispersivity, m	3.3	59
b, cm	0.042	0.63
effective fracture spacing, cm	4	∞
effective flow porosity	0.0037	0.12
effective fracture porosity	-0-	0.32

## Appendix C Figures

Figure C-1. Generic predicted tracer responses in field tests in dual- and single-porosity media.



Units are arbitrary. "Cons. Low Diff." means nonsorbing solute with small diffusion coefficient, "Cons. High Diff." means nonsorbing solute with large diffusion coefficient, "Matrix Sorption" means sorption only in the matrix, and "Frac & Mat Sorp." means sorption in both fractures and matrix.

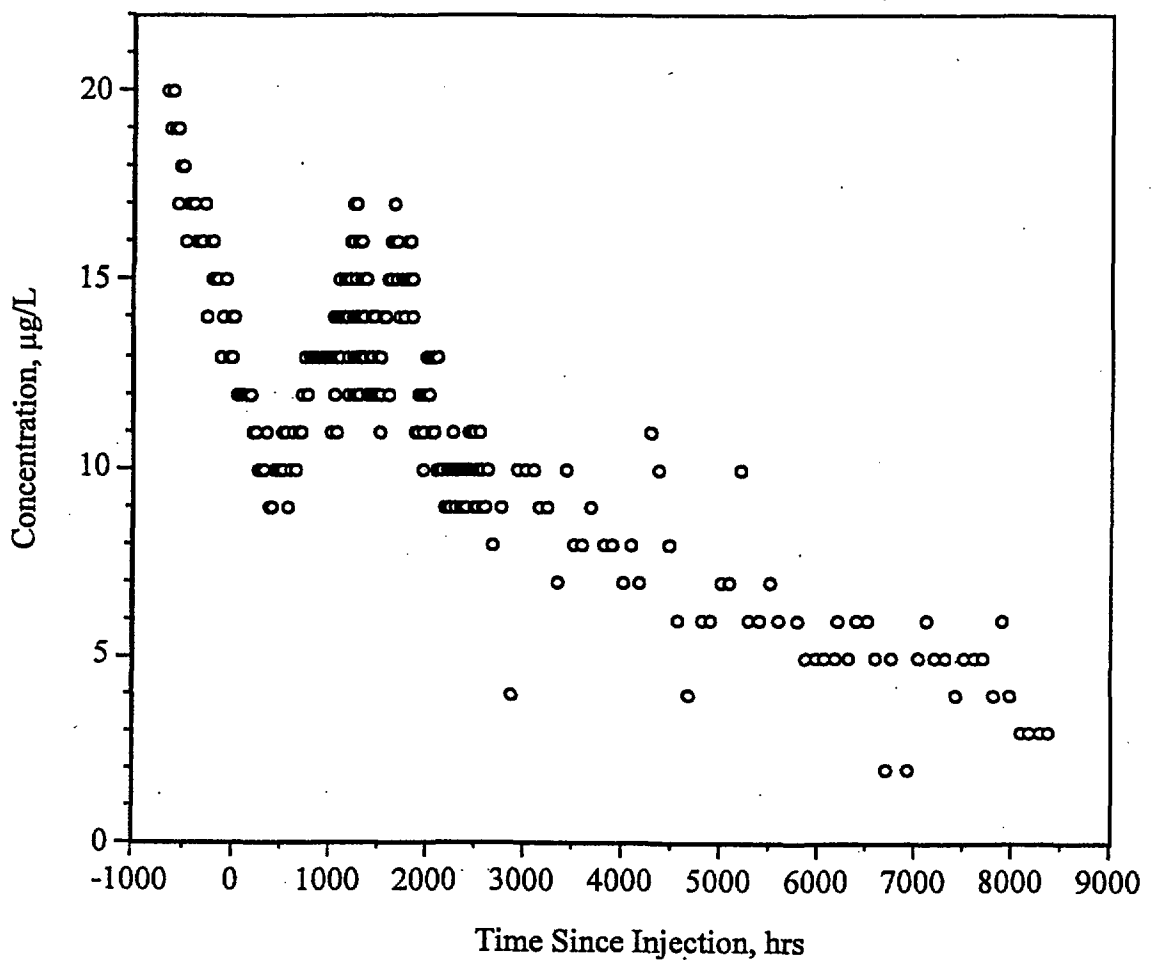


Figure C-2. Breakthrough curve of iodide resulting from injection of ~12.7 kg of iodide into c#1 on June 18, 1996. Declining background prior to and immediately after injection is due to recovery of iodide from a February 1996 iodide injection into c#2. Estimated recovery from c#1 accounting for c#2 background was between 6 and 10% through June 1, 1997. (DTN LAPR831231AQ98.001).

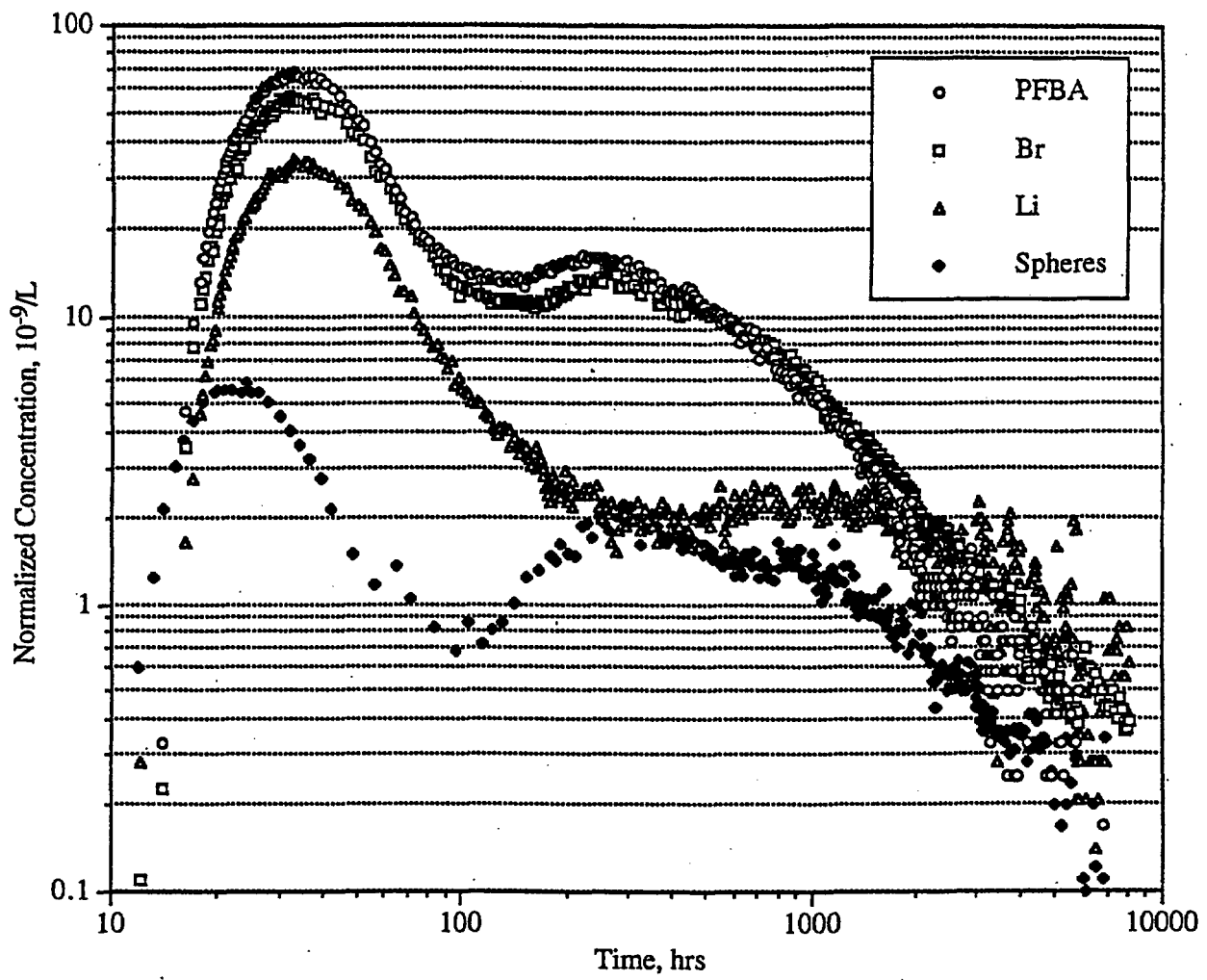


Figure C-3. Normalized tracer breakthrough curves from the reactive tracer test conducted in the lower Bullfrog Tuff between wells c#2 and c#3. Tracer recoveries were ~69% for PFBA, ~69% for bromide, ~39% for lithium, and ~15% for microspheres. (DTN LAPR831231AQ98.001).

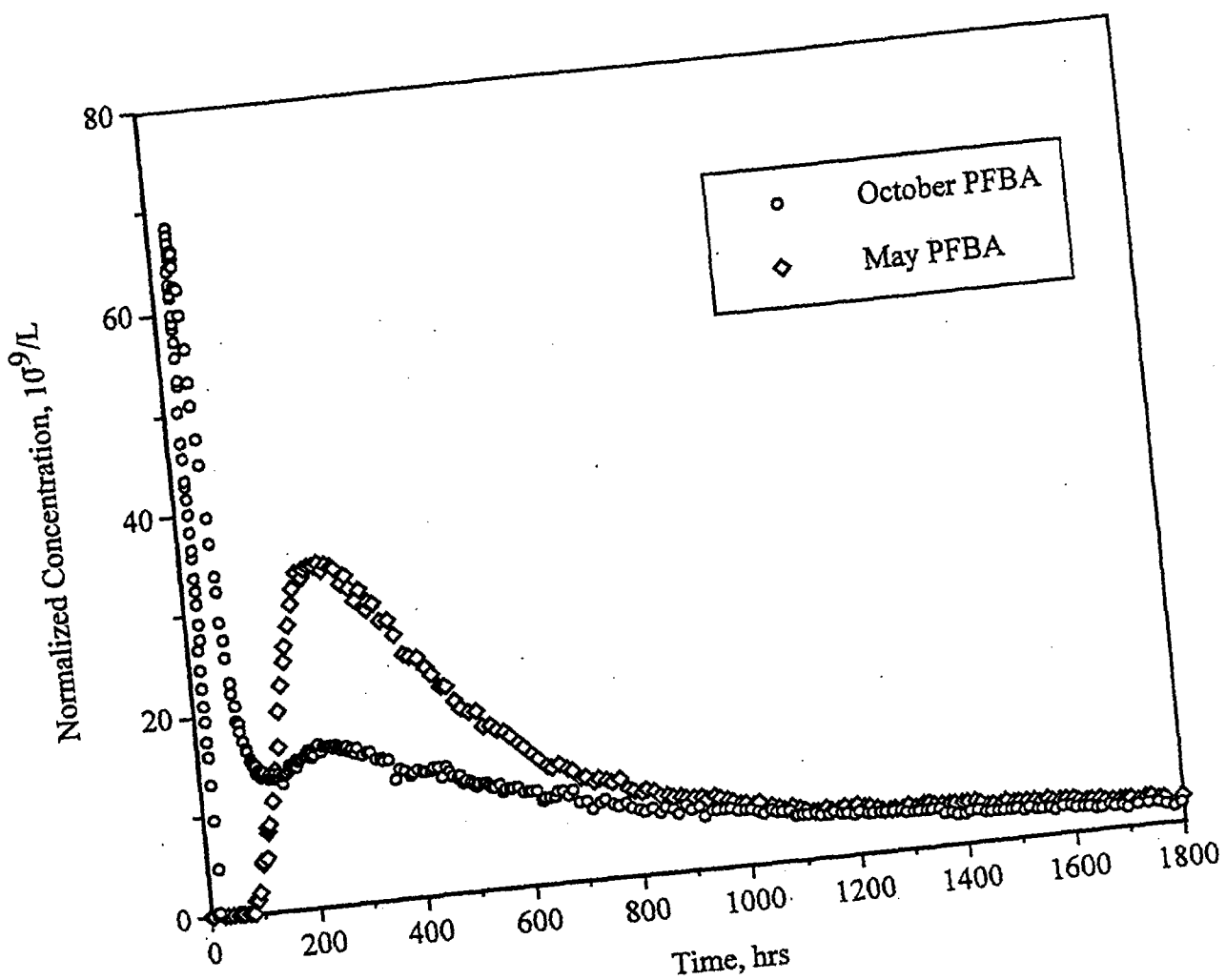
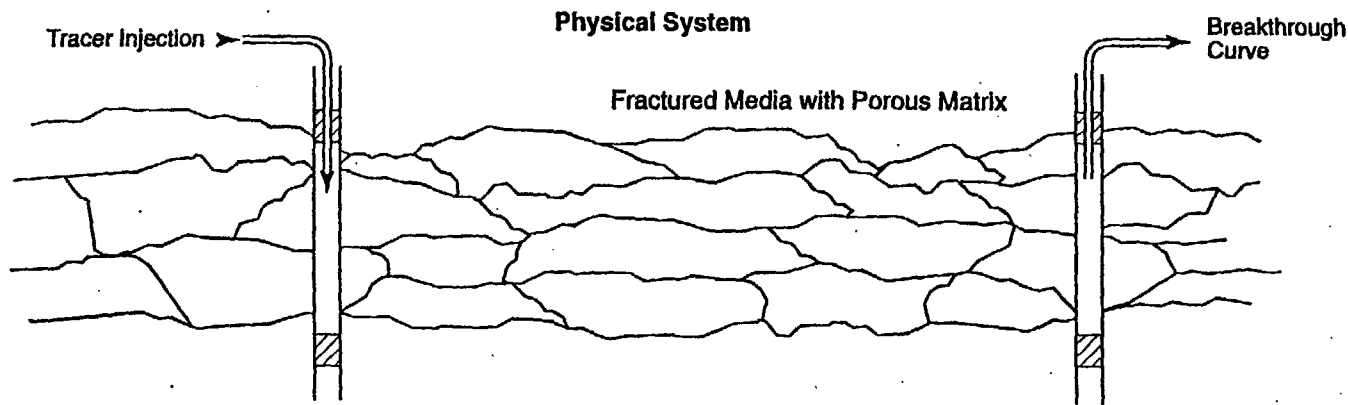


Figure C-4. Normalized breakthrough curves of PFBA at C#3 (through 1800 hrs) from the October and May injections into c#2. (DTN LAPR831231AQ98.001).

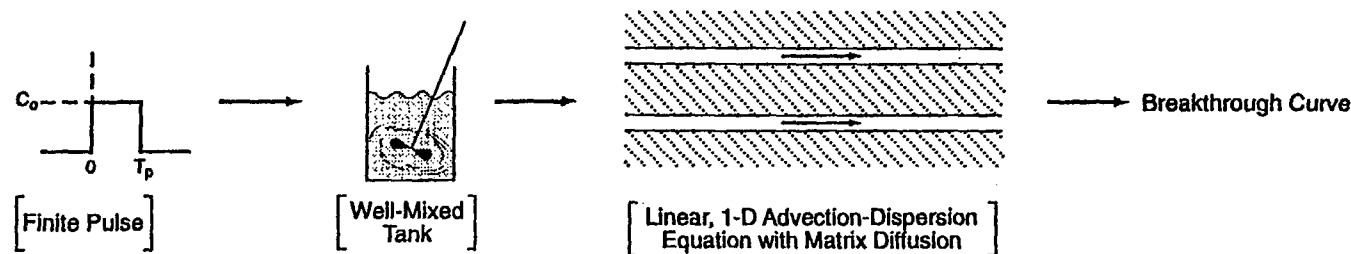
4/21/99

C.32

Milestone SP32E7M4



**Conceptual Model**



**Laplace Transform Transfer Functions**

$$C_0 \left( \frac{1-e^{-Tp s}}{s} \right)$$

$$\frac{a_1}{s + a_1}$$

$$\exp \left[ \frac{Pe}{2} \left( 1 - \sqrt{1 + \frac{4\tau R_f s}{Pe} (1 + \frac{\phi}{b R_f} \sqrt{\frac{R_m D_m}{s}})} \right) \right]$$

$C_0$  = injection concentration  
 $T_p$  = duration of pulse, sec

$a_1$  = decay time<sup>-1</sup>, sec<sup>-1</sup>

$\phi$  = matrix porosity  
 $b$  = fracture half aperture, cm  
 $R_f$  = fracture retardation factor  
 $R_m$  = matrix retardation factor  
 $D_m$  = diffusion coefficient in matrix, cm<sup>2</sup>/sec  
 $\tau$  = mean fluid residence time, sec  
 $Pe$  = Peclet number =  $\frac{L}{\alpha}$  (see text)

$s$  = Laplace transform variable

Figure C-5. Physical system, conceptual model, and Laplace transform transfer functions used to interpret tracer tests.

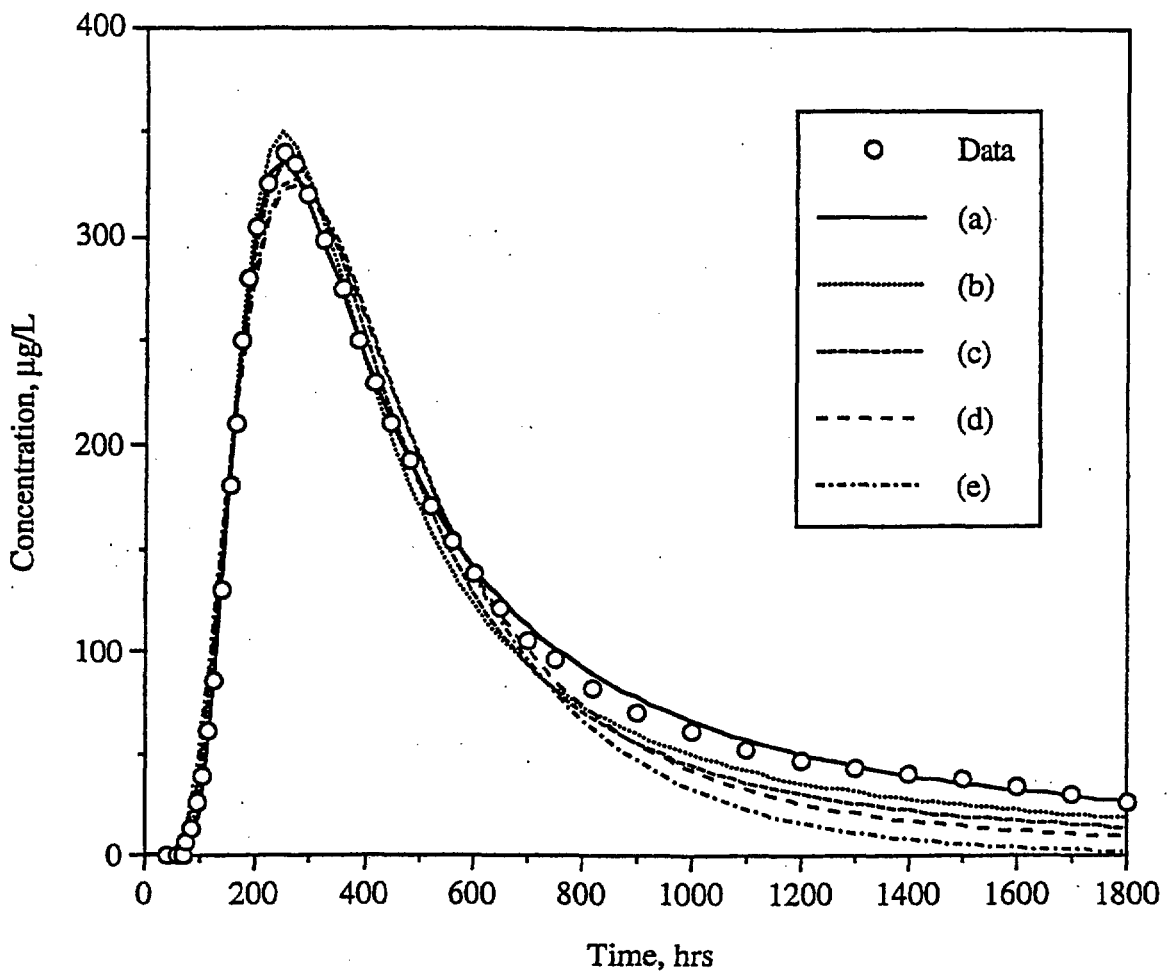


Figure C-6. Fits to the May 1996 PFBA data assuming different values of the lumped matrix diffusion parameter,  $\frac{\phi}{b} \sqrt{D_m}$ : (a)  $0.00346 \text{ cm}^{-1}$ , (b)  $0.00173 \text{ cm}^{-1}$ , (c)  $0.000865 \text{ cm}^{-1}$ , (d)  $0.000346 \text{ cm}^{-1}$ , and (e)  $0 \text{ cm}^{-1}$  (single-porosity system). Parameter values yielding the fits are given in Table C-2. Data points are a subset of the actual data (used for curve-fitting). (DTN LAPR831231AQ98.001 and DTN LAPR831231AN99.001).

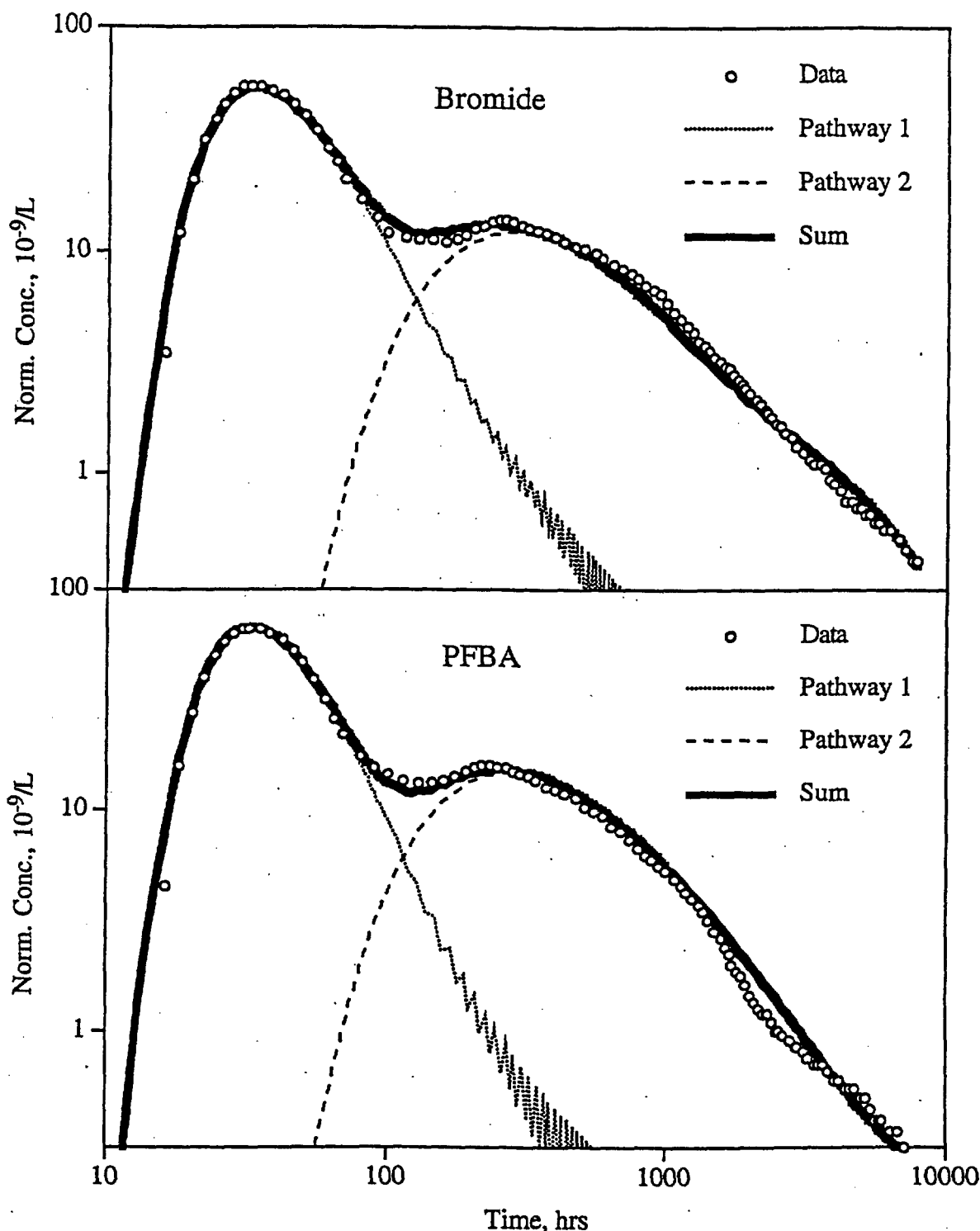


Figure C-7. Fits to the PFBA and bromide data from the reactive tracer test assuming two "pathways." Model parameters corresponding to the fits are given in Table C-3. The data points are a subset of the actual data (used for curve-fitting). (DTN LAPR831231AQ98.001 [data] and DTN LAPR831231AQ99.002 [model fits]).

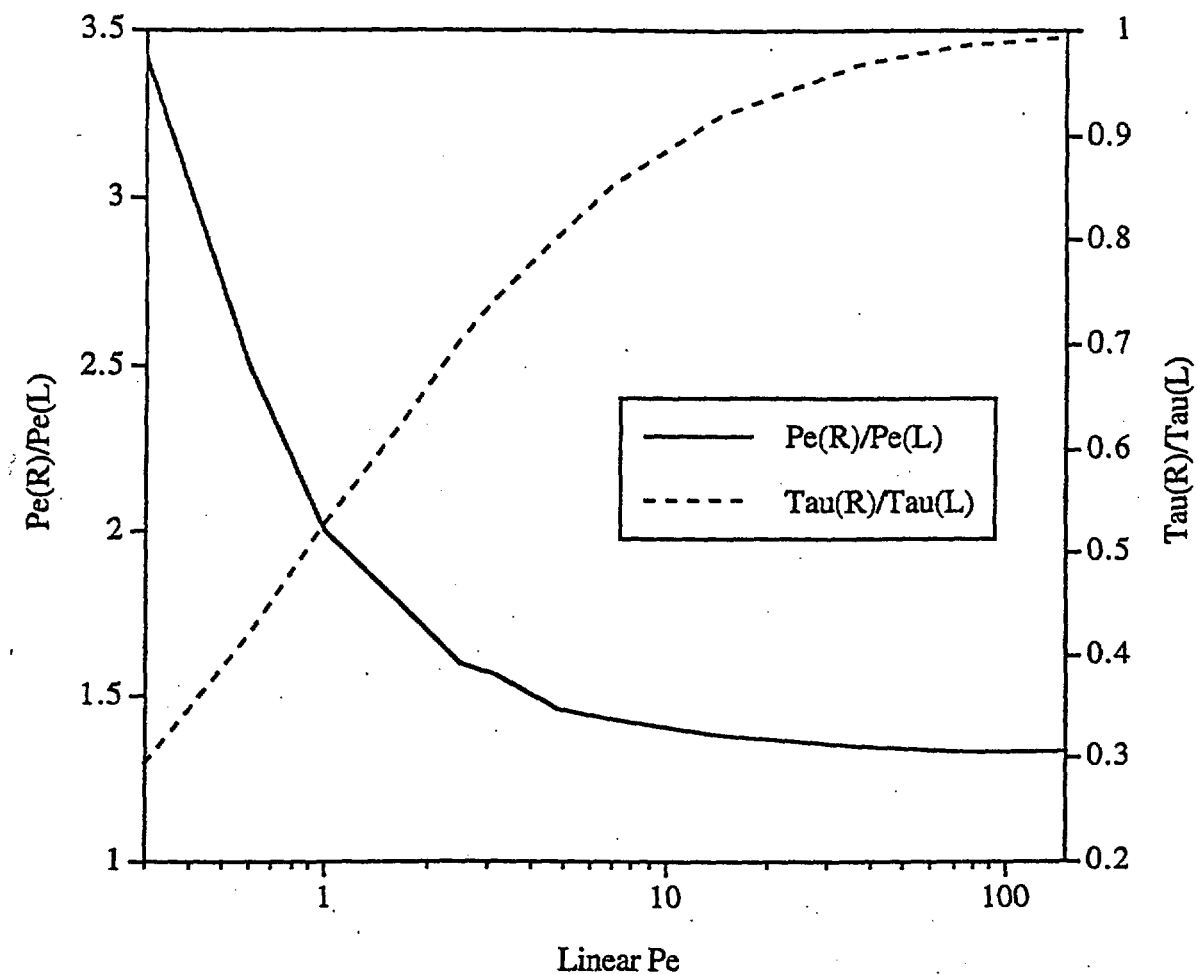


Figure C-8. Ratios of radial and linear mean residence times ( $\tau$ ) and Peclet numbers ( $Pe$ ) as a function of linear Peclet number. Curves were obtained by fitting a linear flow breakthrough curve of known  $\tau$  and  $Pe$  using a radial model in RELAP. (DTN LAPR831231AN99.001).

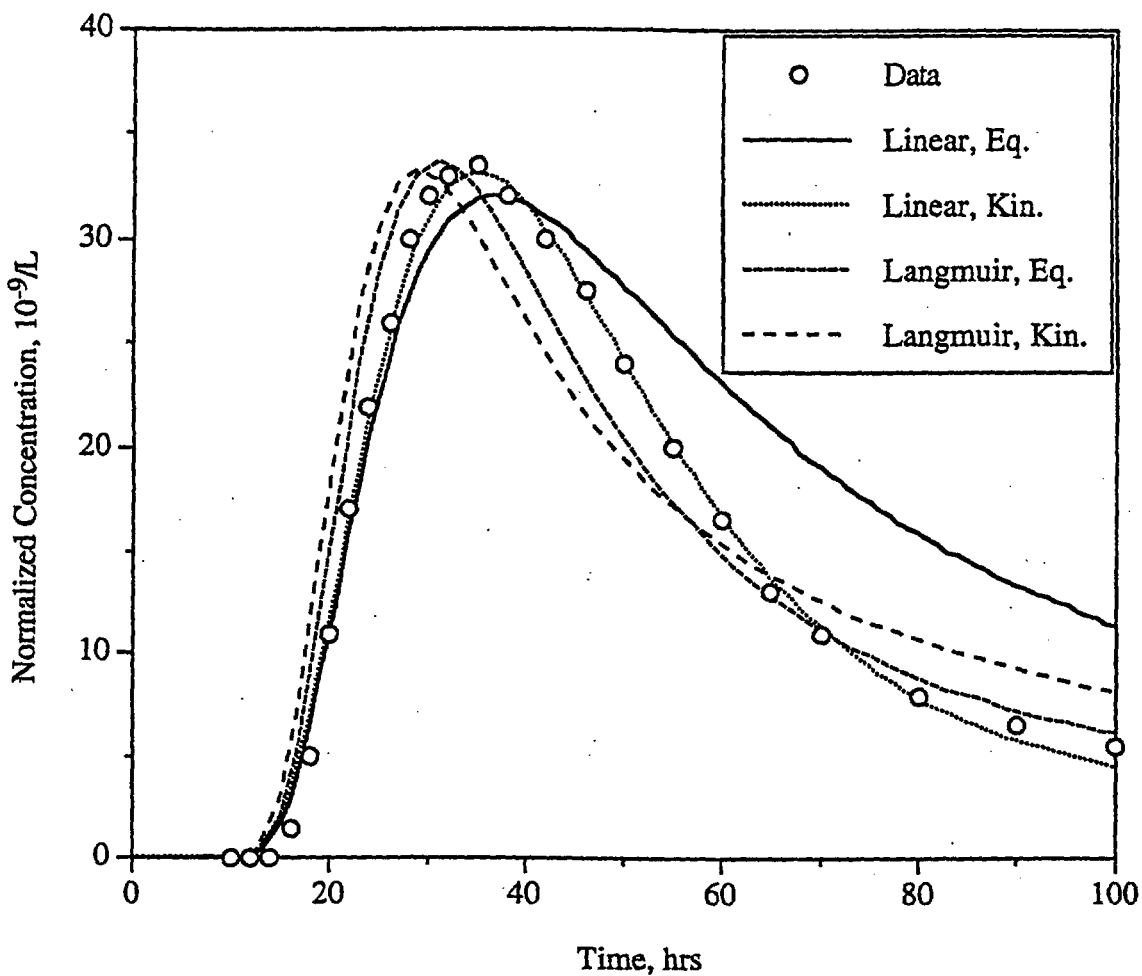


Figure C-9. Fits to the first lithium peak in the reactive tracer test using different isotherms and assuming only a single pathway with the same hydrologic parameters that provided good fits to the PFBA and bromide data. The "Linear" curves were generated using the semi-analytical model, RELAP, while the "Langmuir" curves were generated using the numerical model, RETRAN. Model parameters corresponding to the fits are given in Table C-4. The data points are a subset of the actual data (used for curve-fitting). (DTN LAPR831231AQ98.001 and DTN LAPR831231AQ99.002).

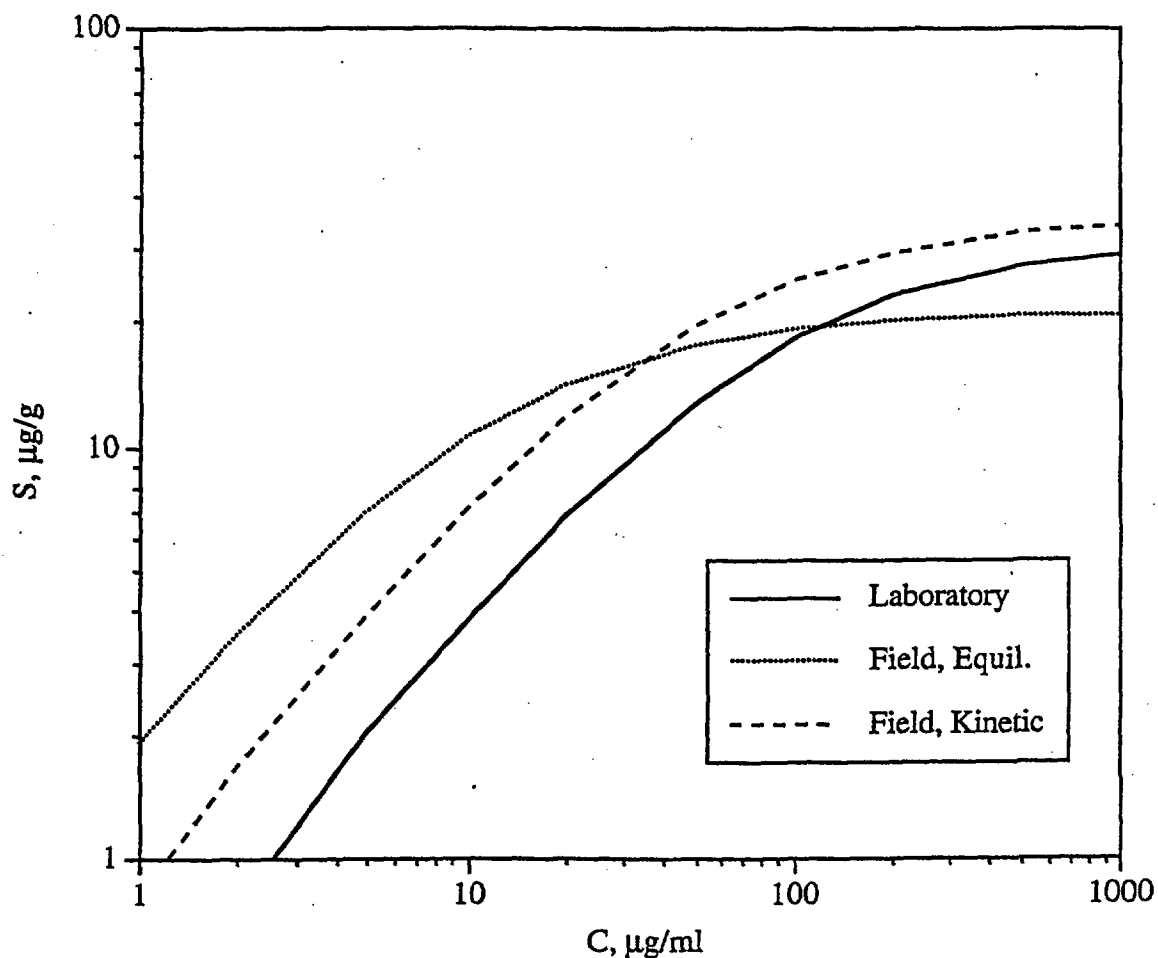


Figure C-10. Langmuir isotherms derived for lithium ion from laboratory testing and from interpretations of the first lithium peak in the reactive tracer test. Table C-4 gives Langmuir isotherm parameters used to generate the curves. (Notebook LA-CST-CW-NBK-98-011).

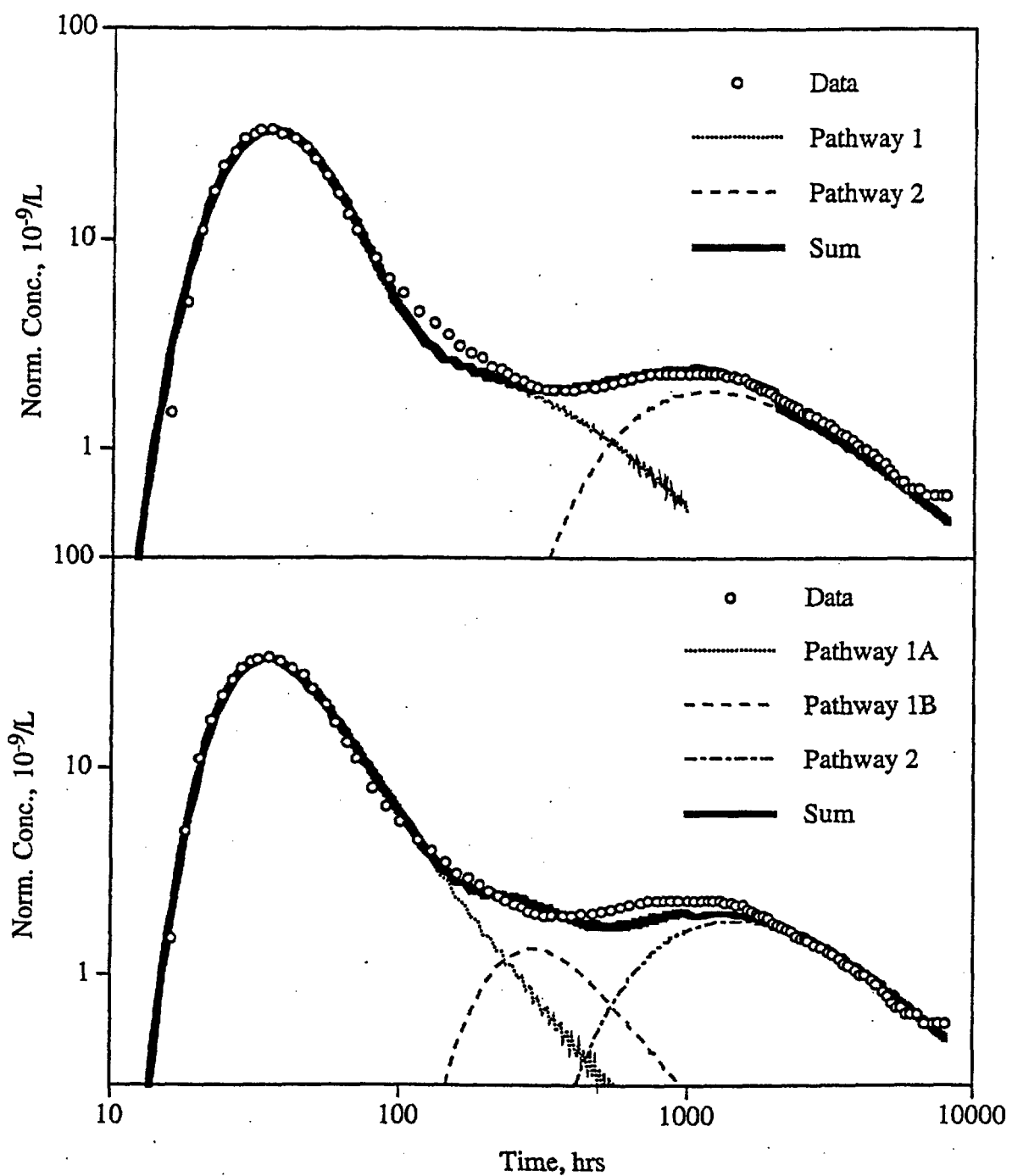


Figure C-11. Fits to the lithium data in the reactive tracer test obtained by assuming linear, rate-limited sorption in the first pathway that results in the first peak (top) and by assuming chemical heterogeneity in the first pathway, resulting in two subpathways (1A and 1B) that each have linear, equilibrium sorption (bottom). Pathway 2 in both cases has linear, equilibrium sorption. Model parameters corresponding to the fits are given in Tables C-3, C-4, C-6, and C-8. The data points are a subset of the actual data (used for curve-fitting). (DTN LAPR831231AQ98.001 [data] and DTN LAPR831231AQ99.002 [model fits]).

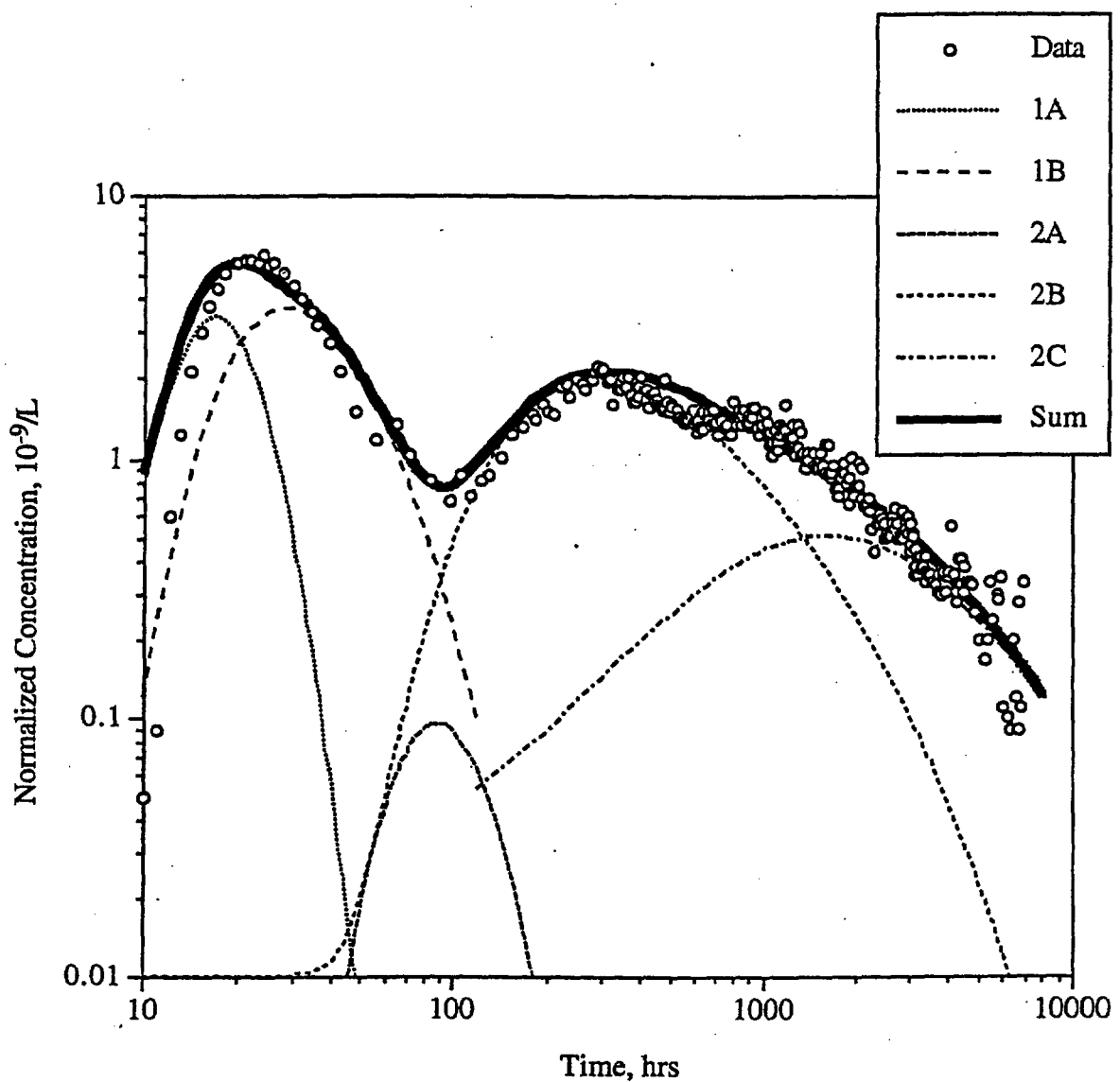


Figure C-12. Split-pathway fits to the microsphere data from the reactive tracer test. Pathways 1A and 1B represent nondetaching and detaching fractions, respectively, of spheres moving through pathway 1. Pathways 2A, 2B, and 2C represent nondetaching and two detaching fractions, respectively, of spheres moving through pathway 2. Filtration and resuspension/detachment rate constants obtained from the fits are given in Table C-10. (DTN LAPR831231AQ98.001 [data] and DTN LAPR831231AQ99.002 [model fits]).

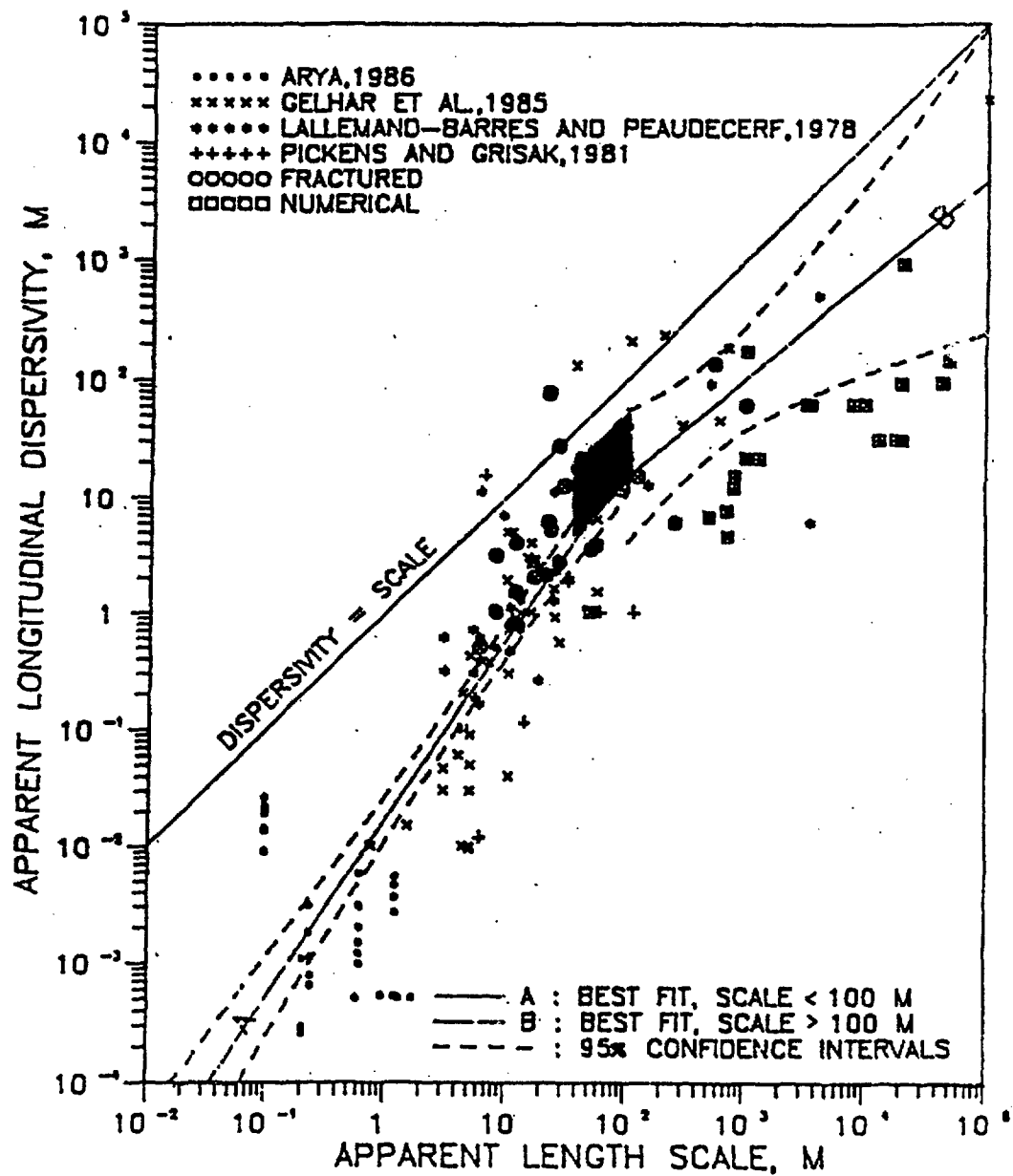


Figure C-13. Plot of dispersivity vs. length scale showing range of C-holes values derived from interpretations of the reactive tracer test (darkened box). Plot taken from Neuman (1990). (DTN LAPR831231AQ99.002 and notebook LA-CST-CW-NBK-98-011).

## Appendix D:

### Description of Mathematical Models in Computer Codes RELAP and RETRAN

To model sorbing tracer transport in a dual-porosity system, we start with a conceptual model for conservative tracer transport in fractured systems originally introduced by Maloszewski and Zuber (1983, 1985), and we extend it to include rate-limited, nonlinear sorbing tracer transport. Fig. D-1 shows the assumed model domain, which consists of parallel-plate fractures of aperture  $2b$  separated by matrix blocks of thickness  $L$ , each of which extend infinitely into the page. Tang et al. (1981) assumed an infinite spacing between fractures, but this is just a special case of a finite matrix with a very large fracture spacing. Others have used similar model conceptualizations but with cylindrical or spherical-shaped matrix blocks (Rasmussen and Neretnieks, 1986). All of these formulations yield similar results when tracer penetration into the matrix is much less than matrix block dimensions; that is, when time scales are short compared to time scales necessary for diffusion to the centerline of the blocks. In Fig. D-1, the fracture apertures, fracture flow velocity, matrix bulk density, matrix porosity, and fracture and matrix sorption parameters are assumed to be the same everywhere in the system (no spatial heterogeneity). This is clearly a simplification, but spatial variation is very difficult to characterize in a field setting, and it also introduces considerable complexity and ambiguity to model interpretations (i.e., more adjustable parameters to fit an observed response). Therefore, we considered it appropriate, as a first approximation, to assume homogeneous properties and use bulk average parameter values.

Referring to Fig. D-1, it is assumed that advective transport occurs only in the  $x$ -direction in the fractures and that diffusion into the matrix is important only in the  $y$ -direction. It is also assumed that there are no concentration gradients in the  $y$ -direction in the fractures. These assumptions allow the equations describing transport in the fractures and the matrix to be decoupled and solved as separate 1-dimensional problems that are linked only through a boundary condition and a single term in the fracture transport equation.

#### **Linear Flow in Fractures**

For a constant flow velocity in fractures (i.e., linear flow), the differential equations and boundary conditions describing rate-limited, nonlinear sorbing tracer transport in the fractures and matrix (the most general case) are:

Fractures, Solution Phase:

$$\frac{\partial C_f}{\partial t} + v_f \frac{\partial C_f}{\partial x} - D_f \frac{\partial^2 C_f}{\partial x^2} + \left( \frac{\rho_f}{\eta} \right) \frac{\partial S_f}{\partial t} - \frac{\phi D_m}{b \eta} \frac{\partial C_m}{\partial y} \Big|_{y=b} = 0 \quad (D1)$$

Fractures, Immobile Phase:

$$\left( \frac{\rho_f}{\eta} \right) \frac{\partial S_f}{\partial t} - k_{ff} \left( \frac{C_f^{\beta_f}}{1 + \alpha_f C_f} \right) + k_{fr} S_f = 0 \quad (D2)$$

Matrix, Solution Phase:

$$\frac{\partial C_m}{\partial t} - D_m \frac{\partial^2 C_m}{\partial y^2} + \left( \frac{\rho_B}{\phi} \right) \frac{\partial S_m}{\partial t} = 0 \quad (D3)$$

Matrix, Immobile Phase:

$$\left( \frac{\rho_B}{\phi} \right) \frac{\partial S_m}{\partial t} - k_{mf} \left( \frac{C_m^{\beta_m}}{1 + \alpha_m C_m} \right) + k_{mr} S_m = 0 \quad (D4)$$

subject to initial and boundary conditions

$$C_f(x, 0) = 0 \quad (D1a)$$

$$C_f(0, t) = \delta(t) \quad (D1b)$$

$$C_f(\infty, t) = 0 \quad (D1c)$$

$$S_f(x, 0) = 0 \quad (D2a)$$

$$C_m(y, x, 0) = 0 \quad (D3a)$$

$$C_m(b, x, t) = C_f(x, t) \quad (D3b)$$

$$\frac{\partial C_m}{\partial y} \left( \frac{L}{2}, x, t \right) = 0 \quad (D3c)$$

$$S_m(y, x, 0) = 0 \quad (D4a)$$

where,  $C_f$  = tracer concentration in solution in fractures,  $M/L^3$

$C_m$  = tracer concentration in solution in matrix,  $M/L^3$

$S_f$  = tracer surface concentration on fracture surfaces,  $M/M$  solid

$S_m$  = tracer surface concentration on matrix surfaces,  $M/M$  solid

$v_f$  = fluid velocity in fractures,  $L/T$

$D_f$  = dispersion coefficient in fractures,  $L^2/T$

$D_m$  = molecular diffusion coefficient in matrix,  $L^2/T$

$\rho_f$  = bulk density of material in fractures,  $M/L^3$

$\rho_B$  = bulk density of matrix,  $M/L^3$

$\eta$  = porosity within fractures,

$\phi$  = matrix porosity,

$b$  = fracture half aperture,  $L$

$L$  = distance between parallel fractures in medium,  $L$

$k_{ff}$  = rate constant for sorption to surfaces in fractures,  $1/T$  (if linear)

$k_{fr}$  = rate constant for desorption from surfaces in fractures,  $M/L^3 T$

$k_{mf}$  = rate constant for sorption to surfaces in matrix,  $1/T$  (if linear)

$k_{mr}$  = rate constant for desorption from surfaces in matrix,  $M/L^3 T$

$\alpha_i, \beta_i$  = sorption isotherm parameters defined in equation (D5) ( $i = f$ , fractures;  $i = m$ , matrix), and

$\delta(t)$  = dirac delta function.

Coupling between the fractures and matrix is achieved through boundary condition (D3b) and through the last term on the left-hand side of equation (D1). We make use of the expression

$\left(\frac{\rho_f}{\eta}\right)$  to account for surface area available for sorption in fractures. In reality, fractures could be completely open (i.e.,  $\eta = 1$ ,  $\rho_f = 0$ ), and sorption might occur only on the walls. In this case, the expression  $\left(\frac{\rho_f}{\eta}\right)$  can be considered a proportionality constant that should be adjusted to an appropriate value to describe sorption to the walls. Alternatively, sorption in fractures can be completely ignored by setting this term equal to zero. We use the dirac-delta function as the inlet boundary condition (equation (D1b)) because the solutions obtained using this boundary condition are residence time distributions that can be mathematically convoluted with any generalized input function to obtain a generalized breakthrough curve.

In the above equations, we have used a general expression for the sorption isotherms in both the fractures and the matrix:

$$S = \frac{KC^\beta}{1 + \alpha C} \quad (D5)$$

This expression allows a linear, a Freundlich, or a Langmuir isotherm to be defined. A Freundlich isotherm is obtained by setting  $\alpha = 0$ , a Langmuir isotherm is obtained by setting  $\beta = 1$ , and a linear isotherm is obtained by setting  $\alpha = 0$  and  $\beta = 1$ . Equations (D2) and (D4) also assume nonlinearity of the adsorption reaction (i.e., not first-order in concentration) while the desorption reaction is assumed to be linear (first-order in surface concentration). Note that  $K = k_f/k_m$ , where  $k_f$  and  $k_m$  are the rate constants for sorption and desorption, respectively.

If equilibrium sorption is assumed, the sorption isotherm expression can be substituted directly for  $S_f$  and  $S_m$  in equations (D1) and (D3), respectively. This eliminates the need for the immobile phase equations (D2) and (D4). Recognizing that  $\frac{\partial S}{\partial t} = \frac{\partial S}{\partial C} \cdot \frac{\partial C}{\partial t}$ , the fracture and matrix transport equations become

Fractures:

$$\frac{\partial C_f}{\partial t} + v_f \frac{\partial C_f}{\partial x} - D_f \frac{\partial^2 C_f}{\partial x^2} + \left( \frac{\rho_f}{\eta} \right) \left[ \frac{K_f \beta_f C_f^{\beta_f - 1}}{1 + \alpha_f C_f} - \frac{\alpha_f K_f C_f^{\beta_f}}{(1 + \alpha_f C_f)^2} \right] \frac{\partial C_f}{\partial t} - \frac{\phi D_m}{b \eta} \frac{\partial C_m}{\partial y} \Big|_{y=b} = 0 \quad (D6)$$

Matrix:

$$\frac{\partial C_m}{\partial t} - D_m \frac{\partial^2 C_m}{\partial y^2} + \left( \frac{\rho_m}{\phi} \right) \left[ \frac{K_m \beta_m C_m^{\beta_m - 1}}{1 + \alpha_m C_m} - \frac{\alpha_m K_m C_m^{\beta_m}}{(1 + \alpha_m C_m)^2} \right] \frac{\partial C_m}{\partial t} = 0 \quad (D7)$$

where the terms in brackets, [ ], are  $\frac{\partial S}{\partial C}$  for the fractures and matrix, respectively, and

$$K_m = \frac{k_{mf}}{k_{mr}} \text{ and } K_f = \frac{k_{ff}}{k_{fr}}$$

When the sorption isotherm is nonlinear (either rate-limited or equilibrium), the appropriate equations given above are solved numerically using an implicit alternating-direction

finite-difference method. By assuming 1-D transport in both the fractures and the matrix and using an explicit time discretization for the adsorption (nonlinear) term, the model equations are reduced to a single tridiagonal linear system for the fractures and a set of independent tridiagonal linear systems for each row of grid points extending into the matrix (perpendicular to the fractures). These tridiagonal systems can be solved very efficiently, and the implicit time discretization provides unconditional stability. The computer code developed to obtain the numerical solution is called RETRAN (REactive TRANsport code).

For linear sorption isotherms (either rate-limited or equilibrium), it is possible to obtain a semi-analytical solution of the transport equations by following the Laplace transform technique of Maloszewski and Zuber (1983). The Laplace transform removes the time derivatives from the governing equations, rendering them ordinary differential equations that can be solved by standard methods. The Laplace transforms of the general rate-limited equations (D1), (D2), (D3), and (D4), assuming linear isotherms, are

Fractures, Solution Phase:

$$s\bar{C}_f + v_f \frac{\partial \bar{C}_f}{\partial x} - D_f \frac{\partial^2 \bar{C}_f}{\partial x^2} + \left( \frac{\rho_f}{\eta} \right) s\bar{S}_f - \frac{\phi D_m}{b\eta} \frac{\partial \bar{C}_m}{\partial y} \Big|_{y=b} = 0 \quad (D8)$$

Fractures, Immobile Phase:

$$\left( \frac{\rho_f}{\eta} \right) s\bar{S}_f - k_{ff} \bar{C}_f + k_{fr} \bar{S}_f = 0 \quad (D9)$$

Matrix, Solution Phase:

$$s\bar{C}_m - D_m \frac{\partial^2 \bar{C}_m}{\partial y^2} + \left( \frac{\rho_B}{\phi} \right) s\bar{S}_m = 0 \quad (D10)$$

Matrix, Immobile Phase:

$$\left( \frac{\rho_B}{\phi} \right) s\bar{S}_m - k_{mf} \bar{C}_m + k_{mr} \bar{S}_m = 0 \quad (D11)$$

where,  $s$  = Laplace transform independent variable (replacing time), and  
 $\bar{X}$  = Laplace transform of dependent variable.

Equations (D9) and (D11) are now algebraic equations that can be solved for  $\bar{S}$ , and the result(s) can be substituted into equations (D8) and (D10) to obtain (see also, Maloszewski and Zuber, 1991):

Fractures:

$$\left[ 1 + \frac{\left( \frac{\rho_f}{\eta} \right) k_{ff}}{\left( \frac{\rho_f}{\eta} \right) s + k_{fr}} \right] s\bar{C}_f + v_f \frac{\partial \bar{C}_f}{\partial x} - D_f \frac{\partial^2 \bar{C}_f}{\partial x^2} - \frac{\phi D_m}{b\eta} \frac{\partial \bar{C}_m}{\partial y} \Big|_{y=b} = 0 \quad (D12)$$

Matrix:

$$\left[ 1 + \frac{\left(\frac{\rho_B}{\phi}\right)k_{mf}}{\left(\frac{\rho_B}{\phi}\right)s + k_{mr}} \right] s \bar{C}_m - D_m \frac{\partial^2 \bar{C}_m}{\partial y^2} = 0 \quad (D13)$$

The equilibrium sorption case is readily apparent from equations (D12) and (D13) if we set  $k_f$  and  $k_r$  to very large values and recognize that  $K_d = \frac{k_f}{k_r}$  and  $R = 1 + \left(\frac{\rho_B}{\phi}\right)K_d$ . The equilibrium case was also derived by Tang et al. (1981) for an infinite matrix boundary condition.

Equations (D12) and (D13) are in the same form as the equations solved by Maloszewski and Zuber (1983). The only difference is that the sorption expressions in brackets in equations (D12) and (D13) were equal to 1 in Maloszewski and Zuber's equations because they only considered conservative solute transport. Thus, the solution of equations (D12) and (D13) subject to Laplace-transformed boundary conditions (D1a) through (D4a) is identical to the solution presented by Maloszewski and Zuber except that the  $s\bar{C}_f$  and  $s\bar{C}_m$  terms now have more complicated coefficients. Referring to Maloszewski and Zuber (1983) for details of the derivation, the final result for transport in the fractures coupled with diffusion into the matrix is a single Laplace-domain equation given by

$$\bar{C}_f(x) = \exp \left\{ \frac{v_f x}{2D_f} \left[ 1 - \sqrt{1 + \frac{4D_f R_f(s)}{v_f^2} s + \frac{4D_f \phi}{v_f^2 b \eta} \sqrt{R_m(s) D_m s} \operatorname{Tanh} \left( \sqrt{\frac{s R_m(s)}{D_m}} \left( \frac{L}{2} - b \right) \right)} \right] \right\} \quad (D14)$$

where,

$$R_f(s) = 1 + \frac{\left(\frac{\rho_f}{\eta}\right)k_{ff}}{\left(\frac{\rho_f}{\eta}\right)s + k_{fr}} \quad (D15)$$

$$R_m(s) = 1 + \frac{\left(\frac{\rho_B}{\phi}\right)k_{mf}}{\left(\frac{\rho_B}{\phi}\right)s + k_{mr}} \quad (D16)$$

If we introduce the mean fluid residence time in fractures,  $\tau = \frac{x}{v_f}$ , and the dimensionless Peclet number,  $Pe = \frac{Xv_f}{D_f}$ , which are related to the first and second moments of fluid residence time in the system, respectively, equation (D14) can be rewritten as

$$\bar{C}_f(x) = \exp \left\{ \frac{Pe}{2} \left[ 1 - \sqrt{1 + \frac{4\tau}{Pe} \left\{ sR_f(s) + \frac{\phi}{b\eta} \sqrt{R_m(s)D_m} s \operatorname{Tanh} \left( \sqrt{\frac{sR_m(s)}{D_m}} \left( \frac{L}{2} - b \right) \right) \right\}} \right] \right\} \quad (D17)$$

Equation (D17) is arguably a more natural expression to work with than equation (D14) when considering field data because actual distances and fluid velocities in a field experiment will be dependent on flow pathways in the system, but the concepts of the first and second moments of fluid residence time are less ambiguous. Equation (D17) also clearly delineates the expression  $\frac{\phi}{b\eta} \sqrt{R_m(s)D_m}$  as an effective mass transfer coefficient for matrix diffusion. This expression can be further divided into a flow-system-dependent part,  $\frac{\phi}{b\eta}$ , and a tracer-dependent part,  $\sqrt{R_m(s)D_m}$ . In chemical engineering, Laplace-domain expressions such as equations (D14) and (D17) are used extensively in control theory and are referred to as "transfer functions."

We now consider three simplifications to equation (D17). First, by setting  $R_f(s)$  and  $R_m(s)$  equal to 1, we reproduce the result for a nonsorbing tracer obtained by Maloszewski and Zuber (1983). Second, in the case of an infinite matrix, as was assumed by Tang et al. (1981), the argument of the hyperbolic tangent approaches infinity and hence the hyperbolic tangent itself becomes unity. The resulting expression is identical to that derived by Tang et al. (1981) except that the reaction terms have now been generalized to allow rate-limited as well as equilibrium sorption. Finally, if we set the matrix porosity,  $\phi$ , equal to zero, the entire term accounting for diffusive transport in the matrix (the term containing the hyperbolic tangent) drops out of the equation, and we get an expression describing reactive transport in a single-porosity medium. Thus, the transport expression derived for a dual-porosity medium is consistent in that it reduces to a single-porosity medium when  $\phi = 0$ .

## Radial Convergent Flow in Fractures

The derivations in the preceding section were strictly for a spatially invariant flow rate in fractures (linear flow). In reality, the flow field in a weak recirculation tracer test in a confined, heterogeneous aquifer is likely to range between linear and radial (National Research Council, 1996, pp. 252-259), with these two cases representing end members. In a completely unconfined aquifer, spherical flow might be an appropriate end member, but we do not consider that here because of the partially-confined nature of the Bullfrog tuff.

In the case of radial flow, we only have to modify the equations for solution phase transport in the fractures in the preceding section. Specifically, all  $x$ -derivatives become  $r$ -

derivatives and the  $D_f \frac{\partial^2 C_f}{\partial x^2}$  terms become  $\left(\frac{1}{r}\right) \frac{\partial}{\partial r} \left(r D_f \frac{\partial \bar{C}_f}{\partial r}\right)$ . Equations (D1), (D6), (D8), and (D12) then become, respectively:

$$\frac{\partial C_f}{\partial t} + v_f \frac{\partial C_f}{\partial r} - \left(\frac{1}{r}\right) \frac{\partial}{\partial r} \left(r D_f \frac{\partial \bar{C}_f}{\partial r}\right) + \left(\frac{\rho_f}{\eta}\right) \frac{\partial S_f}{\partial t} - \left.\frac{\phi D_m}{b\eta} \frac{\partial C_m}{\partial y}\right|_{y=b} = 0 \quad (D18)$$

$$\frac{\partial C_f}{\partial t} + v_f \frac{\partial C_f}{\partial r} - \left(\frac{1}{r}\right) \frac{\partial}{\partial r} \left(r D_f \frac{\partial \bar{C}_f}{\partial r}\right) + \left(\frac{\rho_f}{\eta}\right) \left[ \frac{K_f \beta_f C_f^{\beta_f-1}}{1 + \alpha_f C_f} - \frac{\alpha_f K_f C_f^{\beta_f}}{(1 + \alpha_f C_f)^2} \right] \frac{\partial C_f}{\partial t} - \left.\frac{\phi D_m}{b\eta} \frac{\partial C_m}{\partial y}\right|_{y=b} = 0 \quad (D19)$$

$$s \bar{C}_f + v_f \frac{\partial \bar{C}_f}{\partial r} - \left(\frac{1}{r}\right) \frac{\partial}{\partial r} \left(r D_f \frac{\partial \bar{C}_f}{\partial r}\right) + \left(\frac{\rho_f}{\eta}\right) s \bar{S}_f - \left.\frac{\phi D_m}{b\eta} \frac{\partial \bar{C}_m}{\partial y}\right|_{y=b} = 0 \quad (D20)$$

$$\left[ 1 + \frac{\left(\frac{\rho_f}{\eta}\right) k_f}{\left(\frac{\rho_f}{\eta}\right) s + k_f} \right] s \bar{C}_f + v_f \frac{\partial \bar{C}_f}{\partial r} - \left(\frac{1}{r}\right) \frac{\partial}{\partial r} \left(r D_f \frac{\partial \bar{C}_f}{\partial r}\right) - \left.\frac{\phi D_m}{b\eta} \frac{\partial \bar{C}_m}{\partial y}\right|_{y=b} = 0 \quad (D21)$$

All other equations are the same as for the linear flow case if the model domain is the same as in Fig. D-1.

Becker (1996, pp. 110-115, 119-131) have solved the radial flow transport problem in the special case of convergent flow with no sorption or matrix diffusion (i.e., a single-porosity system). Their solution differs from other radial convergent transport solutions in the literature (e.g., Moench, 1989, 1995) in that their boundary condition at the production well is an “absorbing” boundary that dictates that any solute mass reaching the production well immediately disappears from the system. This boundary condition is consistent with a transfer function approach to interpreting tracer test responses, discussed below. The resulting Laplace domain solution for the case of no sorption or matrix diffusion in terms of  $\tau$  and  $Pe$  (analogous to equation (D17)) is (Becker 1996, pp. 110-115):

$$\bar{C}_f(r_w) = \exp \left[ \frac{Pe}{2} \left( 1 - \frac{1}{r_{LW}} \right) \right] \frac{\text{Ai}(\sigma^{1/3} y_L)}{\text{Ai}(\sigma^{1/3} y_w)} \quad (D22)$$

where,  $r_w$  = production well radius,

$r_{LW}$  = production well radius divided by separation between injection and production wells,

$$y_L = Pe + \frac{1}{4\sigma},$$

$$y_w = \frac{Pe}{r_{LW}} + \frac{1}{4\sigma},$$

$$\sigma = \left( \frac{r_{LW}}{Pe} \right)^2 \frac{2\tau s}{(r_{LW}^2 - 1)},$$

$Ai(z)$  = Airy function (Spanier and Oldham, 1987, pp. 555-562).

Becker (1996, pp. 119-131) extended this result to a dual-porosity system (with the geometry of Fig. D-1) for a tracer that exhibits equilibrium, linear sorption behavior. We extend it further here to allow for rate-limited, linear sorption. The result, without derivation, is identical to equation (D22) but with  $\sigma$  redefined as

$$\sigma = \left( \frac{r_{LW}}{Pe} \right)^2 \frac{2\tau s \Psi(s)}{(r_{LW}^2 - 1)} \quad (D23)$$

where,  $\Psi(s) = R_f(s) + \frac{\phi}{b\eta} \sqrt{\frac{R_m(s)D_m}{s}} \operatorname{Tanh} \left( \sqrt{\frac{sR_m(s)}{D_m}} \left( \frac{L}{2} - b \right) \right)$  and  $R_f(s)$  and  $R_m(s)$  are as defined in equations (D15) and (D16).

Equation (D22) using  $\sigma$  defined in equation (D23) is the Laplace transform transfer function expression that should be used in lieu of equation (D17) for the case of radial convergent transport of a linearly sorbing tracer in a dual-porosity system. For nonlinear sorption, a numerical formulation of equation (D18) in conjunction with equations (D2), (D3), and (D4) is required for the rate-limited case, and equations (D19) and (D7) are required for the equilibrium case. The numerical model RETRAN can be used to solve these nonlinear, convergent radial flow equations.

### Convolution of Transfer Functions to Obtain Tracer Test Responses

Before we can obtain a meaningful field-scale transport prediction, we must convolute equation (D17) or (D22) with a realistic tracer injection function. In the time domain, such a convolution is accomplished by a convolution integral, but in the Laplace domain it becomes a simple multiplication (Jenson and Jeffreys, 1977, pp. 169-170):

$$C(t) = \int_0^t A(\tau) \cdot B(t - \tau) d\tau \Rightarrow \bar{C}(s) = \bar{A}(s) \cdot \bar{B}(s) \quad (D24)$$

where,  $X(t)$  = time-domain function,  
 $\bar{X}(s)$  = Laplace transform of time-domain function, and  
 $s$  = Laplace transform variable.

This process can be extended to more than two transfer functions by taking the product of all applicable functions. Thus, in a field tracer test, transfer functions for tracer injection, pipeline delays, and storage in the injection and production wellbores can all easily be convoluted with the groundwater system transfer function (e.g., equations (D17) or (D22)) to

obtain an overall transfer function for the test. We assume the most practical injection function in a field tracer test: a finite-duration, constant concentration pulse, which has a Laplace transform given by

$$\bar{I}(s) = C_o \left( \frac{1 - \exp(-T_p s)}{s} \right) \quad (D25)$$

where,  $C_o$  = concentration of injection pulse,  $M/L^3$

$T_p$  = duration of injection pulse,  $T$ .

Wellbore storage is accounted for by assuming that the wellbores are well-mixed regions (Moench, 1989, 1995). The Laplace domain transfer function for a well-mixed region is given by

$$\bar{W}(s) = \frac{\gamma}{\gamma + s} \quad (D26)$$

where,  $\gamma$  = time constant, generally assumed to be the volumetric flow rate divided by the volume of well-mixed region,  $1/T$ .

Pipeline delays can be accounted for by a transfer function of the form

$$\bar{P}(s) = \exp(-T_d s) \quad (D27)$$

where,  $T_d$  = delay time,  $T$ .

Reinjection of produced water (i.e., recirculation of tracers) can be accounted for with transfer functions as follows:

$$\bar{F}_R(s) = \frac{\bar{F}(s)}{1 - \varepsilon \bar{F}(s)} \quad (D28)$$

where,  $\bar{F}_R(s)$  = transfer function with recirculation,

$F(s)$  = transfer function without recirculation,

$\varepsilon$  = recirculation ratio ( $0$  = no recirculation,  $1$  = full recirculation).

A computer model called RELAP (REactive transport LAPlace transform inversion code) was developed to predict field tracer transport by convoluting (i.e., multiplying) either the linear or radial dual-porosity transfer functions (equations (D17) or (D22), respectively) with the transfer functions described above. RELAP numerically inverts the resulting Laplace-domain product of transfer functions to obtain a time domain solution. The numerical inversion procedure is described in the next section.

We have given considerable emphasis here to the Laplace transform modeling approach despite the fact that the numerical model RETRAN is more general because it can accommodate nonlinear sorption isotherms and ultimately spatial heterogeneity. The Laplace transform

approach, however, has a distinct advantage over the numerical modeling approach in that it is very easy to account for the effects of processes other than transport in the aquifer (by the convolution procedure described above). The transfer function approach is also well suited to estimating model parameters by matching solutions to experimental breakthrough curves. The Laplace transform inversion executes in a fraction of a second on a typical computer workstation, so RELAP can be exercised with different values of transport parameters literally thousands of times per minute. By contrast, a typical RETRAN simulation with comparable numerical accuracy takes 2-3 minutes of compute time on the same workstation. RELAP contains a parameter search algorithm to minimize the sum-of-squares differences between model predictions and a given tracer data set. This feature allows rapid estimation of model parameter values that are consistent with the test data. Because of the fast execution times of the RELAP inversion algorithm and the fact that sum-of-squares response surfaces for the transport problem typically have multiple minima, the search algorithm simply adjusts parameters over a specified range in systematic, brute-force manner to achieve a least-squares fit to the data. The resulting fits can then be used to provide good initial estimates to RETRAN for obtaining estimates of nonlinear sorption parameters.

Another reason for developing the Laplace transform model is to provide semi-analytical solutions against which more general numerical models can be compared and verified. This is important because numerical models will ultimately be used to account for spatial heterogeneity and temporal variations in boundary conditions when making predictions of radionuclide transport over large time and length scales.

The Laplace transform and numerical models were tested by (1) inverting several simple Laplace transforms with known time-domain solution to ensure that the Laplace transform inversion algorithm was working properly, (2) comparing predicted nonsorbing solute breakthrough curves in a single-porosity medium to analytical solutions (Kreft and Zuber, 1978; Levenspiel, 1972, pp. 273-282), and (3) comparing the semi-analytical (RELAP) and numerical (RETRAN) model predictions for sorbing tracers with linear isotherms (both rate-limited and equilibrium). In all cases, excellent agreement was obtained between model predictions and analytical solutions, or between the two models.

### Numerical Inversion of Laplace Transforms

The final step in obtaining a transport prediction from the transfer functions is to invert the solution from the Laplace domain to the time domain. We accomplish this by using a Fourier transform procedure embodied in an algorithm obtained over the World Wide Web (Lindhardt, 1995). We have found this algorithm to be more stable for Laplace transform inversions than any others we have tried (e.g., Stehfest, 1970; de Hoog et al., 1982).

The basic principles of the algorithm used for numerical inversion of Laplace transforms are given below. We thank Sven Lindhardt (unknown affiliation) for providing the algorithm in the form of a MathCad® worksheet at the World Wide Web address:  
<http://www.mathsoft.com/appsindex.html>. The worksheet can be found under the program name invsfft.mcd at this web site. Sven also provided much of the following description of the mathematical basis for the algorithm.

The Laplace transform is defined by

$$F(s) = \int_0^{\infty} f(t)e^{-st} dt \quad (D29)$$

where,  $s$  = Laplace transform variable,  
 $t$  = time,  
 $f(t)$  = time domain function,  
 $F(s)$  = Laplace domain function.

If we set  $s = \sigma + j\omega$ , where  $j = \sqrt{-1}$ , in equation (D29) and change the lower limit of integration to  $-\infty$  (which is permissible for any initial-valued problem because  $f(t) = 0$  for  $t < 0$ ) we obtain

$$F(s) = \int_{-\infty}^{\infty} f(t)e^{-\sigma t} e^{-j\omega t} dt \quad (D30)$$

If  $\sigma$  is a constant, equation (D29) can be rewritten as

$$F(j\omega) = \int_{-\infty}^{\infty} f_l(t)e^{-j\omega t} dt \quad (D31)$$

where,  $f_l(t) = f(t)e^{-\sigma t}$ .

Equation (D31) is the Fourier transform of  $f_l(t)$ , for which very efficient inversion algorithms exist to find  $f_l(t)$  given  $F(j\omega)$ . However, the choice of  $\sigma$  must be such that the integral in equation (D31) converges. This is accomplished by choosing

$$\sigma = \frac{-\ln(0.05)}{1.5 \cdot T_{max}} \quad (D32)$$

where,  $T_{max}$  = maximum time at which the function  $f(t)$  is to be evaluated.

Now, if we have an arbitrary Laplace transform,  $F(s)$ , we can obtain a spectrum by setting  $s = \sigma + j\omega$  and computing  $F(s)$  for equally-spaced values of  $\omega$ ; i.e., for

$$\omega_i = \frac{2\pi i}{T_{max}} \quad (D33)$$

where,  $i = 0, 1, 2, 3 \dots$

The inverse Fourier transform of this spectrum will give the function  $f_l(t)$  in equation (D31), from which the desired function  $f(t)$  is easily generated from

$$f(t) = f_l(t)e^{\sigma t} \quad (D34)$$

The inversion algorithm has been extensively tested on equations where time-domain solutions are known, and it has proven to be very accurate. Accuracy for the purposes of this work was ensured by using more and more terms in the Fourier transforms until the solutions no longer changed.

## Appendix D References

- Becker, M. W. 1996. *Tracer Tests in a Fractured Rock and Their First Passage Time Mathematical Models*. Ph.D. dissertation. Austin, Texas: University of Texas at Austin, pp. 110-115, 119-131. TIC Catalog # 236855. RIS Accession # MOL.19980601.1733.
- de Hoog, F. R., J. H. Knight, and A. N. Stokes. 1982. "An Improved Method for Numerical Inversion of Laplace Transforms." *SIAM J. Sci. Stat. Comput.*, 3(3), 357-366. (Submitted to RIS for Accession # 5/21/99.)
- Jenson, V. G., and G. V. Jeffreys. 1977. *Mathematical Models in Chemical Engineering*, 2nd ed., London, Academic Press, pp. 169-170. (Submitted to RIS for Accession # 5/21/99.)
- Kreft, A., and A. Zuber. 1978. "On the Physical Meaning of the Dispersion Equation and Its Solutions for Different Initial and Boundary Conditions." *Chem. Eng. Sci.*, 33, 1471-1480. (Submitted to RIS for Accession # 5/21/99.)
- Levenspiel, O. 1972. *Chemical Reaction Engineering*, 2nd ed. New York: John Wiley and Sons, pp. 273-282. RIS Accession # NNA.19910207.0115.
- Lindhardt, S. MathCad® worksheet at the World Wide Web address:  
<http://www.mathsoft.com/appsindex.html>, 1995.
- Maloszewski, P., and A. Zuber. 1983. "Interpretation of Artificial and Environmental Tracers in Fissured Rocks with a Porous Matrix." In *Isotope Hydrology*, pp. 635-651. Vienna, Austria: International Atomic Energy Agency (IAEA). (Submitted to RIS for Accession # 5/21/99.)
- Maloszewski, P., and A. Zuber. 1985. "On the Theory of Tracer Experiments in Fissured Rocks with a Porous Matrix." *J. Hydrology*, 79, 333-358. TIC Catalog # 222390.
- Maloszewski, P., and A. Zuber. 1991. "Influence of Matrix Diffusion and Exchange Reactions on Radiocarbon Ages in Fissured Carbonate Aquifers." *Water Resour. Res.*, 27(8), 1937-1945. (Submitted to RIS for Accession # 5/21/99.)
- Moench, A. F. 1989. "Convergent Radial Dispersion: A Laplace Transform Solution for Aquifer Tracer Testing." *Water Resour. Res.*, 25(3), 439-447. TIC Accession # 238281.

- Moench, A. F. 1995. "Convergent Radial Dispersion in a Double-Porosity Aquifer with Fracture Skin: Analytical Solution and Application to a Field Experiment in Fractured Chalk." *Water Resour. Res.*, 31(8), 1823-1835. TIC Catalog # 233132.
- National Research Council. 1996. *Rock Fractures and Fluid Flow: Contemporary Understanding and Applications*. Washington, D.C: National Academy Press, pp. 252-259. TIC Catalog # 235913.
- Rasmuson, A., and I. Neretnieks. 1986. "Radionuclide Migration in Strongly Fissured Zones: The Sensitivity to Some Assumptions and Parameters." *Water Resour. Res.*, 22(4), 559-569. (Submitted to RIS for Accession # 5/21/99.)
- Spanier, J., and K. B. Oldham. 1987. *An Atlas of Functions*. New York: Hemisphere Publishing, pp. 555-562. (Submitted to RIS for Accession # 5/21/99.)
- Stehfest, H. 1970. "Numerical Inversion of Laplace Transforms." *Commun. ACM*, 13, 47-49. (Submitted to RIS for Accession # 5/21/99.)
- Tang, D. H., E. O. Frind, and E. A. Sudicky. "Contaminant Transport in a Fractured Porous Media: Analytical Solution for a Single Fracture." *Water Resour. Res.*, 17(3), 555-564. TIC Catalog # 225368. RIS Accession # NNA.19900711.0084.

## Appendix D Figure

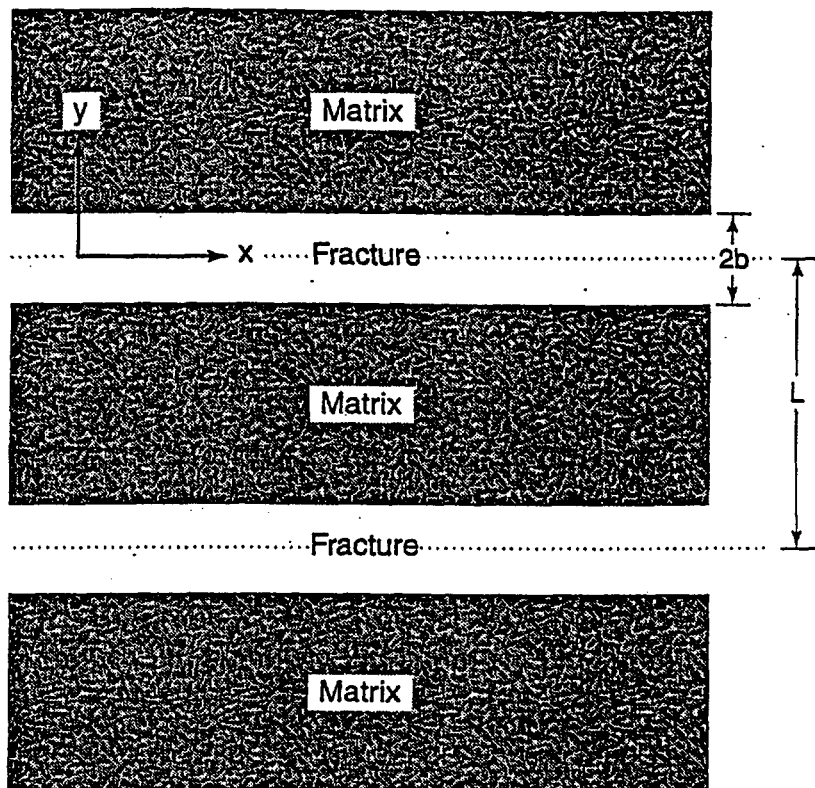


Figure D-1. System geometry assumed in conceptual dual-porosity model.